

# **Numerical and Analytical Modelling of Battery Thermal Management using Passive Cooling Systems**

**Angelo GRECO**

This thesis is submitted in partial fulfilment  
of the requirements for the degree of  
Doctor of Philosophy

November 2015

Lancaster University  
Faculty of Science and Technology  
Engineering Department

# Table of contents

List of Figures .....	6
Abstract .....	14
Acknowledgement .....	15
Nomenclature .....	16
Chapter 1: Literature review of the battery thermal management systems .....	22
1.1. Introduction.....	22
1.2. Thermal modelling of the battery .....	24
1.2.1. Lumped thermal model .....	25
1.2.2. Three-dimensional and two-dimensional thermal modelling of the battery.....	26
1.3. Heat generation modelling.....	29
1.3.1. Heat generation with irreversible and reversible terms.....	29
1.3.2. Electrochemistry of a battery cell.....	31
1.4. Battery thermal management systems .....	32
1.4.1. Active cooling systems and configurations.....	32
1.4.2. Optimization of active cooling systems .....	38
1.4.2.1. Optimization of an active cooling system for cylindrical battery pack .....	39
1.4.2.2. Optimization of cold plate in the case of prismatic battery pack .....	40
1.4.2.3. Mini channel liquid cold plate .....	45
1.4.3. Passive cooling management systems .....	48
1.4.3.1. Heat pipe .....	48
1.4.3.2. Phase change material.....	50
1.5. Experimental methods .....	62
1.6. Conclusions.....	63
Chapter 2: A theoretical and computational study of lithium-ion battery thermal management for electric vehicles using heat pipes.....	65
2.1. Introduction.....	65
2.2. Design of the battery cooling system.....	67
2.3. Problem description and modelling simplification.....	69
2.3.1 Model formulation of the heat pipe .....	69
2.3.2 Thermal model formulation of the battery .....	71
2.4. Research methods: analytical solution, 1D model and 3D numerical simulation .....	72
2.4.1 One-dimensional analytical model .....	72
2.4.2 One-dimensional computational model .....	75

2.4.3	<i>Three-dimensional numerical simulation</i> .....	76
2.5.	Results and discussions.....	77
2.5.1	<i>Forced convection and fixed temperature</i> .....	77
2.5.2	<i>Theoretical test of linear temperature vapour in the heat pipe</i> .....	79
2.5.3	<i>Battery cell sandwiched by two heat pipe sets</i> .....	80
2.5.4	<i>Equivalent thermal conductance of the heat pipe</i> .....	83
2.5.5	<i>Thermodynamic process within the heat pipe</i> .....	84
2.6.	Concluding Remarks.....	85
Chapter 3: An investigation of lithium-ion battery thermal management using paraffin/porous-graphite-matrix composite.....		87
3.1.	Introduction.....	87
3.2.	Geometry and problem description.....	89
3.2.1.	<i>Battery</i> .....	90
3.2.2.	<i>PCM/CENG</i> .....	91
3.3.	Analytical methodology.....	91
3.3.1.	<i>Analytical solution of a forced convection cooling</i> .....	91
3.3.2.	<i>Analytical solution of the cooling by PCM/CENG</i> .....	95
3.3.3.	<i>1D computational model</i> .....	101
3.4.	Results and discussions.....	103
3.4.1.	<i>Test case</i> .....	103
3.4.2.	<i>Comparison of 3D CFD and analytical model for forced convection cooling</i> ...	104
3.4.3.	<i>Comparison of 3D CFD model, analytical solution and 1D computational model for PCM/CENG cooling without latent heat</i> .....	106
3.4.4.	<i>Comparison 1D-analytical-PCM/CENG solution and 1D-computational model with addition of the latent heat</i> .....	109
3.5.	Comparison of PCM/CENG cooling with forced convection cooling .....	112
3.6.	Effects of the bulk density and the PCM .....	114
3.6.1.	<i>Bulk density</i> .....	114
3.6.2.	<i>PCM</i> .....	117
3.7.	Conclusions.....	119
Chapter 4: Development of the cell-centred Lagrangian diffusion code.....		121
4.1.	Introduction.....	121
4.2.	CCLAD generality .....	121
4.2.1.	<i>Flux calculation</i> .....	122

4.2.2.	<i>Global cell-centered system</i> .....	124
4.3.	Test case and validation .....	126
4.3.1.	<i>Temperature and phase change validation</i> .....	127
4.3.2.	<i>Effects of the electrochemistry</i> .....	129
4.4.	Conclusion .....	133
Chapter 5: A coupled thermal and electrochemical study of lithium-ion battery cooled by paraffin/porous-graphite-matrix composite.....		134
5.1.	Introduction.....	134
5.2.	Cylindrical battery cell cooled by a PCM/CENG composite .....	137
5.3.	Electrochemistry model .....	138
5.3.1.	<i>Pseudo two-dimensional model (P2D)</i> .....	138
5.3.2.	<i>Average model</i> .....	139
5.3.3.	<i>Solid phase diffusion</i> .....	141
5.3.4.	<i>Solution phase diffusion</i> .....	144
5.4.	Analysis of the battery module scale .....	146
5.5.	Comparison between the new and usual battery module design configurations .....	150
5.5.1.	<i>Analysis of both configurations with constant heat generation</i> .....	151
5.5.2.	<i>Analysis of both configurations with the electrochemistry model (AM)</i> .....	153
5.6.	Summary.....	157
Chapter 6: Conclusions and future recommendations .....		159
6.1.	Introduction.....	159
6.2.	Heat Pipe Modelling .....	161
6.3.	CCLAD code .....	163
6.4.	Optimization of BTMS .....	164
6.4.1.	<i>Active cooling</i> .....	164
6.4.2.	<i>Dynamic compact thermal model using genetic algorithm</i> .....	167
6.4.2.1.	<i>DELPHI Methodology</i> .....	167
6.4.2.2.	<i>Boundary conditions set or scenarios</i> .....	168
6.4.2.3.	<i>Choice of the nodes</i> .....	169
6.4.2.4.	<i>Genetic algorithm</i> .....	170
6.4.2.5.	<i>Error estimation</i> .....	171
References.....		173
Appendix A.....		179
Appendix B .....		181

Appendix D.....	185
Appendix E.....	186

## List of Figures

Fig. 1. Different Battery geometries and level of analysis. ....	23
Fig. 2. Single battery unit and a single cell unit composed of separator ( $\delta_1, \delta_5, \delta_9$ ), negative electrode ( $\delta_2, \delta_4$ ), positive electrode ( $\delta_6, \delta_8$ ), current collector of the anode ( $\delta_3$ ) and the cathode ( $\delta_7$ ). ....	24
Fig. 3. Equivalent circuit of the battery: (a) Gao et al. [7] and (b) Chen et al. [8]. ....	25
Fig. 4. Numerical simulation of a cylindrical battery cell with isotropic conductivity ((a), (b)) and anisotropic conductivity (c) [13]. ....	27
Fig. 5. Comparison of cell temperature between CFD and the Foster Network model [14]. ...	27
Fig. 6. Example of foster network with four RC pairs, where R is a resistor and C a capacitor. ....	28
Fig. 7. Comparison of cell temperature between CFD and the Foster Network model. ....	28
Fig. 8. Internal resistance of the battery (a) and entropy of the battery cell (b) in function of the SOC [12]. ....	30
Fig. 9. Temperature distribution for a series (a) and parallel (b) distribution cooling [6]. ....	32
Fig. 10. Localisation (a) and description of the Serpentine channel (b) in the battery pack [27]. ....	33
Fig. 11. Schematic of the battery pack with 20 battery units and two surrounding cooling ducts [17]. ....	33
Fig. 12. Transient temperature distribution at the mid-plane (y-direction) (a) and overall temperature distribution at the end of the discharge (b) of the battery pack at 2C discharge rate with air and $h = 7W.m^{-2}K^{-1}$ [17]. ....	34
Fig. 13. Distribution of the average temperature and voltage from battery-to-battery in the pack at the end of the 2C discharge rate with air and $h = 7W.m^{-2}K^{-1}$ [17]. ....	34
Fig. 14. Transient temperature distribution at the mid-plane (y-direction) (a); overall temperature distribution at the end of the discharge (b); and average battery-to-battery voltage distribution (c) of the battery pack at 2C discharge rate with air and forced convection cooling $h = 50W.m^{-2}K^{-1}$ [17]. ....	35
Fig. 15. Schematic view of the reciprocating flow system: (a) from the right to left side and (b) from left to right side [30]. ....	36
Fig. 16. Geometric characteristic of a line-bank cylinder battery cells [30]. ....	37
Fig. 17. Comparison of the maximum cell temperature between CFD and lumped-capacitance model with a reciprocating cooling flow [30]. ....	38
Fig. 18. Battery pack with 150 tubes use as cooling media [31]. ....	39

Fig. 19. (a) Schematic of the CFD analysis, (b) Description of the cooling plate channel by 18 design variables [32].....	41
Fig. 20. Set of initial cooling channel designs selected using Latin Hypercube Sampling (LHS) [32]. .....	42
Fig. 21. Cooling plate geometry (cooling channel in black) and optimized designs [32]. .....	42
Fig. 22. Temperature distributions on the bottom face for the different objective function [32].....	43
Fig. 23. Four linear heat flux gradients from 0 (blue) to 1000 W m <sup>-2</sup> (red). From Left to right: +y, -y, +x, -x. +y indicates a heat flux whose magnitude increases linearly from zero in the direction of the positive y axis [33]. .....	44
Fig. 24. Cooling plate geometry of four designs $T_c$ -optimized, with non-uniform heat flux distributions and a coolant flow rate of 0.001 kg s <sup>-1</sup> . (a) +y, (b) -y, (c) +x, (d) -x [33]. .....	44
Fig. 25. (a) External dimensions of ultra-thin liquid cold plate, (b) Structure dimensions (mm) of ultra-thin LCP [34]. .....	45
Fig. 26. (a) Boundary layer of a conventional straight channel, (b) Boundary layer of channel with oblique cuts [34]. .....	46
Fig. 27. The secondary flow effects on the flow mixing in the main channel [34]. .....	46
Fig. 28. (a) Flow distribution of a single-inlet-outlet configuration, (b) Flow distribution of a two-inlet-outlet configuration [34]. .....	47
Fig. 29. Average surface temperature of straight channel and oblique fin LCP [34]. .....	47
Fig. 30. Overall heat transfer coefficient of straight channel and oblique fin LCPs [34]. .....	48
Fig. 31. Experimental setup of a battery cell cooled by heat pipe [36] .....	49
Fig. 32. Mesh of the cylindrical battery cell cooled by PCM [41]. .....	51
Fig. 33. Temperature variation in the radial direction with $h = 5W.m^{-2}K^{-1}$ and the thermal conductivity of the PCM $k_{PCM} = 3W.m^{-1}K^{-1}$ [41]. .....	51
Fig. 34. Single (a) and double PCM (b) shells configuration [42]. .....	51
Fig. 35. (a) Experimental set up and (b) positions of the thermocouples for the study of PCM 1 [43]. .....	52
Fig. 36. (a) Measured temperature during melting of the PCM around the heater; (b) heater temperature in air, and with PCM 1 protection, subject to constant heat rate [43]. .....	53
Fig. 37. (a) Simulation of cyclic temperature variation around a PCM 1 protected battery; (b) schematic of melting of a phase change material with a line heat source [43]. .....	53
Fig. 38. Melting PCM around a heater [43]. .....	54

Fig. 39. Schematic representation of 5S4P module configuration: (a) PCM filled closed box, (b) Li-ion cells, (c) battery module [47].	55
Fig. 40. (a) Air cooling; (b) PCM cooling; (c) Cell temperature at $T_{amb} = 40^{\circ}C$ [47].	56
Fig. 41. Temperature profiles in two adjacent cells $T_{amb} = 40^{\circ}C$ : (a) air cooling; (b) PCM/graphite cooling [47].	56
Fig. 42. Propagation of thermal runaway due to a single runaway cell with: (a) air cooling, (b) interstitial PCM/graphite [47].	57
Fig. 43. Top view of the half module with insulating stands [47].	57
Fig. 44. The design structure of the generic battery cooling system using heat pipes.	67
Fig. 45. Schematic presentation of the heat transfer working process of a heat pipe.	68
Fig. 46. The design and geometrical properties of the heat pipe with a groove structure.	69
Fig. 47. Thermal network of a heat pipe.	70
Fig. 48. Groove structure at: (a) the evaporator; and (b) the condenser.	71
Fig. 49. The simplified thermal network of heat pipe.	71
Fig. 50. The 1D domain of study.	73
Fig. 51. Nodes of the 1D computational model of the battery connected to the heat pipe set.	76
Fig. 52. Mesh of the battery cell in the 3D numerical simulation.	77
Fig. 53. Temperature distribution of the battery with fixed temperature and convective heat coefficient.	78
Fig. 54. Battery cell temperature with fixed temperature and convective coefficient for the three cases.	79
Fig. 55. Comparison of battery temperature between the 1D computational and analytical models with a linear vapour temperature in the heat pipe.	80
Fig. 56. Battery cell sandwiched by two heat pipe sets.	81
Fig. 57. Comparison of maximum temperature for the forced convection (CS1) and heat pipe set (CS2) in a distributed configuration using the same convective heat coefficient.	81
Fig. 58. Comparison of temperature distribution between CS1 and CS2.	82
Fig. 59. Maximum temperature of the battery cell using equivalent approach for the heat pipe set.	83
Fig. 60. Minimum temperature of the battery cell using equivalent approach for the heat pipe set.	84
Fig. 61. Verification of the sub-cooling condition of the heat pipe operation, using the method proposed in [37].	85
Fig. 62. Geometry of the cylindrical battery cell.	90
Fig. 63. Cylindrical battery cell surrounded by a PCM/CENG composite.	91

Fig. 64. Description of the battery cooling by PCM/CENG.....	98
Fig. 65. Thermal network of the battery cooled by PCM/CENG. ....	101
Fig. 66. Partition of the entire domain. ....	102
Fig. 67. CFD results ( $^{\circ}\text{C}$ ) of the forced convection of the battery. ....	104
Fig. 68. Maximum temperature of 3D CFD simulation and Analytical solutions (1D and 3D) at different heights. ....	105
Fig. 69. 2D-axisymmetric CFD model after application of the symmetry conditions. ....	106
Fig. 70. Comparison of the mesh for the CFD Simulation. ....	107
Fig. 71. Comparison between natural convection and adiabatic condition at the top for the 3D CFD model. ....	107
Fig. 72. Comparison between the 3D CFD model, 1D analytical-PCM/CENG solution and 1D computational model, when $l_f=0$ and $h_z=0$ . ....	108
Fig. 73. Maximum temperature of the battery for different time-steps. ....	110
Fig. 74. Maximum temperature of the battery cooled by PCM/CENG for the 1D analytical and computational models. ....	111
Fig. 75. Contact temperature and minimum temperature of the Battery cooled by PCM/CENG for the 1D analytical and computational models. ....	111
Fig. 76. Comparison between the forced convection cooling and the PCM/CENG cooling for $h_f=20 \text{ W.m}^{-2}.\text{K}^{-1}$ . ....	112
Fig. 77. Maximum temperature with the equivalent convective coefficient applied on the battery cell. ....	113
Fig. 78. Minimum temperature with the equivalent convective coefficient applied on the battery cell. ....	114
Fig. 79. Maximum temperature of the battery cell cooled by PCM/CENG for various bulk densities. ....	115
Fig. 80. Relative discrepancy of the maximum temperature (steady state) for different bulk densities relative to $\rho_{CENG}=200 \text{ kg.m}^{-3}$ . ....	116
Fig. 81. Equivalent thermal resistance and Biot number of the PCM/CENG versus the bulk density.....	117
Fig. 82. Maximum temperature of the battery cell for the n-octadecane and n-heptadecane. .....	118
Fig. 83. Zoom-in of Fig. 82.....	118
Fig. 84. Notation for sub-cells surrounding the node $p$ located in the computational domain. .....	122
Fig. 85. Notation for sub-cells surrounding the node $p$ located at the boundary with Robin boundary condition applied at the external half-edge. ....	124

Fig. 86. Triangular meshes on SALOME with an inner cell $\omega_c$ and a cell $\omega_c^*$ close to the boundary. ....	125
Fig. 87. Meshes of the test case of the cylindrical battery cell cooled by a PCM/CENG matrix. ....	127
Fig. 88. Comparison of the maximum and minimum temperatures of the battery cell cooled by PCM/CENG matrix between the CCLAD code, 1D computational model, analytical solution and SYRTHES. ....	128
Fig. 89. Comparison between the 1D computational model and the CCLAD code with the addition of the phase change model. ....	128
Fig. 90. Comparison between the 1D computational model and the CCLAD code with the addition of the electrochemistry model (AM) for the 2C discharge rate. ....	129
Fig. 91. Comparison between the 1D computational model and the CCLAD code with the addition of the electrochemistry model (AM) for the 4C discharge rate. ....	130
Fig. 92. Comparison between the 1D computational model and the CCLAD code with the addition of the electrochemistry model (AM) for the 8C discharge rate. ....	130
Fig. 93. Impact of the enthalpy on the temperature rise for the 2C discharge rate of cylindrical battery cell cooled by a PCM/CENG composite. ....	131
Fig. 94. Impact of the enthalpy on the temperature rise for the 4C discharge rate of cylindrical battery cell cooled by a PCM/CENG composite. ....	132
Fig. 95. Impact of the enthalpy on the temperature rise for the 8C discharge rate of cylindrical battery cell cooled by a PCM/CENG composite. ....	132
Fig. 96. P2D model of the Li-ion battery. ....	138
Fig. 97. (a) Spatial discretization of the spherical particle in the solid phase, and the normalised Li-ion concentration at the surface of the electrode particles for the discharge rate of: (b) 2C; (c) 4C; and (d) 8C. ....	143
Fig. 98. (a) Comparison between the transient 1D computational solution diffusion model and the steady state analytical solution for different discharge rates. (b) Solution phase concentration at different discharge rates at t=25s and t=100s. ....	145
Fig. 99. Cylindrical battery cells embedded in a PCM/CENG block: (a) 3D simulation; (b) 2D simulation. (c) Comparison between the 2D and 3D results for battery cells 1 and 2. ....	148
Fig. 100. A new design of the battery module: a quarter of the battery module cooled by the PCM/CENG with fins ( $L_{fin}=3\text{ mm}$ ; $r_{PCM}=9\text{ mm}$ ; $W_{fin}=1\text{ mm}$ ). ....	149
Fig. 101. Battery module configurations (a quarter of the domain is shown): (a) the usual design; (b) the new design; and (c) the new design without the fins. ....	151

Fig. 102. (a) Comparison between SYRTHES, CCLAD code and the 1D computational model for the new design with constant heat generation. (b) Comparison between SYRTHES and CCLAD code for the usual design with constant heat generation. (c) Comparison of the maximum and minimum temperatures with constant heat generation between the new and usual designs. ....	153
Fig. 103. (a) Positions and names of the monitored cells. Comparisons between the new and usual designs at T65, T226, T382, T580, T786, T929, T623 for the discharge rate of: (b) the 4C; (c) the 8C, with modified $c_{s,n,max}$ and $c_{s,p,max}$ . (d) Comparison of the maximum and minimum temperatures for the new design configuration with and without the fins. ....	156
Fig. 104. Prismatic battery module cooled by heat pipe sets. ....	162
Fig. 105. Geometries and corresponding domains for three heat pipe configurations [76]...	163
Fig. 106. Schematic of the coupling between the thermal and fluid dynamic software .....	165
Fig. 107. Geometry generated in SALOME7.4 with a python script .....	165
Fig. 108. Temperature results of the cooling of a prismatic battery cell by a cold plate: (a) solid domain of the cold plate, (b) liquid domain at the end of the simulation. ....	166
Fig. 109. Comparison between analytical model and CFD model for the optimization modelling procedure. ....	166
Fig. 110. DELPHI methodology .....	167
Fig. 111. 3D detailed model of the electronic component QFN32. ....	168
Fig. 112. Choice of the internal and external node of the QFN32. ....	169
Fig. 113. Initial compact model before optimization process. ....	170
Fig. 114. Genetic Algorithm process [79]. ....	171

## List of Tables

Table 1. Summary and comparison of the different thermal and heat generation models and their coupling .....	59
Table 2. Comparisons of the different BTMS presented. ....	61
Table 3 Mechanical characteristics and thermo-physical properties of the battery ([53]). ....	72
Table 4 Position of the nodes studied for the 1D analytical and numerical models. ....	78
Table 5 Discrepancy of temperature between the 1D computational and analytical models. .	78
Table 6 Directional Biot number. ....	79
Table 7: Physical properties of the cylindrical battery cell 26650 [13] .....	90

Table 8: Physical Properties of the PCM.....	103
Table 9: Physical Properties of the CENG .....	104
Table 10: Effective Physical properties of the PCM/CENG composite based on the test case data.....	106
Table 11. Particle size radius in function of the discharge rate [25].....	143
Table 12. Surface and volume cooling of the two module designs. ....	150
Table 13. Example of boundary condition set .....	169

## **Declaration**

I declare that this thesis consists of original work undertaken solely by myself at Lancaster University between 2013 and 2015 and that, where work by other authors is referred to, it has been properly referenced.

Angelo GRECO

## Abstract

This thesis presents the battery thermal management systems (BTMS) modelling of Li-ions batteries and investigates the design and modelling of different passive cooling management solutions from single battery to module level. A simplified one-dimensional transient computational model of a prismatic lithium-ion battery cell is developed using thermal circuit approach in conjunction with the thermal model of the heat pipe. The proposed model is compared to an analytical solution based on variable separation as well as three-dimensional (3D) computational fluid dynamics (CFD) simulations. The three approaches, i.e. the 1D computational model, analytical solution, and 3D CFD simulations, yielded nearly identical results for the thermal behaviours. Therefore the 1D model is considered to be sufficient to predict the temperature distribution of lithium-ion battery thermal management using heat pipes. Moreover, a maximum temperature of 27.6°C was predicted for the design of the heat pipe setup in a distributed configuration, while a maximum temperature of 51.5°C was predicted when forced convection was applied to the same configuration. The higher surface contact of the heat pipes allows a better cooling management compared to forced convection cooling. Accordingly, heat pipes can be used to achieve effective thermal management of a battery pack with confined surface areas.

In addition, the thermal management of a cylindrical battery cell by a phase change material (PCM) / compressed expanded natural graphite (CENG) is investigated. The transient thermal behaviour of both the battery and the PCM/CENG is described with a simplified one-dimensional model taking into account the physical and phase change properties of the PCM/CENG composite. The 1D analytical/computational model predicted nearly identical results to the three-dimensional simulation results for various cooling strategies. Therefore, the 1D model is sufficient to describe the transient behaviour of the battery cooled by a PCM/CENG composite. Moreover, the maximum temperature reached by the PCM/CENG cooling strategy is much lower than that by the forced convection in the same configuration. In the test case studied, the PCM showed superior transient characteristics to forced convection cooling. The PCM cooling is able to maintain a lower maximum temperature during the melting process and to extend the transient time for temperature rise. Furthermore, the graphite-matrix bulk density is identified as an important parameter for optimising the PCM/CENG cooling strategy.

Finally, the lithium-ion battery cooling using a passive cooling material (PCM) / compressed expanded natural graphite (CENG) composite is investigated for the battery module scale. An electrochemistry model (average model) is coupled to the thermal model, with the addition of a one-dimensional model for the solution and solid diffusion using the nodal network method.

The analysis of the temperature distribution of the battery module scale has shown that a two-dimensional model is sufficient to describe the transient temperature rise. In consequence, a two-dimensional cell-centred finite volume code for unstructured meshes is developed with additions of the electrochemistry and the phase change. This two-dimensional thermal model is used for investigating a new and usual battery module configurations cooled by PCM/CENG at different discharge rates. The comparison of both configurations with a constant source term and heat generation based on the electrochemistry model, showed the superiority of the new design. In this study, comparisons between the predictions from different analytical and computational tools as well as open-source packages were carried out, and close agreements have been observed.

### **Acknowledgement**

I want to thank my supervisor Professor Xi Jiang for his support and trust. Besides, I am really thankful for the freedom I had, which was essential to achieve the work done during the PhD.

I would like to thank also Dr Mauro Mineo for the good conversations and advices during these years.

*“Calm is a safe guide which could not get lost by any labyrinth”*

*Hamadou Hampate Ba*

*“Ubi pater sum, ibi patria”*

*Friedrich Nietzsche*

## Nomenclature

$a$	Height of the groove channel [ $m$ ]
$a_s$	Active surface area [ $m^2$ ]
$A$	Geometric area of the electrodes [ $m^2$ ]
[ $A$ ]	Global matrix of the thermal conductance in the CCLAD code [ $W.K^{-1}$ ]
$b$	Width of the groove channel [ $m$ ]
$Bi$	Biot number
$c_e$	Concentration of $Li^+$ in the electrolyte [ $mol.m^{-3}$ ]
$c_s$	Concentration of reduced lithium in the solid phase [ $mol.m^{-3}$ ]
$c_p$	Specific heat per unit mass [ $J.kg^{-1}.K^{-1}$ ]
$c_{vc}$	Specific heat per unit mass of a cell $\omega_c$ in the CCLAD code [ $J.kg^{-1}.K^{-1}$ ]
$C$	Capacity of the battery cell [Ah]
[ $C$ ]	Matrix of the thermal capacitance [ $J.K^{-1}$ ]
[ $C_v$ ]	Global matrix of thermal capacity in the CCLAD code [ $J.K^{-1}$ ]
$D_e$	Electrolyte phase diffusion coefficient [ $m^2.s^{-1}$ ]
$D_s$	Solid phase diffusion coefficient [ $m^2.s^{-1}$ ]
$e_b$	Thickness of the battery cell [ $m$ ]
$F$	Faraday constant [ $C.mol^{-1}$ ]
$f$	Transcendental function in the case of the PCM/CENG cooling
$f_l$	Liquid fraction of the PCM
[ $G$ ]	Matrix of the conductance [ $W.K^{-1}$ ]
$G_{conv}$	Thermal conductance of convection [ $W.K^{-1}$ ]
$G_e$	Conductance of electrolyte solution [ $m^{-3}.s^{-1}$ ]
$G_s$	Conductance of electrode [ $m^{-3}.s^{-1}$ ]
$h_{conv}$	Heat transfer coefficient for natural convection [ $W.m^{-2}.K^{-1}$ ]
$h_{fg}$	Latent heat of vaporisation [ $J.kg^{-1}$ ] in Chapter 2
$h_r$	Heat transfer coefficient in the radial direction [ $W.m^{-2}.K^{-1}$ ]
$h_z$	Heat transfer coefficient in the axial direction [ $W.m^{-2}.K^{-1}$ ]
$I$	Current intensity flowing through the system [A] in Chapter 5
$i$	Discharge current per unit volume [ $A.m^{-3}$ ]

$i_0$	Exchange current density [ $A.m^{-2}$ ] in Chapter 5
$J_0$	Zero-order Bessel function of the first kind
$J_1$	First-order Bessel function of the first kind
$j_f$	Current per unit volume [ $A.m^{-3}$ ]
$k$	Thermal conductivity [ $W.m^{-1}.K^{-1}$ ]
$k_c$	Thermal conductivity of a cell $\omega_c$ in the CCLAD code [ $W.m^{-1}.K^{-1}$ ]
$K$	Permeability of the capillary structure [ $m^2$ ] in Chapter 2 Thermal conductivity tensor in the CCLAD code [ $W.m^{-1}.K^{-1}$ ] in Chapter 4
$k_{wall}$	Thermal conductivity of the heat pipe material envelop [ $W.m^{-1}.K^{-1}$ ]
$L$	Length of the cylindrical battery cell [m] in Chapter 2 Length of the solution phase in the electrochemistry model [m] in Chapter 5
$L_{adia}$	Length of the adiabatic section [m]
$l_b$	Width of the battery cell [m]
$L_b$	Length of the battery cell [m] in Chapter 2 Height of the battery cell [m] in Chapter 5
$L_c$	Length of the condenser section [m]
$L_{ev}$	Length of the evaporator section [m]
$L_{fin}$	Length of a fin [m] in Chapter 5
$l_f$	Latent heat of fusion [ $J.kg^{-1}$ ]
$L_{total}$	Length of the heat pipe [m]
$L_z$	Half length of the battery cell [m]
$M$	Working fluid merit number [ $m^2$ ]
$n$	number of electron exchange during the discharge
$N_C$	Capillary number [ $W.m^2$ ]
$N_{GS}$	Number of groove section in one heat pipe
$N_{HP}$	Number of heat pipe in the set
$[P]$	Matrix of internal power [W]
$q$	Internal heat generation in the battery [ $W.m^{-3}$ ]
$q_k$	Production term in the solution phase in the domain $k$ [ $mol.s^{-1}.m^{-3}$ ]
$q_{ext}$	Heat removed by the cooling system [ $W.m^{-3}$ ]

$Q_{\max}$	Capillary limit [W]
$[Q]$	Matrix of the source term in the CCLAD code [W]
$r_1$	Position of the interface battery/CENG in the PCM/CENG cooling case [m]
$r_2$	Position of the external surface of the PCM/CENG composite in the radial direction [m]
$R$	Radius of the cylindrical battery cell in convection cooling case [m] in Chapter 3 Radius [m] in Chapter 2 Ideal gas constant [ $\text{J.K}^{-1} \cdot \text{mol}^{-1}$ ] in Chapter 5
$R_{\text{conv}}$	Thermal resistance of convection [ $\text{W.K}^{-1}$ ]
$R_i$	Internal equivalent resistance per unit volume [ $\Omega \cdot \text{m}^3$ ]
$\tilde{R}_{i,n}$	$n$ th eigenfunction of the $i$ th solid in the radial direction for the PCM/CENG cooling
$R_s$	Radius of spherical particle in the electrode [m]
$\Delta S$	Entropy of an electrode [ $\text{J.K}^{-1} \cdot \text{mol}^{-1}$ ]
$S_b$	Surface of the battery cell at $x = e_b$ [ $\text{m}^2$ ]
$S_{\text{conv}}$	Surface cooled in the radial direction in the PCME/CENG cooling [ $\text{m}^2$ ]
$S_l$	Liquid section of the heat pipe [ $\text{m}^2$ ]
$t$	Time [s]
$t^+$	Li-ion transference number
$T$	Temperature [ $^{\circ}\text{C}$ ]
$[T]$	Matrix of the temperature [ $^{\circ}\text{C}$ ] in Chapters 2 and 3 Matrix of the cell-centered temperature in the CCLAD code [ $^{\circ}\text{C}$ ] in Chapter 4
$[\bar{T}]$	Matrix of the half-edge temperature in the CCLAD code [ $^{\circ}\text{C}$ ]
$U$	Thermodynamic equilibrium voltage [V]
$V$	Volume allocated to a node [ $\text{m}^3$ ]
$V_{\text{cell}}$	Cell voltage [V]
$w_{pc}$	Sub-cell surface of a cell $\omega_c$ [ $\text{m}^2$ ] in Chapter 4
$w_c$	Cell surface of a cell $\omega_c$ [ $\text{m}^2$ ] in Chapter 4
$W_{\text{fin}}$	Width of a fin [m]
$Y_0$	Zero-order Bessel function of the second kind
$Y_1$	First-order Bessel function of the second kind
$x_s$	Normalised Li-ion concentrations at the surface of an electrode

*Greek letters*

$\alpha_i$	Thermal diffusivity of the $i$ th solid
$\alpha_{ox}$	Charge transfer coefficient of anodic reaction
$\alpha_{red}$	Charge transfer coefficient of the reduction reaction
$\beta_p$	$p$ th eigenvalue associated with the $p$ th eigenfunctions $\tilde{\Phi}_p$
$\gamma$	Geometric ratio in the PCM/CENG cooling case in Chapter 3 Flux of particle in the solid phase [mol. s <sup>-1</sup> ] in Chapter 5
$\delta$	Thermal diffusivity ratio in the PCM/CENG cooling case in Chapter 3 Length of electrode and separator [m] in Chapter 5
$\Delta$	Variation
$\varepsilon$	Porosity of the CENG graphite matrix
$\varepsilon_e$	Volume fraction of the electrolyte
$\varepsilon_s$	Volume fraction of the active material
$\varepsilon_f$	Volume fraction of the filler
$\eta$	Electrode overpotential [V]
$\Theta$	Thermo-physical property group [m <sup>2</sup> ]
$\Theta_n$	Time-variable function PCM/CENG cooling case
$\kappa$	Ionic conductivity [S.m <sup>-1</sup> ]
$\lambda_{i,n}$	$n$ th eigenvalue associated with the $n$ th eigenfunction $\tilde{R}_{i,n}$ in the PCM/CENG cooling
$\lambda_{ev}$	Equivalent thickness at the evaporator in chapter 2
$\mu$	Viscosity [kg.m <sup>-1</sup> .s <sup>-1</sup> ]
$\mu_n$	$n$ th eigenvalue associated with the $n$ th eigenfunctions $\tilde{X}_n$
$\Pi$	Function defined by Eq. (3.32a)
$\rho$	Density [kg.m <sup>-3</sup> ]
$\sigma$	Surface tension [N.m <sup>-1</sup> ] in Chapter 2 Half width of the melting interval temperature [°C] in Chapter 3 Solid phase conductivity [S.m <sup>-1</sup> ] in Chapter 5
$\varphi_{gen}$	Heat generation [W] in Chapter 5
$\varphi_i$	Time-variable function of the $i$ th solid for the homogeneous equation in the PCM/CENG cooling case
$\phi$	Electric potential [V] in Chapter 5

$\phi_{1,n}$	Function defined by Eq. (3.31b) in Chapter 3
$\Phi$	Geometric dimensions group [m <sup>2</sup> ]
$\tilde{\Phi}_p$	$p$ th eigenfunctions in the axial direction for the convection cooling case
$\tilde{X}_n$	$n$ th eigenfunctions in the radial direction in the convection cooling case
$\Psi$	Dimensionless number defined in Eq. (2.16) [37]
$\Psi_{n,p}$	Time-variable function in the convection cooling case in Chapter 3

*Subscripts and acronyms*

<i>adia</i>	Adiabatic
<i>AM</i>	Average model
<i>Amb</i>	Ambient
<i>Brugg</i>	Bruggman coefficient
<i>c</i>	Condenser in chapter 2
	Cell of the computational domain in chapter 4
<i>CENG</i>	Compressed expanded natural graphite
<i>comp</i>	PCM/CENG composite
<i>e</i>	Electrolyte
<i>eff</i>	Effective
<i>ev</i>	Evaporator
<i>GS</i>	Groove section
<i>g</i>	Graphite (CENG)
<i>gen</i>	Generated
<i>H</i>	Homogeneous
<i>HP</i>	Heat pipe
<i>i=1,2</i>	Index number for the battery and the PCM/CENG composite respectively
<i>m</i>	Melting
<i>max</i>	Maximum
<i>min</i>	Minimum
<i>n</i>	Negative electrode
<i>ox</i>	Relative to oxidation reaction
<i>p</i>	Positive electrode
<i>PCM</i>	Passive Cooling Management in Chapter 2
	Phase change material in Chapters 3 and 5

*PP* Porous electrode with polynomial approximation  
*P2D* Pseudo two-dimensional  
*red* Relative to reduction reaction  
*s* Solid phase  
*sep* Separator in the electrolyte domain  
*SOC* State of charge  
*SP* Single particle  
*v* Vapour  
*x,y,z* Coordinates

*Superscript*

*eff* Effective  
*surf* Relative to the surface of the spherical particle at the electrode  
*n* *n*th time step

# Chapter 1: Literature review of the battery thermal management systems

## 1.1. Introduction

The depletion of the global oil resources conjugated to the effort of reduction of the carbon dioxide has made the development of EV (Electric Vehicle)/HEV (Hybrid Electric Vehicle) a major issue for the future. The battery used to provide power to the EV/HEV during driving operation has been studied in order to provide an optimal performance. In terms of this, the Li-ions battery technology globally used in electronic applications, has been designated as the best candidate, due to its higher energy density and lower self-discharge. However, the temperature has an important impact on the reliability, lifespan, safety and performances [1, 2]. The battery life is reduced by corrosion of the components, when higher temperatures (superior to 50 °C [3]) are reached. Besides, decompositions of materials in the battery can lead to safety issue such as explosions [1]. The operating temperature of the battery must be kept between 20 °C and 40 °C [2] for achieving good performances and long lifespan. At very cold temperature, the battery performs sluggishly due to high internal resistance. Pesaran [4] had investigated experimentally and numerically different preheating method for prismatic battery module with different aspect ratio, in order to bring the module to a reasonable temperature range and obtain good performances. The best method was the core heating of the battery module by applying AC power to the battery terminals, instead of a DC current, which can damage the battery due to the high internal resistance.

Moreover, temperature uniformity across the battery pack is important, in order to avoid short circuit or local degradation due to hot spots. Considering, the temperature dependence of the battery cell voltage, a large temperature variation in the battery pack generates unbalanced battery voltage, leading to safety issue. Therefore, it is prescribed to keep the temperature difference from cell to cell and module to module below 5 °C [3].

Efficient cooling systems need to be design for maintaining the battery in the prescribed temperature range [2, 3]. The battery thermal management system (BTMS) is aimed to provide effective cooling solutions and also to develop new tools simulating the behaviour of the battery during operation depending on the cooling solution applied to it. The development of faster model prediction will allow to improve the design process of the BTMS and to reduce manufacture cost.

Different models have been developed, addressing generally or specifically a design issue. With respect to this, the lifespan of a battery pack was studied by Yuksel and Michalek [5]. They developed a model estimating the improvement of battery life by air cooling using a thermal management and battery degradation model based on experimental data for a battery pack. They performed simulations in two cities Miami and Phoenix, with daily driving scenarios and average seasonal ambient temperature. When the thermal management is used, the battery had a longer life in Phoenix than in Miami. However, the non-use of the thermal management system led to a battery life decrease of one year only in Miami and three years in Phoenix, even with the temperature in Phoenix lower than Miami for half the year but with

higher peak temperature observed. These results showed that considering an identical battery pack, the thermal management efficiency is dependant of the region and is also critical to peak temperatures.

Their model could be improved by considering daily or hourly ambient temperature averages instead of seasonal ones, since the peak temperatures have important influences on the battery life. Besides, they considered a uniform temperature distribution in the pack and constant temperature surface in their cooling design configuration, which will be unlikely in practical applications [6]. Nevertheless, this model is fast and well dedicated to system level analysis.

In consequence, the development of models used to predict the behaviour of the temperature and to design the BTMS is depending on the level of analysis and geometry as shown in Fig. 1

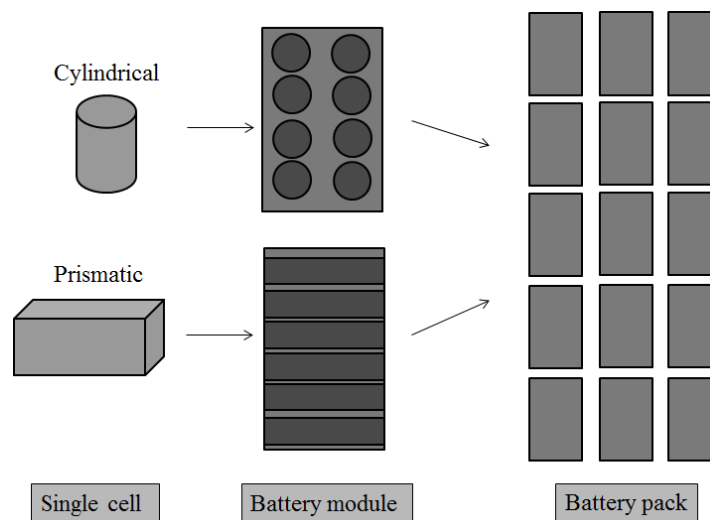


**Fig. 1.** Different Battery geometries and level of analysis.

A very detailed model will be time-consuming and will require huge computing resources, while addressing specific level of analysis and using certain battery and BTMS characteristics can help to have faster and relatively efficient model prediction. The chapter is dedicated to the general presentation of the modelling of the battery thermal management and to describe different BTMS approach strategies. The design of a cooling system implies to know the temperature field of the battery during operation and to measure the impact of the BTMS on this temperature fields. The thermal modelling of the battery cell and architecture will be presented first, followed by the mathematical description of the heat generation during driving operation. Next, the different battery thermal management system are described and analysed through different publication addressing this issue. As shown before, this study of the BTMS is dedicated to the modelling of the battery for predicting the thermal behaviour in function of the cooling solution applied. Different new cooling strategies are presented in subsequent chapters of this thesis, and a paragraph in this chapter will present different experimental study which could be used in future work and for the validation of the models developed.

## 1.2. Thermal modelling of the battery

A single battery unit is made of different layers as presented in Fig. 2 for the prismatic shape and round up in a spiral form in the case of a cylindrical cell. A single cell unit is composed of a negative and positive electrode separated by a separator with an electrolyte allowing the diffusion of the Li-ions between both electrodes. Two current collectors are positioned at the electrode for transferring the electrons during discharge/charge (Fig. 2). The details of the electrode material and chemistry will be fully presented later in this chapter.

A battery cell is made of many single cell units in order to reach the electrical voltage needed. Each layer has different properties with certain mechanisms in action during discharge/charge. The thermal equation of the problem can be described by Eq. (1.1), where  $q_{gen}$  represents the heat generated by the battery and  $q_{ext}$  the heat removed from the battery by the cooling system.

$$\frac{\partial(\rho c_p T)}{\partial t} = \nabla \cdot (\lambda \nabla T) + q_{gen} + q_{ext} \quad (1.1)$$

The modelling of these terms is addressed subsequently and the modelling of the conduction is presented first. The application of Eq. (1.1) to all the different layers of the battery can be very time-consuming. Therefore, certain simplifications depending on the level of analysis and accuracy were developed.

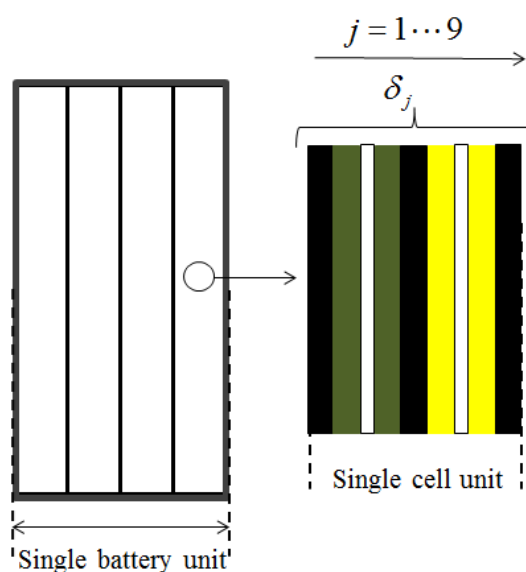


**Fig. 2.** Single battery unit and a single cell unit composed of separator ( $\delta_1, \delta_5, \delta_9$ ), negative electrode ( $\delta_2, \delta_4$ ), positive electrode ( $\delta_6, \delta_8$ ), current collector of the anode ( $\delta_3$ ) and the cathode ( $\delta_7$ ).

### 1.2.1. Lumped thermal model

A lumped model consists of one node for representing the battery cell with the total volume allocated to it and with equivalent physical properties. This model is mainly used in the case of battery pack simulation and also in electrochemistry analysis of the battery cell. In fact, the study of the electrochemistry needs to account for the temperature effect, by coupling with the energy equation.

Gao et al. [7] modelled the transient behaviour of a commercial Li-ion battery with a cooling system effect modelled by heat transfer coefficients. The authors intended to replicate the electrical and thermal properties of the battery as it interacts with the external world. At this level they ignored all spatial variation of concentrations, phase distribution and considered the electro-thermal and electro-chemical process as uniform throughout the entire battery. These assumptions allow them to represent the battery by an equivalent electric circuit model.

This electric circuit provides the main characteristics of a battery cell such as the internal resistance, the equilibrium voltage, the voltage. In addition, these characteristics were fitted with experimental data in order to improve the accuracy of their model. Moreover, Chen et al. [8] developed a similar approach with a simplified electric circuit presented in Fig. 3. The internal resistance of battery cell is still fitted with experimental data and represented by  $R_1$  and  $R_2$ . Their results were less accurate than the one predicted by Gao et al. [7] due to the simplifications but were more faster and simpler to compute. In both cases, the model shows satisfactory results in average temperature and low discharge rate. Besides, it is simple to use and applicable to other batteries without referring to the specific geometry.

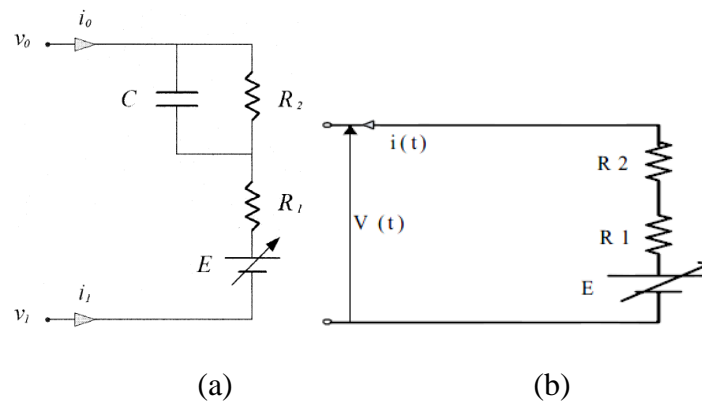


**Fig. 3.** Equivalent circuit of the battery: (a) Gao et al. [7] and (b) Chen et al. [8].

However, the thermal approach is too simple to predict the temperature distribution in the cell, which can be problematic in the case of high gradient of temperature. Additionally, deviations were observed at low temperature and at high discharge rate. The accuracy of the lumped model depends on the cooling strategy, discharge/charge rate and on the characteristic of the battery cell modelled.

Nonetheless, the knowledge of temperature gradient is important for the BTMS design. In this regard, an approach considering global physical properties calculated from the properties of each layers (Fig. 2) of the battery was developed.

### *1.2.2. Three-dimensional and two-dimensional thermal modelling of the battery*

The layered-structure of the battery cell can be simplified by using global average values. These values in the case of the prismatic shape battery are obtained by analysing the different heat flux paths. Chen et al. [9] studied the impact of using the layered-structure presented in Fig.2 and the global average properties approach on a three-dimensional model of a prismatic battery cell. Both models were in good agreement with a lower simulation time in the case of the global average property approach. Besides, this simplification was also validated numerically by Lin et al. [10] in the case of prismatic battery cell.

Moreover, Niculuta and Veje [11] performed a numerical and experimental study on a prismatic battery cell using global average properties. They obtained close results between the numerical simulation and experiments.

Close agreements between experiments and numerical method were also obtained by Inui et al. [12] on cylindrical and prismatic shape battery cell. The authors developed their own three-dimensional and two-dimensional code including heat generation model which will be presented in the next paragraph. Their model allowed them to study different cooling strategy by modifying the cross section of a prismatic battery cell, while keeping the height constant, i.e. a constant volume for each case. The laminated cross-section presented better cooling efficiency in reducing the maximum temperature, due to its higher surface of cooling but was unable to reduce the unevenness of the battery cell.

The prismatic battery cell studied by the different authors cited before presents an anisotropic thermal conductivity. A lower conductivity 10 to 20 time inferior in the thickness direction of the prismatic cell compared to the other direction. Therefore, a higher temperature gradient is expected in the thickness direction and the cooling system should be designed accordingly.

Furthermore, Drake et al. [13] developed an analytical model to calculate the physical properties of a cylindrical battery cell. The model was validated against experimental measurement and showed an anisotropic thermal conductivity with the radial conductivity 150 inferior to the one in the axial direction. They also demonstrated the importance of considering this anisotropy in order to design an effective cooling system. A simulation using ANSYS had highlighted that using the wrong thermal conductivity could lead to either an oversized cooling system in Fig. 4(a) or a safety issue in Fig. 4(b).

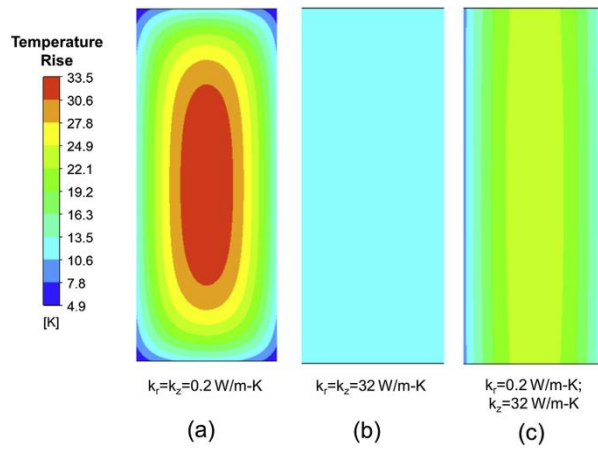


**Fig. 4.** Numerical simulation of a cylindrical battery cell with isotropic conductivity ((a), (b)) and anisotropic conductivity (c) [13].

Another approach developed by Hu et al. [14] used behavioural model to simulate the transient thermal rise of the battery cell cooled by forced cooling convection. The authors saw the thermal problem of the battery as an LTI (Linear Time Invariant) system. However, this is possible only if the boundary conditions are linear (radiative heat transfer not permitted), the velocity fields of the cooling system is frozen and both thermodynamic and transport properties are kept constant.

When the system can be defined as an LTI system, the output response is the convolution product of the impulse step and the input. The authors [14] showed by comparison (on one cell battery) with CFD results that an approximation of a thermal problem as an LTI was possible (Fig. 5). However, for a battery pack with many cells, the convolution can be long and complex to treat. That is why the authors used the Foster network [14].

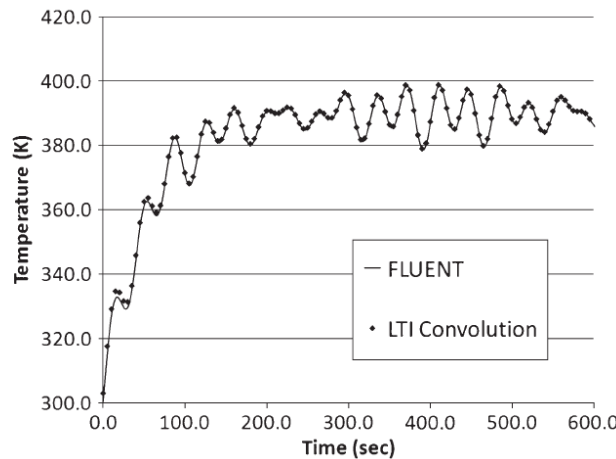


**Fig. 5.** Comparison of cell temperature between CFD and the Foster Network model [14].

The transient average volume temperature of the cell is approximated by a foster network presented in Fig. 6. This method was used in electronic cooling in order reduce the simulation time.

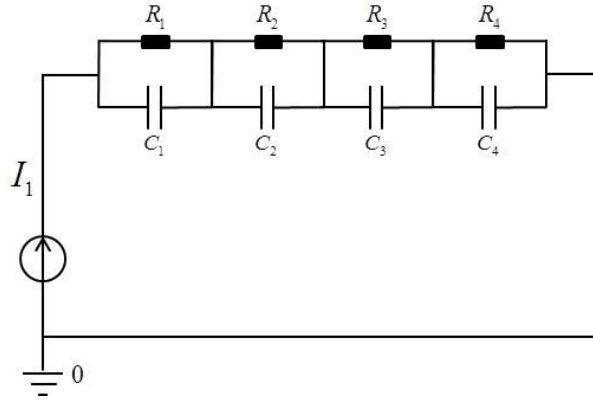


**Fig. 6.** Example of foster network with four RC pairs, where R is a resistor and C a capacitor.

Since both Foster network and battery cell cooling can be considered as LTI systems, they become equivalent if they have the same impulse response. The results from the three-dimensional behaviour presented before, considering global average properties are curve-fitted in order to obtain the parameter  $R_i$  and  $\tau_i$  presented in Eq. (1.2), with  $m$  designating the number of RC pairs (Fig. 6).

$$V = I \sum_{i=1}^m R_i (1 - e^{-t/\tau_i}) \quad (1.2)$$

A close agreement is obtained between the numerical simulation and the model as shown in Fig. 7. This behavioural model is fast to compute and is well suitable for large system simulation. However, its accuracy depends on the CFD model results and a simple modification of the initial CFD model will imply to recalculate everything. This method becomes interesting when the CFD simulation is finalised and unchanged.

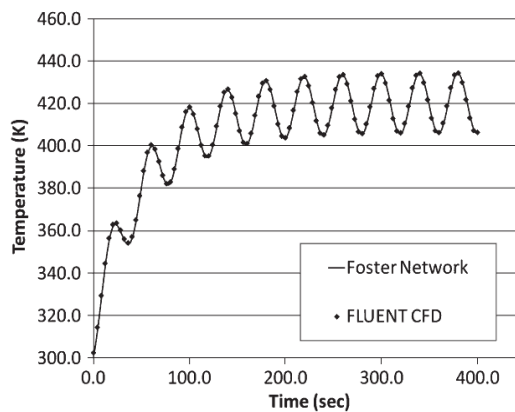


**Fig. 7.** Comparison of cell temperature between CFD and the Foster Network model [14].

Different approaches to model a battery cell are possible, depending on the geometry and level of analysis. The battery can be modelled with only one node, but without information

on the temperature gradient, which is crucial to estimate in order to design an effective cooling system. A multi-dimensional model considering the geometries was the best approach to analyse the temperature gradient during transient temperature rise of the battery. However, the layered-structure of a battery cell unit was time-consuming in the case of complex geometry. Accordingly global properties were used in order to reduce the simulation and this approach was validated against numerical and experimental study.

The heat generation modelling is discussed in the following paragraph with the analysis of the advantages and limits of different models.

### 1.3.Heat generation modelling

The heat generation depends on the chemical reaction in the battery cell. The modelling of this term is still subject to study in order to have a simple and cost-effective simulation time. Bernardi et al. [15] proposed a model of heat generation made of a reversible term and an irreversible term. This model is widely used because of its simplicity of use with thermal models, from lumped thermal model to more complex ones. Nevertheless, this model does not describe all the phenomena occurring in the battery during discharge and it is limited at high discharge rates. A model considering more details of the electrochemistry will allow improving the design of the Li-ions battery in term of safety, lifespan and efficiency. In this regard, Horie et al. [16] showed that the discharge time was depending on the electrode designs. This discharge time could be improved by optimizing the electrode parameters such as the film thickness and reduced particle of the electrode.

A heat generation calculation based on the electrochemistry of the battery is important to accurate prediction of the thermal behaviour of the battery cell in order to provide effective BTMS. The heat generation based only on the irreversible and reversible heat is presented first, followed by the presentation of the electrochemistry models.

#### 1.3.1. Heat generation with irreversible and reversible terms

The following equation presents the model developed by Bernardi et al. [15] with the first term designating the irreversible heat and the second one the reversible one.

$$q_{gen} = \frac{I}{V_{bat}} \left( (E_{OCV} - V) - T \frac{dE_{OCV}}{dT} \right) \quad (1.3)$$

The irreversible heat or Joule heat is a consequence of ohmic and other internal resistances present in the battery cell. The expression of the reversible heat is obtained from the thermodynamic study of the chemical reaction. This term is endothermic in the case of charge and exothermic in discharge process. Eq. (1.3) can be rewritten into the following equation with  $R_i$  representing the equivalent internal resistance and  $i$  designating the volumetric intensity of discharge/charge. This intensity is positive for discharge and negative for the charge in this case.

$$q_{gen} = R_i i^2 - T \Delta S \frac{i}{nF}; \quad i = \frac{I}{V_{bat}}; \quad \Delta S = nF \frac{dE_{OCV}}{dT} \quad (1.4)$$

With  $n$  representing the number of electron exchanged during the chemical reaction. The internal equivalent resistance and the entropy are both function of the state of charge and the temperature. The State of Charge (SOC) for a constant discharge/charge (or galvanostatic discharge/charge) rate is calculated by the following equation and represent the level of capacity of the battery during operation at an instant  $t$ , i.e. an equivalent to a fuel gauge. Therefore, the battery is full when the SOC is at 1 or 100% and empty when reach 0. In practical case, the battery is never completely discharge to 0% due to safety issue.

$$SOC = 1 - i \frac{t}{c_0} \quad (1.5)$$

Inui et al. [12] measured at three different temperatures the internal resistance  $R_i$  of a battery cell in function of the SOC as presented in Fig. 8(a). They performed the same measurement on the entropy  $\Delta S$  and showed that the entropy was mainly dependent on the SOC as shown in Fig. 8(b).

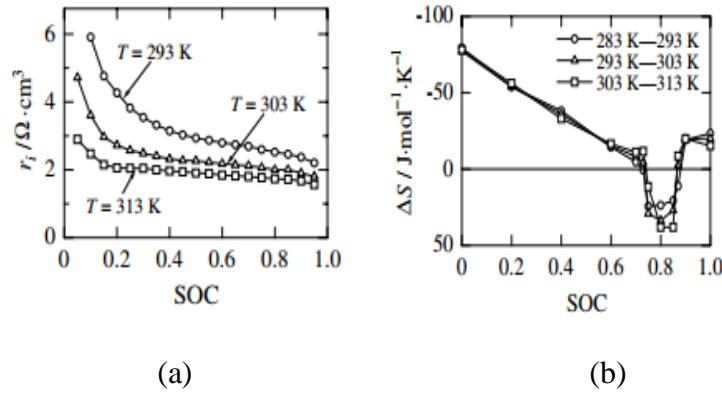


**Fig. 8.** Internal resistance of the battery (a) and entropy of the battery cell (b) in function of the SOC [12].

Correlation based on these measurement were used by Karimi and Li [17] and Liu et al. [18] to represent the heat generation in the battery module in order to analyse different cooling strategy which will be presented subsequently.

Besides, the discharge rate may play an important role in the accuracy of the heat generation model when compared to experiment. For example, Nieto et al [19] observed a very close match with their numerical model using the heat generation formulation presented before at low discharge. However, discrepancies at high discharge rate were observed, mainly due to the limitation of this heat generation formulation to describe and/or take into account other phenomena.

Moreover, the internal resistance of the battery is rarely provided by the battery manufacturer and therefore, experimental tests are always necessary to measure it, since its value and behaviour depends on the chemistry of the battery cell. Nevertheless, this formulation [15] is simple to use and fast enough when complex geometry such as battery module or pack need to be study [11, 19], despite some discrepancies at high discharge rate.

The generality of the electrochemistry of the Li-ions battery is presented in the next paragraph with example of application in the thermal modelling of a battery cell.

### *1.3.2. Electrochemistry of a battery cell*

The improvement of the battery cell capabilities and a better prediction during various discharge/charge operations are crucial for the future of the EV/HEV. Therefore, the modelling of the electrochemistry plays an important role for describing and predicting the capacity loss of the battery during time. Besides, the mechanisms highlighted by the electrochemistry provide a more accurate heat generation prediction, which is necessary for designing an efficient cooling system. In addition, electrical parameters can be studied at the same time.

The Pseudo Two-Dimensional (P2D) model developed by the team of Newman [20, 21] is the reference electrochemistry model for describing the mechanisms of the Li-ions battery. The model was well validated against experiments in constant discharge/charge operations. In their model, the electrodes of the battery cell are porous solid matrix that consists of active particles with spherical shapes of uniform sizes. For a discharging operation, the oxidation at the negative electrode produces Li-ions, which diffuse first from the centre of the spherical particle representing the solid phase. The Li-ions are then transferred to the positive electrode by migration and diffusion in the electrolyte. Finally, the Li-ions are transferred by diffusion in the solid particle of the positive electrode, where a reduction reaction occurred. Besides, for the conservation of the charge, electrons are collected by the current collector.

The electrochemistry must be coupled to a thermal model in order to add the impact on the temperature. However, a lumped thermal model is often considered, when the study is focused on the electrochemistry and also in the case complex problem such as battery pack simulation. In fact, the coupling of both P2D model and three-dimensional thermal model can become very time-consuming and necessitate high computing resources. In consequence a lumped thermal model is used instead to represent the thermal behaviour of each battery of the pack [22, 23].

Moreover, Ye et al. [24] performed a coupling study of the P2D model with experimental correlations for the solid and liquid diffusion coefficients, and a lumped thermal model using the commercial software COMSOL MULTIPHYSICS. Their performed experiments until a discharge rate of 2C with a  $\text{LiMn}_2\text{O}_4$  prismatic battery and obtained a close agreement with numerical results. They used a lumped heat transfer coefficient validated against experiment and accounting for radiative and convective heat at the external surface of the battery cell.

Simplifications of the P2D model were investigated in order to have efficient and cost effective simulation with lumped thermal model and more complex thermal model [25, 26]. The full details of the mathematical description of the P2D model, as well as the simplifications [25] and modifications applied to it as part of this thesis will be presented subsequently in Chapter 5 of this manuscript.

The next chapter will present the different BTMS strategies considering their advantages and weaknesses in terms of the prescribed condition of temperature and gradient.

## 1.4. Battery thermal management systems

The thermal prediction of the battery via different approaches was presented before. The thermal prediction is very important in the choice and design of the BTMS. The cooling solution can be divided into active and passive cooling category. In the active category, fluid is used for cooling in function of the thermal behaviour of the battery pack during driving operation. On the other hand, the passive cooling management category in this work implies to use systems exploiting the phase change of certain materials, in order to cool the battery without a control system.

The active cooling category is analysed first with the presentation of their advantages and limits through different studies. Next, the state of art of the passive cooling method and modelling are presented.

### 1.4.1. Active cooling systems and configurations

Pesaran [6] studied the battery thermal models for hybrid vehicle, considering a lumped capacitance thermal model dedicated for a system level analysis, and a second one using CFD and Finite Element Analysis. His study showed that, a parallel cooling flow is better than a series one for obtaining better temperature uniformity (Fig. 9).

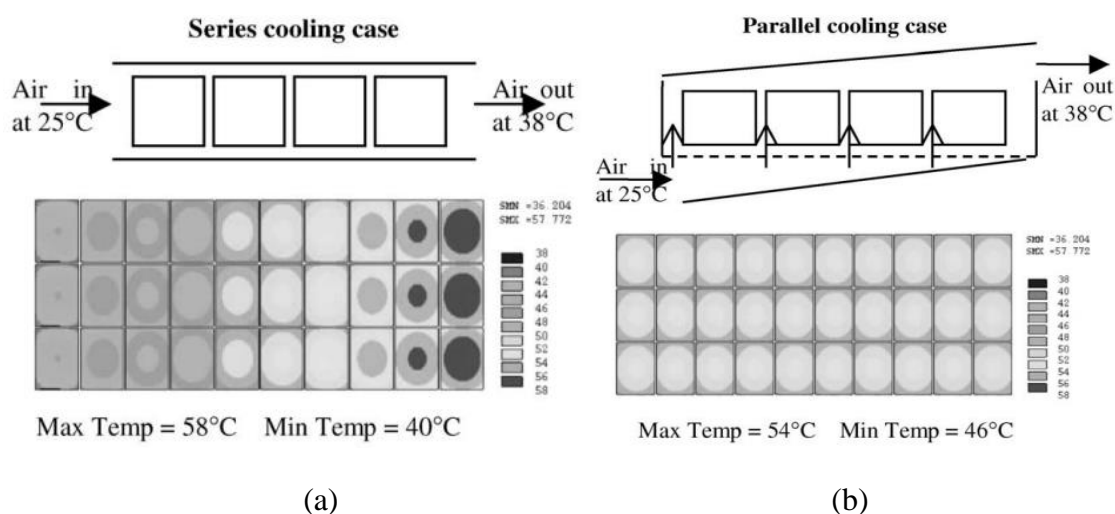


**Fig. 9.** Temperature distribution for a series (a) and parallel (b) distribution cooling [6].

However, air-flow cooling is not efficient for cooling the battery pack due to its low thermal conductivity and thermal capacity. In fact, the minimum temperature as presented in Fig. 9 is superior or equal to 40 °C. Liquid cooling is therefore preferred due to better cooling efficiency. In this way, Chacko [27] used liquid cooling, where each battery module is sandwiched between two cooling plates. A liquid cooling plate consists of a serpentine channel as presented in Fig. 10.

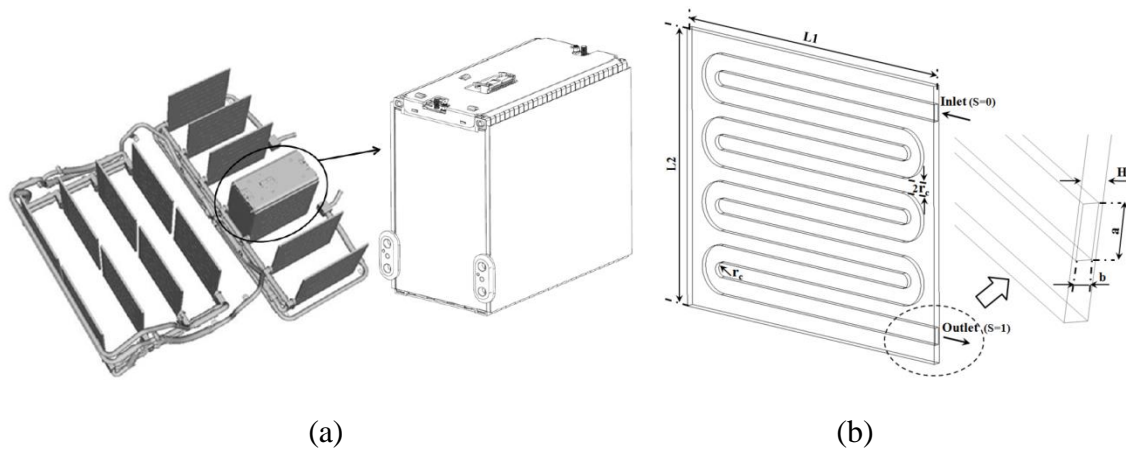


**Fig. 10.** Localisation (a) and description of the Serpentine channel (b) in the battery pack [27].

The different parameters improving the efficiency of the serpentine were also studied by Chacko [27]. The number of bend, the distance between each straight part, and the mass flow were considered in the analysis and had an impact on the efficiency but also on the cost of the cooling system. For example, the increase of the bend will enhance the cooling efficiency, but will increase the pressure drop, necessitating a more powerful pump to move the fluid. In consequence, the cost of the battery thermal management system will increase.

However, the impact on the cooling system to the temperature gradient in the module was not studied and the temperature uniformity could not be analysed. In this respect, Karimi and Li [17] studied a configuration similar to the one used by Chacko [27] for a prismatic battery pack of 20 battery units, with a two-dimensional thermal model with heterogeneous thermal-physical properties of different layers. The cooling system presented in Fig. 11 consists of two cold plates made of several straight cooling ducts instead of serpentine. The two cold plates are located at the external surface of the battery pack and different fluid can be used for the cooling.

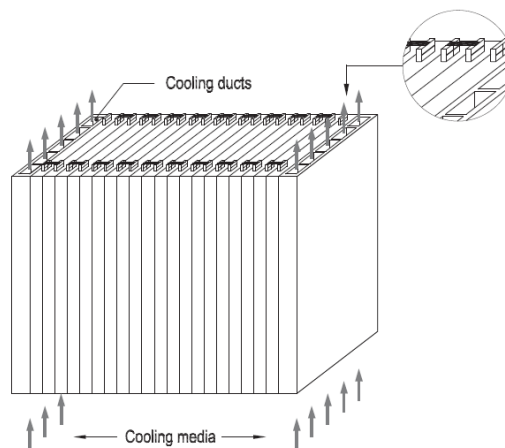


**Fig. 11.** Schematic of the battery pack with 20 battery units and two surrounding cooling ducts [17].

For the configuration shown in Fig. 11, the pack was cooled by air natural convection first. The transient temperature distribution at the mid-plane of the battery pack in the y-direction, while discharging the battery pack at 2C rate from SOC=1 to SOC=0.2, is shown in Fig. 12.

In addition, the capacity  $C$  of a battery cell is in Ah and a discharge at  $2C$  means that 30 minutes are necessary to discharge the battery, while an hour is required at  $1C$ -rate.

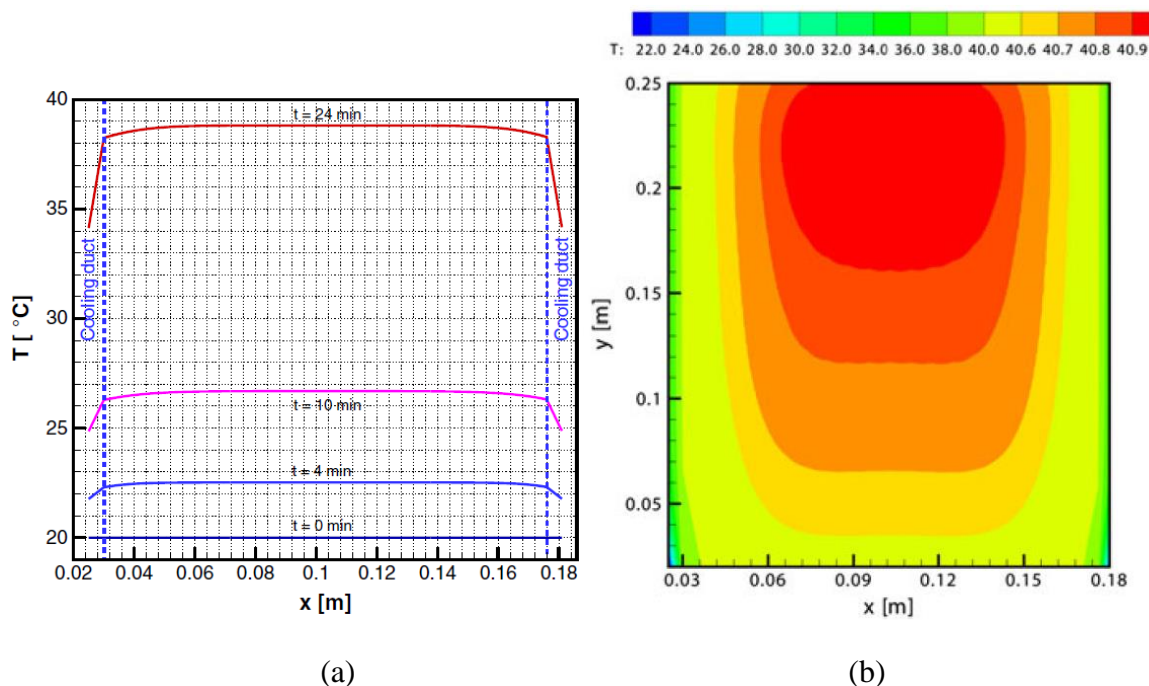


**Fig. 12.** Transient temperature distribution at the mid-plane ( $y$ -direction) (a) and overall temperature distribution at the end of the discharge (b) of the battery pack at  $2C$  discharge rate with air and  $h = 7W.m^{-2}K^{-1}$  [17].

The temperature of the battery pack was kept under  $40$  °C at the condition presented in Fig. 12. However, the unevenness of the temperature had affected the voltage and internal resistance of each battery unit of the pack as shown in Fig. 13.

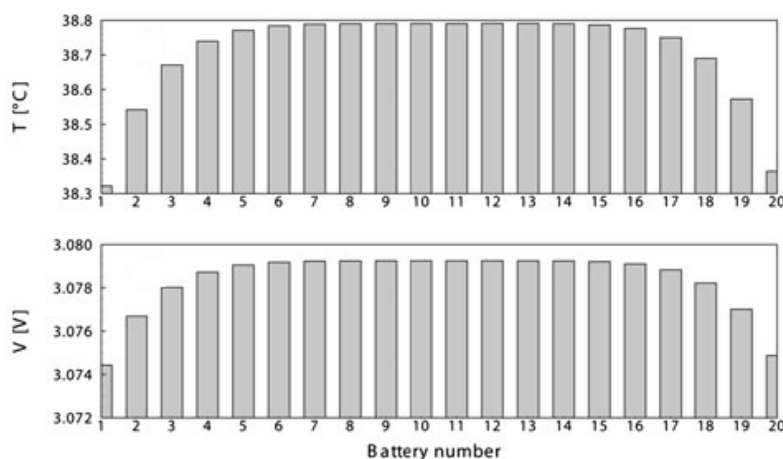


**Fig. 13.** Distribution of the average temperature and voltage from battery-to-battery in the pack at the end of the  $2C$  discharge rate with air and  $h = 7W.m^{-2}K^{-1}$  [17].

The unevenness of temperature led to unbalanced voltage in the battery pack, which can reduce the battery performances in time and raise safety issue. In consequence, the authors [17] proposed a distributed configuration where each battery unit is separated from one to another by a cold plate. This modification increased the volume of the battery pack by 14%

compared to the previous one. Besides, the distributed configuration provided better temperature uniformity across the battery pack, leading to a well-balanced voltage, as presented in Fig. 14.

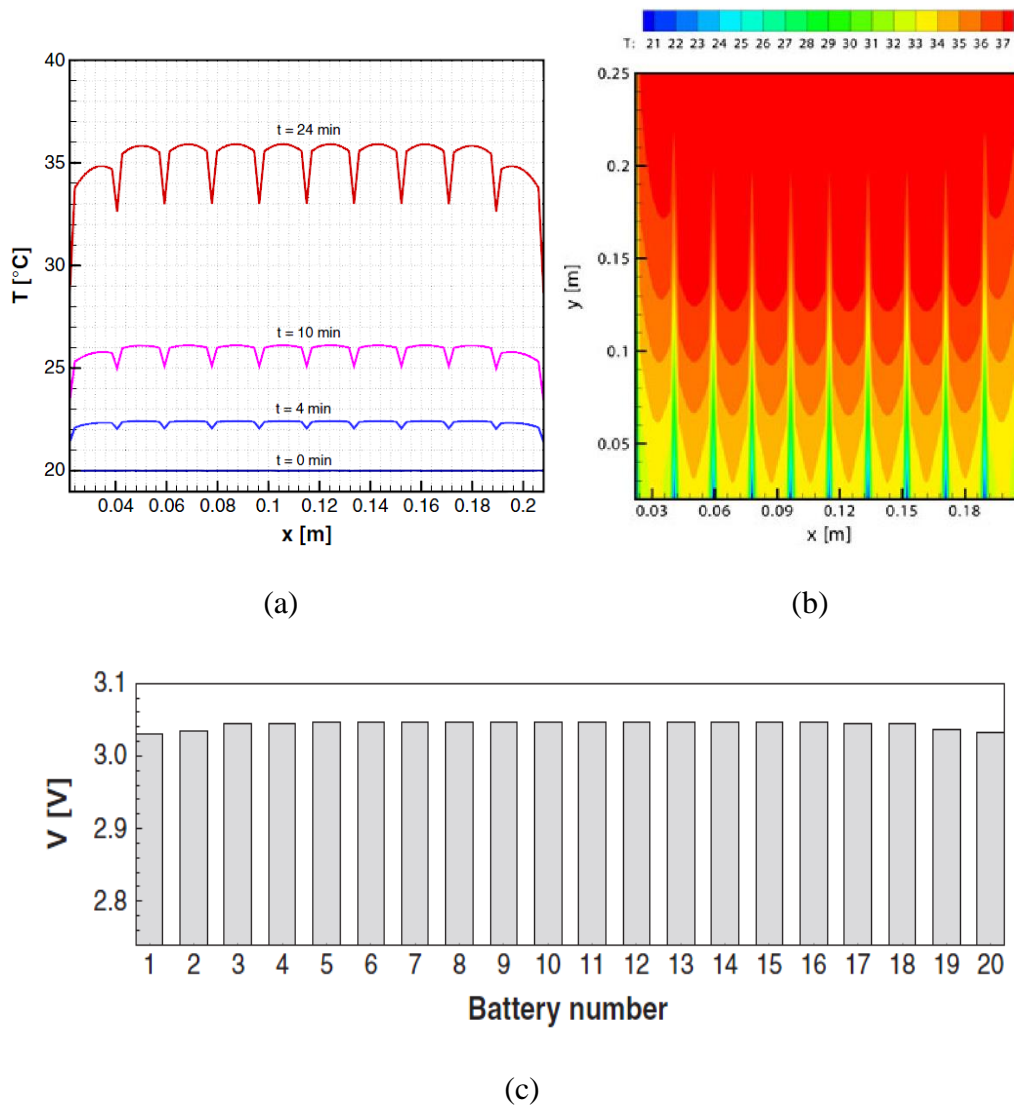


**Fig. 14.** Transient temperature distribution at the mid-plane (y-direction) (a); overall temperature distribution at the end of the discharge (b); and average battery-to-battery voltage distribution (c) of the battery pack at 2C discharge rate with air and forced convection cooling  $h = 50W.m^{-2}K^{-1}$  [17].

A parametric study was performed by Liu et al. [28] on the first configuration used by Karimi and Li [17], i.e. the one presented in Fig. 11. They analysed the impact of the discharge rate, the Reynolds number of the flow in the cooling ducts and the ambient temperature in function of air, liquid and phase change material (PCM) cooling. They used the commercial software FLUENT for running different simulations in order to understand and develop general guideline for choosing the appropriate cooling materials in function of the operating strategies.

They showed that liquid cooling was more efficient for cooling the battery pack. Besides, the PCM cooling was better for keeping a uniform temperature distribution. Nevertheless, the PCM cooling was modelled with a high convective heat transfer coefficient ( $h = 250W.m^{-2}K^{-1}$ ) and the thermal mass was not considered. The other effects of a PCM

cooling were not considered in their study and will be addressed in the next paragraph dedicated to the passive cooling management.

Additionally to this study, the effect of the cooling channel design on Li-ion battery stacks was investigated by Xun et al. [29] for cylindrical and prismatic battery cells. The heat generation was modelled using the model of Bernardi et al [15]. The authors [29] performed analytical and numerical study using FLUENT. The analytical model was developed only for the prismatic battery cells and considered a lumped thermal model for each battery unit of the prismatic battery pack. A close agreement was obtained between the analytical model and the two-dimensional CFD model simulated with FLUENT. A three-dimensional model was considered for the cylindrical battery pack with certain simplifications applied due to symmetry.

A good BTMS must be efficient, cost-effective and compact. The authors [29] introduced subsequently the compactness and the cooling energy efficiency, defined respectively by the volume of the cooling channel over the volume of the battery unit and by the heat taken by cooling air over the power consumption for supplying the cooling air. It was found that for the same compactness, changing the cooling channel size and the number of cooling channels results in similar volume averaged temperature of the stack. However, increasing the cooling channel size improves the cooling energy efficiency but results in more unevenly distributed temperature in the battery pack.

In addition, the general behaviour described before is identical in both cylindrical and prismatic battery stacks, with the cylindrical one less compact but more energy-efficient than the prismatic battery stacks. Moreover, the unevenness of the temperature in the case of the cylindrical cell can be reduced by a counter flow arrangement of the cooling channels or changing the flow direction of the co-flow arrangement periodically.

The periodically changing co-flow arrangement was analysed by Mahamud and park [30]. They performed the simulation of the series cooling of a line-bank cylinder battery cells with a reciprocating air flow system. They also compared a two-dimensional numerical simulation to a lumped thermal model using experimental correlation. Fig. 15 presents the schematic of the reciprocating flow system. The principal parameters used to enhance the heat transfer and assure better temperature uniformity are the reciprocating period  $\tau$ , the battery cell spacing  $S_T/D$  and  $S_L/D$ .

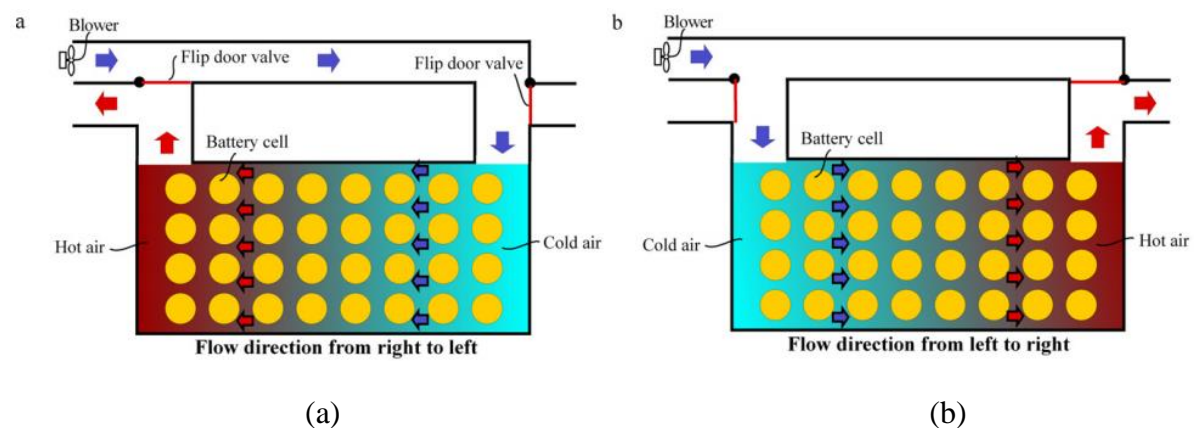


**Fig. 15.** Schematic view of the reciprocating flow system: (a) from the right to left side and (b) from left to right side [30].

The cyclic periodic  $\tau$  of the reciprocating flow is defined as the time for a reciprocating flow to recover its initial flow direction. Note that the uni-directional flow with no change in flow direction is a special case of reciprocating flow having an infinite reciprocating period ( $\tau = \infty$ ). The geometric characteristics of the battery cell spacing  $S_T/D$  and  $S_L/D$  are illustrated in Fig. 16, with only the symmetry plane simulated.

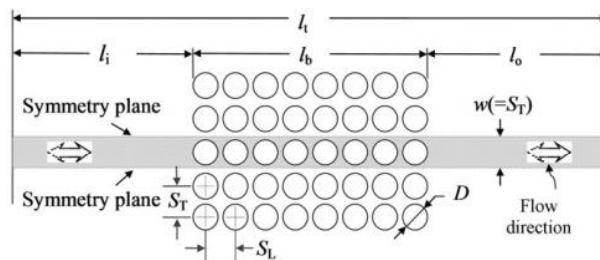


**Fig. 16.** Geometric characteristic of a line-bank cylinder battery cells [30].

Mahamud and Park [30] studied the effect of the reciprocating period ( $\tau=120$  s,  $\tau=1200$  s,  $\tau = \infty$ ) and showed that the shorter the reciprocating periods, the lower the cell temperature difference and the maximum cell temperature (of both instantaneous and time-averaged) of the system. It was shown from the numerical results that the reciprocating flow using  $\tau=120$  s reduces the cell temperature difference by about 4 °C (72% reductions) and the maximum cell temperature by 1.5 °C as compared with the uni-directional case ( $\tau = \infty$ ). The improvement by the reciprocating flow mainly attributes to the heat redistribution and disturbance of the boundary layers formed on the cells, due to the periodic flow reversal.

They also studied the effect of the battery cell spacing. They showed that the maximum temperature decrease with a larger longitudinal spacing ( $S_L$ ) and smaller transverse spacing ( $S_T$ ). The first spacing characteristic  $S_L$  is explained by the creation of bigger eddies and the second spacing characteristic  $S_T$  by an acceleration of the flow, increasing the heat exchange. However, these modifications will increase the pressure drop, implying the use of a more powerful pump.

Besides, a lumped thermal model and flow network model was used and compared to the CFD results. This lumped-capacitance model was considered because the temperature of the each cell could be taken uniform. This assumption was verified by the calculation of the Biot number described by Eq. (1.6). This number represents the ration between the conductive thermal resistance over the one by convection. The Biot calculated in this case was inferior to 0.1, confirming that the cell temperature could be considered as uniform.

$$B_i = \frac{L_c h_f}{k_s} \quad (1.6)$$

The comparison between both lumped and CFD model are presented in Fig. 17, with close agreement for  $Re < 13000$ . Discrepancies appeared after  $Re > 13000$ , because the correlations used in the lumped model predict the averaged heat transfer for the cells in the system and do not take into account recirculation and other effects due to the flow turbulence.

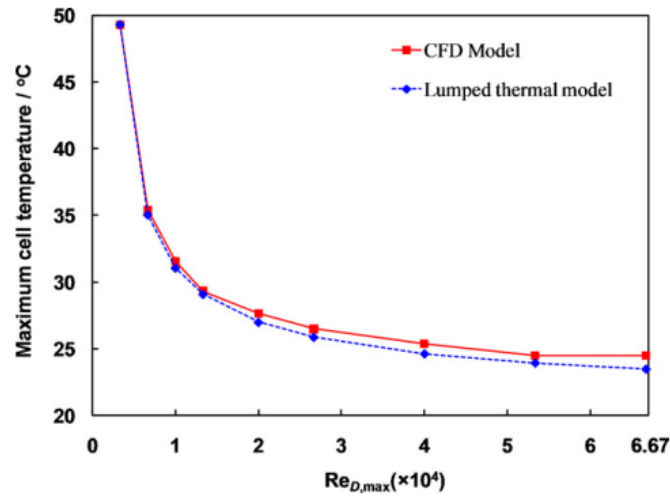


**Fig. 17.** Comparison of the maximum cell temperature between CFD and lumped-capacitance model with a reciprocating cooling flow [30].

Despite this difference, Fig. 17 showed that the prediction of the maximum temperature is very close to the CFD model. Therefore, a lumped thermal model coupled with a flow network model could be used in order to simplify the calculation and reduce the computation time.

Different active cooling strategies were analysed here. Liquid cooling was more suitable for keeping the battery in the prescribed temperature and parallel cooling for maintaining a uniform temperature in the battery pack during operation. Cold plates using serpentine and cooling ducts were analysed in terms of performances and parametric designs. The choice of the fluid, the flow rate and the increase of contact surface were shown to be important in achieving a high efficiency. In addition, in the case of series cooling for cylindrical battery pack, a reciprocating flow had shown to be a reasonable approach for reducing the maximum temperature while keeping the temperature distribution uniform. Nevertheless the use of liquid cooling implies to use a pump drawing power from the battery. Therefore a balance must be found between the power of the pump and the thermal efficiency of the cooling system. The next chapter is dedicated to different approaches to conciliate pump power and thermal requirement during operation.

#### 1.4.2. Optimization of active cooling systems

The battery packs are year after year more compact, in order to increase the power per volume and reduce the mass of the vehicle. In consequence, the heat generated per surface has been increased. Due to this compactness, the active cooling systems must be robust and therefore use paradoxically more power from the battery pack to cool it. A balance must be found between the size of the cooling system, the electric power consumption and the thermal efficiency. The optimization of an active cooling system is in concrete terms, the minimization of the electric consumption of the pump (liquid cooling) or fan (air cooling) with regard to the completion of the thermal prescription. For example in the case of a liquid cooling, the minimum pump power requirement will be obtained by reducing the pressure

drop and by choosing the right mass flow and liquid coolant. The cooling system used or designed depends on the type of battery pack and also of the temperature requirements.

#### 1.4.2.1. Optimization of an active cooling system for cylindrical battery pack

The multiplicity of parameter in an active cooling solution makes the optimization procedure complex and time consuming. In the case of a cylindrical pack, the coolant is the air flow from outside generated by the vehicle movement. Additionally, a fan is integrated in the system for stop and start position and also to help for the cooling when the air flow is no sufficient. Moussavi et al. [31] had optimized the air-cooling system for a cylindrical Li-ion battery pack using a genetic algorithm. Their study was focused on the increasing of the heat transfer rate from the cells to the air. The Number of Transfer Unit (NTU) was a good candidate for quantifying the transfer and measures the cooling efficiency.  $NTU = hA_s / \dot{m}c_p$ , where  $h$  is the heat transfer coefficient,  $A_s$  is the total surface of cooling (Fig. 18),  $\dot{m}$  is the air mass flow and  $c_p$  the thermal heat capacity per unit mass.

The system presented in Fig. 18 is a pack of cylindrical battery cells located around tubes (150) used as cooling media when air passes through them.

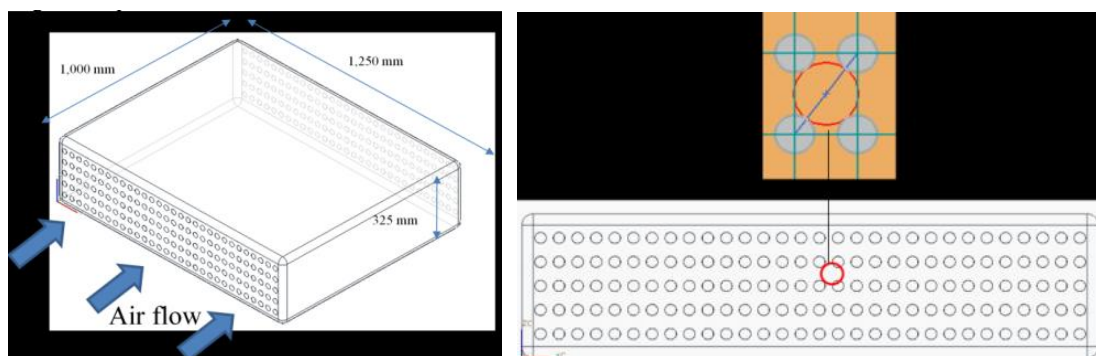


**Fig. 18.** Battery pack with 150 tubes use as cooling media [31].

Based on the efficiency calculation of the system, it can be shown that the maximum heat transfer is obtained for  $NTU = 5$ . It comes naturally in this case to use the NTU as an objective function for the optimization process. In pursuance of fast calculation, simplifications were made to reduce the number of parameters. The surface temperature of the cylindrical battery cells was fixed at  $T_s = 90^\circ C$ , and the physical properties of the coolant were supposed constant. The thermal power transferred from the battery to the environment was evaluated by:

$$Q_{conv} = hA_s \Delta T_{avg}; \quad \Delta T_{avg} = T_s - (T_e + T_i)/2 \quad (1.7)$$

where  $T_i$  and  $T_e$  represents the inlet and outlet temperature of the air respectively. In addition, the heat transfer coefficient was obtained using the following Chilton-Colburn Nusselt correlation:

$$Nu = 0.125 f Re Pr^{1/3}; \quad h = Nu.k/D \quad (1.8)$$

where  $k$  represents the air conductivity and  $D$  is the tube diameter. After 10 runs of the genetic algorithm a value of 4.95 (very close to the maximum) is reached for the NTU, thereby a tube diameter of 0.05 m and an air velocity of 2.559 are obtained. The optimization case presented, was applied on a simplified case, however, this methodology may lead to solve more complex problems.

Nevertheless, some simplifications are important and may completely change the analysis of the prediction. According to Fig. 18, each battery cells was located between the cooling media (tube). In fact each cooling tubes have only 4 contact lines with the battery cells. A thermal transfer by conduction would normally occur at these contacts, between the tubes and the surface of the cells. In consequence, the tubes cannot be directly at the surface temperature of the battery cell. Therefore, the material of the tubes and their behaviour at the contact must be studied. In conclusion, these simplifications led to an overestimation of the total surface of exchange and at the same time to an overestimation of the transfer. An improvement could be done by taking into account the conduction and heat generation of each battery cells and observed the impact of the cooling design on the temperature distribution. Besides, considering the gradient specification (within 5°C), an even temperature in all the pack must be achieved regardless of the characteristics of the cooling system design. However, it has been shown that the unevenness of the temperature distribution increase with the intensity of the forced cooling process [6, 17, 28]. The next part is dedicated to the optimization of the serpentine channel of a cold plate, in the case of prismatic battery pack.

#### *1.4.2.2. Optimization of cold plate in the case of prismatic battery pack*

The prismatic battery cell presents a real advantage in regard of the compactness [29] and the cooling process. Each cell in the pack can be isolated one to another and cooled at the same time [17]. The design of the serpentine channel embedded in the cold plate and the liquid coolant properties have an impact on the performances and efficiency of the cooling process. Therefore, Jarret and Kim [32] studied the optimization of the geometry of the single serpentine channel, subject to a constant heat flux as presented in Fig. 19(a), for three different objective functions. The design variable of the channel is represented in Fig. 19(b) by a vector  $d$  composed of 18 geometric parameters. Besides, a different vector was generated according to the different objective functions.

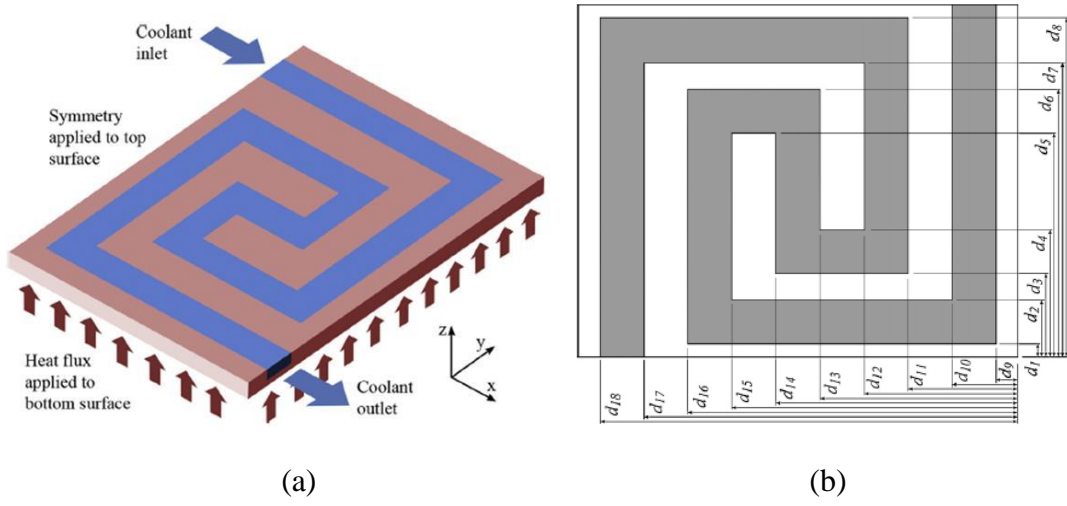


**Fig. 19.** (a) Schematic of the CFD analysis, (b) Description of the cooling plate channel by 18 design variables [32].

The objective functions are based on the pressure drop, the average temperature, and the standard deviation of temperature, respectively described by Eq. (1.9), Eq. (1.10) and Eq. (1.11). The average temperature (Eq. (1.10)) and the standard deviation of the temperature (Eq. (1.11)) are defined over the bottom surface of the plate, where the heat flux is applied.

$$P_{fluid}(d) = P_{inlet} - P_{outlet} \quad (1.9)$$

$$T_{avg}(d) = \frac{\int_{A_0} T dA}{\int_{A_0} dA} \quad (1.10)$$

$$T_{\sigma}(d) = \sqrt{\frac{\int_{A_0} (T - T_{avg})^2 dA}{\int_{A_0} dA}} \quad (1.11)$$

where  $A_0$  and  $d$  represent the bottom surface of the plate and the design variable respectively. In order to reduce the risk of convergence to a local minimum, the optimization where performed from eight different initial design (Latin Hypercube Sampling) shown in Fig. 20.

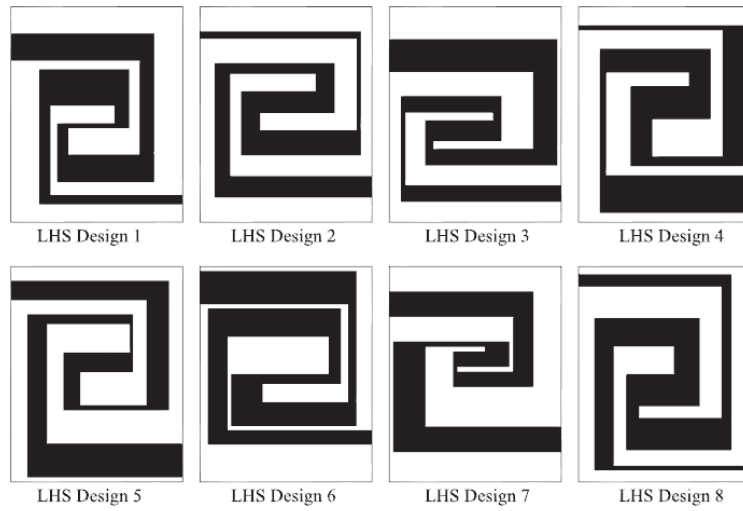


**Fig. 20.** Set of initial cooling channel designs selected using Latin Hypercube Sampling (LHS) [32].

The schematic process for the three optimization functions is presented in Fig. 21, where the geometry and the mesh were created by GAMBIT based on the initial design variable  $d$ . Moreover, the CFD calculation of the case was solved by FLUENT and the output treatments (temperature, pressure drop) and calculation of the objective functions was made by MATLAB. This process was repeated with perturbation of the design variable until the convergence was reached.

The optimization process using the three objective functions was performed on the reference design of the cold plate in Fig. 19(a) and the new designs based on the three objective functions are presented in Fig. 21.

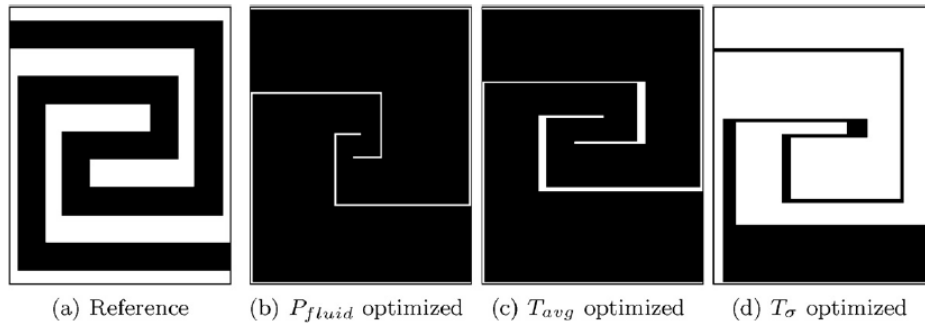


**Fig. 21.** Cooling plate geometry (cooling channel in black) and optimized designs [32].

The  $T_{avg}$  optimization decreased the average temperature by about 14% compared to the reference design presented in Fig. 21(a), the  $P_{fluid}$  and  $T_{\sigma}$  optimizations showed both improvements of greater than 50%. The impact of the serpentine geometry on the temperature distribution is presented in Fig. 22. The gradient of temperature (i.e. the difference between the minimum and maximum temperature) on the bottom surface of the cold plate is equal to 10°C (Fig. 22). Consequently, the gradient of temperature in a battery cell if connected to the cold plate would have been at least equal to 10°C. The requirement of a maximum gradient of 5°C in the battery cell was not respected.

Nonetheless, the study had shown the impact of the optimization on the performance of the cold plate. The fluid flow was in a laminar regime for all the simulations, and never reached the turbulent flow regime, which would be problematic for reducing the pump power. In reality, a turbulent flow would enhance the heat transfer and therefore improving the efficiency of the cold plate, but would also increase the pressure drop. A study of the impact of turbulence on the power consumption of a pump would be useful. Moreover, the optimization routine used in this study is unable to modify the cooling plate topology (Fig. 19(a)).

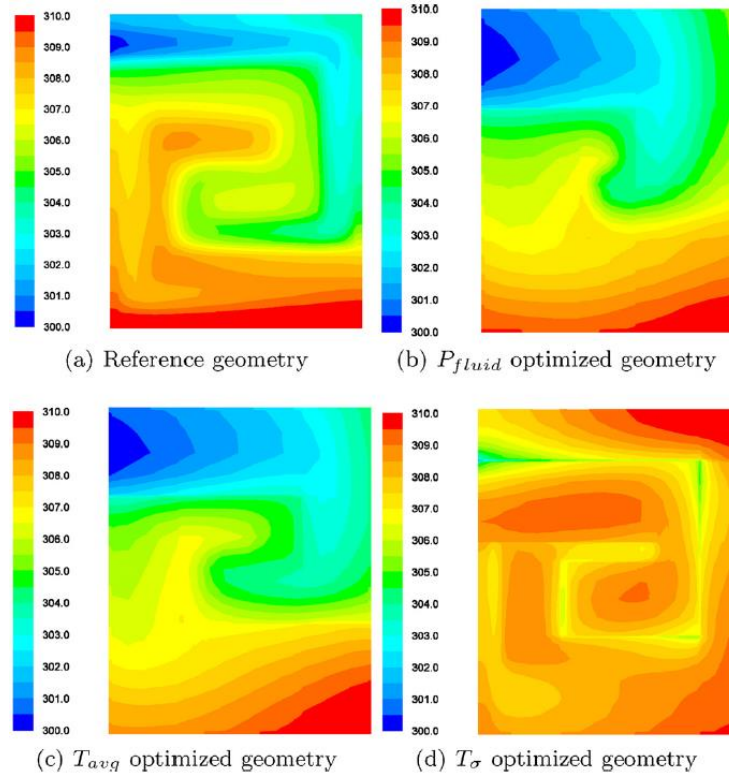


**Fig. 22.** Temperature distributions on the bottom face for the different objective function [32].

In addition, the boundary conditions (mass flow, heat flux) were kept constant during the optimization. However, a real driving case is characterized by a non-uniform heat generation at various discharge rates. In regard of such behaviour, different mass flow will be needed in order to deal with different magnitude of heat generation.

The same authors [33] analysed the impact of the boundary conditions on the optimum cooling plate using the methodology developed previously. A non-uniformity heat flux was modelled by a linear gradient (positive and negative gradients in both the x- and y-directions) with an average magnitude of  $500 \text{ W m}^{-2}$  presented in Fig. 23. This choice was made in order to compare with the previous optimization [32], which was performed with a uniform heat flux of  $500 \text{ W m}^{-2}$  and a mass flow of  $0.001 \text{ kg s}^{-1}$ . Besides, the coolant flow rates from  $0.0004$  to  $0.002 \text{ kg s}^{-1}$  were also used in this study in addition of the  $0.001 \text{ kg s}^{-1}$  used before. The reference geometry presented in Fig. 19(a) was subject to the optimization process for the three objective functions ( $T_{avg}$ ,  $P_{fluid}$ ,  $T_{\sigma}$ ) [32].

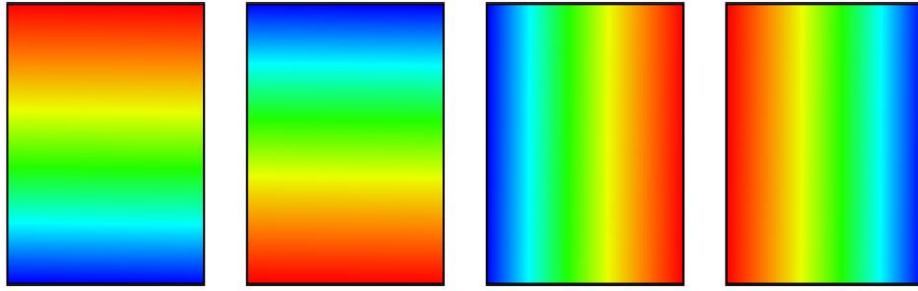


**Fig. 23.** Four linear heat flux gradients from 0 (blue) to  $1000 \text{ W m}^{-2}$  (red). From Left to right: +y, -y, +x, -x. +y indicates a heat flux whose magnitude increases linearly from zero in the direction of the positive y axis [33].

Two classes of test were performed for each objective function. The first one had a constant coolant flow rate of  $0.001 \text{ kg s}^{-1}$  and the four non-uniforms heat flux presented in Fig. 23, applied on the bottom face of the cold plate. The last class was performed with a uniform heat flux of  $500 \text{ W m}^{-2}$  and different coolant flow rates ( $0.0004$ ,  $0.002$ , and  $0.001 \text{ kg s}^{-1}$ ).

As expected, different designs were obtained for these two classes of test with the different objective functions. For example, Fig. 24 shows the  $T_c$  optimization with the first class of boundary conditions.

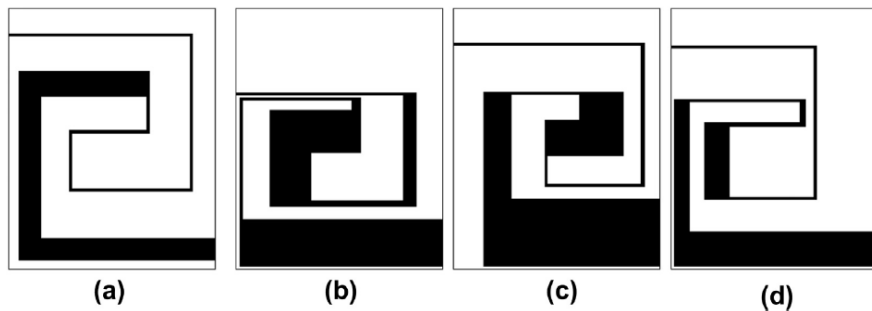


**Fig. 24.** Cooling plate geometry of four designs  $T_c$ -optimized, with non-uniform heat flux distributions and a coolant flow rate of  $0.001 \text{ kg s}^{-1}$ . (a) +y, (b) -y, (c) +x, (d) -x [33].

The robustness of the designs was tested with off-design boundary conditions, i.e. with boundary conditions not used to set the optimum solutions. The  $T_c$  optimum obtained in Fig. 24(b) was tested with the (-y) and (+y) non-uniform heat fluxes. The temperature standard deviation with the same heat flux (-y) used for the optimization was 1.6 K. The application of a different heat flux (+y) led to a temperature deviation of 7 K. In some cases, the penalty for not optimizing with the appropriate boundary condition was a factor of two or more. Furthermore, identical test were performed for the coolant flow rate. At off-design boundary conditions, their performance is significantly degraded. According to these tests, it came that a global optimum solution was really complicated to achieve.

This study had shown the complexity of the optimization process and just a modification of fluid coolant will completely change the results predicted before. A numerical and

experimental investigation of a liquid cold plate design is presented subsequently in the next paragraph.

#### 1.4.2.3. Mini channel liquid cold plate

The Ultra-thin mini channel Liquid Cold Plate (LCP) is made of straight lines, manufactured with a very small hydraulic diameter. This technology increases the thermal transfer and reduces the unevenness of the temperature compared to the previous cold plate studied. However, in conventional straight channels, convective heat transfer deteriorates along the axial direction with the development of the hydrodynamic boundary layer, resulting in elevated maximum temperature and significant temperature gradient in the fully developed region. In this regard, Jin et al. [34] modified the usual straight line configuration by the addition of oblique cuts, in order to enhance the performance with minimal penalty. The new design is presented in Fig. 25.

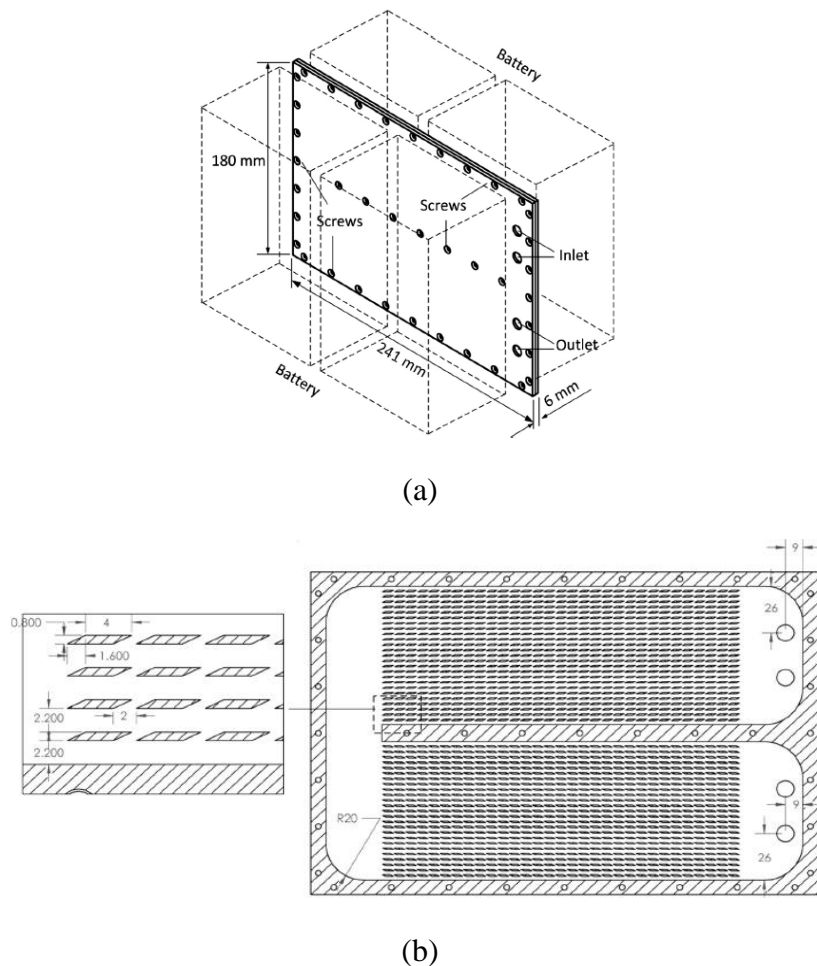


**Fig. 25.** (a) External dimensions of ultra-thin liquid cold plate, (b) Structure dimensions (mm) of ultra-thin LCP [34].

The oblique cuts helped to re-initialize the boundary layer at each thin and avoided consequently to reach a fully developed boundary layer in the entire LCP, which limits the heat transfer with the coolant. Besides, the thermal exchange is more important at the

initialization of the boundary layer, therefore the constant re-initialization induced by the oblique cuts increased the overall heat transfer of the LCP, as presented in Fig. 26.

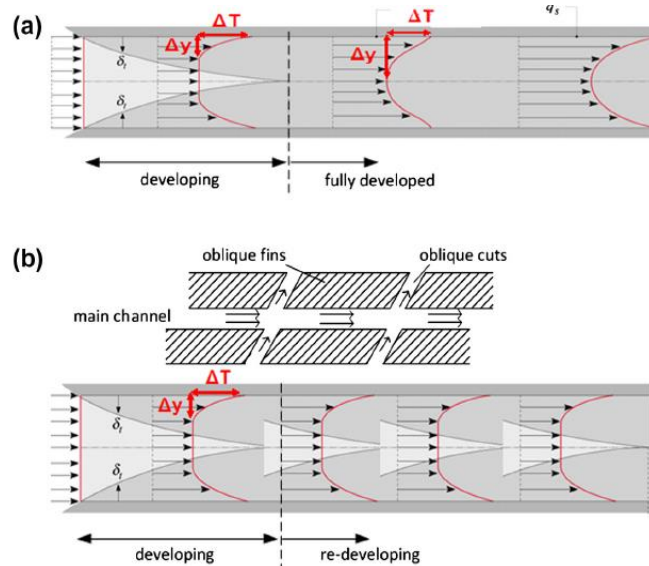


**Fig. 26.** (a) Boundary layer of a conventional straight channel, (b) Boundary layer of channel with oblique cuts [34].

Numerical studies of the system were performed in order to determine the impact of the oblique cuts on the velocity field and to analyse the uniformity of the velocity field in LCP designs made of a single-inlet-outlet and a two-inlet-outlet as presented respectively in Fig. 27 and Fig. 28. Besides, the addition of the oblique cuts had created secondary flow observed at the junction of the main channel and the oblique path (Fig. 27), mixing the flow and therefore enhancing the convective heat transfer.



**Fig. 27.** The secondary flow effects on the flow mixing in the main channel [34].

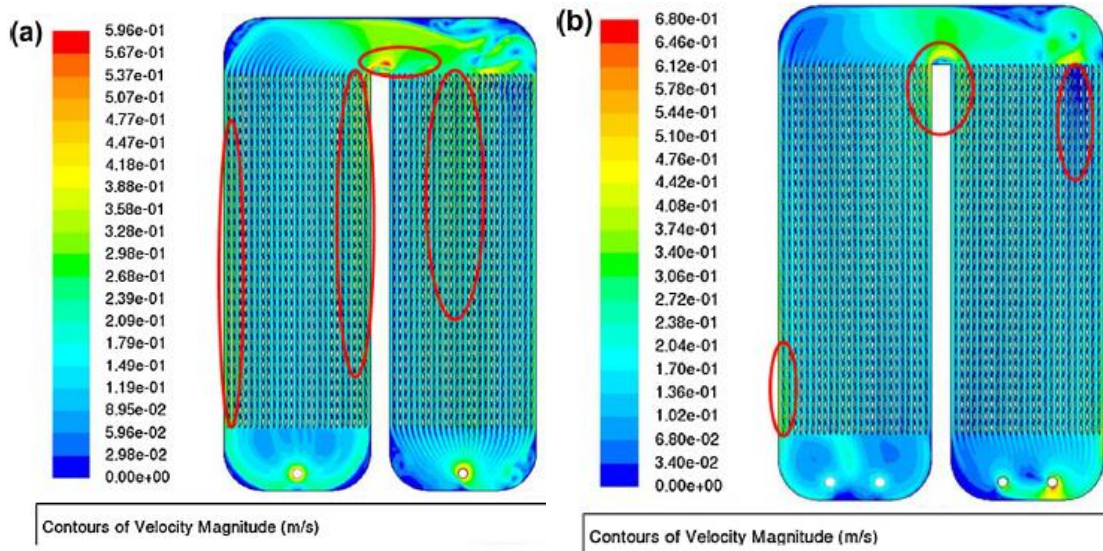


**Fig. 28.** (a) Flow distribution of a single-inlet-outlet configuration, (b) Flow distribution of a two-inlet-outlet configuration [34].

An experimental study of the oblique LCP was performed and compared to a conventional straight mini channel LCP fabricated on the same baseline. The surface average temperature of both design were compared for different heat flux loads and coolant flow rate in Fig. 29.

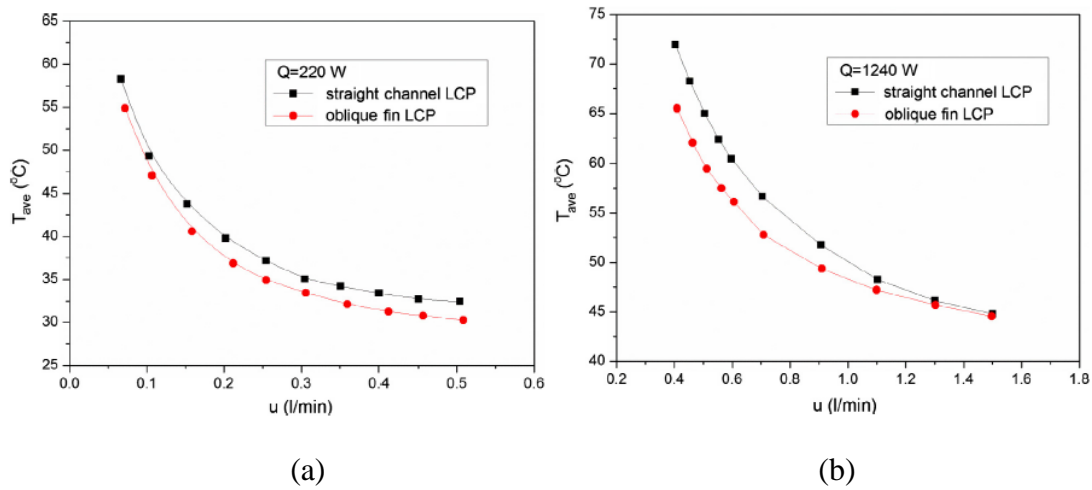


**Fig. 29.** Average surface temperature of straight channel and oblique fin LCP [34].

Fig. 29 shows that the difference between both designs is significant at higher heat flux, with a better efficiency for the oblique fin LCP. The enhancement of thermal exchange brought by the oblique cuts was measured by calculating the overall heat transfer for both oblique and straight fin LCP, as presented in Fig. 30.

The overall heat transfer coefficient was calculated by Eq. (1.12), where  $Q_{eff}$ ,  $T_w$  and  $T_f$  are respectively the actual heat flux, the external wall temperature of the LCP and the liquid temperature averaged from the inlet and outlet temperature.

$$h = \frac{Q_{eff}}{A(T_w - T_f)}; \quad Q_{eff} = \dot{m}c_p \Delta T_{out-in} \quad (1.12)$$

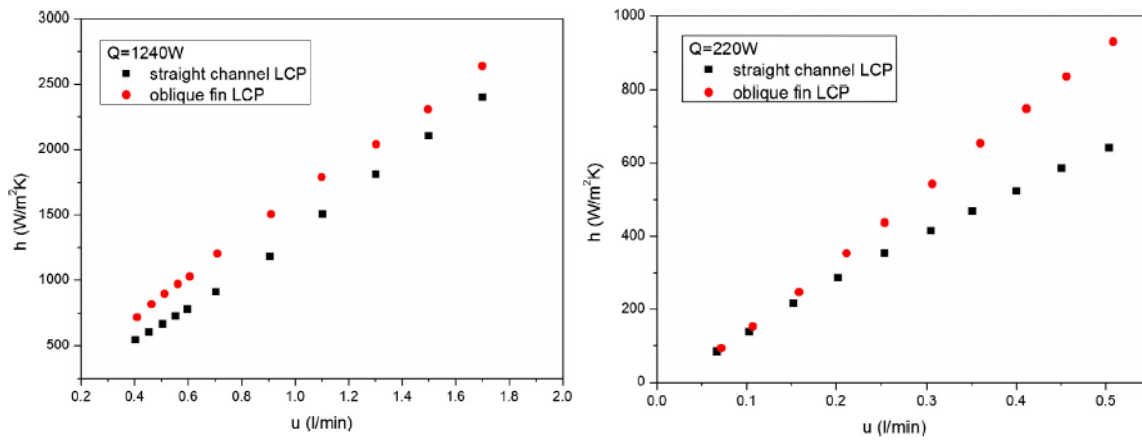


**Fig. 30.** Overall heat transfer coefficient of straight channel and oblique fin LCPs [34].

A simple addition of oblique cuts had completely changed the behaviour of the LCP and had improved its efficiency. Significant penalty of pressure drop between the straight and oblique fins LCPs was not observed [34]. Nevertheless, a test to quantify the pressure drop between both LCPs would be useful in order to confirm their observation.

The active cooling solution are simple to manufacture and easy to use. However, this technology implies a bulky management system in order to cool the battery pack. The optimization of the different active cooling system is a good solution to reach a balance between thermal efficiency, system volume and power consumption of the pump or fan. The study of the previous article showed that the active cooling management is really complex to apply, with regard to the thermal requirement of maximum temperature and even temperature distribution.

Passive Cooling Management has been developed and studied, for providing a better thermal efficiency in more compact battery pack, but also to reduce the volume of the battery thermal management system.

#### 1.4.3. Passive cooling management systems

The passive cooling management systems presented in this chapter are based on phase change phenomenon in order to remove quickly the heat or to slow down the rise of the temperature during driving operation. Heat pipe and Phase change material were shown by Rao and Wang [2] as a way to cool effectively a battery under real driving application.

##### 1.4.3.1. Heat pipe

Heat pipe is a cooling device in flat or cylindrical shape, based on liquid/vapour phase change phenomenon. A liquid in a saturated state is sealed in a conductive material with groove structures in order to increase the performances. In the case of a cylindrical heat pipe, when one side is heated the liquid is transformed in vapour and moved by difference of pressure to the other side of the heat pipe with a colder temperature. The vapour arriving at the colder part of the heat pipe is transformed in liquid by condensation and bring back to the hot side of

the pipe (i.e. the one where the heat is applied) by capillarity through the groove structures. Therefore, the system works as long as the difference of temperature is maintained at both sides of the heat pipe. Heat pipes are used mainly in thermal regulation for satellite and in electronic cooling.

Wu et al. [35] studied experimentally the possibility of heat pipes for cooling a cylindrical battery cell. They showed that the surface contact is very important for achieving a high efficiency. In fact, no appreciable change was obtained in the rise of temperature when they attached two heat pipes on a battery cell due to a bad contact between them. In consequence, they inserted aluminium, due to its high conductivity and emissivity, for improving the contact between both heat pipe and battery. This modification had led to a temperature decreasing from 45°C to 38°C.

Rao et al. [36] performed an experimental investigation on thermal management of electric vehicle battery with heat pipe. The importance of surface connection [35] was considered, with four cylindrical heat pipes distributed evenly and contacted compactly with thermal silica (ZC-801). According to the experimental results, the heat pipes were effective for thermal management of the power battery with a heat generation rate lower than 50 W, with start and transient acceleration. Moreover, the temperature gradient was inferior to 5°C, when the heat generation from the battery cell was not exceeding 30W.

This following picture presents the schematic of the experimental set-up:

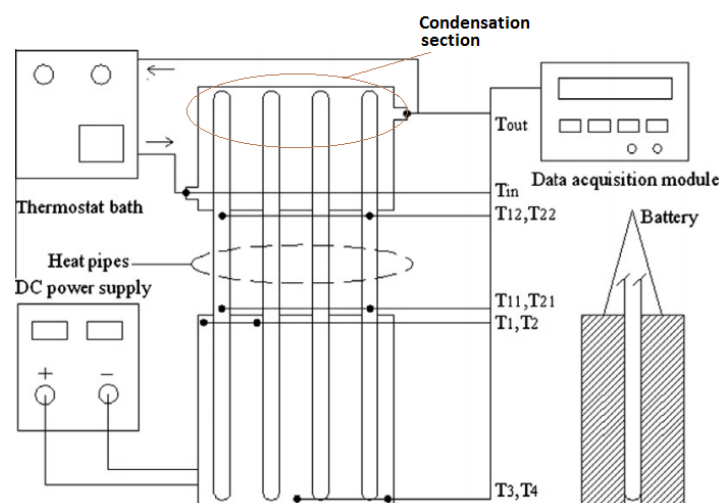


**Fig. 31.** Experimental setup of a battery cell cooled by heat pipe [36]

However, the choice and design of a heat pipe depends of the maximum heat generated by the heat source (battery cell). Therefore, the design of a heat pipe in order to reach a high efficiency will differ from a maximum power of 30W to 50W. Moreover, the study of the different parameters such as the global conductivity, the groove structure, the pressure drop, is crucial for future design.

The modelling of a heat pipe in order to predict and analyse the different design parameters, is very important for testing the design efficiency during operation. The modelling of a heat pipe is really complex due to the coupling of hydrodynamic, phase change and thermal transfer effect.

Zuo and Faghri [37] developed a thermal model based on the nodal circuit method. This method treats the thermal problem by analogy with an electric circuit and was completed with analytical content taking into account the hydrodynamic behaviour of the fluid during operation.

The theoretical and experimental study of the heat pipes subject to high acceleration was performed by Romestant [38]. This study was aimed to understand and quantify the effect of the gravity and acceleration on the heat pipe during operation. In fact, the gravity may strongly reduce the performances of a heat pipe. Besides, Bertossi [39] studied the impact of the solid/liquid interface on the performances of the heat pipe during normal use and for rotating movement. The solid/liquid interface plays an important role in the efficiency of the heat pipe. In addition, the modelling of flat heat pipe for high density heat generation was investigated by Avenas [40].

The modelling of a battery cell by heat pipes will be fully discussed at the Chapter 2 of this thesis. The phase change materials are presented next, with the presentation of their impact on the battery cooling, as well as their modelling.

#### *1.4.3.2. Phase change material*

Thermal management system should be compact, lightweight, easy packed in the vehicle, reliable and low cost. The interest of passive cooling management has grown for few years in the Battery Thermal Management research. They have been used in aerospace industry for their efficiency and capacity of working alone with only the temperature as a trigger. The latent heat due to the phase change (solid/liquid, or liquid/vapour) has conferred to this technology a huge advantage in term of heat removal efficiency and delay of the temperature rise.

Rao et al. [41] performed a numerical simulation of heat dissipation with PCM for cylindrical power battery, presented in Fig. 32. Their model took into account unsteady heat generation, internal conduction, and external natural convection. They simplified the study by taking a heat generation rate instead of the electrochemistry model and by assuming the physical properties of the PCM and battery cell constant during the whole computation. In addition, the density change of the PCM due to solid-liquid phase change was supposed negligible, and the melting point  $T_m$  of the PCM was taken constant instead of a temperature range. The PCM was supposed also homogeneous and isotropic and the radiative heat transfer was not considered. The phase change model was enthalpy-based and the complete model was run with the commercial software FLUENT.

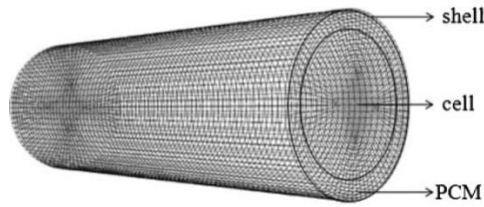


**Fig. 32.** Mesh of the cylindrical battery cell cooled by PCM [41].

The PCM was able to maintain the temperature below 45°C with natural convection, when the right material was chosen. However, the low conductivity of the PCM can lead to a large temperature difference between the centre and the outer part of the cylinder, as shown in Fig. 33.

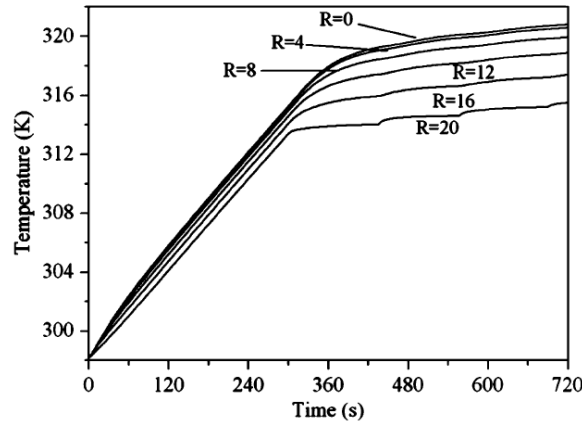


**Fig. 33.** Temperature variation in the radial direction with  $h = 5W.m^{-2}K^{-1}$  and the thermal conductivity of the PCM  $k_{PCM} = 3W.m^{-1}K^{-1}$  [41].

Beside, Ramandi et al. [42] studied the heat transfer and thermal management of electric vehicle by PCM. A numerical simulation on a prismatic shape battery, surrounded by PCM was performed in three different situations. A single PCM shell system with and without insulated walls were considered first, followed by a double PCM shells system with insulated walls. The situations are presented in Fig. 34.

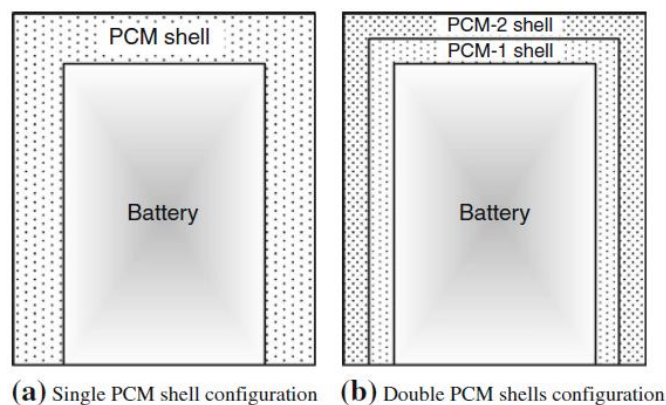


**Fig. 34.** Single (a) and double PCM (b) shells configuration [42].

They considered a constant discharge rate in order to have a uniform heat generation. Moreover, the thermo-physical properties of the PCMs were taken constant with the neglecting of radiative heat transfer. They showed that the PCM could be used as a thermal

management system, but the heat from the environment reduces the efficiency of the PCM and could make the PCM useless during an electric vehicle operation. Moreover, the double shells configuration did not largely increase the PCM efficiency compare to the single shell.

PCMs have great potential for reducing peak temperature during intermittent discharge and also overcome performance losses at cold temperature. Duan and Naterer [43] investigated experimentally the behaviour of two PCMs, called PCM 1 and PCM 2, during discharge with various environmental conditions. A Neslab bath was used to control the boundary conditions and settle different ambient temperatures. A battery cell is simulated by an electric heater and located in the centre of an aluminium container placed in the Neslab bath (Fig. 35(a)) with the PCM 1. The PCM 1 has a phase change temperature of 18°C, a specific heat of 2.1kJ/kg K, a latent heat of 195 kJ/kg, a density of 840 kg/m<sup>3</sup> and a thermal conductivity of 0.55 W/m K. It is liquid at room temperature and filled the aluminium container and surrounding the electric heater as presented in Fig. 35(a).

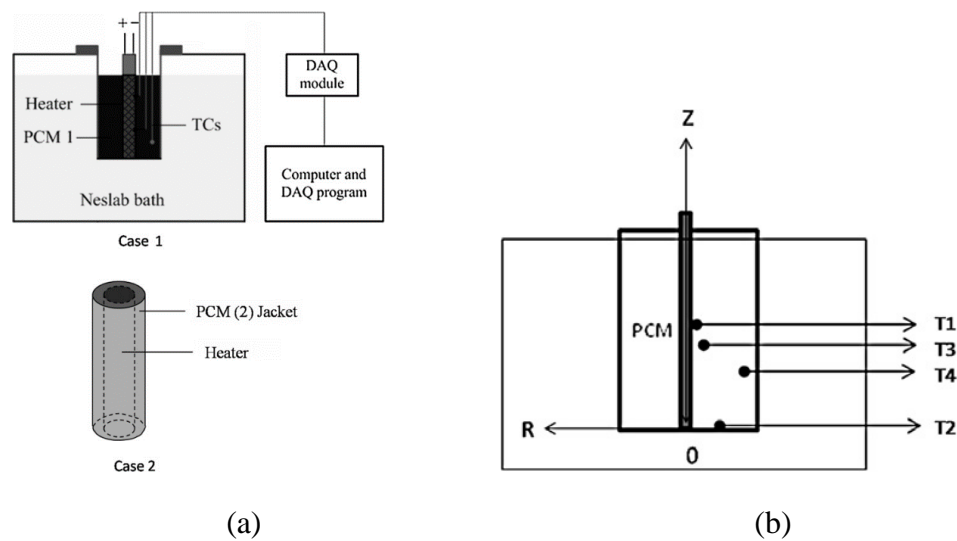


**Fig. 35.** (a) Experimental set up and (b) positions of the thermocouples for the study of PCM 1 [43].

In the second case, the electric heater was wrapped by jackets of PCM 2. The jackets were made with PCM flexible sheets (T-PCM 920) and the PCM has a phase change temperature of 50°C. Moreover, the heater, wrapped in the PCM jacket, was installed into the Neslab bath and exposed to different simulated ambient temperature. Fig. 35(b) shows the positions of the thermocouples used to follow and study the melting process of the PCM 1.

The temperature measurement via the experimental setup had helped to understand the behaviour of the PCM during a freezing ambient temperature and melting operation due to the heat generation of the battery cell. The temperatures monitored by the thermocouples presented in Fig. 35(b), during melting process, are shown in Fig. 36(a).

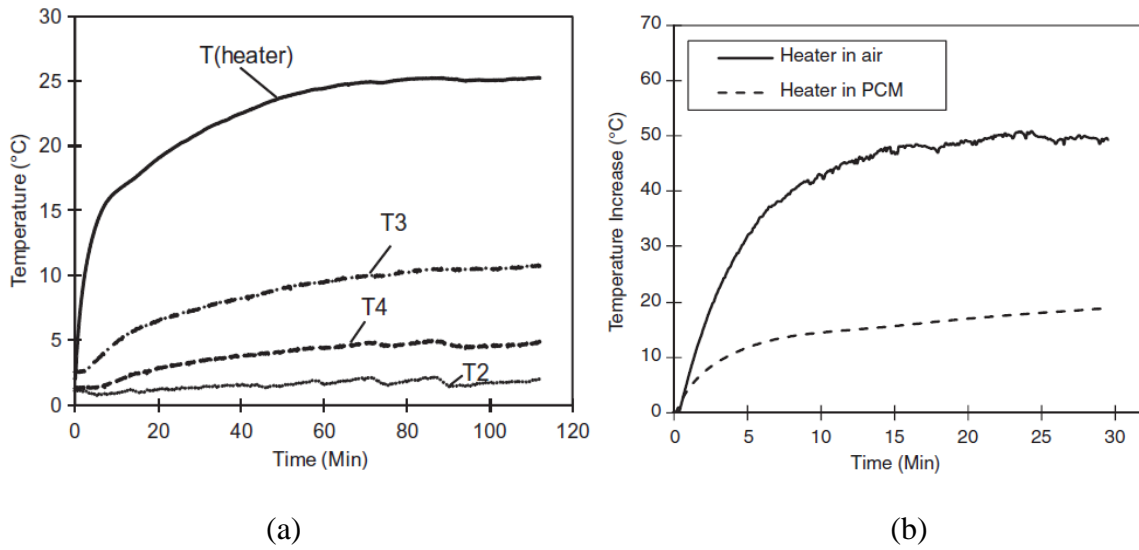


**Fig. 36.** (a) Measured temperature during melting of the PCM around the heater; (b) heater temperature in air, and with PCM 1 protection, subject to constant heat rate [43].

Besides, the effectiveness of the PCM cooling was measured by comparison to natural air convection, of the heater surface temperature. Fig. 36(b) showed that the case with PCM 1 led to a faster transient rise and a surface temperature lower than 30°C. In the meantime, the air natural convection led to slower transient rise and a higher maximum surface temperature. An identical behaviour was observed in the case of PCM 2.

Furthermore, the impact of variable or cyclic ambient temperature on the heater surface temperature was studied by the authors [43]. In fact, the ambient temperature variation can be very large, especially in the northern climate. Fig. 37(a) showed the temperature variation of the heater, the PCM 1 and the ambient air in function on time. The heater temperature experienced small fluctuations despite significant variation of the ambient temperature through time. This behaviour was due to the properties of the PCM, which had maintained its inner surface temperature quasi constant after the initial heating period. Additionally, only the outer surface of the PCM experienced a larger fluctuation.

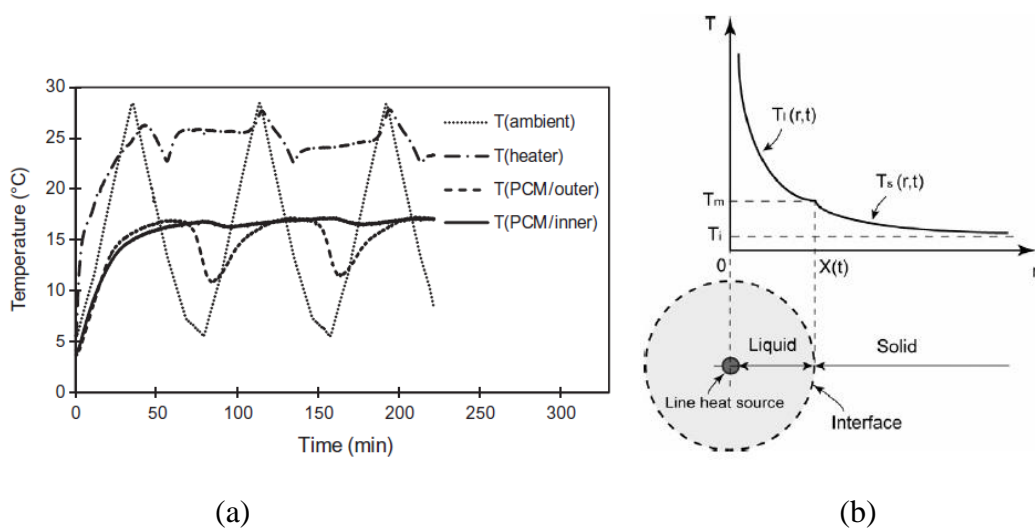


**Fig. 37.** (a) Simulation of cyclic temperature variation around a PCM 1 protected battery; (b) schematic of melting of a phase change material with a line heat source [43].

In conclusion, both PCM (1 and 2) were effective to keep the heater temperature in the defined range of temperature and despite very important variation of ambient temperature. Besides, their efficiency and lightweight are important advantages for the improvement of battery thermal management system. Moreover, the authors [43] solved the Stefan equation of the phase change problem in one-dimensional cylindrical coordinates. The solution described the propagation of the liquid phase in the initial solid PCM depending on the heat generation. In Fig. 37(b), a line heat source is located at  $r = 0$  in an infinite solid at uniform temperature  $T_i$ , lower than the melting temperature  $T_m$ .

However, the model was not used for comparison with the experimental test due to buoyancy effects observed within the melted phase change material during the experiment, as shown in Fig. 38.

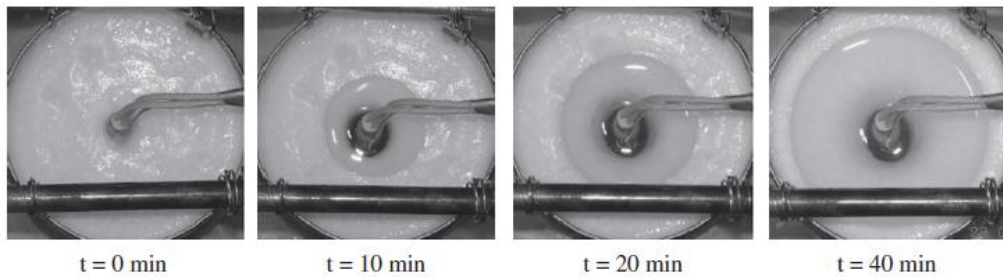


**Fig. 38.** Melting PCM around a heater [43].

Nonetheless, the low thermal conductivity of the Passive change materials limits their use as cooling system for battery pack and could be deficient in the case of very stressful condition leading to a thermal runaway. In consequence, the thermal conductivity of the PCM was enhanced by the addition of high conductive material. The composite created by its association was studied experimentally and analytically by Py et al. [44] in the case of graphite matrix. They showed experimentally that the thermal conductivity of the composite PCM/graphite was equal to the thermal conductivity of the graphite matrix. Besides, an anisotropic thermal conductivity was observed in the final composite depending on graphite density. A similar behaviour concerning the independence of the overall thermal conductivity from the PCM was observed by Lingamneni et al. [45] in the case of composite with metallic matrix.

An experimental and numerical investigation of a composite PCM/graphite was performed by Ling et al. [46]. They used the commercial software FLUENT and an enthalpy-based model for describing the phase change. Moreover, the batteries were modelled by cylindrical heaters, surrounded by the PCM/graphite. Different PCM/graphite composition was compared to each other using two parameters in order to characterize their performances. The parameters were the time for the heat surface temperature to reach  $60^{\circ}\text{C}$  and the maximum temperature difference in the PCM/graphite composite. Slight differences were observed between experiment and simulation, with a faster rise in the numerical simulation. This difference was due to small heat losses in experiment, despite thermal isolation. The author advised to use a composite with a graphite density of  $890 \text{ kg}\cdot\text{m}^{-3}$  and 75% of paraffin wax in order to avoid the leakage of the PCM from the graphite matrix, and to have a better overall thermal conductivity.

In addition, Kizilel et al. [47] studied numerically a PCM (paraffin wax) enhanced by a graphite matrix structure during stressful conditions. The overall conductivity obtained by this modification increase the conductivity to the PCM/graphite to 16.6 W/m K. The main objective was to determine the effectiveness of a PCM/graphite during a thermal runaway by comparison with a conventional active air-cooling condition. In order to predict the temperature distribution in the module, the heat generated by the runaway and the discharge reactions were fitted from experiments performed on one of the battery cell.

The battery pack studied, was composed of 67 battery module. Each battery module was composed of 20 commercially available cylindrical battery cells with a capacity of 1.5 Ah as presented in Fig. 39. Each module consisted of five strings of four cells in series with the fives strings connected in parallel. The active air-cooling and PCM/graphite cooling are presented in Fig. 40(a) and Fig. 40(b).

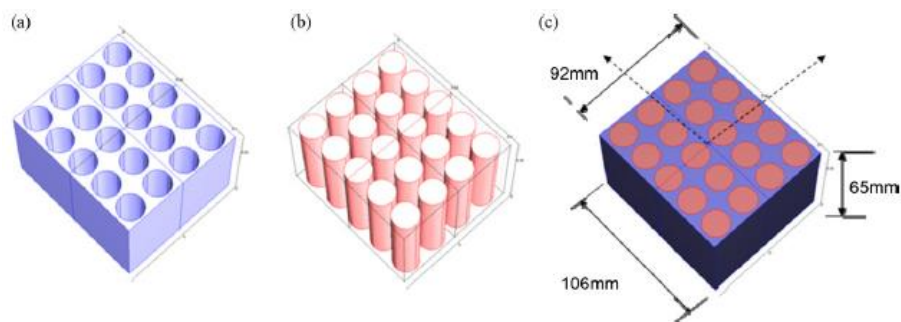
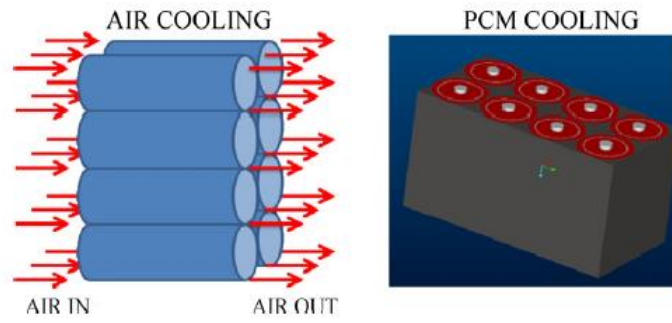
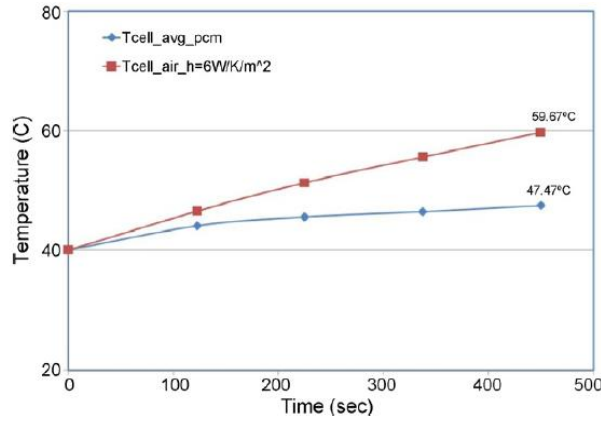


**Fig. 39.** Schematic representation of 5S4P module configuration: (a) PCM filled closed box, (b) Li-ion cells, (c) battery module [47].

The first simulation analysed the maximum average temperature of a cell subject to an active air-cooling and PCM cooling, and also the impact of both cooling case to the temperature distribution at an ambient temperature of 40°C. The maximum average temperature presented in Fig. 40(c) was 10°C lower with a PCM/graphite cooling than an active air-cooling of  $h=6 \text{ W/m}^2 \text{ K}$ .



(a) (b)



(c)

**Fig. 40.** (a) Air cooling; (b) PCM cooling; (c) Cell temperature at  $T_{amb} = 40^{\circ}C$  [47].

The temperature uniformity presented in Fig. 41 was better in the PCM cooling compared to the air cooling. Moreover, a thermal runaway was simulated by triggering a failure on one cell of the battery module.

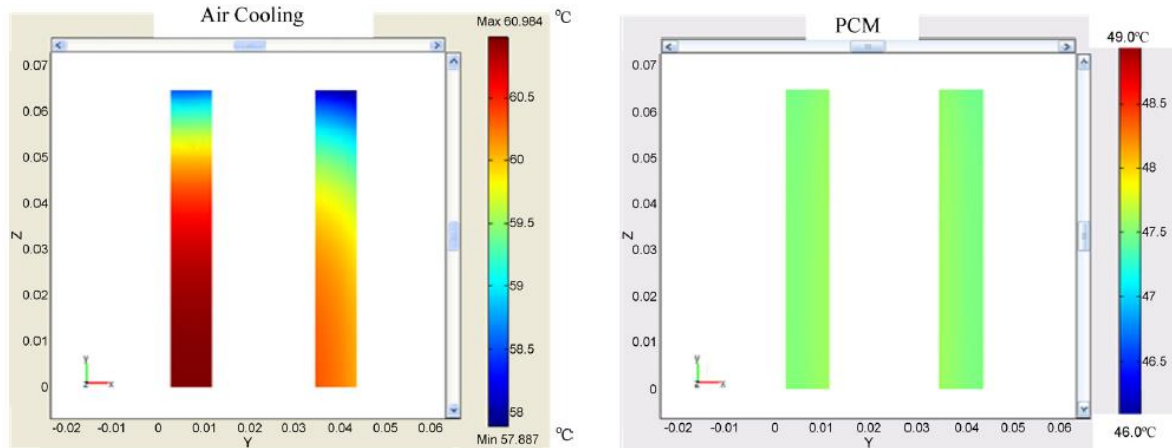
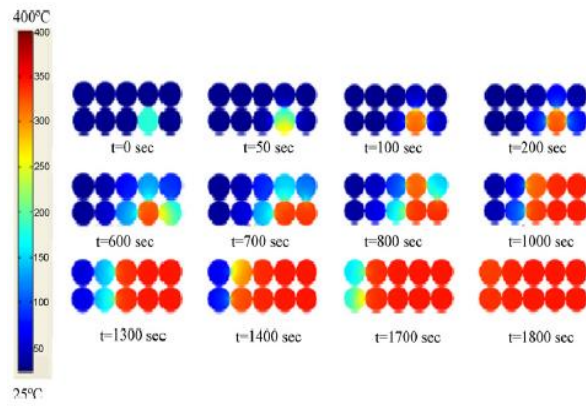
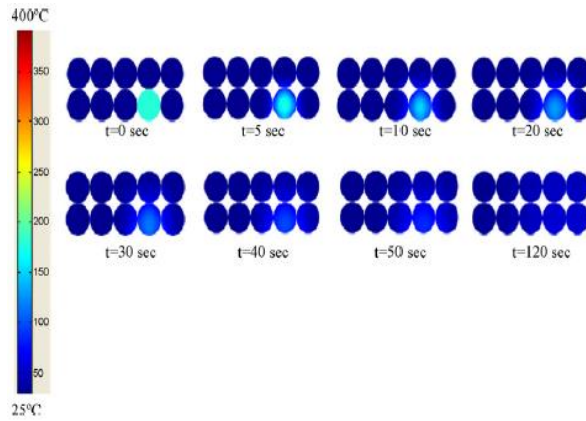


**Fig. 41.** Temperature profiles in two adjacent cells  $T_{amb} = 40^{\circ}C$  : (a) air cooling; (b) PCM/graphite cooling [47].

In the air cooling system, with an ambient temperature of  $25^{\circ}C$  and a convective coefficient of  $h = 10 \text{ W/m}^2 \text{ K}$ , the runaway had propagated throughout the battery module as shown in Fig. 42(a), while the propagation was stopped in the PCM cooling and the module returned to near-ambient temperature as shown in Fig. 42(b).



(a)



(b)

**Fig. 42.** Propagation of thermal runaway due to a single runaway cell with: (a) air cooling, (b) interstitial PCM/graphite [47].

The impact of the spacing between battery cells was finally studied in the case of air-cooling case. The battery cells presented in Fig. 43 were kept 1 mm and 2 mm apart from each other by placing an insulator (nylon  $k = 0.25 \text{ Wm}^{-2}\text{K}^{-1}$ ,  $\rho = 1140 \text{ kg m}^{-3}$ ,  $c_p = 1700 \text{ J kg}^{-1}\text{K}^{-1}$ ). The objective in this test was the measurement of the temperature rise of the neighbouring cell when a thermal runaway was applied to cell 1 (Fig. 43). For the 2 mm spacing, the temperature neighbouring cells changed only 7 °C during thermal runaway of the cell. On the other hand, the 1 mm spacing led to a temperature increase of 9.5 °C. The authors [47] showed that despite the increase of the spacing area the thermal runaway throughout the module was unavoidable. In contrary of air-cooling, PCM do not need spacing to cool properly or absorb a thermal runaway. Subsequently, PCM has to be close to the battery cell, reducing at the same time the entire volume of the battery module.

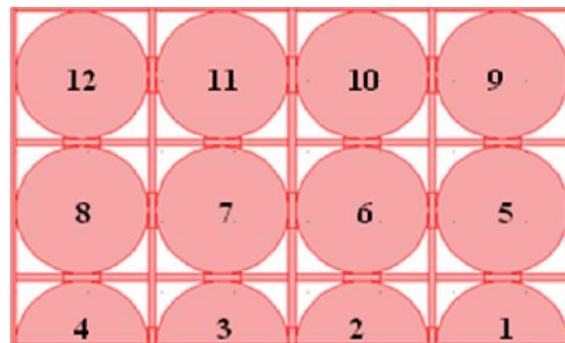


**Fig. 43.** Top view of the half module with insulating stands [47].

These results showed the capacity of PCM/graphite to prevent a thermal runaway, occurring randomly in any cell, from spreading in the entire battery module. In addition the PCM/graphite was able to keep the battery module uniform during discharge. Nevertheless, Kizilel et al. [47] did not consider the phase change property of the PCM and consider a unique conductivity, where Py et al. [44] had found an anisotropic overall thermal conductivity.

A PCM/graphite composite was investigated experimentally for the cooling of a cylindrical battery module, by Kim et al. [48]. The PCM/graphite cooling was compared to active cooling and experimental measurements were compared to a lumped thermal model. Each cell of the module of the battery module was represented by a lumped model due to a Biot number much less than one, i.e. approximately 0.005. Besides, the equivalent capacity method was used for representing the phase change. At high discharge rate, the PCM/graphite matrix surrounding the battery cells (Fig. 40(b)) was able to limit the peak temperature, but the heat rejection to the environment was less effective when only natural convection was used on the external surface. The addition of the graphite increase the thermal conductivity of the composite and improve the temperature uniformity, but reduce the surface cooling as shown in Fig. 40(b), while this surface was larger in a forced cooling system. In consequence, the author preconized to use both forced and PCM/graphite cooling for high discharge rate, i.e. a relatively low convection cooling (superior to natural convection) would be needed, instead of the higher intensity of cooling used in a pure forced cooling case. This combination is necessary at high discharge rate in order to remove quickly the heat from the battery module and to keep an even temperature distribution without an important cooling intensity in case of peak temperature.

Table 1 presents the advantages and disadvantages of the different heat generation and thermal model presented in this chapter. In addition, the coupling between the different thermal battery models and heat generation models is briefly discussed. For example if a lumped thermal model is used as thermal modelling for the battery, its advantages and disadvantages are listed first in the table1. Besides, an identical description is made for the modelling of the heat generation in the case of a constant heat generation. The final advantage/disadvantage of the coupling between the constant heat generation and the lumped thermal model is represented by the intersection of the row and column respectively.

**Table 1.** Summary and comparison of the different thermal and heat generation models and their coupling

		Thermal modelling of the battery	Lumped thermal model	3D or 2D thermal model with global physical properties
		Advantages	<ul style="list-style-type: none"> <li>- Fast and simple to use [7, 8]</li> <li>- Close agreement with experiment at Biot number much lower to 1 [49]</li> <li>- Good approximation in the case of Electrochemistry study [25, 26]</li> </ul>	<ul style="list-style-type: none"> <li>- Give access to the thermal gradient in the battery [9, 10, 11, 13, 17, 19]</li> <li>- Excellent agreement with experiment for various cooling method [12, 13, 19, 52]</li> </ul>
Heat generation	Advantages	Disadvantages	<ul style="list-style-type: none"> <li>- Limited at high discharge rate [52]</li> <li>- No information about the gradient</li> </ul>	<ul style="list-style-type: none"> <li>- Time consuming</li> </ul>
Maximum Constant power [55,66]	<ul style="list-style-type: none"> <li>- Useful for cooling system analysis only [32,33,55, 66]</li> <li>- Provide conservative cooling design [55, 66].</li> </ul>	<ul style="list-style-type: none"> <li>- The cooling system may be oversized</li> </ul>	<ul style="list-style-type: none"> <li>- The coupling conserves the advantages and disadvantages of both models</li> </ul>	<ul style="list-style-type: none"> <li>- The coupling allows to design a cooling system with crucial information on the transient temperature gradient during operation</li> <li>- The cooling prediction can be too conservative and do not give information about the electrical parameter of the battery cell</li> </ul>

<p>Reversible and irreversible term [15]</p>	<ul style="list-style-type: none"> <li>- Close Agreement with experiment at low and average discharge rate [11, 12, 18, 19]</li> <li>- Give access to important electrical information of the battery [12]</li> <li>- Relatively faster compared to a complete electrochemistry model</li> <li>- Simple to implement in any thermal model</li> </ul>	<ul style="list-style-type: none"> <li>- Discrepancies at high discharge rate [19]</li> <li>- Do not give access to design parameter of the battery electrodes</li> <li>- Cannot be used to study the mechanisms of the battery capacity loss</li> </ul>	<ul style="list-style-type: none"> <li>- The coupling between both models lead to a fast calculation but with discrepancies at high discharge rate</li> </ul>	<ul style="list-style-type: none"> <li>- The addition of this heat generation formulation to the 3D or 2D thermal model led to results close to experiment in term of transient temperature rise and temperature gradient during discharge/charge. [12, 19]</li> <li>- A relatively fast time simulation compared to the use of the P2D model for the electrochemistry [19]</li> <li>- Few discrepancies were observed at high discharge rate due to the limitation of the heat generation formulation for describing major phenomena [25, 26].</li> </ul>
<p>Electrochemistry model (P2D) [20, 21]</p>	<ul style="list-style-type: none"> <li>- Validated against experiment from low to high discharge rate [24]</li> <li>- Close description of the different phenomena occurring in the battery cell [22, 23]</li> <li>- Can be used to study the capacity loss and improve the electrode design of the battery cell [16]</li> </ul>	<ul style="list-style-type: none"> <li>- Time consuming [22, 23]</li> </ul>	<ul style="list-style-type: none"> <li>- The coupling between them is well dedicated to study the P2D model at battery pack scale [22, 23]</li> </ul>	<ul style="list-style-type: none"> <li>- Complete model describing accurately the electrochemistry of the battery cell as well as its thermal behaviour during various discharge/charge.</li> <li>- Very time-consuming and therefore not advised at battery module/pack analysis.</li> </ul>

Moreover, Table 2 is a summary of the different battery thermal management systems presented in this chapter, with their advantages, disadvantages. Besides, improvements are proposed in order to obtain a better efficiency.

**Table 2.** Comparisons of the different BTMS presented.

Battery thermal management systems	Advantages	Disadvantages	Improvements
Active cooling	<ul style="list-style-type: none"> <li>- Technology well known in automotive industry and easy to build like cold plate [17, 27] or heat exchanger</li> <li>- Effective at low discharge rate</li> </ul>	<ul style="list-style-type: none"> <li>- Bulky and necessitate a flow management system using energy from the battery</li> <li>- Lead to uneven temperature distribution in the battery module/pack at high discharge rate [6, 17]</li> </ul>	<ul style="list-style-type: none"> <li>- Optimization of the cooling systems in order to find a compromise between the active cooling system and the maximum temperature prescribed [32, 33].</li> <li>- Parallel [6] or distributed [17] configuration in order to maintain an even temperature distribution in the battery module or pack</li> </ul>
Passive cooling - Heat pipe	<ul style="list-style-type: none"> <li>- Heat pipe remove quickly the heat during high discharge rate [36]</li> <li>- Work alone as long as a temperature difference is maintained between the evaporator and condenser.</li> </ul>	<ul style="list-style-type: none"> <li>- The surface contact between the battery cell and the heat pipes is very important for guaranteeing a good efficiency [35].</li> <li>- The performances are sensitive to the gravity</li> </ul>	<ul style="list-style-type: none"> <li>- Design properly the heat pipe in function of the heat rejected by the battery cells [55]</li> <li>- Thermosyphon position in order to reduce the sensitivity to gravity</li> </ul>
Passive cooling - Phase Change Material	<ul style="list-style-type: none"> <li>- The PCM was able to maintain the temperature below 45°C with natural convection [41]</li> <li>- Temperature rise is slowed down compared to forced or natural convection [43]</li> <li>- The PCM is effective to keep the battery cell in the prescribed temperature range despite important ambient temperature [43].</li> <li>- Good property for preventing thermal runaway when enhanced with high conductive material [47]</li> </ul>	<ul style="list-style-type: none"> <li>- A very low thermal conductivity when taken alone</li> </ul>	<ul style="list-style-type: none"> <li>- Addition of a very conductive material in the PCM in order to enhance the conductivity [44, 45, 47].</li> </ul>

The next chapter is dedicated to different experimental approach in order to validate certain model.

## 1.5. Experimental methods

In order to predict the temperature behaviour during various discharge rates, extreme environment conditions and for cycling procedures of a battery cell alone or in a module, different models have been proposed. These theoretical/computational models provide efficient tools for choosing the suitable and efficient cooling design for the EV/HEV. Nevertheless, experimental methods are always important to practical applications.

It is worth noting that some models described before are based on experimental correlations. For example the internal battery resistance, can be measured by different methods. In this respect, Onda et al. [49] performed a study on the thermal behaviour of small lithium-ion battery and measure the internal resistance by different methods. In fact, they model the heat generation by the approach of Bernardi et al. [15], i.e. a joule heat and reversible heat. They measured the internal resistance necessary for calculating the joule heat by four different methods. The resistance was measured first by  $V-I$  characteristics during constant-current charge/discharge cycle, then by the difference between open-circuit voltage and also by intermittent charge/discharge. These three methods were mostly in good agreement. However, the fourth method using AC impedance, measured a resistance half to the values predicted to the previous three methods.

Besides, the heat capacity of the battery was measured using a twin-type calorimeter (SETARAM C-80), increasing the battery temperature from 20 to 90 °C at a constant rate of 0.4 °C min<sup>-1</sup>. The heat capacity was approximated by a linear function temperature. They also compared a lumped thermal model and a one-dimensional model depending on the radius of the cylindrical cell to experimental measurement. The results obtained from the  $V-I$  characteristics were used to calculate the heat generation. The one-dimensional agreed well with experiment until 3C discharge rate, while a small discrepancy was obtained in the case of the lumped model, with an overall deviation of 1.6 °C in case of 3C discharge rate.

The lumped thermal model is simple to use and in case of Biot number much less than one, provides results in well agreement with experiments. The thermal comparison between the experiment and models are mainly performed by putting the battery cell or module in a climate chamber in order to control the environment, i.e. maintaining a constant external temperature and controlling the heat exchange to the environment. The surface temperature of the cell is measured by placing different thermocouple around the cell studied in the chamber. This approach avoids opening the battery but adds discrepancies when a lumped model is used. This is why another node is added for representing the surface temperature and linked to the main node by a thermal resistance depending on the geometry of the battery cell. Besides, the addition of this surface is very useful when the case of the cell need to be integrated in the calculation.

The prediction of the thermal runaway is very important in order to understand the phenomena occurring and to provide the solutions guaranteeing a better safety during driving solution. A thermal runaway model was investigated by Guo et al. [50]. They obtained close qualitative and quantitative agreement between their model and experiment. The battery was placed in an oven ranging between 140 °C to 160 °C in order to create the conditions necessary for triggering the thermal runaway.

It happens that the battery manufacturer did not provide precisely the data of the battery. Therefore, it is preferable to build directly one for experimental tests. Despite the cost of this approach, it will be possible to insert thermocouple in the cell and follow more precisely the thermal behaviour of the battery cell. The present work is focused on the development of analytical and numerical model predicting the temperature of the battery cell and module. Designs of heat pipe cooling as well as PCM/graphite cooling are proposed with their dedicated modelling in subsequent chapters. Experiment for measuring the temperature of the battery and validating certain hypotheses are planned for future work. Collaboration with the Technical University of Munich is on the road, where their team will provide us the data and also facilities for testing the models. They have also the technical capacity of building their own battery and in consequence capable of placing strategically thermocouple and other captor inside the battery cell.

## **1.6.Conclusions**

An overview of the battery thermal management systems is presented in this chapter. The uniform temperature distribution in battery module and pack as well as the maximum and minimum temperature prescribed were shown to be really important for the lifespan, safety and efficiency of the batteries. The design of a BTMS is depending on the prediction of the temperature prediction of the battery. In consequence, the modelling of the thermal behaviour of the cell is crucial and was investigated by different approaches.

The thermal behaviour was represented by a lumped thermal model, when the Biot number of the problem was much less to one. The lumped model is fast and well dedicated to large system analysis. However, discrepancies were observed a high discharge rate where the gradient in the battery cell is not negligible. Besides the heat generation was mainly modelled by the Bernardi et al. [15] method, i.e. an irreversible heat and reversible term, with also close agreement to low discharge rate.

The modelling of the heat generation of the cell during discharge is very important in order to have a model predicting the temperature behaviour in different condition of discharge/charge. In this respect, electrochemistry models were developed in order to improve the temperature prediction and to have a better description of the behaviour of the cell during abuse driving condition and cycling simulation. Moreover, improvements of the lifespan, safety and efficiency can be addressed by the analysis and modelling of the electrochemistry.

The electrochemistry model is very complex and is usually coupled with a lumped thermal model in order to reduce the computation time. The Pseudo two-Dimensional model developed by the team of Newman [20, 21] was presented as the reference model for describing the electrochemistry of the cell during constant discharge/charge. Amiribavandpour et al. [51] coupled the P2D model with a resistive network for calculating the heat dissipation of a battery pack. Discharge rate until 4C was considered and cycling simulation was performed, based on real EV driving cycles. Forced cooling convection was used during their study and the authors showed that an adaptive flow cooling system was more useful in order to reduce the electric consumption of the fan. Their model was compared to experiment with a discrepancy of 1.34% for constant discharge up to 4C.

The Passive Cooling Management using heat pipes and PCM/graphite was presented in this chapter. The heat pipe had shown experimentally the capacity to remove the heat from the battery cell. Besides, the PCM/graphite composite was shown to be efficient for keeping a uniform temperature throughout the battery module or pack. However, the low heat rejection from the composite to the environment, combined to the reduction of the cooling surface had made natural convection not sufficient for cooling a battery module at high discharge rate. Nevertheless a relatively low forced cooling convection would be needed compare to a pure forced cooling convection.

In addition, the anisotropic thermal conductivity of the cylindrical and battery cells coupled to the cooling strategy can help to simplify the analysis of the battery cooling. Al Hallaj et al. [52] used a one-dimensional model of a cylindrical battery in the radial direction, subject to forced convection cooling. Their model was in close agreement with experimental results, with small discrepancies observed at high discharge rate mainly due to a local reaction rate near the centre of the cell. In addition they used the Bernardi et al [15] model for the heat generation which is limited at very high discharge rate.

The PhD project is aimed to provide fast and accurate simulation approaches for battery thermal management as well as the development of passive cooling management solutions. Numerical and analytical models are developed in order to model at different scale the mechanisms of a battery cell during discharge/charge and to design the different passive cooling methods. These models are used to study the coupling between of a battery cell/module and the passive cooling solution, during transient temperature rise.

Chapter 2 will study analytically the cooling of a prismatic battery cell by a heat pipe set. The heat generation was taken constant and the maximum volumetric heat generated monitored at the highest discharge rate was considered. This choice was made to provide a consistent heat pipe design capable of keeping the battery cell under the maximum temperature prescribed. This project is followed by the development of a model describing the cooling of a cylindrical battery cell by a PCM/graphite composite. The method used for developing the model as well as design parameters will be presented. An extension of this work is made to a cylindrical battery module using an electrochemistry model for the description of the heat generation. In this respect, a two-dimensional finite volume code for unstructured mesh was developed in PYTHON using an open-source mesh generator. Finally future recommendations are presented.

## **Chapter 2: A theoretical and computational study of lithium-ion battery thermal management for electric vehicles using heat pipes**

### **2.1.Introduction**

Electrical vehicles can be used to reduce the emissions from the traditional internal combustion engine powered vehicles. A wider spread usage of electrical vehicles depends on the development of rechargeable batteries. Lithium-ion (Li-ion) battery has been dominantly utilised for electric vehicles, due to its excellent performance characteristics, such as high energy density, long life-time and low self-discharge. However, its narrow desirable operating temperature range imposes a significant challenge on the thermal management of Li-ion batteries. Thermal management of Li-ion batteries is crucial to safety issues like thermal runaway or overheating during operation. These issues can strongly affect the battery performances and lifespan. In addition, more research needs to be done for transport applications of Li-ion batteries where high electric power is used in a relatively short time period.

It has been shown that temperature affects the longevity, efficiency, and safety of the battery. Thermal runaway, electrolyte fire, and in certain cases explosions [1] can occur when the temperature in the battery is too high. Therefore, an efficient battery thermal management system (BTMS) is required in order to maintain the battery temperature between 20°C and 40°C [2]. Moreover, to avoid any short circuit leading potentially to destroy the battery, an even temperature distribution must be achieved in the battery module and pack. For achieving a uniform temperature distribution, the temperature difference from cell to cell and module to module should be normally within 5°C.

The thermal behaviour of the battery is strongly coupled to the electrochemical process. To simplify the analysis, the heat generated by exothermic chemical reaction during discharge can be represented by a global term linked to the major electrochemical characteristics. Gao et al. [7] modelled the transient behaviour of a commercial Li-Ion battery using an equivalent electric circuit. Based on their work, Chen et al. [8] simplified the mathematical solution. However, these simplified models were not sufficiently developed to describe the temperature distribution in a battery cell to aid the design of the thermal management system.

Different two- and three-dimensional (2D and 3D) numerical models of temperature prediction were developed in the past. Inui et al. [12] developed 2D and 3D codes for cylindrical and prismatic shaped batteries respectively, to predict the transient distribution of temperature during discharge. Karimi and Li [17] extended the study by Inui et al. to a 2D numerical simulation of an entire pack of prismatic battery cooled by natural and forced convection. They also demonstrated that a distributed configuration of the cooling system was the best solution to maintain an equal temperature distribution in the battery pack (stack of prismatic battery cell).

Three-dimensional numerical simulations using global thermo-physical properties to represent the physical properties of the battery multilayer structure were carried out [10, 11]. The battery was cooled by active air cooling and the results showed a good agreement between simulations and measurements. Taheri et al. [53] developed a 3D analytical model to

predict the transient thermal behaviour of a Li-ion battery cell cooled by convection. The modelling was based on integral-transform technique and used an internal heat generation term. The derived analytical solution was efficient to compute the different values of convective heat coefficient applied at different positions of the battery cell. A surface averaged Biot number was proposed to simplify the solutions in 1D or 2D depending on the value of thermo-physical properties of the battery and the heat transfer coefficient applied on the battery's surfaces.

Researches have also been performed on effective thermal control of the battery pack. Pesaran [6] showed that for heat exchanger design, a parallel cooling flow was effective in order to achieve an even temperature distribution in the battery pack. Chacko [27] used a liquid cooling plate composed of a serpentine channel, but this configuration was not developed to achieve an even temperature distribution. Mahamud and Park [30] performed a numerical analysis of cylindrical cells cooled by reciprocating air flow. Their results showed a 4°C decrease in the temperature difference in the battery pack.

Active air or liquid flow convection as a cooling solution implies a bulky flow management system and additional costs due to the maintenance and the weight. Therefore, as an alternative method, passive cooling management (PCM) is investigated as a BTMS solution, especially for confined spaces where intensive heat transfer is required. For example, phase change materials [41, 42] are very simple to use, but their low conductivity limits their applications. A possible solution for further improvements is to add a high conductive matrix in the structure of the phase change materials to enhance the thermal conductivity.

Wu et al. [35] showed experimentally the importance of a large surface contact between the heat pipe and the battery in achieving effective cooling. Rao et al. [36] performed experimental studies of a prismatic shape battery cooled by heat pipes. Their results showed a maximum battery cell temperature under 50°C for a heat generation rate lower than 50W and a temperature variation within 5°C for a heat generation rate not exceeding 30W. This work can be completed by analysing the impact of heat pipe on the temperature distribution of the battery cell or pack. Besides, further studies need to be done to choose or design the right heat pipes according to the maximum range of temperature reached by the battery cell. In general, there is still a lack of understanding on the effectiveness of heat pipes used as a PCM system solution.

This work was motivated by the need to develop reliable and possibly simple methods to analyse heat pipes used as a PCM solution, in order to guide the BTMS design. A study of a prismatic battery cell, cooled by heat pipes during constant-current discharge rate, is performed using different computational/analytical methods. The heat pipe used for the simulations was designed according to the maximum heat generated by the battery cell. The transient thermal behaviour of the heat pipe was modelled by a thermal network method [37-40]. The battery cell used in this study was the ePLB C020 battery (capacity of 20 Ah), fabricated by EiG Corporation, Korea. All simulations were performed using geometrical and electrochemical characteristics from the literature [53]. The other objective is to show that with the right design, heat pipes are able to remove more heat much quicker than normal active cooling. For conservatism in the design, the simulation was performed with the maximum discharge rate of 5C, corresponding to a discharge current of 100 A.

This chapter presents results from a study numerically and analytically investigating the PCM of a Li-ion battery cell using heat pipes. Different configurations were studied and compared to forced convection during a constant current discharge process. The transient computational model based on the thermal circuit method is 1D and consistent with the analytical solution, while the numerical simulation was performed in 3D. The cooling system and heat pipe design are presented first, followed by descriptions of the model development including the heat pipe and thermal models, and descriptions of the three different approaches. Results and discussions are then presented. Finally, some conclusions are drawn.

## 2.2.Design of the battery cooling system

A generic battery cooling system design is shown in Fig. 44, where the heat pipes are integrated within a copper structure that allows a desirable conductive heat transfer between the battery and the heat pipe set. To cover the entire surface of the battery cell and enhance the heat transfer, eighteen heat pipes with a 10 mm diameter and a 0.8 mm gap are considered in this design. For a battery pack with a number of cells, the battery cooling system can be designed using a layout with alternate battery cell and heat pipe set. For the understanding of the effectiveness of the system, it is crucial to understand the fundamental heat transfer characteristics of a single battery cell in conjunction with the heat pipe set.

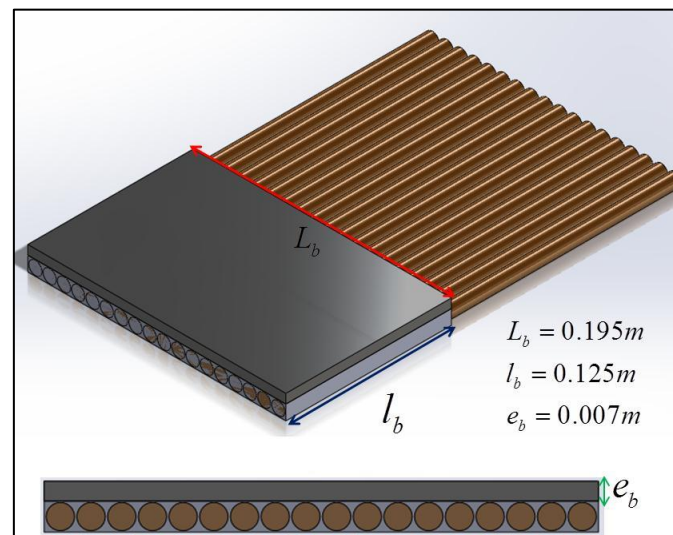


**Fig. 44.** The design structure of the generic battery cooling system using heat pipes.

Figure 45 depicts the heat transfer principle of a heat pipe, where the heat pipe is a tube filled by a working fluid in a saturated state. When the evaporator section is heated up, vapour is generated and carries the heat to the condenser section where the heat pipe is usually cooled down by convection. Then, the liquid in the condenser section is brought back to the evaporator by the capillary forces, as seen in Fig. 45. The capillary forces can be increased by an addition of a wick or groove structure, which will be discussed later in Fig. 46. Therefore, the process works continuously as long as the evaporator is heated and the condenser is cooled.

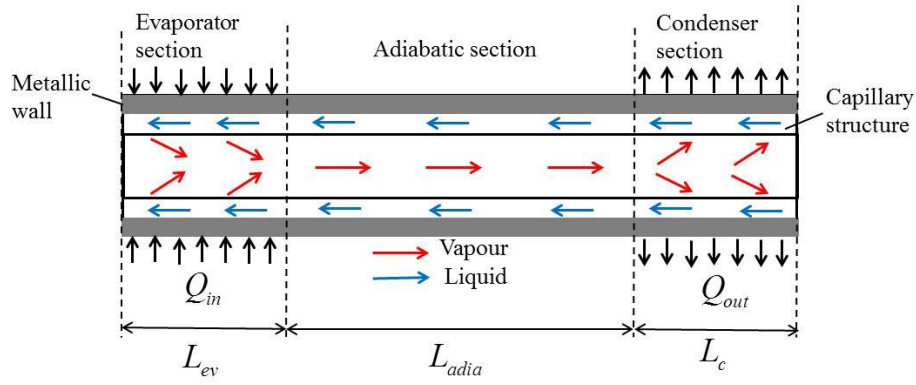


**Fig. 45.** Schematic presentation of the heat transfer working process of a heat pipe.

However, there are a number of limits on the heat pipe heat transfer capacity (or efficiency), due to the thermo-physical properties of the working fluid, the geometry of the heat pipe as well as the friction in the fluid channels. In this analysis, only the capillary limit is considered, which refers to the maximum heat transferrable by the heat pipe without stopping the return of the fluid from the condenser to the evaporator. The analytical formulations for this limit take into account the capillary forces and the friction in the channels (liquid and vapour). The influence of the gravity was not included in the analysis because the heat pipe can be arranged in a horizontal position. However, it is worth noting that the gravity helps to improve the capillary limit when the cooling system is arranged in a thermo-siphon configuration [38].

The choice of working fluid has an influence on the heat transfer capacity of the heat pipe. Working fluid with a high wettability and chemical stability for the pipe material is desirable. In addition, the operating temperature of the battery cell needs to be kept within the saturated state temperature interval of the working fluid. The pressure drop in the vapour channel is much lower compared to the pressure drop in the liquid channel. The pressure drop in the vapour channel is thus assumed to be negligible to simplify the calculations. Based on the above considerations and assumptions, the capillary limit is calculated as follows [38, 39]:

$$Q_{\max} = N_c * M \quad \text{with } N_c = \frac{2S_l K}{bL_{\text{eff}}} \quad \text{and } M = \frac{\sigma \rho_l h_{fg}}{\mu_l} \quad (2.1)$$

where the capillary number  $N_c$  can be used to choose the groove section (as shown in Fig. 46), and is also related to the dimensions of the heat pipe. The working fluid merit number  $M$  can be used to select the working fluid. The larger the merit number is, the higher the capillary limit will be.

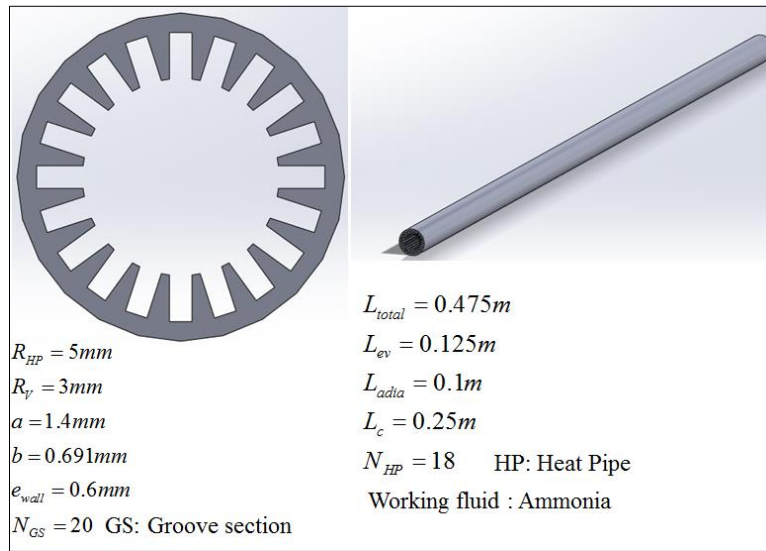


**Fig. 46.** The design and geometrical properties of the heat pipe with a groove structure.

Figure 46 shows the design of a single heat pipe with a groove structure. In this study, the maximum transferrable heat power by a single heat pipe is chosen to be 400 W, as an example. The heat pipe is oversized to reflect the design conservatism in terms of the 41 W maximum power generated by the battery. This design choice is made in order to assure an effective working process during discharge, but also for the purpose of future experimental study. The geometrical parameters of the heat pipe are determined accordingly and presented in Fig. 46. Heat transfer analysis of a single heat pipe is complex, since different phenomena need to be considered, such as thermal conduction, phase change, and fluid dynamics. CFD simulations and analyses have been broadly used including those using commercial software packages. However, the CFD approach is often very costly in terms of computing resources needed and requires validations especially for changed conditions. Due to these reasons, simplified models are often used in practical applications.

### 2.3.Problem description and modelling simplification

A 3D numerical simulation of a battery pack cooled by heat pipes is complex and time consuming. In the case of simulating one pipe, it will also necessitate high computing resources in order to describe the mass and heat transfer, during the transient discharge of the battery. In light of this, another computationally efficient approach is adopted. The thermal behaviour of the battery is modelled by a thermal network using the thermal circuit method. Additionally, for the temperature prediction of a detailed battery cell (multi-layer structure), considering the electro-chemical reactions is also too complex to execute. Therefore, models are proposed to simulate the heat generation due to the electro-chemical reaction of the battery and to describe the thermal properties of the multi-layer structure of the battery cell.

#### 2.3.1 Model formulation of the heat pipe

Zuo and Faghri [37] developed a thermal network model of heat pipe that showed a good agreement with the experimental data. In this study, a further simplified thermal network is proposed, as shown in Fig. 47. In this model, the thermal resistances  $R_{th3}$  and  $R_{th5}$  are due to the phase change, while the thermal resistance  $R_{th4}$  is due to the flow of vapour. Because of

the high thermal conductance ( $G_{th} \approx 10^5$ ) of these heat transfers, the thermal resistance  $R_{th3}$ ,  $R_{th4}$  and  $R_{th5}$ , can be neglected ( $G_{th} = 1/R_{th}$ ).

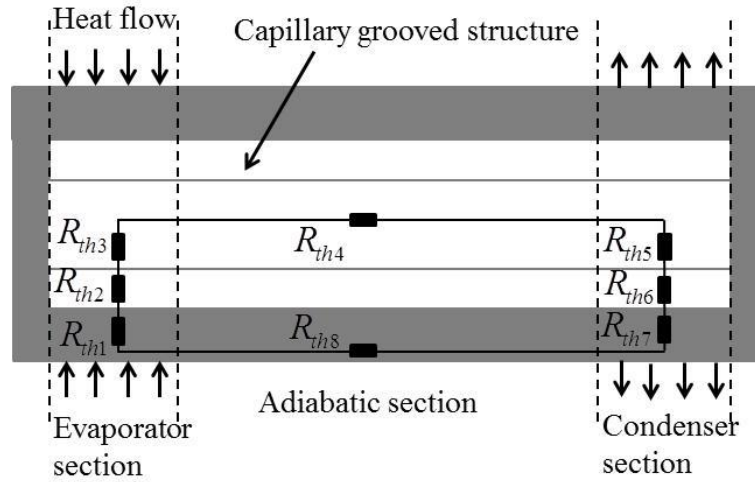


**Fig. 47.** Thermal network of a heat pipe.

A macroscopic approach based on parallel or series heat transfer is used to calculate the thermal resistances of the network. The porous media in the heat pipe (wick or groove section) should be taken into account. This modelling method is based on the heat pipe geometry and the choice of the porous media.  $G_{th1}$  and  $G_{th7}$ , representing the thermal conductance per the surface, are calculated from  $k_{wall}/e_{wall}$ , where  $k_{wall}$  is the thermal conductivity of the heat pipe material envelop and  $e_{wall}$  is the thickness of the wall. For the evaporating area ( $G_{th2}$ ) containing the groove section and the liquid (seen in Fig. 48(a)), the Chi model [38] is used to determine an equivalent thermal conductivity:

$$k_{ev} = \frac{(k_l k_s A E) + W k_l (0.185 E k_s + A k_l)}{(W + E)(0.185 E k_s + A k_l)} \quad \text{and} \quad G_{th2} = \frac{k_{ev}}{A} \quad (2.2)$$

The Chi model is obtained by considering two paths for the heat flux [38]. The first one is a series conduction between the groove structure and a liquid film with thickness of  $0.185E$ . The second path is a parallel conduction pattern between the series pattern presented and a liquid film with a thickness of  $A$ . The thermal conductivity of the condensing area (Fig. 48(b)) is calculated using a series pattern  $G_{th6} = (A(W + E)/(W k_l + E k_s))^{-1}$ . However in this formula, the liquid film is not taken into account. Romestant [38] showed that this film can have a strong impact on the thermal conductance, and recommended to divide  $G_{th6}$  by 100 to calibrate the impact of the film, based on the experimental results. Finally,  $G_{th8}$  is neglected due to the small thickness of the envelop and the length of the heat pipe.

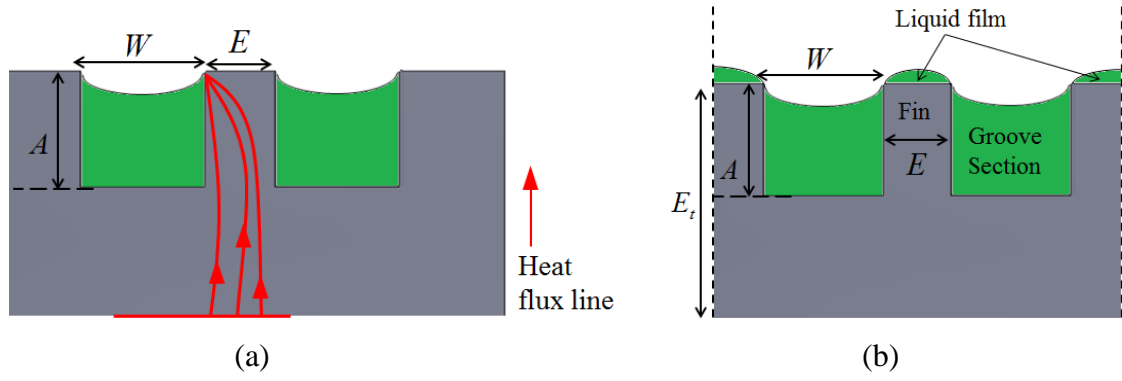


**Fig. 48.** Groove structure at: (a) the evaporator; and (b) the condenser.

Based on the above modelling assumptions and simplifications, the final thermal network model obtained for the heat pipe is presented in Fig. 49. The thermal network of the heat pipe is composed of 4 nodes. Each section has 2 nodes: one node for the vapour and the other for the wall or envelop of the heat pipe.

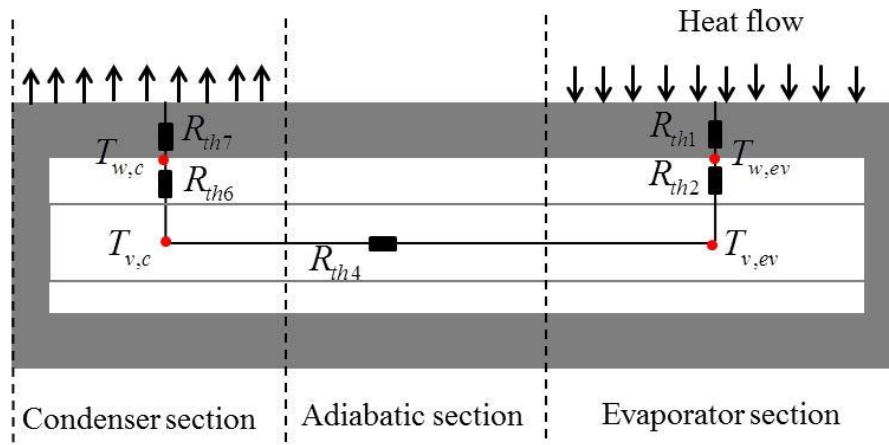


**Fig. 49.** The simplified thermal network of heat pipe.

### 2.3.2 Thermal model formulation of the battery

Different models of heat generation exist in the literature, for representing the internal source term of the battery during discharging. The heat generation rate per volume in a battery cell is calculated, by adopting the following model [12]:

$$q = R_i i^2 - T \Delta S i / (nF) \quad (2.3)$$

In the above equation, the first term,  $R_i i^2$ , represents the heat due to the internal equivalent resistance, and the second term,  $T \Delta S i / (nF)$ , represents the reversible heat caused by the entropy change of electrochemical reactions.

The battery used in this study is the same as that in the literature [53], where only geometrical and nominal thermo-physical characteristics of the battery are available and summarised in Table 3. The source term is assumed to be a constant value during the entire discharging process. The value of the source term is taken as the maximum power generated by the battery during the highest supportable constant current discharge rate (5C discharge rate corresponding to 100 A for a capacity of 20Ah) [53]. In this study, the heat generation rate per volume  $q$  is assumed to be  $240 \text{ kWm}^{-3}$ .

**Table 3** Mechanical characteristics and thermo-physical properties of the battery ([53]).

Material layer	Thickness [m]	Number of layers	Density [kg.m <sup>-3</sup> ]	Heat capacity [J.kg <sup>-1</sup> .K <sup>-1</sup> ]
Aluminium foil	2.10E-05	17	2702	903
Copper foil	1.20E-05	18	8933	385
Separator Sheet	2.50E-05	36	1017	1978
Positive electrode	7.00E-05	34	2895	1270
Negative electrode	7.90E-05	36	1555	1437

For modelling the battery properties, global thermo-physical properties can be used to represent the physical properties of the battery multi-layer structure. This simplification approach has been validated using the experimental data and used in CFD simulation analyses [10, 11]. Moreover, Taheri et al. [53] used this approach to represent the thermo-physical properties of the battery in their 3D analytical model. Based on the geometrical characteristics and thermo-physical properties of the battery multi-layer structure given in Table 3, the global properties are calculated as follows [10, 11, 53]:

$$k_x = \frac{\sum_{j=1}^N l_j}{\sum_{j=1}^N (l_j / k_j)}; k_y = k_z = \frac{\sum_{j=1}^N l_j k_j}{\sum_{j=1}^N l_j}; \rho c_p = \frac{\sum_{j=1}^N \rho_j c_{p_j} v_j}{v} \quad (2.4)$$

The following results are then obtained:  $k_x = 0.97 \frac{W}{m.K}$ ;  $k_y = k_z = 26.57 \frac{W}{m.K}$ ;  $\rho c_p = 2767.45 \frac{KJ}{m^3.K}$ .

## 2.4. Research methods: analytical solution, 1D model and 3D numerical simulation

In this study, the 1D approach is composed of a 1D model (analytical or computational) of the battery, connected to the thermal network model of the heat pipe. Such simplified 1D approach is expected to sufficiently predict the transient thermal behaviour of the battery cooled in different configurations including forced convection and heat pipe sets. The 1D analytical model of the battery is used as a baseline reference in this study, for which the solution developed takes into account the transient behaviour of the cooling process applied on the battery surfaces. A 3D numerical model of the battery cell is simulated using a commercial CFD code, in order to verify the reliability of the 1D approach.

### 2.4.1 One-dimensional analytical model

The transient energy equation for temperature of the battery cell cooling by the heat pipes is solved using the separation of variable method [54]. This method necessitates homogeneous and linear boundary conditions for the equation to be applied. Besides, the time dependence of certain boundary conditions of the heat pipe has added further complexities to apply the method. Therefore, simplifications are needed in order to reduce the complexity of the solution. The battery studied belongs to a battery type where an orthotropic conductivity is observed and the thickness direction (x direction in Fig. 50) has a very low conductivity compared to the other directions (y and z directions in Fig. 50). According to this battery's characteristic, the largest gradient of temperature will be in the x direction. Additionally, the heat pipe cooling is also located in the same direction (x direction in Fig. 50). Consequently, it is reasonable to expect that all the important physics of the heat transfer will be represented

in this particular direction. This assumption has helped to apply the separation of variable method despite the difficulties enumerated before and has led to a 1D analytical solution, which is very easy to use. However, the intensity of the cooling on the other surfaces of the battery located in the y and z directions can have an impact on the model proposed, and a comparison with a 3D resolution by CFD is performed (described in sub-section 2.5.1) in order to verify the assumption made. Finally, the energy equation for temperature in 1D is:

$$C \frac{\partial T}{\partial t} - k_x \frac{\partial^2 T}{\partial x^2} = R_i i^2 \quad \text{and} \quad \begin{cases} q = R_i i^2 \\ C = \rho c_p \end{cases} \quad (2.5)$$

The domain of study is shown in Fig. 50:

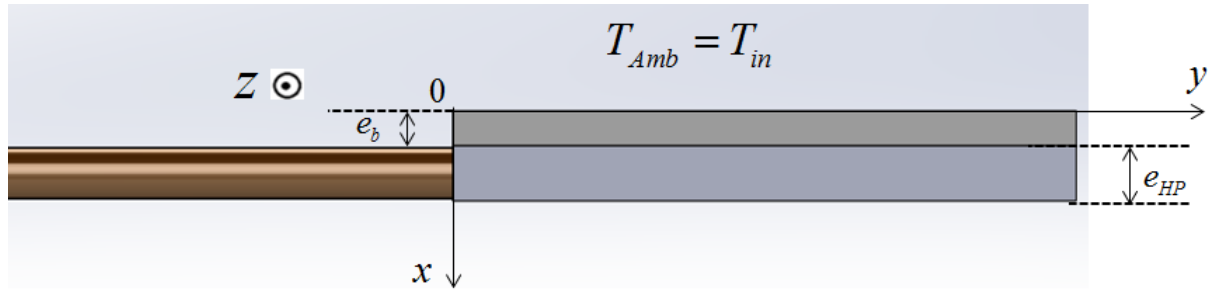


**Fig. 50.** The 1D domain of study.

The 1D thermal equation of the battery cooling is finally solved using the separation of variables method. However, the solution found needs the vapour temperature function of the heat pipe. This vapour temperature function can be obtained experimentally. At  $x = e_b$ , the boundary condition due to the heat exchange between the battery cell and the heat pipe is represented by:

$$-k_x S \frac{\partial T}{\partial x}(x = e_b, t) = \frac{k_{ev} A_{ev}}{\lambda_{ev}} (T - T_v)(x = e_b, t) \quad (2.6)$$

This condition is transformed to the following formulation, using a variable change necessary for the separation of variables:

$$\left( k_x S \frac{\partial (T - T_{in})}{\partial x} + \frac{k_{ev} A_{ev}}{\lambda_{ev}} (T - T_{in}) \right) (x = e_b, t) = f(t) \quad (2.7)$$

where  $f(t)$  is a function taking into account the conductivity of the evaporator and the vapour temperature in time. Therefore, the complete temperature of the battery can be obtained, by knowing the temperature of the vapour experimentally. Moreover,  $f(t)$  can be any function corresponding to different cooling solutions. The only condition needs to satisfy is  $f(t = 0) = 0$  in order to apply the separation of variables.

In this study, two analytical solutions are proposed for two different types of boundary conditions. The first type (**Case 1**) is derived in view of a theoretical case for testing the function and different hypotheses. In this case, one side of the battery has a fixed temperature and the other side is cooled by the heat pipe. The second type (**Case 2**) is formulated for a battery cell sandwiched between two sets of heat pipes.

- **Case 1:**

The boundary conditions are presented as follows (Fig. 50):

$$\begin{aligned}
 T(x,0) - T_{in} &= 0 \\
 T(0,t) - T_{in} &= 0 & f(t) &= F(T_v(t) - T_{in}) \\
 \left( \frac{\partial(T - T_{in})}{\partial x} + \frac{k_{ev} A_{ev}}{\lambda_{ev} k_x S_b} (T - T_{in}) \right) (x = e_b, t) &= f(t) & \text{with} & F = \frac{k_{ev} A_{ev}}{\lambda_{ev} k_x S_b} \\
 f(t = 0) &= 0
 \end{aligned} \tag{2.8}$$

And the solution can be derived as:

$$T_i(x,t) - T_{in} = \sum_{n=0}^{\infty} (H_0(t) - H_0(0) \exp(-\gamma_n t)) \sin(\beta_n x) + \frac{x(x - e_b)}{e_b} f(t) \tag{2.9a}$$

$$\begin{aligned}
 \Omega_n H_0(t) &= \left( \frac{2[1 - \cos(\beta_n e_b)]}{e_b \beta_n^3} - \frac{\sin(\beta_n e_b)}{\beta_n^2} \right) f(t) + \frac{[1 - \cos(\beta_n e_b)] R_i i^2}{k_x \beta_n^3} \\
 &+ \left( \frac{k_x \sin(\beta_n e_b)}{C} \right) \left[ \int_0^t f(t) \exp(\gamma_n t) dt \right] \exp(-\gamma_n t)
 \end{aligned} \tag{2.9b}$$

$$\Omega_n = \frac{\beta_n e_b - \cos(\beta_n e_b) \sin(\beta_n e_b)}{2\beta_n} \tag{2.9c}$$

$$\gamma_n = \frac{k_x \beta_n^2}{C} \tag{2.9d}$$

where  $\beta_n$  is the root of the transcendental equation:  $\beta_n e_b \cot an(\beta_n e_b) + \frac{2k_{ev} A_{ev} e_b}{\lambda_{ev} k_x S_b} = 0$ .

- **Case 2:**

In this case, due to the symmetry of the system layout, only one half of the domain is studied. The boundary conditions are then given as:

$$\begin{aligned}
 T(x,0) - T_{in} &= 0 \\
 \frac{\partial(T - T_{in})}{\partial x} (x = 0, t) &= 0 \\
 \left( \frac{\partial(T - T_{in})}{\partial x} + F(T - T_{in}) \right) (x = e_c, t) &= f(t) \\
 f(t = 0) &= 0 \\
 e_c &= \frac{e_b}{2}
 \end{aligned} \tag{2.10}$$

The solution can thus be acquired as:

$$T_i(x,t) - T_{in} = \sum_{n=0}^{\infty} (H_0(t) - H_0(0) \exp(-\mu_n t)) \cos(\alpha_n x) - \cos\left(\frac{\pi x}{e_c}\right) \frac{f(t)}{F} \tag{2.11a}$$

$$\Omega_n H_0(t) = \frac{\cos(\alpha_n e_c)}{\left(\frac{\pi}{e_c}\right)^2 - \alpha_n^2} f(t) + \frac{Ri^2 \sin(\alpha_n e_c)}{k_x \alpha_n^3} + \left(\frac{k_x \cos(\alpha_n e_c)}{C}\right) \left[ \int_0^t f(t) \exp(\mu_n t) dt \right] \exp(-\mu_n t) \quad (2.11b)$$

$$\Omega_n = \frac{\alpha_n e_c + \cos(\alpha_n e_c) \sin(\alpha_n e_c)}{2\alpha_n} \quad (2.11c)$$

$$\mu_n = \frac{k_x \alpha_n^2}{C} \quad (2.11d)$$

where  $\alpha_n$  is the root of the transcendental equation:  $\alpha_n e_c \tan(\alpha_n e_c) = Fe_c$ .

Both solutions (for Cases 1 and 2 with heat pipes) can be conveniently modified for convective cooling. For replacing the heat pipes by convective cooling, the minor modifications are:

$$f(t) = 0; \quad \frac{k_{ev} A_{ev}}{\lambda_{ev}} = hS_b \quad (2.12)$$

The analytical model will be used as the reference in certain cases and compared to the 1D computational model and the 3D numerical simulation. Unlike the 1D analytical model, the 1D computational model, as presented in the following sub-section, is able to simulate the battery cell cooling by the heat pipe set in different configurations without using vapour temperature function or experimental data.

#### 2.4.2 One-dimensional computational model

Figure 51 presents the 1D computational model of the battery in conjunction with the heat pipe set, based on the thermal circuit method where the battery is represented by a thermal network. A number of nodes are chosen in the battery and linked by a thermal resistance (or thermal conductance) depending upon the thermo-physical and geometrical properties of the battery. The transient behaviour of the model is obtained by allocating a thermal capacitance to each node, as seen in Fig. 51(b). Each node occupies a volume and generates a thermal power proportional to its volume.

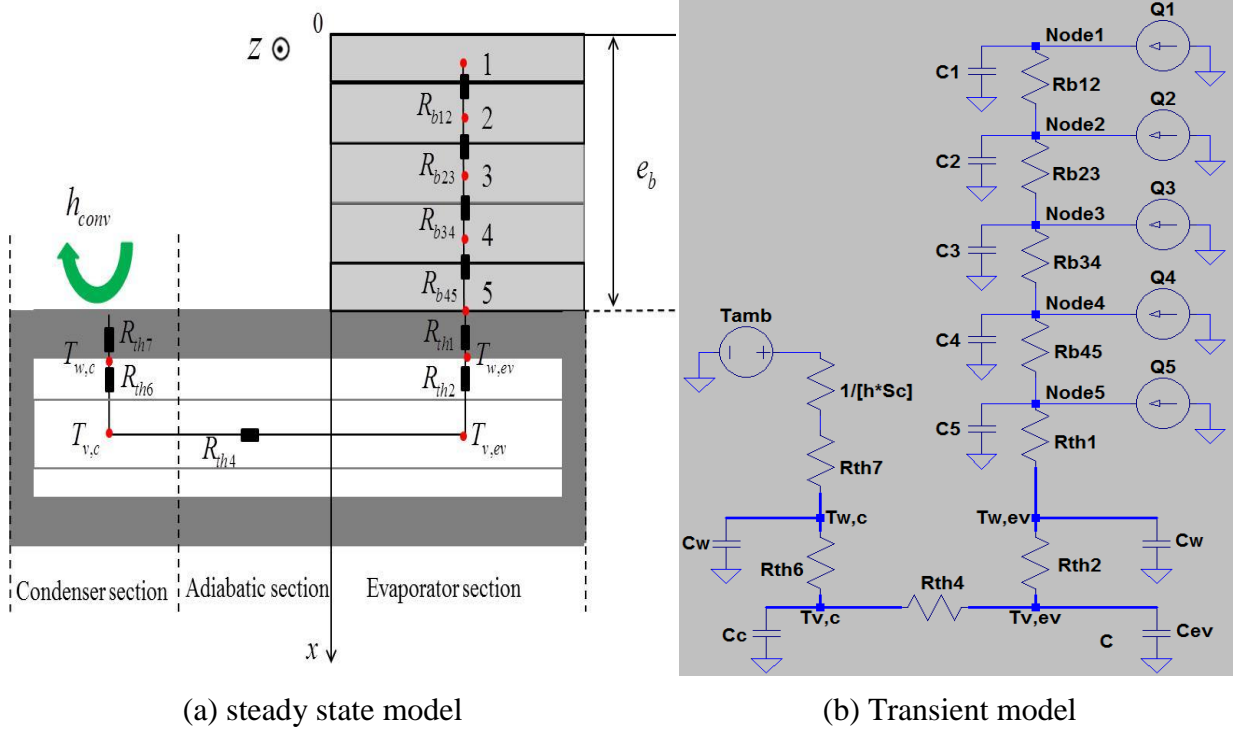


**Fig. 51.** Nodes of the 1D computational model of the battery connected to the heat pipe set.

The preliminary analyses suggest that five nodes are enough to represent the thermal behaviour of the battery considered. The 1D computational approach offers a possibility to treat the battery and heat pipe models separately. Based on this, more nodes can be easily added for a larger battery, without modifying the heat pipe model and the calculation process. It should be noted that the number of nodes for modelling the battery can be optimised using the 1D analytical model derived before.  $R_{bij}$  is the thermal resistance between the nodes  $i$  and  $j$  in the battery cell. The complete model of the battery (using five nodes) connected to the heat pipe set thermal model (four nodes) is represented by the nodal temperature matrix:

$$[C] \frac{d[T]}{dt} = [G][T] + [P] \quad (2.13)$$

This equation can also be used for convective cooling by just removing the nodes of the heat pipe and adding the term due to the convective coefficient.

### 2.4.3 Three-dimensional numerical simulation

The global thermo-physical properties derived in Eq. (2.4) are used in the 3D numerical model. The cooling solution is applied on the battery surface in the  $x$  direction ( $x = 0$  and  $x = e_b$ ). Therefore the other battery surfaces in  $y$  and  $z$  directions develop a free natural convection. For modelling this natural convection, a heat coefficient  $h_{conv} = 5 \text{ Wm}^{-2}\text{K}^{-1}$  is chosen as an example in this study.

Different scenarios are investigated, from constant temperature to forced convection. However, the complexity of the heat pipe does not allow a transient simulation of the battery cooled by the heat pipe set at the moment. Nevertheless, an equivalent conductance per surface area of the heat pipe set can be calculated and used as an input in the CFD code. More

details on this approach will be presented in sub-section 2.5.4. The mesh of the 3D battery model is refined in the  $x$  direction, as shown in Fig. 52, in order to observe properly the expected large temperature gradient and to compare the results with the 1D analytical and computational approaches.

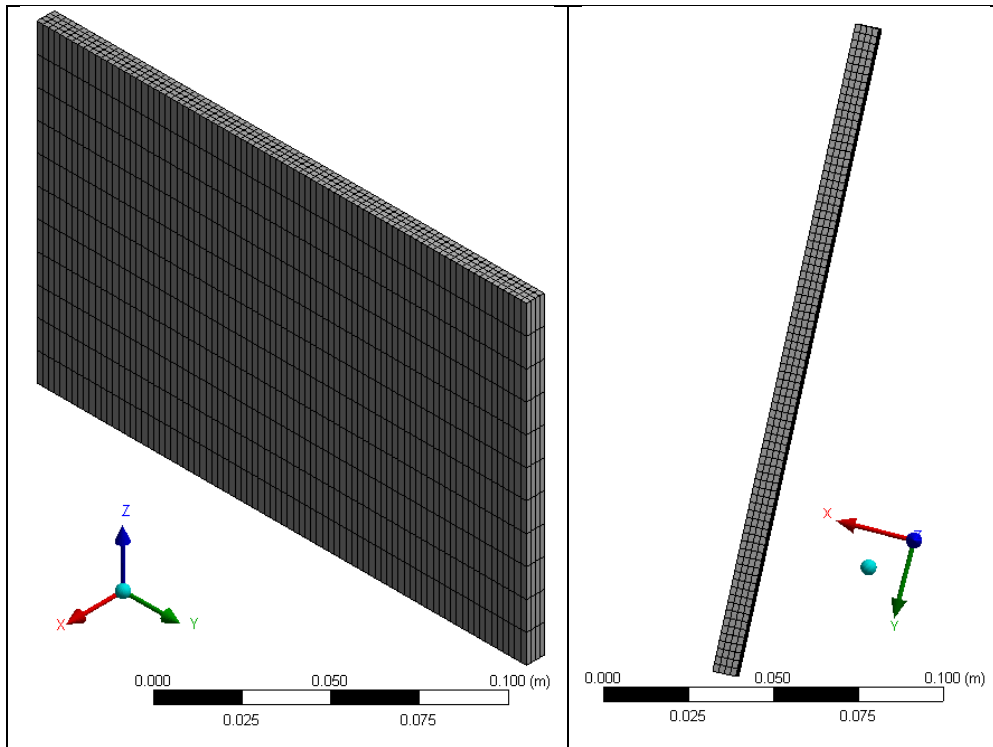


**Fig. 52.** Mesh of the battery cell in the 3D numerical simulation.

## 2.5. Results and discussions

In this section, the 1D computational model developed is analysed in various configurations and compared to the 1D analytical model and the 3D numerical simulation, so as to demonstrate the advantages of the 1D approach in view of the reliability and effectiveness. The results presented will verify if the heat pipe set designed and the distributed configuration recommended are able to meet the requirements of the temperature specifications [6].

### 2.5.1 Forced convection and fixed temperature

In this configuration, the battery surface located at  $x = 0$  has a fixed temperature ( $T(0, t) = T_{amb} = 20^\circ C$ ) and a convective heat coefficient ( $h = 20 W/m^2 K$ ) on the surface located at  $x = e_b$ . Moreover, for the 3D numerical simulation, natural convection ( $h = 5 W/m^2 K$ ) is considered on the surfaces in  $y$  and  $z$  directions. Fig. 53 presents the results obtained from the 3D numerical simulation at the end of the transient simulation. The results show that the gradient of temperature is mainly located in the  $x$  direction. Moreover the temperature in the  $YZ$  plane can be considered as uniform. In fact at  $x = e_b$ , the temperature difference between the maximum and minimum temperatures in the  $YZ$  plane is  $\Delta T(x = e_b) = 0.042^\circ C$ .

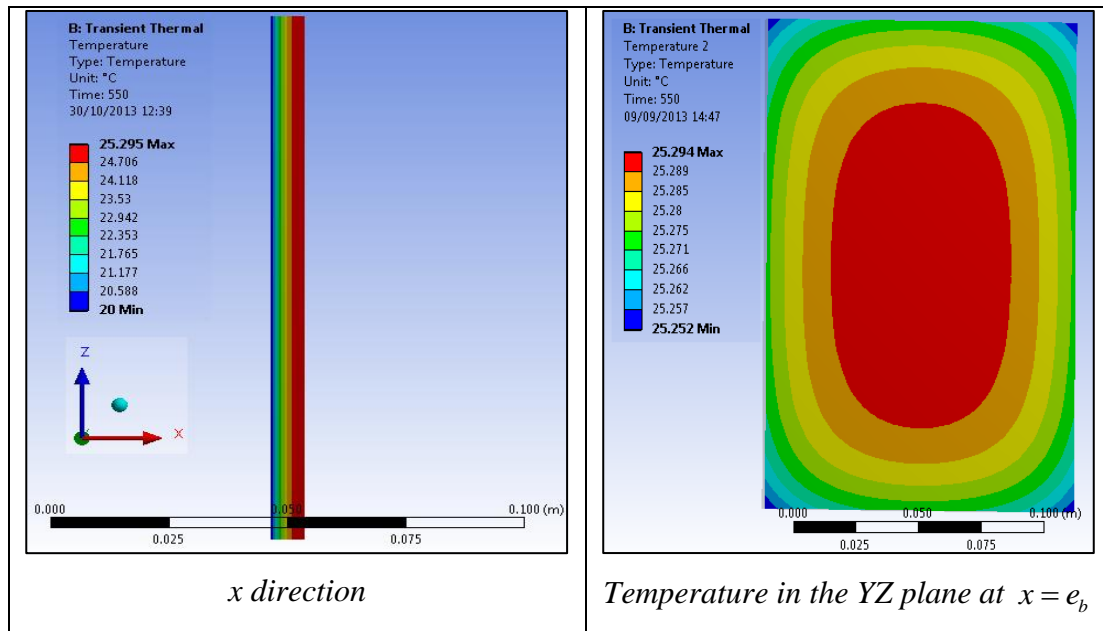


**Fig. 53.** Temperature distribution of the battery with fixed temperature and convective heat coefficient.

The temperature at the different battery locations is compared for the three cases, i.e. 3D simulation and 1D analytical and computational cases. Table 4 classifies the different points studied and their equivalents in the different models, in order to simplify the presentation of the results in Fig. 54. The comparison of the temperature rises for the three cases is presented in Fig. 54. The results clearly show that for the different locations considered in the battery (Table 4), all the three cases (3D and 1D) yield very similar temperature predictions in both the transient and steady states. Moreover, the results suggest that there is a small discrepancy between the 1D computational and analytical models, as seen in Fig. 54. Table 5 further summarises the temperature difference between the 1D computational and analytical models in a quantitative format, which indicates the very small discrepancy (less than 0.5%) at the end of the simulation, predicted by these two models.

**Table 4** Position of the nodes studied for the 1D analytical and numerical models.

1D computational	1D analytical	Position of the node (m)
T1	$x=eb/16$	0.0004375
T2	$x=2*(eb/8)$	0.00175
T3	$x=4*(eb/8)$	0.0035
T4	$x=6*(eb/8)$	0.00525
T5	$x=8*(eb/8)$	0.007

**Table 5** Discrepancy of temperature between the 1D computational and analytical models.

Position of the node (m)	1D computational	1D analytical	Discrepancy
4.38E-04	20.709	20.686	0.11%
1.75E-03	22.553	22.461	0.41%
3.50E-03	24.253	24.164	0.37%
5.25E-03	25.195	25.109	0.34%
7.00E-03	25.380	25.297	0.33%

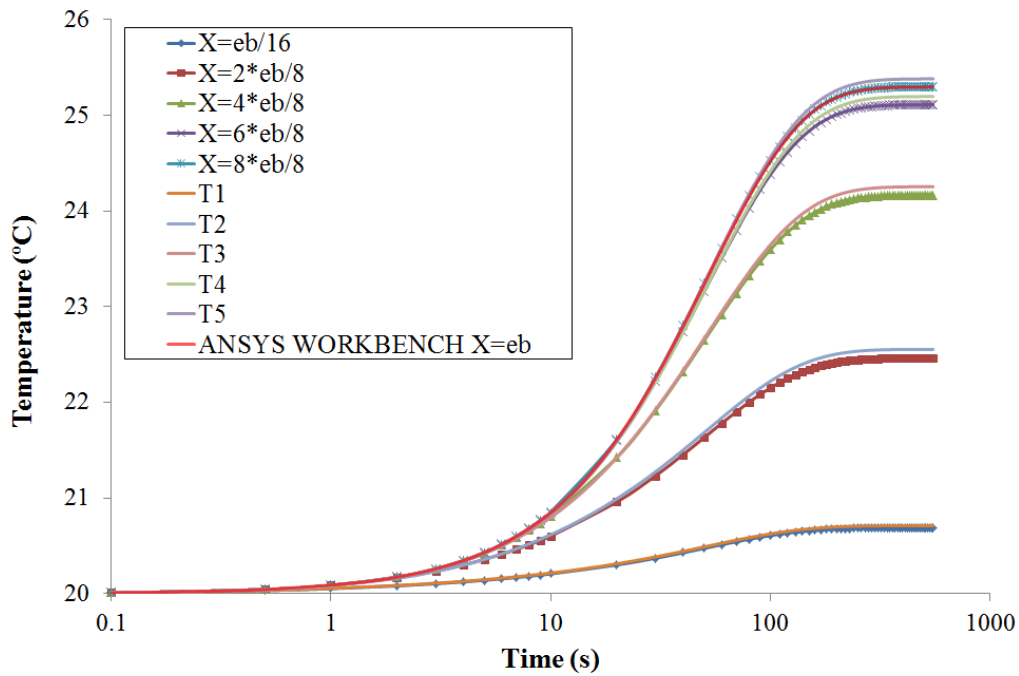


**Fig. 54.** Battery cell temperature with fixed temperature and convective coefficient for the three cases.

The discrepancy of temperature between the 1D computational model and 3D numerical model at the end of the simulation is 0.01%. Therefore, the 1D computational model is sufficient to describe the transient behaviour of the battery cell. This result was predictable using the Biot Number ( $Bi$ ). This number compared the thermal resistance of conduction with the thermal resistance of convection. Therefore the condition,  $Bi \ll 1$ , indicates that the temperature in a body can be considered uniform [53]:  $Bi_j = h_j L_j / k_j$  with  $j$  indicating the direction  $x, y, z$ .

Table 6 shows that the Biot numbers in the  $y$  and  $z$  directions are much less than one. As a consequence, the temperature in the  $YZ$  plan can be considered uniform. Additionally, the 3D numerical model used 18895 nodes, where the 1D computational model used only 5 nodes. The running time of the 1D computational model took much shorter time than the 3D numerical simulation. The run time needed for the 1D computational model is comparable to the analytical solution, which takes almost no time to run.

**Table 6** Directional Biot number.

Direction	$k$	$h$	$L$	$Bi$
$x$	0.97	20.00	0.007	0.14
$y$	26.57	5.00	0.195	0.04
$z$	26.57	5.00	0.125	0.02

### 2.5.2 Theoretical test of linear temperature vapour in the heat pipe

This sub-section attempts to verify the analytical model (Eqs. 2.9a-2.9c) in Case 1 with  $f(t) \neq 0$ . In this case, one surface has a fixed temperature, and the other is cooled by a heat pipe set. The formulation  $f(t) = F(T_v(t) - T_m)$  is calculated with a prescribed vapour temperature. The characteristics of the vapour temperature could vary, which could be

represented by a linear or nonlinear function. To simplify the analysis, a linear function is chosen to perform the calculations. For a relative comparison, the analytical formulation of the vapour temperature can be used which is given by  $T_v(t) = 10t/550 + 20$ , where the slope  $10/550$  is chosen to represent a mild temperature variation. Based on these assumptions, the 1D computational model and analytical solution are compared, and the results are presented in Fig. 55.

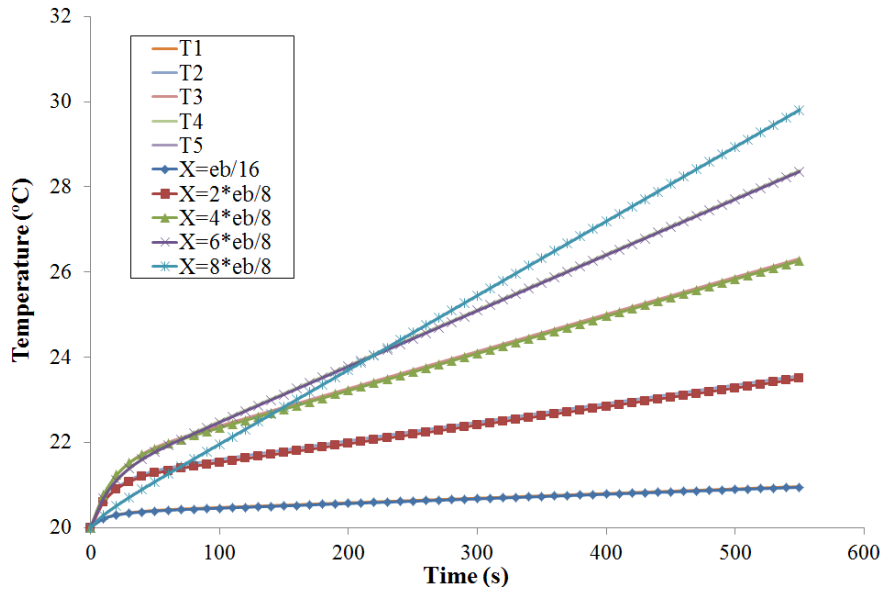


**Fig. 55.** Comparison of battery temperature between the 1D computational and analytical models with a linear vapour temperature in the heat pipe.

The results show a good agreement between the numerical and the analytical solutions, which confirms the effectiveness of the derived analytical solution for a boundary condition that is dependent upon the time. Thus, the analytical model proposed in this study can be used for practical applications with different types of cooling methods.

### 2.5.3 Battery cell sandwiched by two heat pipe sets

The battery sandwiched by two heat pipe sets is presented in Fig. 56, which might be the case in view of large battery packs for electric vehicles. The other cooling solution, forced convection (CS1) directly applied on the battery's surfaces, is compared with the heat pipe cooling solution (CS2, shown in Fig. 57). For a proper comparison, identical convective coefficients ( $h = 28Wm^{-2}K^{-1}$ ) are used for the condensing area of the heat pipe set and also for the convective cooling within the both cooling solutions, respectively. Figure 58 presents the comparison of the characteristics of the maximum temperature in a battery cell for the CS1 and CS2 cooling solutions.

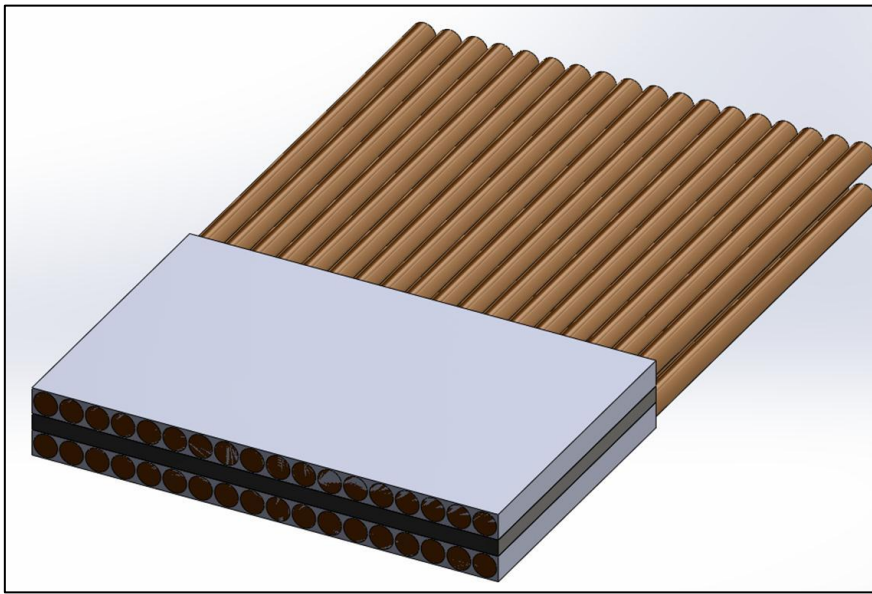


**Fig. 56.** Battery cell sandwiched by two heat pipe sets.

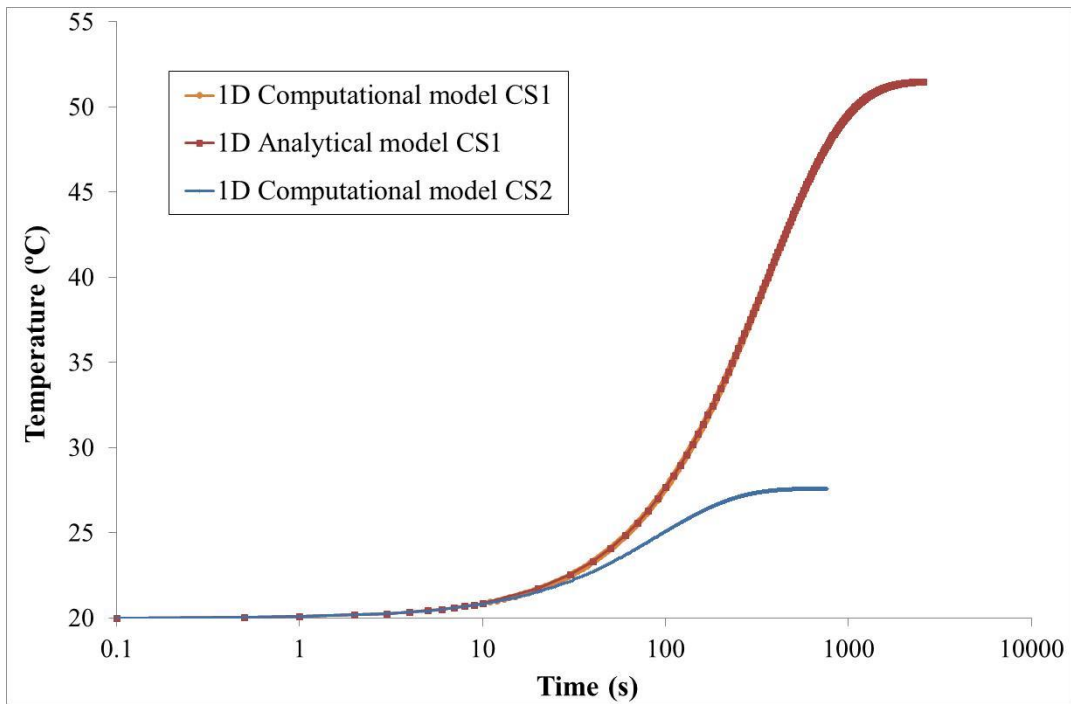


**Fig. 57.** Comparison of maximum temperature for the forced convection (CS1) and heat pipe set (CS2) in a distributed configuration using the same convective heat coefficient.

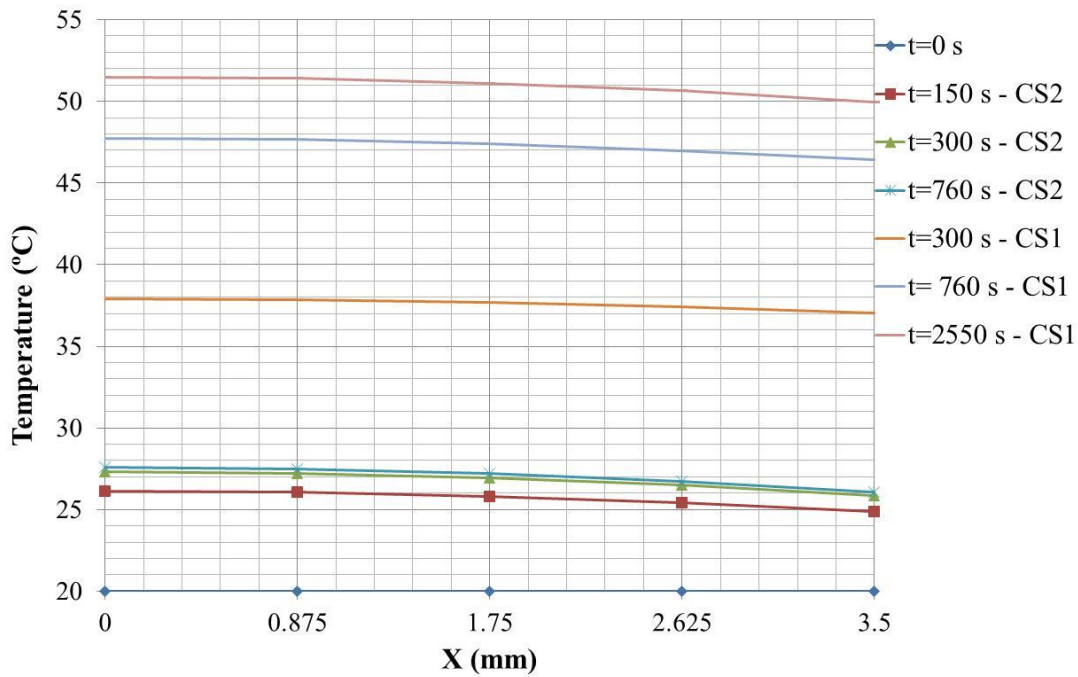


**Fig. 58.** Comparison of temperature distribution between CS1 and CS2.

The efficiency of the heat pipe set depends on its design parameters but also on the cooling process used at the condenser. Contrary to CS1, the heat pipe set (CS2) yields a larger contact area for the same convective heat transfer coefficient. For the simulation conditions considered in this study, the contact areas of CS1 and CS2 can be calculated as:

$S_b = 0.0244m^2$  and  $S_c = 0.14m^2$ , respectively. The gap between the heat pipes in the set is 0.8 mm. These gaps allow the cooling fluid to flow around the pipes, which improves the cooling efficiency of the system. It should be noted that the type and design of the cooling process at the condenser have an effect on the  $S_c$  value of the heat pipe set. In order to simplify the analysis and to be conservative as well, the minimum contact area at the condenser,  $S_c = 0.14m^2$ , is considered.

The maximum temperature is obtained for both cooling solutions, namely 51.5°C for CS1 and 27.6°C for CS2. For the convective heat transfer coefficients considered, using heat pipes yields better cooling than the forced convection. Furthermore, an even temperature distribution in the battery cell must be achieved in order to avoid safety issues. Half of the battery is represented in Fig. 58, because of the symmetric cooling configuration. The temperature difference between the maximum and the minimum is less than 2°C for both cooling solutions. The steady state is reached faster using the heat pipe set. In fact, the approximations or models used (conductance calculation) were chosen to achieve better performances for a real application. Moreover, the efficiency of the heat pipe set in distributed configuration can be significantly improved by:

- An efficient cooling of the condenser
- Increasing the length of the condenser
- Adding fins to the heat pipe sets

The complexity of the heat pipe does not allow a simple CFD simulation. Additionally, the analytical model developed needs an expression or experimental data of the vapour temperature. The approach developed using an equivalent conductance of the heat pipe proves to be effective, in which the 1D computational model of the battery is connected to the

heat pipe. It is therefore taken as the reference to study the impact of the equivalent conductance.

#### 2.5.4 Equivalent thermal conductance of the heat pipe

To achieve a further simplified formulation, the equivalent thermal conductance is defined and calculated using the thermal network of the heat pipes. The analogy between the thermal network (Fig. 49) and the electric circuit is used to derive the equivalent thermal conductance:

$$G_{eq} = (R_{th1} + R_{th2} + R_{th6} + R_{th7} + \frac{1}{hS_c})^{-1} = 3.37W.K^{-1} \quad (2.14)$$

The equivalent convective heat coefficient can correspondingly be defined and obtained by:

$$h_{eq} = G_{eq} / S_b \quad (2.15)$$

Based on the above definition of equivalent convective heat coefficient, Figs. 59 and 60 depict the performance characteristics of the maximum and minimum temperatures of the battery cell for heat pipes. The results suggest that using the equivalent model defined in Eqs. (2.14) and (2.15) yields good approximation of both maximum and minimum temperature to those generated by the complete thermal network model of the heat pipes. However, the computational efficiency based on the equivalent model is improved in the CFD simulation. It should be noted that the CFD simulation of the transient thermal dynamics of the battery with heat pipes is computationally very demanding. Therefore, the proposed equivalent model offers a feasible solution for conducting design and analysis of battery cooling systems at the preliminary design stage.

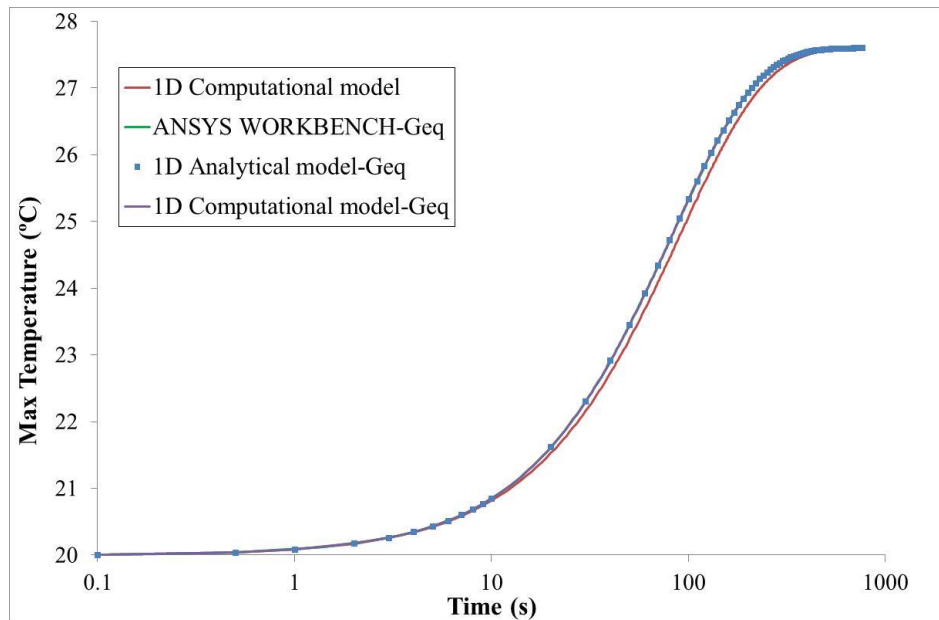


**Fig. 59.** Maximum temperature of the battery cell using equivalent approach for the heat pipe set.

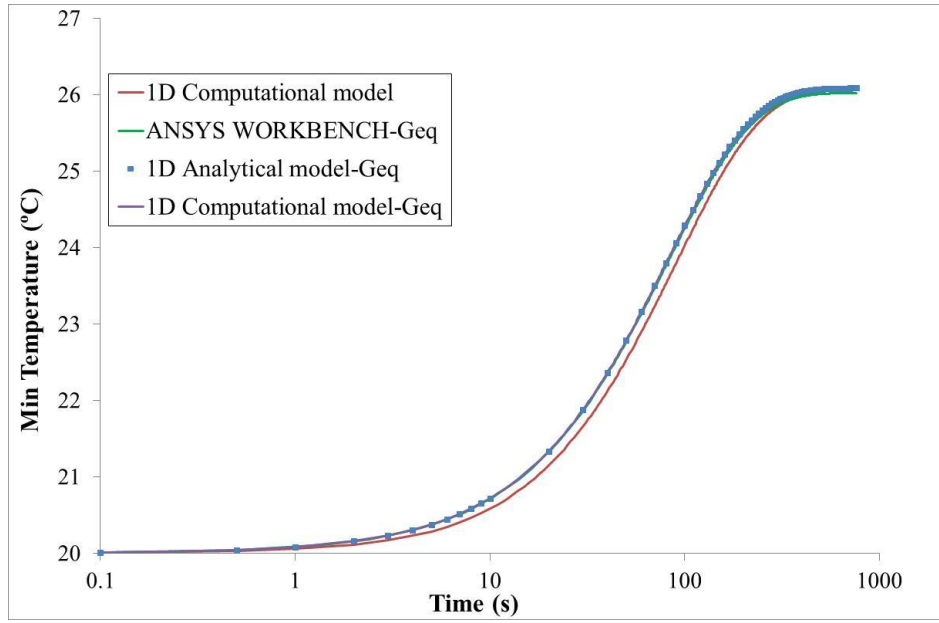


**Fig. 60.** Minimum temperature of the battery cell using equivalent approach for the heat pipe set.

It is also observed from the results that the equivalent approach tends to overestimate the temperature rise, which might be attributed to the conservatism in the parameter determination including the intensity of the convection in the condensing area and the model simplifications. The discrepancy observed between the approaches is due to the thermal capacity of the heat pipe. In the complete 1D computational model, the thermal capacity evolves with the temperature during the simulation process, but the equivalent conductance approach does not consider the thermal capacity and therefore reaches the steady state faster, as seen in Figs. 59 and 60.

### 2.5.5 Thermodynamic process within the heat pipe

The heat pipe is oversized using the working fluid merit number method, which helps to achieve the heat pipe design in a more practical way. Zuo and Faghri [37] proposed a method based on the first law of thermodynamics. The liquid sub-cooling is a requirement for the heat pipe operation when the liquid is traveling from the condenser to the evaporator [37]. This sub-cooling requirement can thus be met if [37]:

$$\Psi = \Phi/\Theta > 1 \quad (2.16)$$

where

$$\Phi = \frac{b}{2R_{HP}} \frac{R_V^4}{L_c(L_e + 2L_a + L_c)} ; \Theta = 2k_{ev} \frac{T_{HP}\mu_v}{(\rho_v h_{fg})^2} ; \text{ and } T_{HP} = \frac{T_{v,ev} + T_{v,c}}{2}$$

In the above equation,  $\Phi$  represents the geometric group (a group of geometrical parameters of the heat pipes), and  $\Theta$  represents the thermo-physical group (a group of thermo-physical properties of the working fluid).

Figure 61 presents the variation of the minimum value of  $\Psi$ , calculated from Eq. (2.16), over the vapour temperature range considered, using the 1D computational model. It can be clearly seen that the  $\Psi$  value is the order of  $10^6$  and much larger than 1, which satisfies the

sub-cooling requirement. The very large value of  $\Psi$  is primarily due to the oversizing in the heat transfer capacity of the heat pipe.

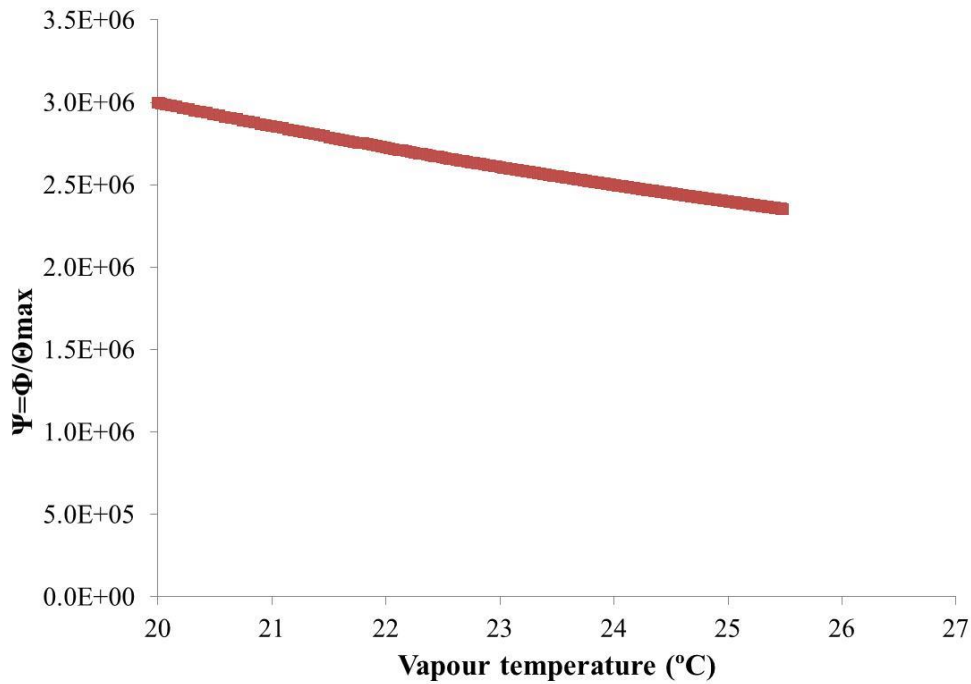


**Fig. 61.** Verification of the sub-cooling condition of the heat pipe operation, using the method proposed in [37].

## 2.6. Concluding Remarks

An analysis of the passive cooling management of the ePLB C020 battery cell by heat pipes was studied in this paper. A one-dimensional approach composed of a 1D computational model of the battery connected to a thermal network of the heat pipe, is proposed. This approach is based on the thermal circuit method and allows to treat the battery and the heat pipe separately. An analytical model with time-dependent boundary conditions and a 3D numerical model were developed in order to test and verify certain hypotheses made for the one-dimensional computational approach.

The lack of experimental data for this study made it difficult to systematically assess the design and modelling approaches. Accordingly the design of the cooling system was made intentionally conservative. Because of this, the heat generation of the battery was taken as a constant at the maximum rate of discharge. Simplifications were also made concerning the model of the heat pipe and its design. Regarding the thermal network model of the heat pipe, the thermal resistance at the evaporator was calculated using the Chi model. The Chi model is very conservative and was useful for this study but not recommended when the size of the heat pipe is a critical issue. Besides, the impact of the liquid film at the condenser was approximated by an experimental factor [38]. Moreover, the design of the heat pipe did not take into account the reduction of the liquid section at the evaporator and the impact of the gravity. In addition, the effect between each heat pipe was neglected in the heat pipe set.

The comparison between the 1D model (computational and analytical) and the 3D numerical simulation by CFD showed a good agreement. The results confirmed the reliability of the one-dimensional approach to simulate the thermal behaviour of the battery cell. Besides, the

1D approach takes much shorter running time than the 3D numerical simulation. Because of this, the 1D approach holds great potentials for practical applications. However, the results cannot be generalized since they depend on the Biot number of the system.

The heat pipe set designed and applied on the battery cell in a distributed configuration was studied using the 1D computational model. This simulation made with conservative correlations and approximations for the heat pipe model, predicted a maximum temperature of 27.6°C. A maximum temperature of 51.5°C is obtained for the same configuration in a forced convection cooling directly applied on the surface of the battery. The results with a conservative design and calculation showed the importance of the heat pipe and the effectiveness of the passive cooling management.

The 1D computational model based on the nodal network method as well as the analytical resolution have been able to predict the transient temperature in a prismatic battery cell. These numerical and analytical models were obtained, considering the very low conductivity in the thickness direction of the prismatic cell compared to the other ones. These approaches are investigated in the next chapter, for studying the cooling of a cylindrical battery cell by PCM/graphite matrix. Besides design parameters of the PCM/graphite are highlighted depending on the characteristics of the cylindrical battery cell.

## **Chapter 3: An investigation of lithium-ion battery thermal management using paraffin/porous-graphite-matrix composite**

### **3.1.Introduction**

The global efforts on reducing the carbon dioxide emission and the diminution of oil resources have made electric vehicle (EV) and hybrid electric vehicle (HEV) alternatives to the vehicle equipped with combustion engines. The requirements of battery power and capacity for HEV/EV vehicles have positioned Li-ion battery as the best candidate amongst various battery types, which has a better energy density and lower discharge rate compared to many other battery types. Nevertheless the performance of Li-ion battery is limited by temperature rise during the discharge process. Temperature affects strongly the safety, reliability and lifespan of the battery [1, 2]. Efficient and safe running during driving operations is obtained by keeping the battery temperature between 20°C and 40°C [2]. Moreover, the temperature from cell to cell and module to module should be normally within 5°C, for ensuring temperature uniformity. An uneven temperature distribution may lead to a short circuit in the battery. Consequent to these requirements, two types of cooling systems are used in the thermal management. One commonly used system is based on active cooling, using fluid flow for cooling the battery. Active cooling systems usually involve a bulky flow management, which increases the system mass and has the risk of fluid leakage. System components such as a pump are also required for moving the fluid. Besides, the cooling must be well distributed [6, 17] in order to maintain an even temperature distribution in the entire pack.

An optimisation of the active cooling system can reduce its cost and size. Moussavi et al. [31] had optimised the air-cooling system for a cylindrical Li-ion battery pack using a genetic algorithm. However, the external surface of the battery had a constant temperature and the gradient in the battery was not analysed. Jarret and Kim [32, 33] studied the optimisation of a cold plate subject to a constant heat flux and the impact of the boundary conditions on this optimum design, but the cold plate design was not considered in detail. Jin et al. [34] improved the design of a mini-channel liquid cold plate by applying oblique cuts in the straight line of the cold plate. This modification avoids the complete development of the hydrodynamic boundary layer responsible of the deterioration of the convective heat transfer in the straight line design. They also showed experimentally an enhancement of the performance with minimal penalty on the pressure drop.

Thermal management system should be compact, lightweight, reliable and low cost. As an alternative to active cooling, passive cooling systems based on phase change phenomena can be potentially advantageous. Heat pipes, based on the liquid/vapour phase change, were studied experimentally by Wu et al. [35]. They showed the importance of maintaining a good surface contact between the heat pipe and the battery. Based on this recommendation, Greco et al. [55] studied and designed the cooling system of a prismatic battery cell by a set of heat pipes embedded in copper material. A 1D computational model was developed and compared

with an analytical approach and a three-dimensional (3D) computational fluid dynamics (CFD) simulation. It was demonstrated that the 1D model was sufficient to predict the temperature distribution of the lithium-ion battery. In addition to heat pipes, PCM based on solid/liquid phase change can be used for passive cooling, which has great a potential in reducing peak temperature during intermittent discharge and in overcoming performance losses at cold temperature. Duan and Naterer [43] investigated experimentally the behaviour of two PCMs during discharge under various environmental conditions. The PCMs allowed reducing the large temperature variations in the battery despite significant ambient temperature variations. In addition, the Stefan equation of the phase change problem in 1D was solved, where the solution described the propagation of the solid-liquid interface with a line heat source located in the centre. However, buoyancy effect was observed experimentally in the axial direction, making the 1D model incomplete to describe the melting process.

In practice, the low conductivity of the PCM can limit its applications [41, 42]. The conductivity of the PCM is improved by adding fins or matrix foam made of high conductive materials. Lamberg and Siren [56] developed an analytical model describing the melting of a semi-infinite PCM with internal fins. The model was based on a quasi-linear, transient, fin equation which predicts the solid-liquid interface location and temperature distribution of the fin in the melting process. The analytical results were compared to the numerical results with a good agreement in general, but the speed of the solid-liquid interface during melting process was slightly under-predicted. In addition, the analytical solution was obtained by considering a semi-infinite space. In reality, the PCM/fins have finite dimensions, and therefore the simplified analytical solution has its limitations. Lamberg and Siren [57] also developed an approximate model for solidification in a finite PCM storage with internal fins, where the solid-liquid interface location and the temperature distribution of the fins were predicted. The comparison with numerical results showed a better agreement in the solid-liquid interface location than the prediction of the temperature distribution in the fin. Moreover, the fraction of solidified PCM was introduced, giving an indication of the amount of PCM solidified at a given time. Additionally, Nithyanandam et al. [58] studied numerically the latent thermal storage of a system with packed bed of encapsulated PCM. Design guidelines were derived from their study. The phase change process was modelled within the PCM by the enthalpy-porosity method.

Compared with the metallic compounds, graphite has a higher conductivity and a lower density. Wu and Xing [59] studied numerically the performances of a cylindrical PCM enhanced with graphite. The porosity-enthalpy method was also used to describe the phase change process. Furthermore, the high surface contact between the PCM and the matrix led to a fast local equilibrium between both entities. Therefore the PCM/graphite composite can be modelled by only one equation with equivalent physical properties. The porosity and the graphite conductivity are the most important parameters for improving the thermal performance of the composite. However, an isotropic conductivity was used in their study and Py et al. [44] showed experimentally that the conductivity of the composite was anisotropic in the case of compressed expanded natural graphite. This anisotropy was caused

by the compression of the natural graphite powder during the manufacturing process. In consequence, the conductivity in the axial direction (parallel to the compression force) depending on the bulk density can be ten times lower than the conductivity in the radial direction (perpendicular to the compression force).

Most of the studies of PCM were focused on the latent thermal storage. Kizilel et al. [47] studied numerically the cooling of a cylindrical battery pack by a PCM (paraffin wax) enhanced by a graphite matrix structure during stressful conditions. The overall conductivity obtained by this modification increased the conductivity of the PCM/graphite to 16.6 W/m K. The PCM helped the battery to achieve a more even temperature distribution and to avoid the propagation of a thermal runaway from one cell to the entire pack. Moreover, the temperature in the pack stabilized itself quicker than an air-cooling system. However, the equations presented did not take into account the effect of the latent heat.

Modelling the cylindrical battery cell is important to the design of efficient cooling systems. The thermal analysis of a cylindrical battery was usually performed with isotropic thermal conductivity. Drake et al. [13] studied the thermo-physical properties of a cylindrical Li-ion battery cell. A strong anisotropy of the thermal conductivity with a very low value in the radial direction compared to the axial one was shown. However, the combined effect of the cylindrical battery cell cooled by a PCM/CENG composite with the addition of the melting process has not been fully investigated.

This study was motivated by the lack of investigation on the thermal behaviour of both battery cell and PCM/CENG during the transient temperature rise, which is important for the understanding of the passive cooling system performance. The analysis is aimed to provide information on design parameters, and to optimise cost and efficiency of the PCM/CENG cooling system. Besides, simple and cost-effective models oriented to practical applications are developed for the PCM/CENG and the battery. In this study, the anisotropic thermal conductivity of the battery cell is used, in order to generate a simplified model describing the thermal behaviour of a cylindrical battery cell. A one-dimensional computational model based on the thermal network method [55] is developed taking into account the phase change process in the cylindrical battery cell cooled by PCM/CENG. In this chapter, the geometry and problem descriptions are presented first, followed by the description of the analytical, computational and CFD models. Next, different cooling strategies are studied, along with the effects of the bulk density and PCM on the cooling effectiveness, during the transient temperature rise. Results and discussions are then presented. Finally some conclusions are drawn.

### **3.2. Geometry and problem description**

A cylindrical battery cell with an anisotropic thermal conductivity was considered. This behaviour highlighted by Drake et al. [13] has an impact on the design and modelling strategy. Table 7 presents the physical properties measured [13], which were used in this study.

**Table 7:** Physical properties of the cylindrical battery cell 26650 [13].

Physical properties	Cylindrical cell 26650
Heat capacity [ $\text{J.kg}^{-1}.\text{K}^{-1}$ ]	1605
Density [ $\text{kg.m}^{-3}$ ]	2285
Radial conductivity [ $\text{W.m}^{-1}.\text{K}^{-1}$ ]	0.2
Axial conductivity [ $\text{W.m}^{-1}.\text{K}^{-1}$ ]	32

### 3.2.1. Battery

The dimensions of the battery were chosen to test the models developed, which can be modified easily for a different battery size. The heat generation of the battery is modelled by a constant heat generation rate per volume  $q$ , assumed to be  $240 \text{ kW.m}^{-3}$  [55]. The geometry as shown in Fig. 62 was built using the open source software SALOME (an open-source software that provides a generic platform for pre- and post-processing for numerical simulation <http://www.salome-platform.org/>) on Linux (Ubuntu 13.10). This software is used for building the geometry, the mesh, and also for the post-processing in this study.

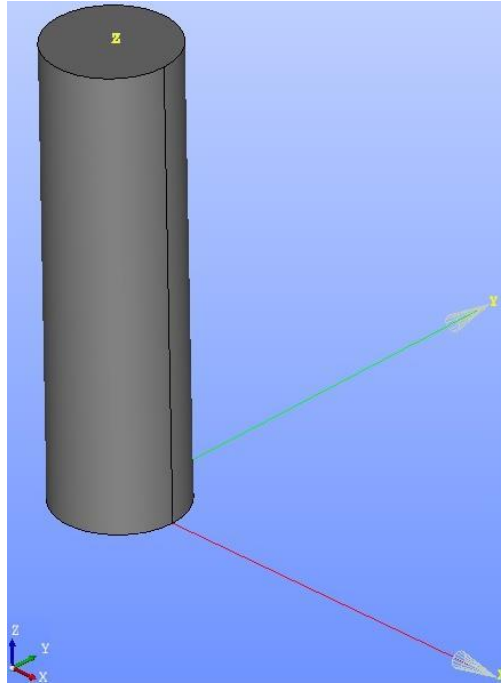


**Fig. 62.** Geometry of the cylindrical battery cell.

The cylindrical battery cell has a diameter of 14 mm and a height of 100 mm. The anisotropic conductivity of the cylindrical battery cell with the radial conductivity much lower than the axial one ( $k_r \ll k_z$ ) is used for simplifying the modelling of the battery cooling. These simplifications are discussed in detail subsequently.

### 3.2.2. PCM/CENG

Wu and Xing [59] showed that the PCM/CENG composite could be modelled by only one equation using equivalent physical properties. The PCM/CENG composite can be modelled by one solid, as shown in Fig. 63, where a thickness of 20 mm was chosen for the test case.

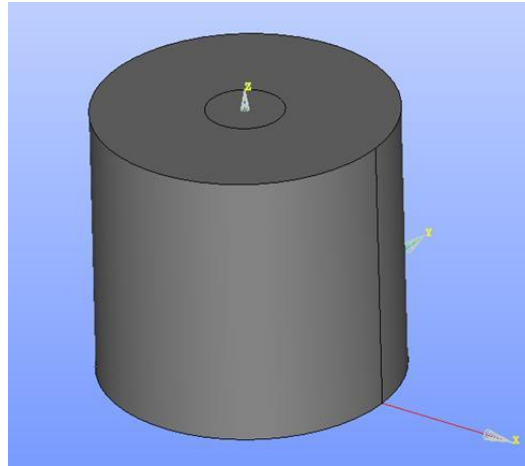


**Fig. 63.** Cylindrical battery cell surrounded by a PCM/CENG composite.

### 3.3. Analytical methodology

The forced convection and the PCM/CENG cooling are investigated in detail in this study. The cooling by forced convection is investigated in 1D and 3D. Additionally a 1D analytical model of the cooling by a PCM/CENG composite is developed.

#### 3.3.1. Analytical solution of a forced convection cooling

The cylindrical battery cell is cooled by convection on the surface located in the radial direction. Subsequent to an axisymmetric boundary condition, the temperature distribution is invariable by rotation and becomes  $T(r,\theta,z,t)=T(r,z,t)$ . The general equation of the problem is presented as follows:

$$\rho c_p \frac{\partial T}{\partial t} - k_z \frac{\partial^2 T}{\partial z^2} - k_r \frac{1}{r} \frac{\partial}{\partial r} \left( r \frac{\partial T}{\partial r} \right) = q \quad (3.1)$$

Moreover, the same convection coefficient (different from the one in the radial direction) is applied at both ends of the cylinder (Fig. 62). Due to this symmetry condition in the z-direction, only the half length of the battery cell is studied. According to this symmetry, the boundary conditions of this convection cooling problems are:

$$T(r, z, 0) = T_{amb} \quad (3.2a)$$

$$\left( \frac{\partial T}{\partial r} \right) (r = 0, z, t) = 0 \quad (3.2b)$$

$$\left( k_r \frac{\partial T}{\partial r} + h_r (T - T_{amb}) \right) (r = R, z, t) = 0 \quad (3.2c)$$

$$\left(\frac{\partial T}{\partial z}\right)(r, z = 0, t) = 0 \quad (3.2d)$$

$$\left(k_z \frac{\partial T}{\partial z} + h_z (T - T_{amb})\right)(r, z = L/2, t) = 0 \quad (3.2e)$$

Equation (3.1) is solved by the separation of variable method [55]. The application of this method requires homogeneous boundary conditions. These conditions are obtained by the variable change  $\theta(r, z, t) = T(r, z, t) - T_{amb}$ . The new system of equation obtained is:

$$\rho c_p \frac{\partial \theta}{\partial t} - k_z \frac{\partial^2 \theta}{\partial z^2} - k_r \frac{1}{r} \frac{\partial}{\partial r} \left( r \frac{\partial \theta}{\partial r} \right) = q \quad (3.3)$$

$$\theta(r, z, 0) = 0 \quad (3.4a)$$

$$\left(\frac{\partial \theta}{\partial r}\right)(r = 0, z, t) = 0 \quad (3.4b)$$

$$\left(k_r \frac{\partial \theta}{\partial r} + h_r \theta\right)(r = R, z, t) = 0 \quad (3.4c)$$

$$\left(\frac{\partial \theta}{\partial z}\right)(r, z = 0, t) = 0 \quad (3.4d)$$

$$\left(k_z \frac{\partial \theta}{\partial z} + h_z \theta\right)(r, z = L_z, t) = 0, \text{ with } L_z = L/2 \quad (3.4e)$$

Therefore, the temperature can be rewritten as  $\theta(r, z, t) = X(r)\Phi(z)\Psi(t)$ . However, Eq. (3.3) is still nonhomogeneous due to the volumetric heat source term. The method applied in this case is the resolution of the associated homogeneous equation (AHE), i.e. resolving the equation for  $q = 0$ . The associated homogeneous equation is presented as follows:

$$\rho c_p \frac{\partial \theta}{\partial t} - k_z \frac{\partial^2 \theta}{\partial z^2} - k_r \frac{1}{r} \frac{\partial}{\partial r} \left( r \frac{\partial \theta}{\partial r} \right) = 0 \quad (3.3a)$$

Two different eigenproblems in r- and z-directions are obtained by applying the decomposition  $\theta(r, z, t) = X(r)\Phi(z)\Psi(t)$  in Eq. (3.3a). The eigenproblem in the r-direction is described by

$$\frac{d^2 X}{dr^2} + \frac{1}{r} \frac{dX}{dr} + \mu^2 X = 0 \quad (3.5)$$

In Eq. (3.5),  $\mu$  represents the eigenvalue. In order to obtain a basic form of the Bessel equation, the variable change  $\xi = \mu r$  is applied to Eq. (3.5) and leads to:

$$\xi^2 \frac{d^2 X}{d\xi^2} + \xi \frac{dX}{d\xi} + \xi^2 X = 0 \quad (3.5a)$$

The general solution of equation (3.5a) when following the separation of variable method is:

$$X_n(r) = A_n J_0(\mu_n r) + B_n Y_0(\mu_n r) \quad (3.6)$$

where  $J_0$  and  $Y_0$  are the zero-order Bessel function of first and second kind respectively. The boundary condition (4b) leads to the eigenfunction  $\tilde{X}_n$  associated with the eigenvalue  $\mu_n$  :

$$X_n(r) = A_n J_0(\mu_n r) = A_n \tilde{X}_n(r) \quad (3.6a)$$

The application of boundary conditions (3.4c) leads to the transcendental equation:

$$x_r J_1(x_r) - Bi_r J_0(x_r) = 0, \text{ With, } x_r = \mu R \text{ and } Bi_r = h_r R/k_r \quad (3.7)$$

Equation (3.7) provides infinity of roots and then infinity of eigenvalues. The second eigenproblem in the z-direction is described by

$$\frac{d^2 \Phi}{dz^2} + \beta^2 \Phi = 0 \quad (3.8)$$

The boundary conditions (3.4d) and (3.4e) lead to the eigenfunction associated with the eigenvalue  $\beta_p$  and the transcendental equation respectively, given by

$$\Phi_p(z) = B_p \cos(\beta_p z) = B_p \tilde{\Phi}_p(z) \quad (3.9)$$

$$x_z \tan(x_z) = Bi_z, \text{ with } x_z = \beta z \text{ and } Bi_z = h_z Lz/k_z \quad (3.10)$$

The next step of the calculation is to verify that the families of eigenfunctions  $\tilde{X}_n(r)$  and  $\tilde{\Phi}_p(z)$  constitute an orthogonal space. This verification is made by the construction of a scalar product providing the orthogonality condition in each space. The scalar product of the family of eigenfunctions  $\tilde{\Phi}_p$  is defined as follows:

$$\langle \tilde{\Phi}_p | \tilde{\Phi}_q \rangle_z = \int_0^{Lz} \tilde{\Phi}_p \tilde{\Phi}_q dz = \begin{cases} 0 & \text{for } p \neq q \\ \Omega_p & \text{for } p = q \end{cases}, \text{ with } \Omega_p = \frac{\beta_p Lz + \cos(\beta_p Lz) \sin(\beta_p Lz)}{2\beta_p} \quad (3.11)$$

The orthogonality condition in Eq. (3.11) is obtained by calculating the integral and by using the transcendental equation (3.10). The same condition is verified for the family of eigenfunctions  $\tilde{X}_n$  and the scalar product is defined and evaluated (Appendix A) as follows:

$$\langle \tilde{X}_n | \tilde{X}_m \rangle_r = \int_0^R r \tilde{X}_n \tilde{X}_m dr = \begin{cases} 0 & \text{for } n \neq m \\ \Omega_n & \text{for } n = m \end{cases}, \text{ with } \Omega_n = \frac{(\mu_n^2 + (h_r/k_r)^2) R^2}{2\mu_n^2} (J_0(\mu_n R))^2 \quad (3.12)$$

The decomposition  $\theta(r, z, t) = \sum_n \sum_p X_n(r) \Phi_p(z) \Psi_{n,p}(t) = \sum_n \sum_p C_{np} \tilde{X}_n(r) \tilde{\Phi}_p(z) \Psi_{n,p}(t)$ ,

with  $C_{np} = A_n B_p$ , is finally replaced in Eq. (3.3) and the scalar products for  $\tilde{X}_n$  and  $\tilde{\Phi}_p$  are applied to it.

$$\frac{d\Psi_{n,p}}{dt} + \left( \frac{k_z \beta_p^2 + k_r \mu_n^2}{\rho c_p} \right) \Psi_{n,p} = \frac{1}{C_{np}} \frac{\left\langle \left\langle \frac{q}{\rho c_p} \right| \tilde{\Phi}_p \right\rangle_z \left| \tilde{X}_n \right\rangle_r}{\langle \tilde{\Phi}_p | \tilde{\Phi}_p \rangle_z \langle \tilde{X}_n | \tilde{X}_n \rangle_r} \quad (3.13)$$

Equation (3.13) is now a simple first order differential equation with a second term. This second term can be time dependant (heat source depending on the time) or taken as a constant, in this case. The denominator of the second term is evaluated (Appendix A) in this way:

$$\left\langle \left\langle \frac{q}{\rho c_p} \left| \tilde{\Phi}_p \right. \right\rangle \right\rangle_z \left| \tilde{X}_n \right\rangle_r = \frac{q}{\rho c_p} \int_0^{L_z} \tilde{\Phi}_p dz \int_0^R r \tilde{X}_n dr = \frac{q}{\rho c_p} E_{n,p}, \text{ with } E_{n,p} = \frac{\sin(\beta_p L_z)}{\beta_p} \frac{RJ_1(\mu_n R)}{\mu_n} \quad (3.14)$$

Then, the final equation describing  $\Psi_{n,p}(t)$  is:

$$\frac{d\Psi_{n,p}}{dt} + \left( \frac{k_z \beta_p^2 + k_r \mu_n^2}{\rho c_p} \right) \Psi_{n,p} = \frac{1}{C_{np}} \frac{q}{\rho c_p} \frac{E_{n,p}}{\Omega_n \Omega_p} \quad (3.13a)$$

The solution of Eq. (3.13a) under boundary condition (3.4a) gives:

$$\Psi_{n,p}(t) = \frac{1}{C_{np}} \frac{q}{k_z \beta_p^2 + k_r \mu_n^2} \frac{E_{n,p}}{\Omega_n \Omega_p} \left( 1 - \exp\left( -\frac{k_z \beta_p^2 + k_r \mu_n^2}{\rho c_p} t \right) \right) \quad (3.15)$$

The 3D analytical solution of a cylindrical battery cell with radial and axial forced convection and an internal heat generation rate per volume is:

$$T_{3D}(r, z, t) - T_{amb} = \sum_{n=0}^{\infty} \frac{q}{k_z \beta_p^2 + k_r \mu_n^2} \frac{E_{n,p}}{\Omega_n \Omega_p} \left( 1 - \exp\left( -\frac{k_z \beta_p^2 + k_r \mu_n^2}{\rho c_p} t \right) \right) \cos(\beta_p z) J_0(\mu_n r) \quad (3.16)$$

The study made by Drake et al. [13] showed a strong anisotropy of the thermal conductivity for a cylindrical battery cell with  $k_r \ll k_z$ . The gradient of the temperature in the r-direction is expected to be more important in the radial direction and very low in the axial one. Moreover, the available surface cooling is more important in the r-direction. Consequent to this observation and therefore applying the major cooling process in the radial direction, an analytical model independent of the z-direction is proposed. This simplification leads to the following equation:

$$\rho c_p \frac{\partial T}{\partial t} - k_r \frac{1}{r} \frac{\partial}{\partial r} \left( r \frac{\partial T}{\partial r} \right) = q \quad (3.17)$$

Equation (3.17) can be solved using the separation of variables. The method use to solve Eq. (3.17) is identical to the one used to solve Eq. (3.1), with only the application of the boundary conditions in the radial direction. In this case, only the radial eigenproblem is considered.

The solution of this 1D analytical solution is presented as follows:

$$T_{1D}(r, t) - T_{amb} = \sum_{n=0}^{\infty} \frac{q}{k_r \mu_n} \frac{2J_1(\mu_n R)}{\left( \mu_n^2 + (h_r/k_r)^2 \right) R (J_0(\mu_n R))^2} \left( 1 - \exp\left( -\frac{k_r \mu_n^2}{\rho c_p} t \right) \right) J_0(\mu_n r) \quad (3.18)$$

The 1D and 3D analytical solutions of a forced convection cooling are compared in different configurations. In addition, a 3D CFD simulation of the cylindrical battery cell is performed using the open source software SYRTHES (software dedicated to transient thermal

simulations in complex solid geometries by EDF (<http://researchers.edf.com/software/syrthes-44340.html>). The simulation is compared to both 1D and 3D analytical solutions. The test case and the details of comparison are presented and discussed subsequently.

### 3.3.2. Analytical solution of the cooling by PCM/CENG

The development of analytical solutions of conduction problems in multilayer bodies has been carried out extensively in various configurations. Singh et al. [60] developed an analytical solution to the transient heat conduction in polar coordinates with multiples layers in the radial direction. Besides, De Monte [61] developed an analytical approach to unsteady heat conduction processes in one-dimensional composite media. The method simplified the analysis and the development of solution in the case of convective cooling of the media at both external faces. Furthermore, Belghazi [62] studied the analytical modelling of two slabs with imperfect contact with an internal source term. In this study, the analytical model of two cylindrical shaped bodies in contact (battery and PCM/CENG), with an internal heat generation rate per volume for the battery and convection on the external radial surface, is investigated, as that shown in Fig. 63.

The possibility of modelling the PCM/CENG by only one entity implies the calculation of equivalent physical properties. The physical properties of the PCM/CENG composite were studied experimentally by Py et al. [44]. The CENG matrix presents favourable mechanical properties and chemical inertness. Besides, various shapes can be easily moulded from expanded graphite powders. The compression process during the manufacture of the graphite matrix leads to a higher conductivity in the direction perpendicular to the compression force and a lower one in the direction parallel to the compression force. Subsequent to this, and considering the geometry (Fig. 63), the conductivity in the radial direction is much higher than that in the axial direction (z-direction). After the manufacture of the CENG matrix, the PCM is incorporated by imbibition. The CENG matrix is soaked in a PCM at a liquid state and weighted until maximum load was reached. The PCM impregnates the CENG by capillary forces, retaining the liquid in the matrix. However, a higher bulk density and long-chain paraffin presenting high value of viscosity will necessitate a more sophisticated process to reach a higher impregnation rate. Furthermore, 3% to 10% of the volume was known to be closed during the manufacture process of the CENG, and could not be filled by the PCM during imbibition process. The theoretical porosity [44] can be calculated using

$$\varepsilon = 1 - (\rho_{CENG} / 2250), \text{ where } 2250 \text{ kg.m}^{-3} \text{ is the theoretical density of graphite} \quad (3.19)$$

Py et al. [44] obtained the experimental data from the imbibition of a CENG matrix at different bulk density for three different PCMs with melting temperatures of -9°C, 18°C and 80°C. To consider a conservative design, the model with 10% of closed volume is used for the porosity calculation. In addition, it was shown experimentally that the PCM (paraffin) does not affect the conductivity of the CENG despite the high level of impregnation. Besides, a similar behaviour was observed for PCM added to a metallic matrix [45]. Accordingly the

bulk density of the CENG matrix gives the conductivity and porosity of the PCM/CENG composite. Empirical correlations of the conductivity in terms of the bulk density were developed [44], given as

$$k_{r,g} = k_{r,eff} = 3(\rho_{CENG}/46)^{4/3+0.17} \quad (3.20)$$

$$k_{z,g} = k_{z,eff} = 3(\rho_{CENG}/46)^{2/3} \left[ 2 - (\rho_{CENG}/46)^{0.17} \right] \quad (3.21)$$

The cylindrical battery cell studied here has  $k_r \ll k_z$ , and the PCM/CENG composite has  $k_{r,eff} \gg k_{z,eff}$ . Besides, the cooling will be applied on the surface located in the radial direction of the PCM/CENG, i.e. where the surface is the most important (Fig. 63). The external surface located in the axial direction of the battery and PCM/CENG is assumed to be adiabatic. This hypothesis is made because of the small surface available and the low convective cooling (mainly by natural convection). Moreover, the natural convection is disrupted by the presence of the electric wire connecting all the batteries in the pack. Accordingly a one-dimensional analytical model of the battery cooled by PCM/CENG composite is considered. Tests will be performed when natural convection is applied on the external surface located in the axial direction (z-direction) and compared to the results of adiabatic condition.

The conservation equations of energy for the CENG and the PCM can be written as follows:

$$(1-\varepsilon)(\rho c_p)_g \frac{\partial T_g}{\partial t} - \frac{k_{r,g}}{r} \frac{\partial}{\partial r} \left( r \frac{\partial T_g}{\partial r} \right) = 0 \quad (3.22)$$

$$\varepsilon(\rho c_p)_{PCM} \frac{\partial T_{PCM}}{\partial t} - \frac{k_{r,PCM}}{r} \frac{\partial}{\partial r} \left( r \frac{\partial T_{PCM}}{\partial r} \right) = -\varepsilon \rho_{PCM} l_f \frac{\partial f_l}{\partial t} \quad (3.23a)$$

The term  $\varepsilon \rho_{PCM} l_f \frac{\partial f_l}{\partial t}$  in Eq. (3.23a) describes the melting process in the PCM, with  $f_l$  representing the liquid fraction. The liquid fraction  $f_l$  is a step function, equal to 1 when  $T_{PCM} > T_m$  and 0 otherwise. The equivalent capacity method is used in this case, by modifying the term describing the melting in Eq. (3.23a). Besides, the derivation of the step function  $f_l$  leads to a Dirac distribution.

$$\frac{\partial f_l}{\partial t} = \frac{\partial f_l}{\partial T_{PCM}} \frac{\partial T_{PCM}}{\partial t} = \delta(T_{PCM} - T_m) \frac{\partial T_{PCM}}{\partial t} \quad (3.23b)$$

Equation (3.23a) is now transformed into a new equation with the Dirac distribution replaced by a Gaussian distribution

$$\varepsilon \left[ (\rho c_p)_{PCM} + \frac{\rho_{PCM} l_f}{\sigma \sqrt{2\pi}} \exp\left( \frac{-(T_{PCM} - T_m)^2}{2\sigma^2} \right) \right] \frac{\partial T_{PCM}}{\partial t} - \frac{k_{r,PCM}}{r} \frac{\partial}{\partial r} \left( r \frac{\partial T_{PCM}}{\partial r} \right) = 0 \quad (3.23c)$$

Natural convection is observed during the melting of the PCM [43] and enhances the heat exchange between the PCM and the graphite. However, Py et al. [44] demonstrated that the natural convection during the melting of the PCM is negligible using a standard size of the pores for the calculation of the Rayleigh number, in the case of PCM/CENG. The absence of

natural convection for enhancing the transfer is replaced by the relevant surface contact between the PCM and the CENG. This large surface contact leads to a fast thermal equilibrium, with  $T_{PCM} = T_g = T_{comp}$ , as pointed out by Wu and Xing [59]. The analysis of the behaviour of the PCM/CENG [44, 59] gives one equation with effective physical properties (Eq. 3.24), where  $\Delta T$  represents the melting temperature range of the PCM.

$$\left[ (\rho c_p)_{eff} + \varepsilon \frac{\rho_{PCM} l_f}{\sigma \sqrt{2\pi}} \exp\left(\frac{-(T_{comp} - T_m)^2}{2\sigma^2}\right) \right] \frac{\partial T_{comp}}{\partial t} - \frac{k_{r,eff}}{r} \frac{\partial}{\partial r} \left( r \frac{\partial T_{comp}}{\partial r} \right) = 0 \quad (3.24a)$$

$$(\rho c_p)_{eff} = \varepsilon (\rho c_p)_{PCM} + (1 - \varepsilon) (\rho c_p)_g; \quad \sigma = \Delta T / 2 \quad (3.24b)$$

The cooling of the battery is finally described by Eq. (3.17) and Eq. (3.24a). In the interest of simplifying the resolution, the subscripts 1 and 2 are applied respectively to designate the battery and the PCM/CENG composite. The resolution of the system is complicated by the phase change term depending on the temperature (Eq. 3.24a). The model proposed only takes into account the specific heat of the PCM/CENG (Eq. 3.24b), i.e. the latent heat of fusion  $l_f$  is taken equal to zero. This model will be used to verify the one-dimensional hypothesis made previously by a comparison to a three-dimensional CFD model.

$$\frac{1}{\alpha_1} \frac{\partial T_1}{\partial t} - \frac{1}{r} \frac{\partial}{\partial r} \left( r \frac{\partial T_1}{\partial r} \right) = \frac{q_1(t)}{k_1}; \quad \alpha_1 = \frac{k_1}{(\rho c_p)_1} \quad (3.25a)$$

$$\frac{1}{\alpha_2} \frac{\partial T_2}{\partial t} - \frac{1}{r} \frac{\partial}{\partial r} \left( r \frac{\partial T_2}{\partial r} \right) = 0; \quad \alpha_2 = \frac{k_2}{(\rho c_p)_2}; \quad (\rho c_p)_2 = (\rho c_p)_{eff}; \quad k_2 = k_{r,eff} \quad (3.25b)$$

Figure 64 presents the problem and locations of the boundary conditions. The boundary conditions can be expressed by the following relations:

$$T_1(r, 0) = T_{amb} \quad (3.26a)$$

$$T_2(r, 0) = T_{amb} \quad (3.26b)$$

$$\left( \frac{\partial T_1}{\partial r} \right) (r = 0, t) = 0 \quad (3.26c)$$

$$\left( k_2 \frac{\partial T_2}{\partial r} + h_r (T_2 - T_{amb}) \right) (r = r_2, t) = 0 \quad (3.26d)$$

$$T_1(r = r_1, t) = T_2(r = r_1, t) \quad (3.26e)$$

$$k_1 \frac{\partial T_1}{\partial r} (r = r_1, t) = k_2 \frac{\partial T_2}{\partial r} (r = r_1, t) \quad (3.26f)$$

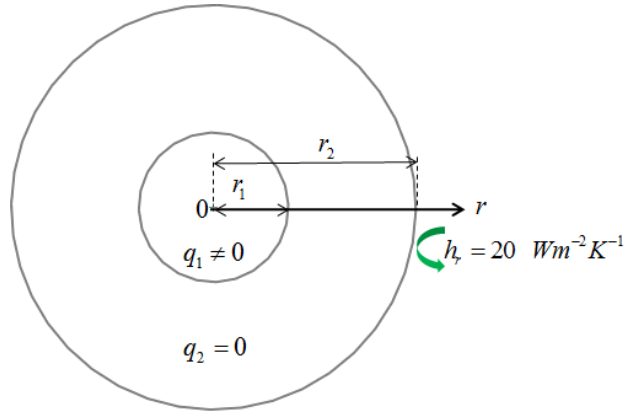


**Fig. 64.** Description of the battery cooling by PCM/CENG.

The separation of variable method is used to solve this problem. The method is similar to the one used in the forced convection cooling (1D and 3D). The homogeneity of the boundary conditions was used when applying the variable change:

$$\theta_1(r, t) = T_1(r, t) - T_{amb} = R_1(r)\Theta(t) \quad (3.27a)$$

$$\theta_2(r, t) = T_2(r, t) - T_{amb} = R_2(r)\Theta(t) \quad (3.27b)$$

$$\frac{1}{\alpha_1} \frac{\partial \theta_1}{\partial t} - \frac{1}{r} \frac{\partial}{\partial r} \left( r \frac{\partial \theta_1}{\partial r} \right) = \frac{q_1(t)}{k_1} \quad (3.28a)$$

$$\frac{1}{\alpha_2} \frac{\partial \theta_2}{\partial t} - \frac{1}{r} \frac{\partial}{\partial r} \left( r \frac{\partial \theta_2}{\partial r} \right) = 0 \quad (3.28b)$$

$$\theta_1(r, 0) = 0 \quad (3.29a)$$

$$\theta_2(r, 0) = 0 \quad (3.29b)$$

$$\left( \frac{\partial \theta_1}{\partial r} \right) (r = 0, t) = 0 \quad (3.29c)$$

$$\left( k_2 \frac{\partial \theta_2}{\partial r} + h_c \theta_2 \right) (r = r_2, t) = 0 \quad (3.29d)$$

$$\theta_1(r = r_1, t) = \theta_2(r = r_1, t) \quad (3.29e)$$

$$k_1 \frac{\partial \theta_1}{\partial r} (r = r_1, t) = k_2 \frac{\partial \theta_2}{\partial r} (r = r_1, t) \quad (3.29f)$$

The AHE is solved with the separation of variable  $\theta_{i,H}(r, t) = R_i(r)\varphi_i(t)$ , in order to obtain the eigenfunctions in the radial directions and the time-variable functions:

$$\frac{1}{\alpha_i} \frac{d\varphi_i}{dt} = -\lambda_i^2 \varphi_i; \quad \varphi_i = \exp(-\lambda_i^2 \alpha_i t); \quad i = 1, 2 \quad (3.30a)$$

$$R_i = A_i J_0(\lambda_i r) + B_i Y_0(\lambda_i r); \quad i = 1, 2 \quad (3.30b)$$

The coefficient  $\lambda_i$  is the eigenvalue of the solid, where  $i$  is associated with the eigenproblem in the radial direction for the solids 1 (battery) and 2 (PCM/CENG). The main difference with the convection resolution is the addition of a new condition at the contact of both solids. The continuity of temperature at the contact (3.29e) implies  $\lambda_2 = \lambda_1 \sqrt{\alpha_1/\alpha_2} = \lambda_1/\sqrt{\delta}$ , with

$\delta = \alpha_2/\alpha_1$ . The application of the boundary condition (3.29c), (3.29d) and (3.29e) leads to the following equations:

$$R_{2,n}(r) = A_{2,n} \left( J_0(\lambda_{2,n}r) - \Pi(\lambda_{2,n}r_2)Y_0(\lambda_{2,n}r) \right) = A_{2,n}\tilde{R}_{2,n}(r) = A_n\tilde{R}_{2,n}(r) \quad (3.31a)$$

$$\Pi(\lambda_{2,n}r_2) = \frac{Bi_2J_0(\lambda_{2,n}r_2) - \lambda_2r_2J_1(\lambda_{2,n}r_2)}{Bi_2Y_0(\lambda_{2,n}r_2) - \lambda_2r_2Y_1(\lambda_{2,n}r_2)}; \quad Bi_2 = h_r r_2/k_2$$

$$R_{1,n}(r) = A_{2,n}\phi_{1,n}J_0(\lambda_{1,n}r) = A_{2,n}\tilde{R}_{1,n}(r) = A_n\tilde{R}_{1,n}(r); \quad \phi_{1,n} = \frac{J_0(\lambda_{2,n}r_1) - \Pi(\lambda_{2,n}r_2)Y_0(\lambda_{2,n}r_1)}{J_0(\lambda_{1,n}r_1)} \quad (3.31b)$$

The functions  $\tilde{R}_{1,n}(r)$  and  $\tilde{R}_{2,n}(r)$  are the eigenfunctions associated with the eigenvalues  $\lambda_{1,n}$  and  $\lambda_{2,n}$  respectively. The transcendental equation of the problem is obtained by using the contact condition between both solids given in Eq. (3.29e) and Eq. (3.29f). The automatic search of the roots can be challenging. The method is to determine the brackets where the roots are located. The asymptotes generated by the convection cooling at the external surfaces can be used as the brackets. However, computations related to the large width of these brackets are time consuming. Methods are developed to reduce the computation time. De Monte [63] proposed a method using physical aspect of the problem to shorten the width of the brackets. This method was developed based on the heat conduction between two-layered slabs in steady state, with convection on both external faces. Nevertheless, it is not always possible to obtain directly the roots within two asymptotes.

In our case, only one side is adiabatic (invariance by rotation due to the convection at  $r = r_2$ ) and convection is applied at the external surface as shown in Fig. 64. In addition, the plot of the transcendental equation (Eq. 3.32b) shows at least three roots between each asymptote. Consequent to this observation, an algorithm written in Fortran 90 is proposed. An initial value  $x_0$  and an increment  $dx_0$  are chosen, followed by the calculation of  $f(x_0)$  and  $f(x_0 + dx_0)$ . If  $f(x_0)f(x_0 + dx_0) < 0$ , then  $x_0$  and  $x_0 + dx_0$  are the brackets for a root and they are not otherwise. This condition implemented in a loop gives all the brackets and the one where the asymptotes are located. All the brackets are saved in a text file and used by a simple bisection algorithm to find all the roots and also the asymptotic values. A test is added in order to remove the asymptotic values from the final file containing the roots. The test, with a different value of  $dx_0$  from the first one is recommended, in order to verify that all the roots are found.

$$\Pi(x) = \frac{Bi_2J_0(x\gamma/\sqrt{\delta}) - (x\gamma/\sqrt{\delta})J_1(x\gamma/\sqrt{\delta})}{Bi_2Y_0(x\gamma/\sqrt{\delta}) - (x\gamma/\sqrt{\delta})Y_1(x\gamma/\sqrt{\delta})}; \quad \gamma = \frac{r_2}{r_1} \quad (3.32a)$$

$$f(x) = J_1(x)J_0(x/\sqrt{\delta}) - (\kappa/\sqrt{\delta})J_0(x)J_1(x/\sqrt{\delta}) - \Pi(x) \left( J_1(x)Y_0(x/\sqrt{\delta}) - (\kappa/\sqrt{\delta})J_0(x)Y_1(x/\sqrt{\delta}) \right) \quad (3.32b)$$

$$\kappa = \frac{k_2}{k_1}, x = \lambda_{1,n}r_1$$

The scalar product used in this case is presented as follows [60, 61], and the demonstration is described in Appendix B:

$$\sum_{i=1}^2 \frac{k_i}{\alpha_i} \int_{r_{i-1}}^{r_i} r \tilde{R}_{i,n} \tilde{R}_{i,m} dr = \begin{cases} 0; & \text{for } m \neq n \\ H_n; & \text{for } m = n \end{cases}, \text{ with } r_0 = 0 \quad (3.33a)$$

$$H_n = \frac{k_1}{\alpha_1} \phi_{1,n}^2 \frac{r_1^2}{2} \left( J_0(\lambda_{1,n} r_1)^2 + J_1(\lambda_{1,n} r_1)^2 \right) + \frac{k_2}{\alpha_2} \left[ \frac{r^2}{2} \left[ \left( J_0(\lambda_{2,n} r) - \Pi(\lambda_{2,n} r_2) Y_0(\lambda_{2,n} r) \right)^2 + \left( J_1(\lambda_{2,n} r) - \Pi(\lambda_{2,n} r_2) Y_1(\lambda_{2,n} r) \right)^2 \right] \right]_{r_1}^{r_2} \quad (3.33b)$$

The solutions of the AHE, i.e. for  $q_1(t) = 0$  are:

$$\theta_{1,H}(r, t) = \sum_{n=0}^{\infty} A_n \tilde{R}_{1,n}(r) \exp(-\lambda_{1,n}^2 \alpha_1 t) \quad (3.34a)$$

$$\theta_{2,H}(r, t) = \sum_{n=0}^{\infty} A_n \tilde{R}_{2,n}(r) \exp(-\lambda_{2,n}^2 \alpha_2 t) \quad (3.34b)$$

After the determination of the eigenfunctions and the relation between the eigenvalues, the functions searched are written as follows:

$$\theta_1(r, t) = \sum_{n=0}^{\infty} \tilde{R}_{1,n}(r) \Theta_n(t) \quad (3.35a)$$

$$\theta_2(r, t) = \sum_{n=0}^{\infty} \tilde{R}_{2,n}(r) \Theta_n(t) \quad (3.35b)$$

Eq. (3.35a) and (3.35b) are replaced respectively in Eq. (3.28a) and (3.28b). The orthogonality condition (Eq. 3.33a) and the condition between the eigenvalues ( $\lambda_2 = \lambda_1 \sqrt{\alpha_1/\alpha_2}$ ) are then applied, leading to the following equation:

$$\left( \langle \tilde{R}_{2,n} | \tilde{R}_{2,n} \rangle_2 + \langle \tilde{R}_{1,n} | \tilde{R}_{1,n} \rangle_1 \right) \left( \frac{d\Theta_n}{dt} + \lambda_{1,n}^2 \alpha_1 \Theta_n \right) = \frac{\alpha_1}{k_1} \langle q_1(t) | \tilde{R}_{1,n} \rangle_1$$

$$\sum_{i=1}^2 \frac{k_i}{\alpha_i} \int_{r_{i-1}}^{r_i} r \tilde{R}_{i,n} \tilde{R}_{i,n} = \langle \tilde{R}_{2,n} | \tilde{R}_{2,n} \rangle_2 + \langle \tilde{R}_{1,n} | \tilde{R}_{1,n} \rangle_1 = H_n \quad (3.36a)$$

$$\frac{\alpha_1}{k_1} \langle q_1(t) | \tilde{R}_{1,n} \rangle_1 = q_1(t) \int_0^{r_1} r \tilde{R}_{1,n} dr = F_n q_1(t); \quad F_n = \frac{J_0(\lambda_{2,n} r_1) - \Pi(\lambda_{2,n} r_2) Y_0(\lambda_{2,n} r_1)}{J_0(\lambda_{1,n} r_1)} \frac{r_1 J_1(\lambda_{1,n} r_1)}{\lambda_{1,n}}$$

$$\frac{d\Theta_n}{dt} + \lambda_{1,n}^2 \alpha_1 \Theta_n = \frac{F_n}{H_n} q_1(t) \quad (3.36b)$$

The calculation of  $F_n$  is detailed in Appendix B. The solution of Eq. (3.36b) is obtained by using the variation of the constant method and the initial condition (Eq. (3.29a) or (3.29b)). The general time-variable solution and its simplified format when the heat generation rate is constant can be given as

$$\Theta_n(t) = \int_0^t q_1(t) \frac{F_n}{H_n} \exp(-\lambda_{1,n}^2 \alpha_1 (t-\tau)) d\tau \quad (3.37)$$

$$\Theta_n(t) = \frac{q_1}{\lambda_{1,n}^2 \alpha_1} \frac{F_n}{H_n} (1 - \exp(-\lambda_{1,n}^2 \alpha_1 t)) \quad (3.38)$$

Finally the solution for the cylindrical battery cell cooled by the PCM/CENG with convection on the external surface and a constant heat generation rate per volume is presented as follows:

$$T_1(r, t) - T_{amb} = \sum_{n=0}^{\infty} \frac{q_1}{\lambda_{1,n}^2 \alpha_1} \frac{F_n}{H_n} \frac{J_0(\lambda_{2,n} r_1) - \Pi(\lambda_{2,n} r_2) Y_0(\lambda_{2,n} r_1)}{J_0(\lambda_{1,n} r_1)} J_0(\lambda_{1,n} r) (1 - \exp(-\lambda_{1,n}^2 \alpha_1 t)) \quad (3.39a)$$

$$T_2(r, t) - T_{amb} = \sum_{n=0}^{\infty} \frac{q_1}{\lambda_{1,n}^2 \alpha_1} \frac{F_n}{H_n} (J_0(\lambda_{2,n} r) - \Pi(\lambda_{2,n} r_2) Y_0(\lambda_{2,n} r)) (1 - \exp(-\lambda_{1,n}^2 \alpha_1 t)) \quad (3.39b)$$

The 1D analytical solution of a cylindrical battery cell by a PCM/CENG was developed. This model only took into account the specific heat of the PCM/CENG. A 1D-computational model based on the hypotheses made, Eq. (3.17) and (3.24a), is developed using the thermal network method [55]. The latent heat is added to this model and compared to the analytical models (convective cooling and PCM/CENG cooling) developed previously.

### 3.3.3. 1D computational model

The thermal network method was used by Greco et al. [55] to build a 1D computational model of a prismatic battery cell cooled by heat pipes. The same method is applied to describe the cooling of a cylindrical battery cell by a PCM/CENG composite. The domain is divided into small volumes with a node allocated to each volume. The nodes are then connected together by thermal conductance, as shown in Fig. 65.

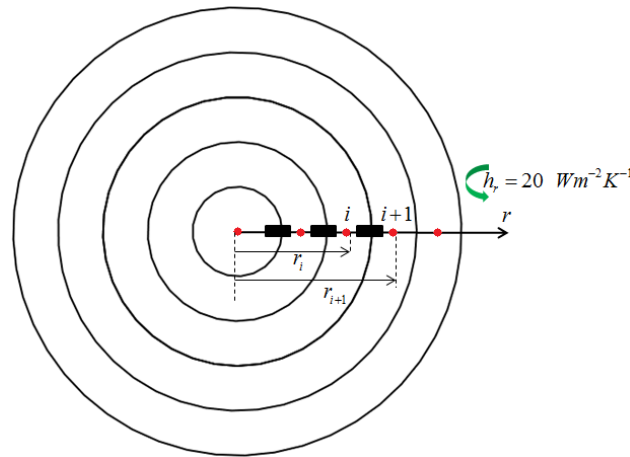


**Fig. 65.** Thermal network of the battery cooled by PCM/CENG.

The thermal conductance between the nodes  $i$  and  $i+1$ , and the conductance of convection (or resistance of convection) can be calculated using the following equations:

$$G_{i,i+1} = \frac{1}{R_{i,i+1}} = \frac{2\pi L k_r}{\log(r_{i+1}/r_i)} \quad (3.40a)$$

$$G_{conv} = \frac{1}{R_{conv}} = h_r S_{conv}, \quad S_{conv} = 2\pi r_2 L \quad (3.40b)$$

The complete domain is divided into two sub-domains: one for the battery and another for the PCM/CENG, in order to have flexibility in the choice of the number of nodes for each domain. The PCM/CENG sub-domain is expected to necessitate fewer nodes compared to the battery sub-domain because of its higher conductivity. Due to the impossibility of placing the first node at the centre of the battery sub-domain ( $r = 0$ ), this node is placed in a small volume close to the centre instead. For this purpose, the battery sub-domain of width  $r_1$  (Fig. 64) is divided in two smaller domains of width  $b = r_1/u$  and width  $r'_1 = ((u-1)/u)r_1$ . The first node is located in the smaller domain of width  $b$ , with  $u$  chosen to be a big enough quantity. Tests are performed for different values of  $u$ , from  $10^4$  to  $10^{10}$  with no major difference observed and accordingly  $10^5$  is finally used. The second smaller domain of the battery with the width  $r'_1$  is divided into  $N_1$  nodes, while the domain of the PCM/CENG with a width  $r'_2 = r_2 - r_1$  is divided into  $N_2$  nodes. This spatial division is illustrated in Fig. 66.

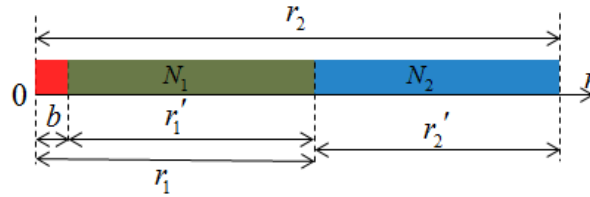


**Fig. 66.** Partition of the entire domain.

The transient behaviour is modelled by calculating the thermal capacity of each volume where a node is allocated. The phase change in the PCM/CENG domain is modelled by the equivalent capacity method presented before (Eq. (3.24a)).

$$C_{eq,comp} = (\rho c_p)_{eff} + \varepsilon \frac{\rho_{PCM} l_f}{\sigma \sqrt{2\pi}} \exp\left(\frac{-(T_{comp} - T_m)^2}{2\sigma^2}\right) \quad (3.41a)$$

$$(\rho c_p)_{eff} = \varepsilon (\rho c_p)_{PCM} + (1 - \varepsilon) (\rho c_p)_g; \quad \sigma = \Delta T / 2 \quad (3.41b)$$

The complete problem can be represented by a matrix equation given as follows. This matrix system is solved by the Euler implicit method, with  $n$  representing the time step.

$$[C(T)] \frac{d[T]}{dt} = [G][T] + [P] \quad (3.42)$$

$$[G'(T^{n-1})][T]^n = [Q]^{n-1} \quad (3.43a)$$

$$[G'(T^{n-1})] = [C(T^{n-1})] - \Delta t [G] \quad (3.43b)$$

$$[Q]^{n-1} = [C(T^{n-1})][T]^{n-1} + \Delta t [P] \quad (3.43c)$$

The Euler implicit decomposition applied on Eq. (3.42) provides stability. However, the heat capacity is calculated at the previous time step (Eq. (3.43b)). This simplification is tested for different time steps in order to verify its impact on the results. The tri-diagonal system formed by Eq. (3.43a) is solved with the Thomas algorithm at each time step.

The 1D computational model is written in Fortran 90 where the choice of the bulk density, PCM and geometry size can be easily modified. The choice of the bulk density modifies automatically the porosity and thermal conductivity of the PCM/CENG, as those indicated in Eq. (3.19) and Eq. (3.20). The temperatures at the nodes are automatically plotted with Python in order to analyse the results and update the design.

The next section is dedicated to the analysis and comparison of the different models developed.

### 3.4. Results and discussions

A test case is built to compare the behaviour of the models and to verify the hypotheses. The battery used for the forced cooling convection and PCM/CENG cooling is described in subsection 3.2.1. Identical convective coefficient is used in both cases.

#### 3.4.1. Test case

The cooling of the battery by forced convection with a convective coefficient of  $h_r=20 \text{ W.m}^{-2}.\text{K}^{-1}$  is studied first. Followed by the cooling of the same battery with a PCM/CENG composite where  $h_r=20 \text{ W.m}^{-2}.\text{K}^{-1}$  is applied on the external surface of the composite (Fig. 64). The 1D hypothesis is tested in both cooling cases and conclusions are drawn. All the results presented are obtained with an ambient temperature of 20°C.

The PCM chosen for the PCM/CENG composite is the n-heptadecane paraffin [64] and its properties are presented in the following Table.

**Table 8:** Physical Properties of the PCM.

Physical properties	n-Heptadecane [26]	n-Octadecane [15]
Number of C atoms	17	18
Melting point [°C]	21.9	28
Latent heat of fusion [kJ.kg <sup>-1</sup> ]	214	241
Density [kg.m <sup>-3</sup> ]	775	777
Specific heat [J.kg <sup>-1</sup> .K <sup>-1</sup> ]	2226.25	2660

The density of the CENG is fixed at  $\rho_{CENG}=200 \text{ kg.m}^{-3}$  with a thickness  $r_2=0.02 \text{ m}$ . In consequence, the properties of the graphite matrix (Eqs. [3.19-3.21]) are given in Table 9.

**Table 9:** Physical Properties of the CENG.

Physical properties	CENG
Porosity(10% closed volume)	0.82
Radial conductivity [W.m <sup>-1</sup> .K <sup>-1</sup> ]	27.3
Axial conductivity [W.m <sup>-1</sup> .K <sup>-1</sup> ]	5.7
Density [kg.m <sup>-3</sup> ]	200
Specific heat [J.kg <sup>-1</sup> .K <sup>-1</sup> ]	700

### 3.4.2. Comparison of 3D CFD and analytical model for forced convection cooling

The convection cooling of the battery described previously is studied. The 3D CFD simulation of the battery is performed on the open-source software SALOME.7.4/SYRTHES.4. The geometry and mesh are created on SALOME7.4 and the thermal problem is solved on SYRTHES.4. The post-processing is also made on SALOME.7.4 via PARAVIEW integrated directly into it. Only half of the battery is simulated due to symmetry of the problem, as that indicated in Eq. (3.2d) and Eq. (3.2e).

The properties of the battery are presented in Table 7 and natural convection at the top ( $z=L/2$ ) is modelled by the convective coefficient  $h_z=5 \text{ W.m}^{-2}.\text{K}^{-1}$ . The result of the CFD simulation is presented in Fig. 67.

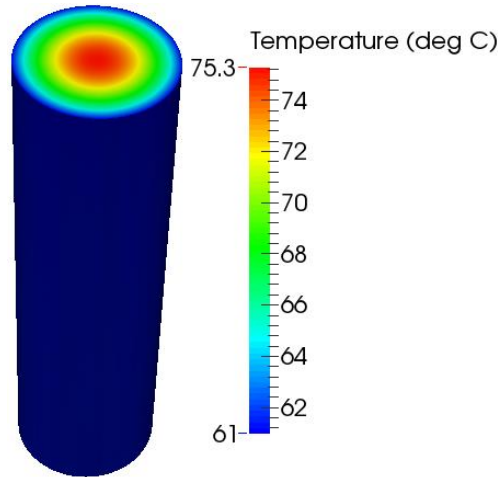


**Fig. 67.** CFD results (°C) of the forced convection of the battery.

To facilitate comparisons with the analytical model, the following indicative temperatures are considered:

$$\begin{aligned}
 T(0,0,t) &= T_{\max 1}; & T(0,L/2,t) &= T_{\max 2} \\
 T(r,0,t) &= T_{\min 1}; & T(r,L/2,t) &= T_{\min 2}
 \end{aligned}
 \tag{3.44}$$

where  $r$  represents the position of surface subject to convection, i.e.  $r = R$ , in the forced convection cooling case and  $r = r_2$  in the PCM/CENG cooling configuration.

The maximum temperature at these points (Eq. (3.44)) is compared to the 3D analytical (Eq. 3.16) and 1D analytical solution (Eq. 3.18) for forced convection cooling, shown in Fig. 68.

There is a very good match in the prediction of the temperature rise between the 3D CFD simulation and 3D analytical solution with natural convection at the top. The temperatures at different heights are very close despite the natural convection on the external surface in the z-direction. This result showed the very small gradient in the axial direction. Therefore the temperature field of the battery can be well described by the radial gradient only. This behaviour is due to the anisotropic thermal conductivity ( $k_r \ll k_z$ ) of the cylindrical cell, as that presented by Drake et al. [13].

This particularity of the cylindrical battery cell was used to develop a 1D analytical model. This model predicts a maximum temperature 2% higher than the temperature predicted by the 3D CFD simulation and 3D analytical solution. The discrepancy is due to the natural convection on the battery top surface. A small amount of heat is removed from the battery cell to the ambient. In reality, this discrepancy is expected to be smaller as a result of limited surface available for convection, compared to the present simulation. In real applications, the top of the battery cell is occupied by electric wire and components, reducing the development of the natural convection.

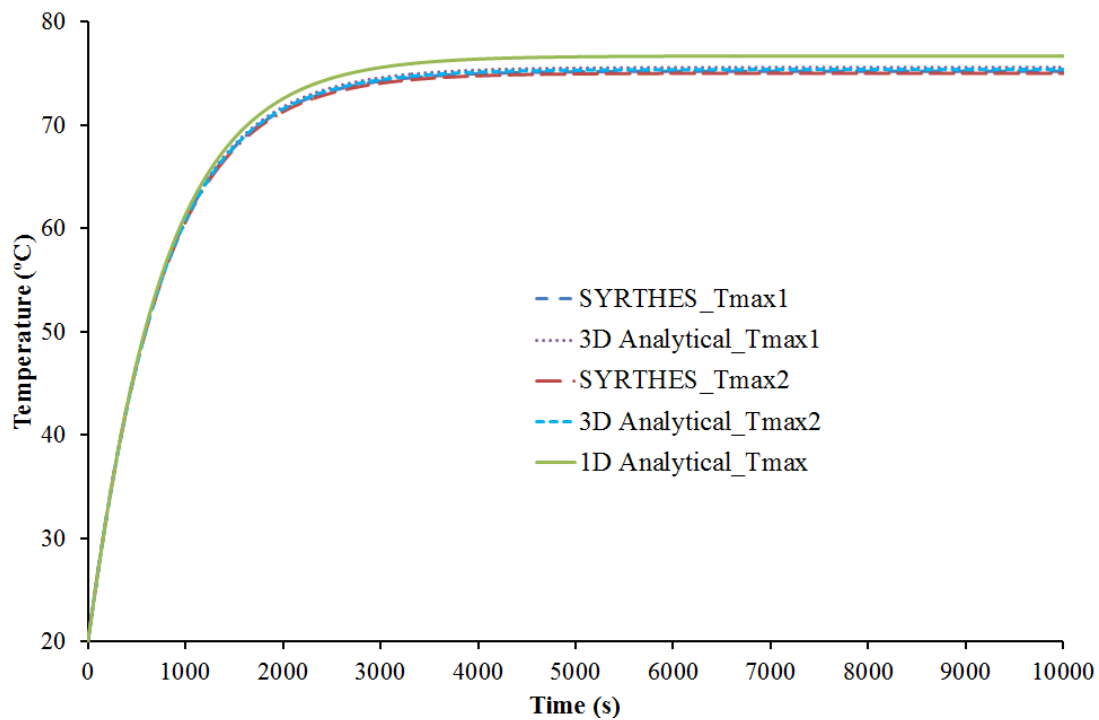


**Fig. 68.** Maximum temperature of 3D CFD simulation and Analytical solutions (1D and 3D) at different heights.

The 1D analytical model is therefore able to predict the temperature rise of a cylindrical battery cell with  $k_r \ll k_z$ , subject to forced convection in the radial direction. The discrepancy expected will be less than 2% compared to a 3D CFD simulation.

The PCM/CENG cooling is addressed in the following sub-section with comparisons between the 3D CFD simulation, analytical solution and the 1D computational model.

### 3.4.3. Comparison of 3D CFD model, analytical solution and 1D computational model for PCM/CENG cooling without latent heat

The application of the same convective coefficient on both external faces in the axial direction ( $z=-L/2$  and  $z=L/2$ ) made it possible to consider only half of the battery cell and PCM/CENG. The application of the symmetry conditions leads to consider the domain  $[0, r_2] \times [0, L/2]$ , with adiabatic boundary conditions at  $r=0$  and  $z=0$ . Finally the 3D domain presented in Fig. 63 is simplified to a 2D axisymmetric domain, shown in Fig. 69, which is much less time-consuming for a CFD simulation.

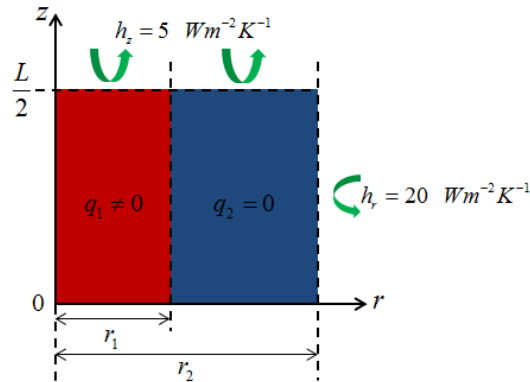


**Fig. 69.** 2D-axisymmetric CFD model after application of the symmetry conditions.

The physical properties of the battery cell are the same as those used in the forced convection case. The global properties of the PCM/CENG composite based on the parameter chosen for the test case are presented in Table 10. Besides, the latent heat is not taken into account for this study.

**Table 10:** Effective Physical properties of the PCM/CENG composite based on the test case data.

Physical properties	PCM/CENG
$\varepsilon$ (10% closed volume)	0.82
$k_{r,eff}$ [ $\text{W}\cdot\text{m}^{-1}\cdot\text{K}^{-1}$ ]	27.3
$k_{z,eff}$ [ $\text{W}\cdot\text{m}^{-1}\cdot\text{K}^{-1}$ ]	5.7
$\rho_{CENG}$ [ $\text{kg}\cdot\text{m}^{-3}$ ]	200
$(\rho c_p)_{eff}$ [ $\text{J}\cdot\text{m}^{-3}\cdot\text{K}^{-1}$ ]	1.44E6

A study of the mesh independence is performed and presented in Fig. 70. The multiplication of the number of nodes by four did not generate a major discrepancy between the results from the two meshes. For consistency, results from the finer mesh (75009 nodes) are presented for the simulations performed.

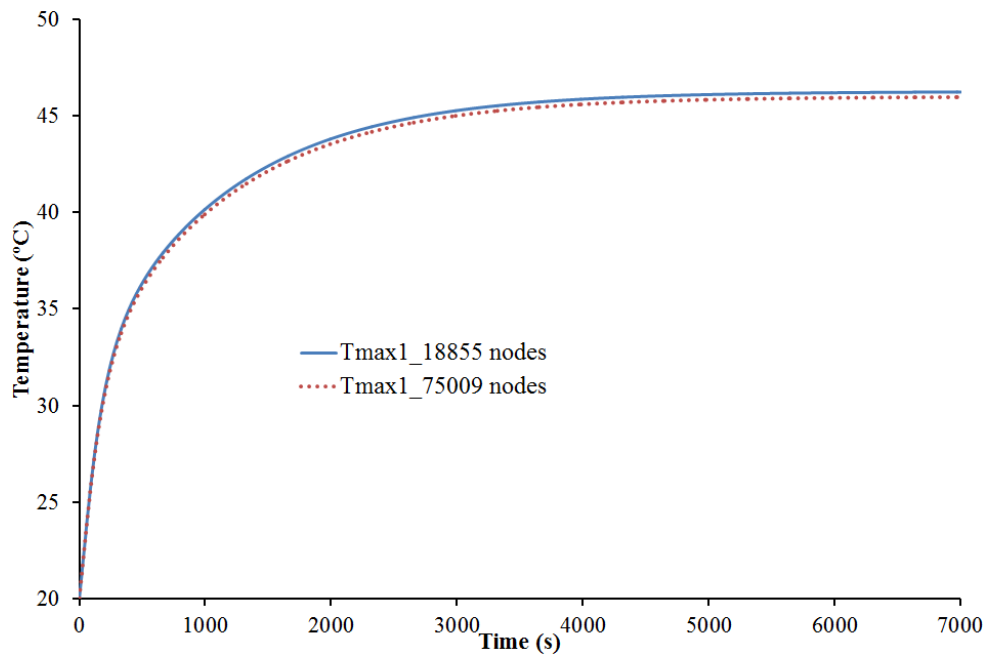


**Fig. 70.** Comparison of the mesh for the CFD Simulation.

The influence of the natural cooling on the top of the battery is studied by considering cases with and without it (adiabatic). The addition of natural convection at the top of the battery cell leads to similar maximum and minimum temperatures at different heights, as shown in Fig. 71. Therefore, like the forced convection cooling, the properties of the battery cell and the PCM/CENG composite lead to a very small gradient in the axial direction. The comparison with the adiabatic hypothesis at the top also shows a maximum of 2% discrepancy. The discrepancy is comparable to that in the forced cooling convection case, which is expected to be less in real applications, for the same reason enumerated before.

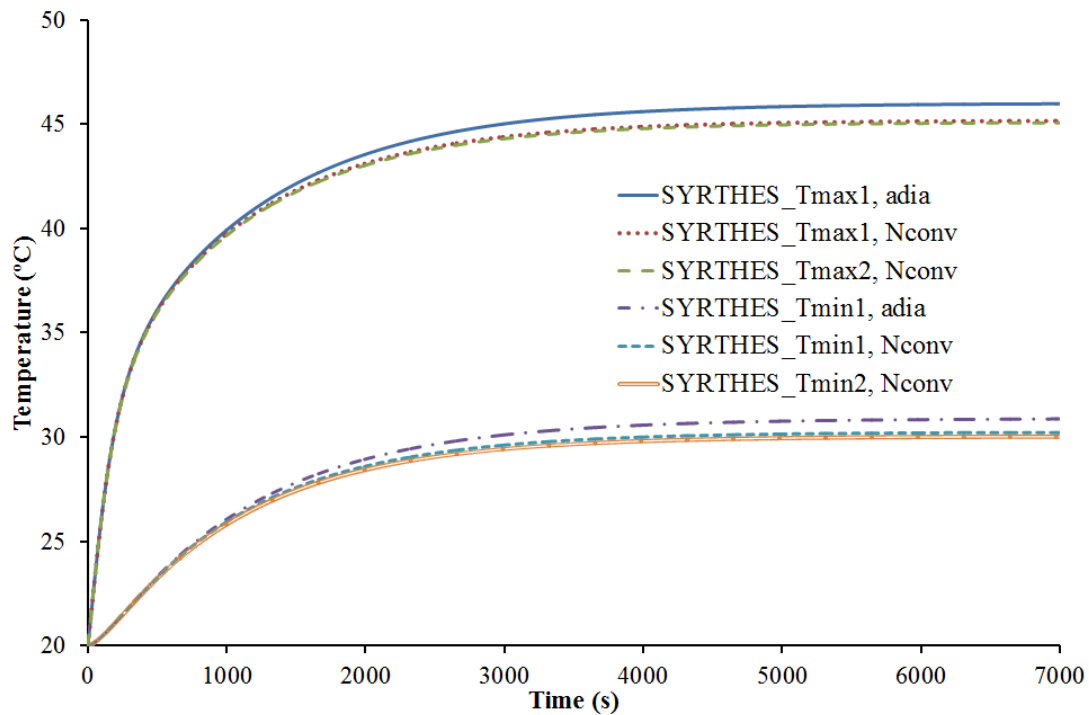


**Fig. 71.** Comparison between natural convection and adiabatic condition at the top for the 3D CFD model.

A comparison between the 1D analytical model of the cooling by PCM/CENG, the 3D CFD model and the 1D computational when the latent heat is not taken into account, is performed. The adiabatic hypothesis is kept due to the small discrepancy compared with the natural convection condition at the top. Furthermore, the 1D analytical solution is computed with 74 roots, presented in Appendix C. A close match is observed for all the models in this configuration, as shown in Fig. 72.

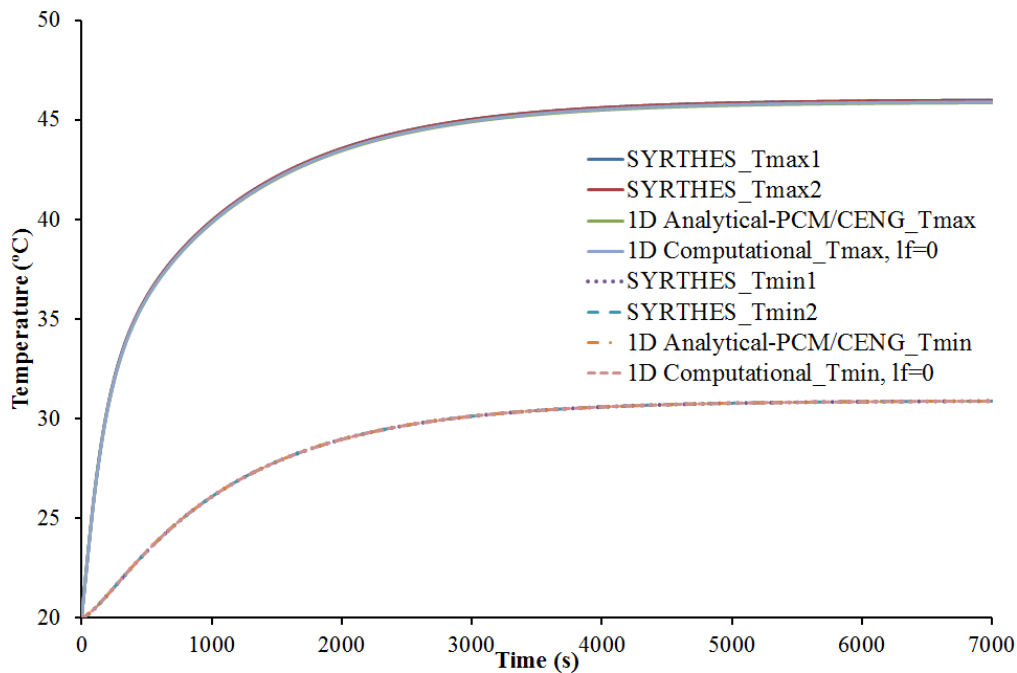


**Fig. 72.** Comparison between the 3D CFD model, 1D analytical-PCM/CENG solution and 1D computational model, when  $l_f=0$  and  $h_z=0$ .

The 1D computational model used twelve nodes for the battery and eleven for the PCM/CENG. This amount of nodes is very low compared to the 75009 nodes needed for the CFD simulation. The comparison between 1D analytical-PCM/CENG, 3D CFD and 1D computational model has shown that a one-dimensional model is sufficient to describe the temperature behaviour. Considering the much reduced costs in comparison with the 3D CFD simulation, the 1D analytical-PCM/CENG solution and 1D computational model are superior in practical applications.

The analysis of the conductivity helped to develop the one-dimensional models. However, the intensity of the cooling also plays a role. It was shown that the most effective direction of cooling was in the radial direction due to the low conductivity and large surface available for cooling. The simplest way to analyse the cooling effect is the calculation of an equivalent Biot number in the radial and axial directions of the battery cooled by the PCM/CENG.

An approximate thermal conductivity can be calculated considering a series path configuration for the heat flux in the radial direction and a parallel path configuration in the axial direction. The centre is approximately located at  $0.1r_1$  when using Eq. (3.40a) in the series configuration, in order to avoid the divergence at zero. The parallel path with the thermal resistance  $R_i = L/k_i S_i$  is considered for both the battery and the PCM/CENG

composite. The equivalent thermal conductivities for the battery and PCM/CENG represented respectively by subscript 1 and 2 are:

$$k_{eq,r} \approx \frac{\ln((r_2)/0.1r_1)k_{1,r}k_{2,r}}{k_{2,r}\ln(r_1/0.1r_1)+k_{1,r}\ln((r_2)/r_1)} = 0.32W.m^{-1}.K^{-1}; \quad k_{eq,z} \approx \frac{k_{1,z}r_1^2 + k_{2,z}((r_2)^2 - r_1^2)}{(r_2)^2} = 7.5W.m^{-1}.K^{-1}$$

Considering the convective coefficient used before, i.e.  $h_z=5 W.m^{-2}.K^{-1}$  at the top in the axial direction and  $h_r=20 W.m^{-2}.K^{-1}$  in the radial direction, the Biot number obtained are:

$$Bi_{eq,r} \approx h_r(r_2)/k_{eq,r} = 1.69 ; \text{ with an approximate characteristic length of } r_2$$

$$Bi_{eq,z} = h_z(L/2)/k_{eq,r} = 0.03$$

The Biot number is the ratio of the thermal resistance of conduction over the resistance of convection. In consequence, the value of these equivalent Biot numbers indicates a lower thermal gradient in the axial direction compared to the radial one. This calculation confirmed what was observed for the comparison between the one-dimensional models (analytical and 1D-computational) and the 3D-CFD simulation.

After the validation of the one-dimensional hypothesis, the 1D computational model is tested with the addition of the latent heat, and compared to the 1D analytical PCM/CENG model.

#### 3.4.4. Comparison 1D-analytical-PCM/CENG solution and 1D-computational model with addition of the latent heat

The latent heat of phase change is added to the 1D-computational with  $l_f \neq 0$ . The calculation of the heat capacity at the previous time-step could lead to errors when applying the Euler discretization on Eq. (3.43) with a large time-step. Therefore, the cooling of the battery by the PCM/CENG presented at the test case is evaluated at two different time-steps. The equivalent capacity method recommends a narrow phase change interval centred on the melting temperature  $T_m$ . A phase change interval of  $\Delta T = 1^\circ C$  is therefore considered in all the simulations [65]. This value may differ for different PCMs and can be modified or updated. The maximum temperature (at the centre of the battery) is calculated by the 1D computational model with the time-steps 0.1s and 0.01s and presented in Fig. 73.

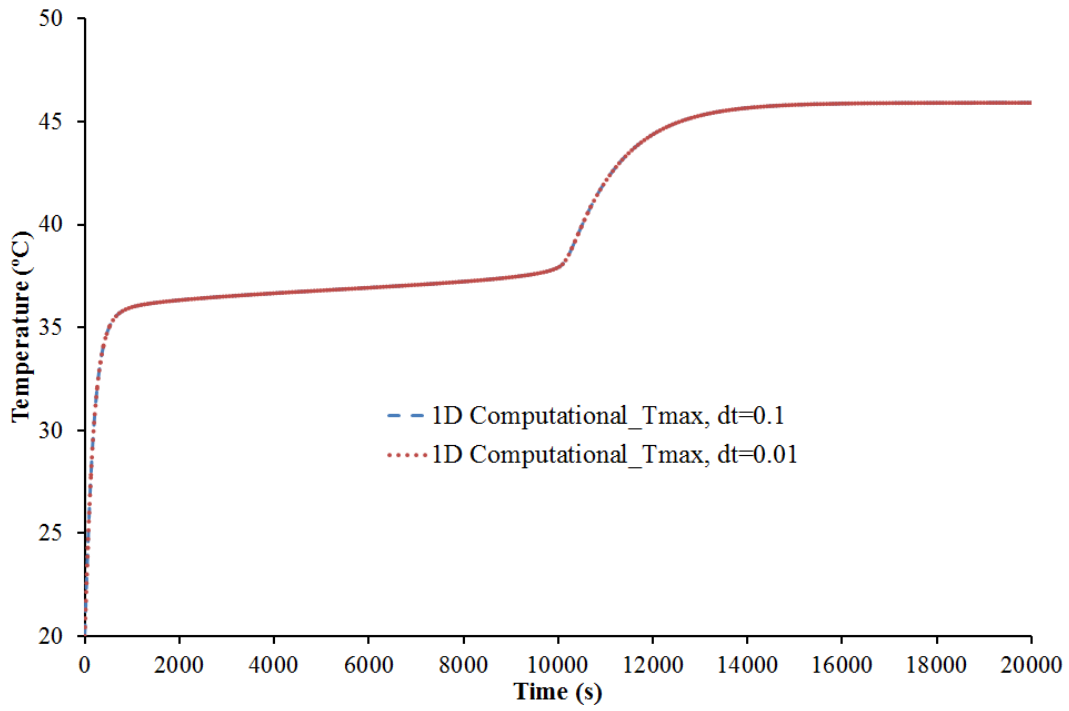


**Fig. 73.** Maximum temperature of the battery for different time-steps.

A time-step ten times smaller than the initial one predicts an identical temperature variation. In consequence, the time step of 0.1s is sufficient to overcome the simplification made on the heat capacity calculation and to describe the temperature rise.

The effect of the latent heat on the maximum temperature rise is shown in Figs. 74 and 75 with the comparison of the 1D computational model to the 1D analytical-PCM/CENG solution. The latent heat of the PCM used, maintains the temperature under 40°C for 2.9 hours. Besides, 18000s are needed to reach the steady state, while 8000s are required in the case of the 1D analytical-PCM/CENG model with only the specific heat taken into account. Furthermore, Fig. 75 depicts the comparison between both models at the surface contact of the battery and the PCM/CENG, and the minimum temperature. This contact temperature denoted by  $T_{int}$  is located at  $r = r_1$  and the minimum temperature  $T_{min}$  is located at the external surface of the PCM/CENG, i.e. at  $r = r_2$ . Both models present a close match at the steady state, as shown in Figs. 74 and 75, and also a very small gradient in the radial direction of the PCM/CENG (Fig. 75). This small gradient is due to the high conductivity in the radial direction, resulted from the choice of the bulk density  $\rho_{CENG}$ .

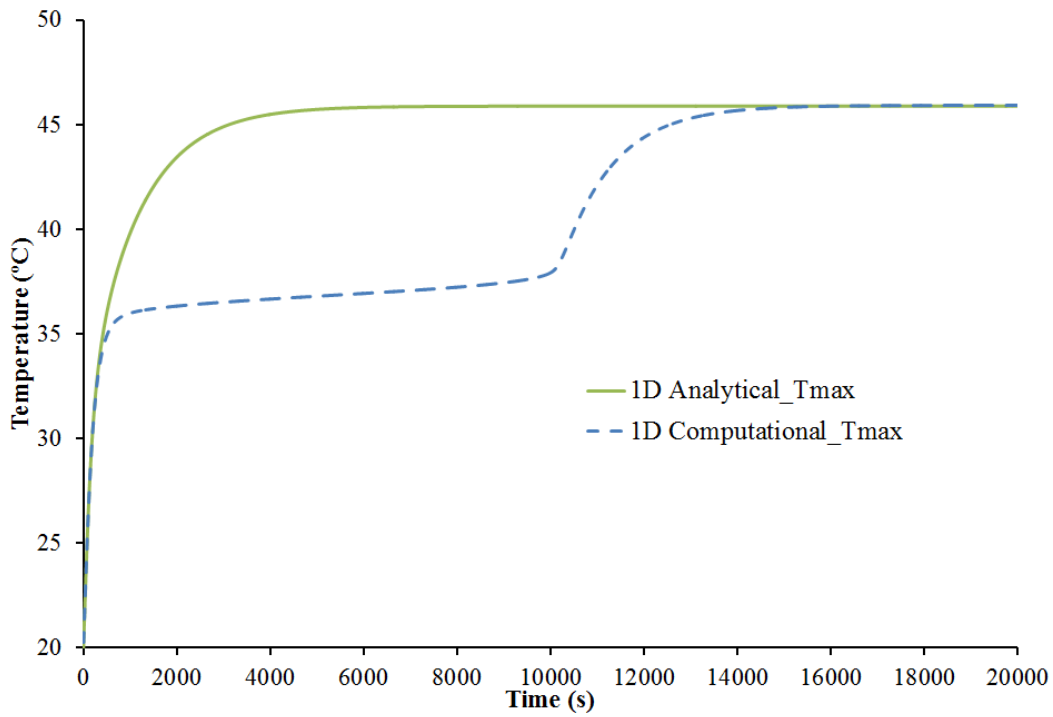


**Fig. 74.** Maximum temperature of the battery cooled by PCM/CENG for the 1D analytical and computational models.

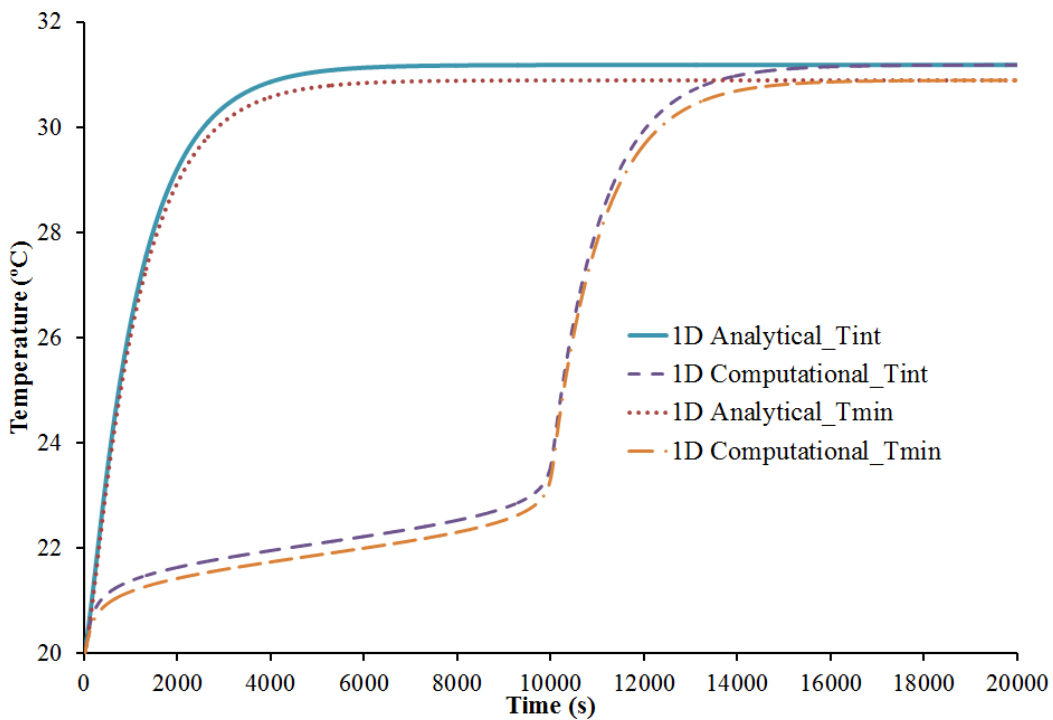


**Fig. 75.** Contact temperature and minimum temperature of the Battery cooled by PCM/CENG for the 1D analytical and computational models.

After the validation of the one-dimensional hypothesis by the comparison to 3D CFD simulations, a complete 1D computational model was compared to a 1D analytical-PCM/CENG model.

Both 1D analytical and computational models have predicted the steady state with a close match. In addition, the 1D computational model is able to represent the phase change phenomenon. This comparison has shown the advantage of the PCM/CENG as a thermal

management solution during temperature rise. The next section is devoted to compare the PCM/CENG cooling to the forced cooling convection.

### 3.5. Comparison of PCM/CENG cooling with forced convection cooling

The cooling of the battery by forced convection with  $h_r=20 \text{ W.m}^{-2}.\text{K}^{-1}$  gives a maximum temperature of 75 °C and a skin temperature (at  $r = r_1$ ) of 61 °C, when the cooling by the PCM/CENG designed for this case leads to a maximum temperature of 45.9 °C and a skin temperature ( $T_{int}$ ) of 31.1 °C with the same convection coefficient at the external surface of the PCM/CENG, as shown in Fig. 76.

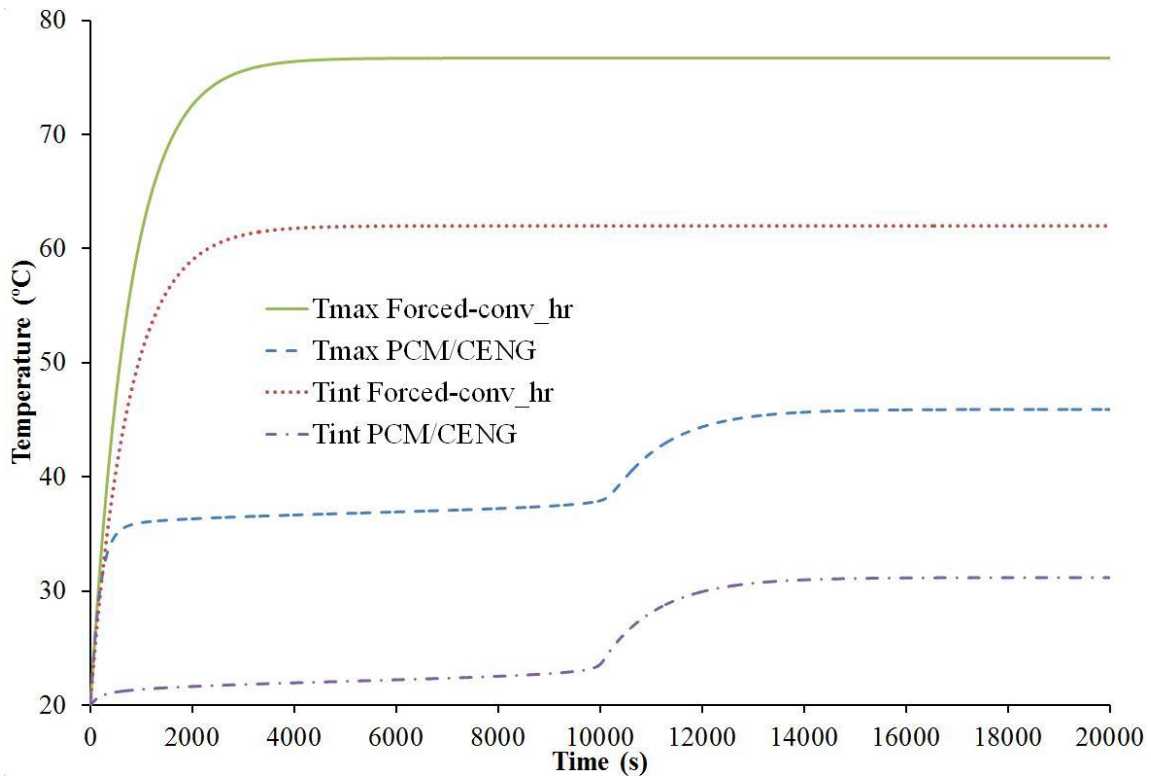


**Fig. 76.** Comparison between the forced convection cooling and the PCM/CENG cooling for  $h_r=20 \text{ W.m}^{-2}.\text{K}^{-1}$ .

Besides, the 1D computational model shows that the PCM/CENG designed for this test case is able to maintain the maximum temperature under 40 °C for 2.9 hours. Despite this slowing down of the temperature rise, the reduction of the final maximum temperature is mainly due to the increase of the cooling surface and the high conductivity of the PCM/CENG. What would be the amount of convection to apply on the battery surface, in order to reach the maximum temperature obtained in the case of the cooling by PCM/CENG?

The Biot number of the PCM/CENG designed for this test case is equal to

$Bi = R_{PCM/CENG}/R_{conv} = 0.027$ . The temperature can be then considered to be quasi-uniform in the solid. The calculation of the thermal equivalent resistance by the consideration of a series configuration can be approximated by:

$$R_{eq} = R_{PCM/CENG} + R_{conv}$$

$$\frac{1}{h_{eq}r_1} = \frac{\ln(r_2/r_1)}{k_{r,eff}} + \frac{1}{h_r(r_2)} \quad (3.45)$$

A  $h_{eq} \approx 3.8h_r$  is necessary for the forced convection cooling to reach the same final temperature in the case of the PCM/CENG cooling. This value is substituted in the analytical solution of the cooling by convection (Eq. 3.18) and compared to the 1D analytical model with PCM/CENG cooling and the 1D computational model. Figs. 77 and 78 show respectively the maximum and skin temperature of the battery cooled by convection with  $h_{eq} \approx 3.8h_r$ . There is a close correspondence between all the models at the steady state, but the fastest temperature rise took place in the forced convection cooling case. Consequently the higher convective coefficient needed in the forced convection cooling implies a more efficient and expensive pump/flow management system. In contrast, the PCM/CENG system provides a lighter system compared to the heavy metallic components used in the forced convection cooling solution equipped with a bulky flow management system.

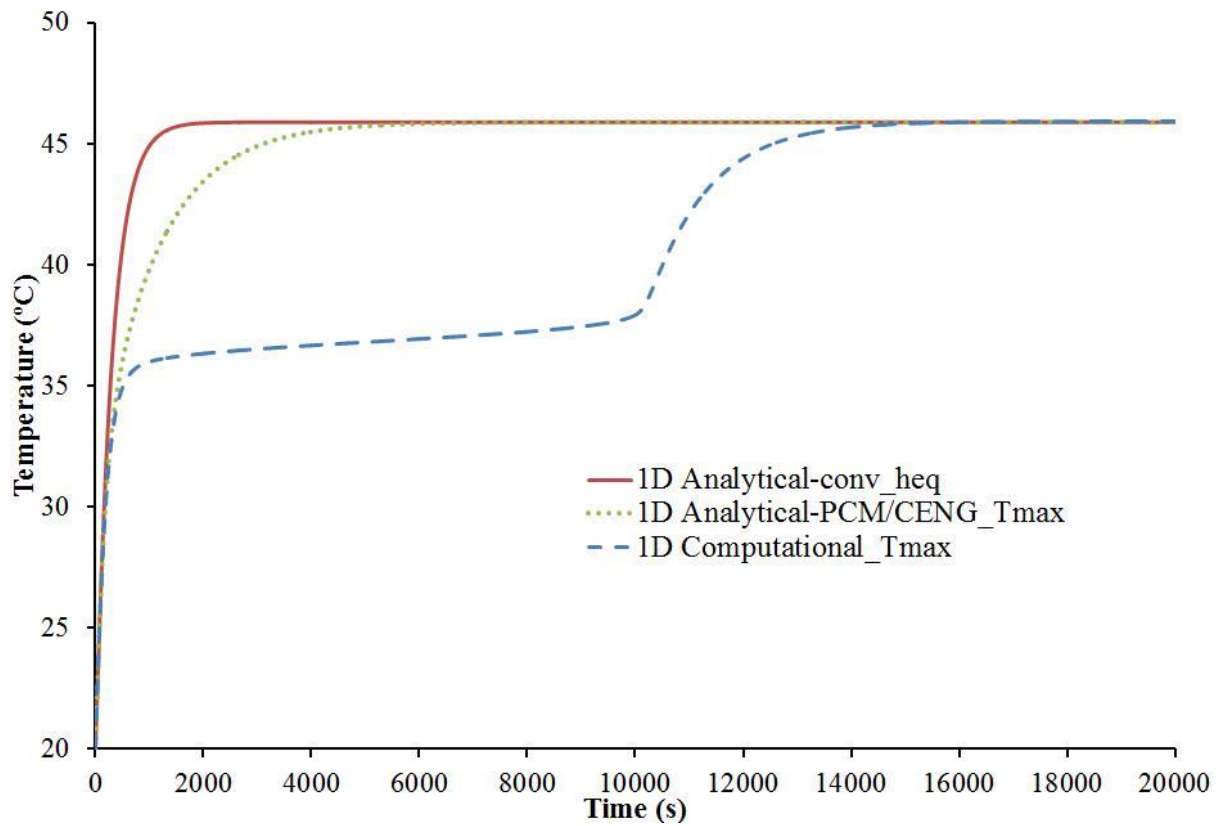


**Fig. 77.** Maximum temperature with the equivalent convective coefficient applied on the battery cell.

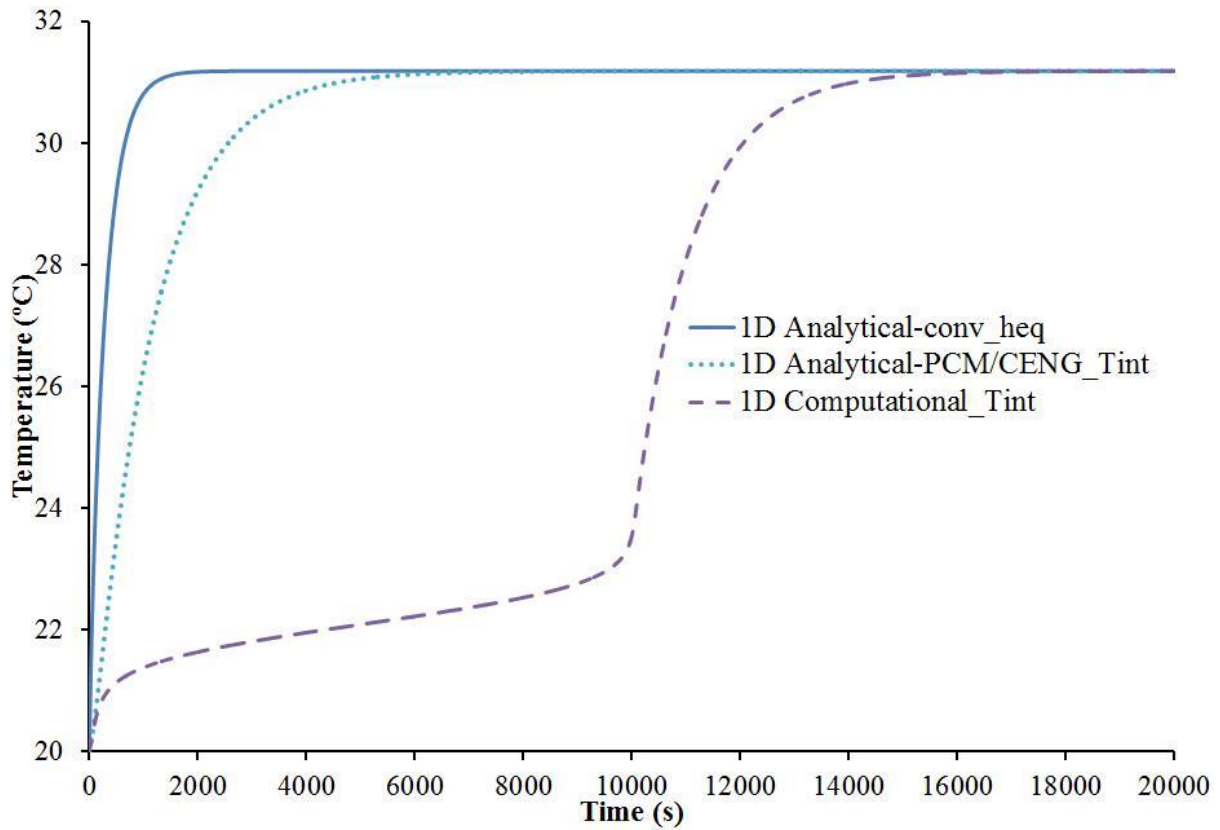


**Fig. 78.** Minimum temperature with the equivalent convective coefficient applied on the battery cell.

The 1D computational model is computationally fast and the implementation of the correlation developed by Py et al. [44] provides a possibility to design the PCM/CENG. The 1D computational model is therefore used to study the influences of the bulk density and PCM on the thermal performances, which are presented in the next section.

### 3.6. Effects of the bulk density and the PCM

To investigate the effects of the bulk density and the PCM, parameters such as those for the battery and the PCM/CENG thickness as well as boundary conditions are identical to the test case described before. The ambient temperature of  $T_{amb} = 20^{\circ}C$  and the convective coefficient  $h_r = 20 W.m^{-2}.K^{-1}$  applied on the external face of the PCM/CENG, are still in use.

#### 3.6.1. Bulk density

The 1D computational model is used to study the effect of the bulk density of the CENG matrix. Due to the limit of mechanical strength [44], the minimum bulk density value used for this study is  $\rho_{CENG} = 50 kg.m^{-3}$ . The maximum temperature decreases and reaches faster the steady state with the increase of the bulk density, as shown in Fig. 79. This tendency is the result of the increase of the effective conductivity when the bulk density increases (Eq. (3.20)). Besides, the increase of the bulk density leads both to the decreasing of the porosity and the reduction of the PCM quantity injected in the CENG matrix. The reduction of the

length of the phase change plateau is clearly observed in Fig. 79. Nevertheless, the reduction of the temperature obtained by the increase of the bulk density becomes insignificant after  $\rho_{CENG}=200 \text{ kg.m}^{-3}$ , while the length of the phase plateau decreases. Therefore, the increase of the bulk density becomes less effective at a certain value and tends only to reduce the gain brought by the phase change.

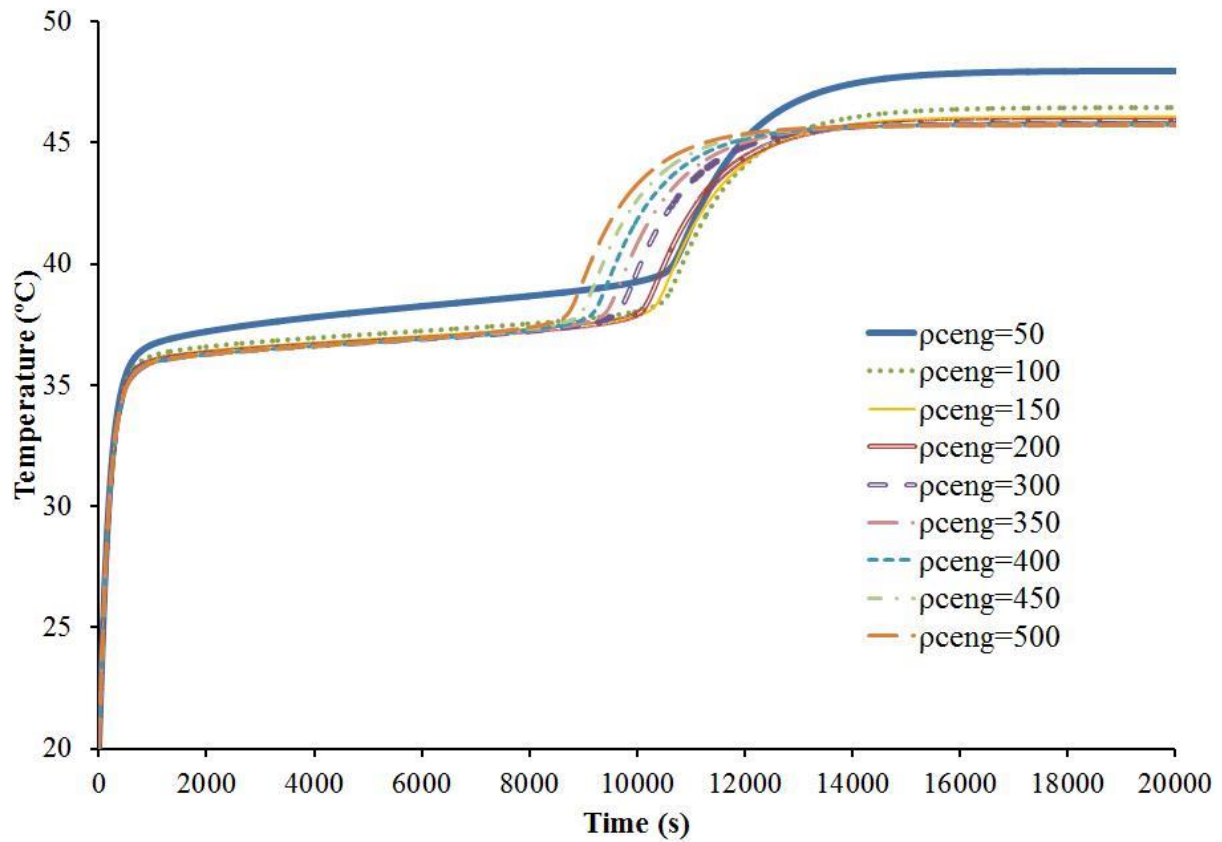


**Fig. 79.** Maximum temperature of the battery cell cooled by PCM/CENG for various bulk densities.

Figure 80 presents the discrepancy of the maximum temperature in steady state, for different bulk densities relative to  $\rho_{CENG}=200 \text{ kg.m}^{-3}$ . The discrepancy drops lower than 0.5% after a bulk density of  $150 \text{ kg.m}^{-3}$ . The analysis presented in Fig. 80 confirmed that a high bulk density becomes ineffective and may penalize the gain added by the PCM, by reducing the phase change plateau as shown in Fig. 79.

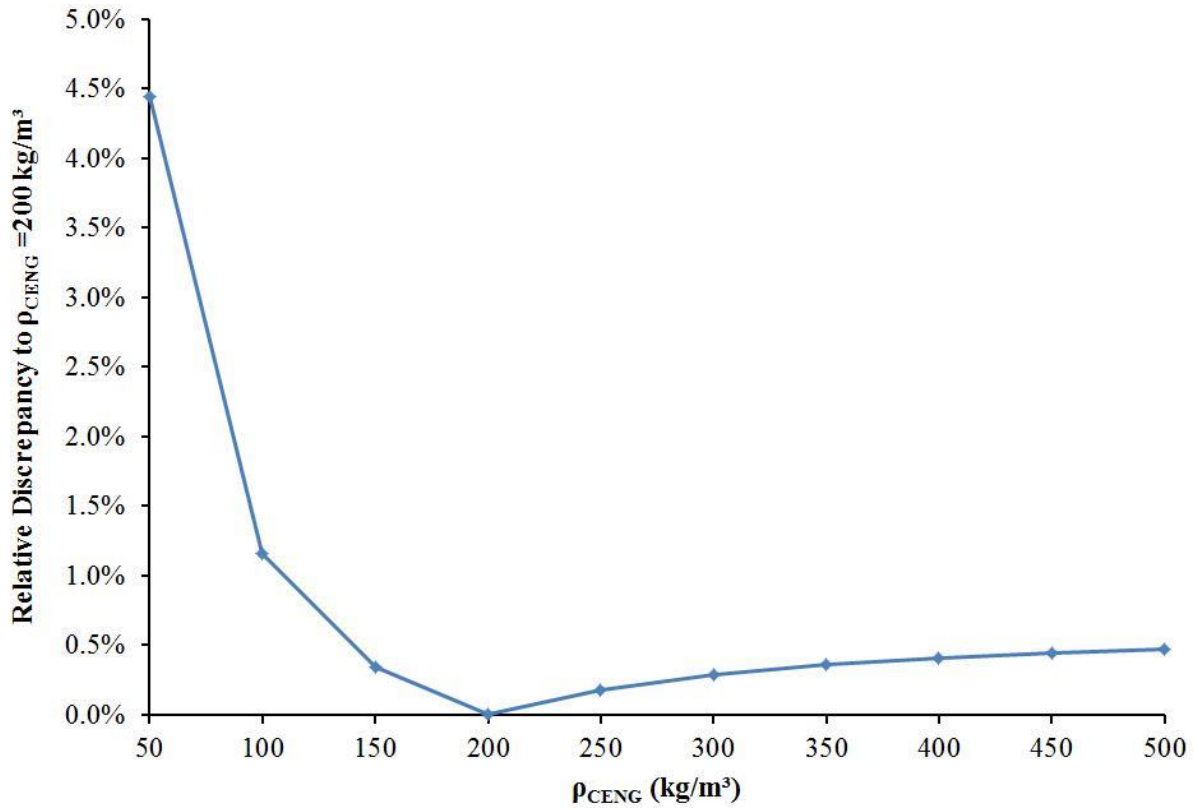


**Fig. 80.** Relative discrepancy of the maximum temperature (steady state) for different bulk densities relative to  $\rho_{CENG} = 200$  kg.m<sup>-3</sup>.

Besides, Py et al. [44] has advised to use a maximum bulk density of 350 kg.m<sup>-3</sup>. This limit is mainly due to the injection method of the PCM in the CENG matrix. In the imbibition method, the impregnation kinetics and PCM quantity started to become too slow with increasing density. In addition, the viscosity of the PCM, increasing with the number of carbon atoms reduces also the impregnation kinetics. Therefore, the choice of 200 kg.m<sup>-3</sup> is sufficient to have a low maximum temperature, a high phase change plateau and good impregnation kinetics during the imbibition of the PCM in the matrix.

The ineffectiveness at high bulk density can be explained by the analysis of the equivalent thermal resistance, as that given in Eq. (3.45). In order to highlight the effect of Biot number of the PCM/CENG, this equation is rewritten as

$$R_{eq} = R_{conv} (Bi_{PCM/CENG} + 1) \quad (3.46)$$

The Biot number and the equivalent thermal resistance are plotted for different values of bulk density in Fig.81. The Biot number decreases with the increase of the bulk density and becomes much less than one. In consequence, the equivalent thermal resistance approaches the thermal resistance of convection with the increase of the bulk density.

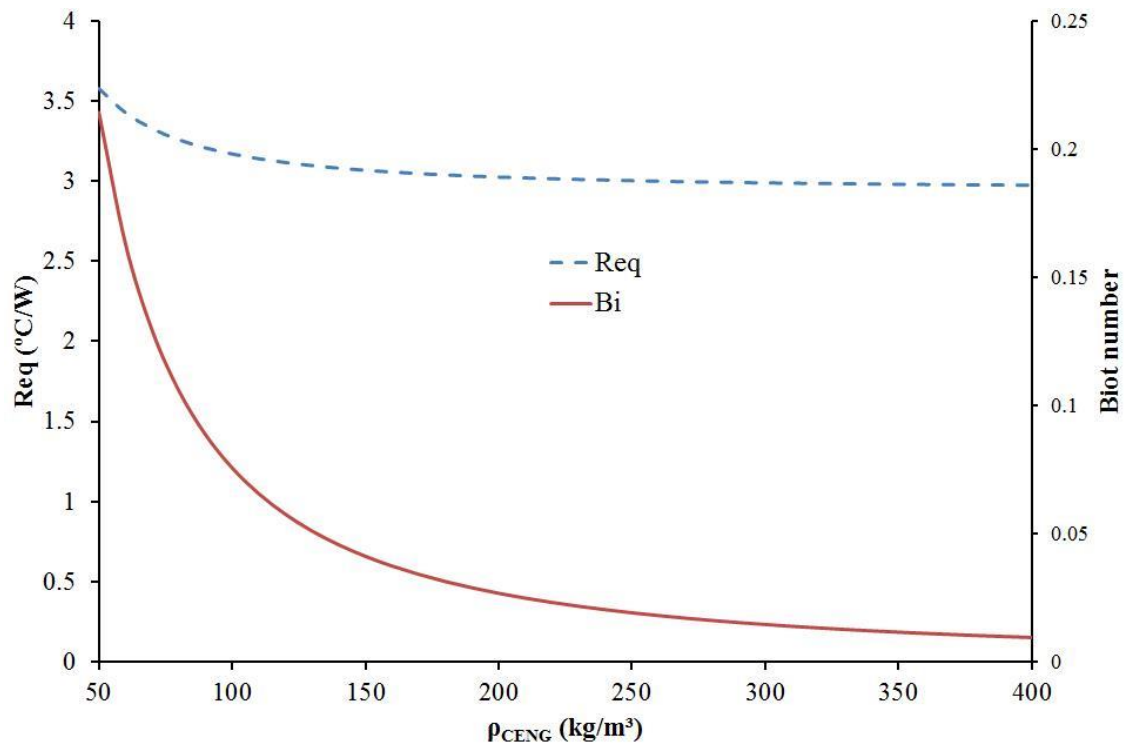


**Fig. 81.** Equivalent thermal resistance and Biot number of the PCM/CENG versus the bulk density.

This limit is approached very fast for bulk densities greater than  $200 \text{ kg}\cdot\text{m}^{-3}$ . Therefore, in this configuration, the only way to improve the performance of the PCM/CENG composite is to reduce the thermal resistance of convection. If the thickness of the PCM/CENG composite is not modified, increasing the convection surface by adding fins and/or the introduction of a higher convective heat coefficient will reduce this resistance. It is also important to notice that the conclusion drawn for the impact of the bulk density on the maximum temperature in steady state is independent of the choice of the PCM. This result is the consequence of the independence of the effective thermal conductivity of the PCM/CENG composite to the PCM. The choice of the PCM only affects the temperature rise.

### 3.6.2. PCM

The bulk density is kept at  $200 \text{ kg}\cdot\text{m}^{-3}$ , along with the configuration of the test case previously described. The PCM is replaced by the n-octadecane paraffin (Table 8) and compared to the analytical solution equipped with the same PCM. This case is also compared to the previous one with the n-heptadecane paraffin. Fig. 82 presents the maximum temperature of the battery cell for the n-octadecane (n=18) and n-heptadecane paraffin injected in the CENG matrix. As stated before, the change of PCM has only modified the early temperature rise but not the final temperature.

Besides, a zoom-in of Fig. 82 is presented in Fig. 83, which shows that the maximum temperature of the battery cell reaches  $40^\circ\text{C}$  before being affected by the phase change process occurring in the PCM/CENG composite. The 1D computational model provides a possibility to design the PCM/CENG with its impact on the battery temperature distribution.

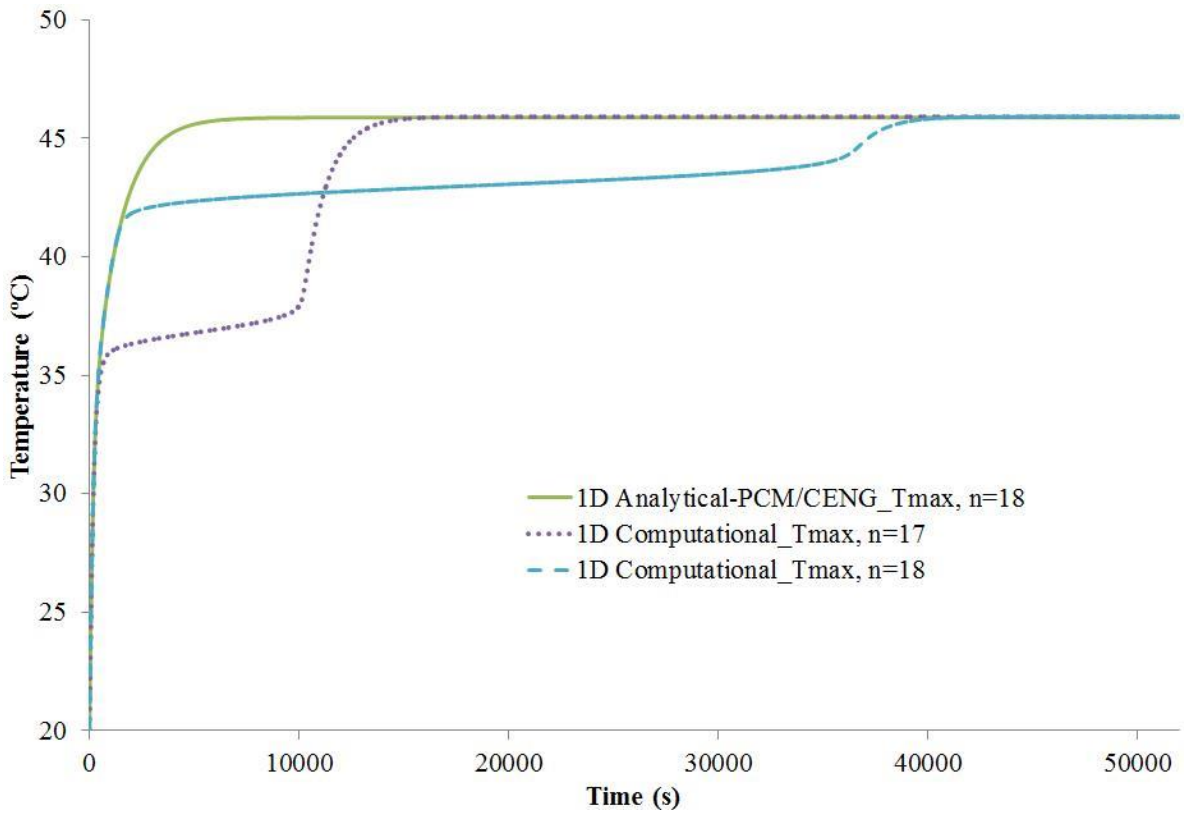


**Fig. 82.** Maximum temperature of the battery cell for the n-octadecane and n-heptadecane.

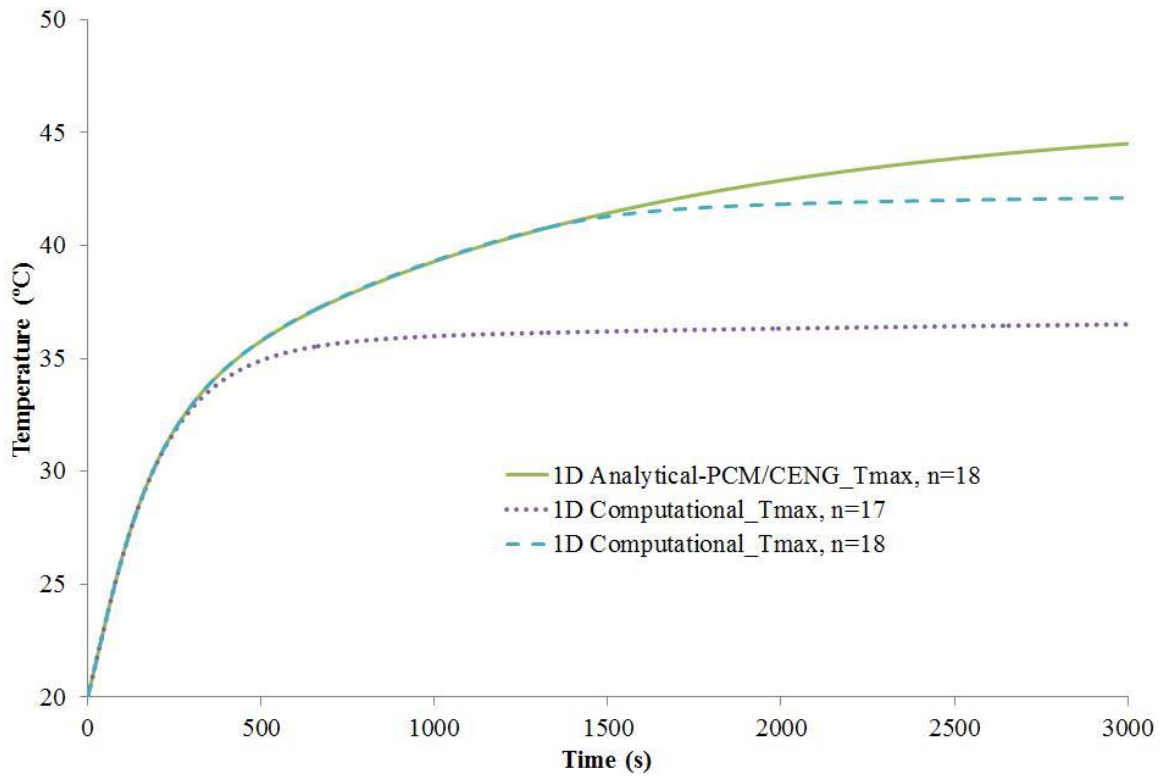


**Fig. 83.** Zoom-in of Fig. 82.

The thickness of the PCM/CENG chosen for the test case in this study has an impact on the thermal behaviour of the battery. If the convective heat coefficient is kept constant, the reduction of this thickness leads to an increase of the thermal resistance of convection by decreasing the external surface of the PCM/CENG. Consequently, an increase of the

maximum temperature is expected in the steady state. Furthermore, this reduction has an impact on the transient rise of the temperature, by shortening the phase change plateau, due to the decrease of the quantity of PCM injected in the CENG matrix. Therefore, the Biot number presented in subsection 3.6.1, which depends on the PCM/CENG thickness, is modified, as well as the optimized value of the bulk density obtained previously. This parameter will be addressed in the next study dedicated to the cooling of the battery pack with PCM/CENG.

### 3.7. Conclusions

The passive cooling management of the cylindrical battery by a PCM/CENG composite was investigated and different models were proposed. Despite the high level of impregnation, a PCM/CENG composite possesses a high conductivity, independent of the PCM thermal conductivity. The forced convection cooling was studied first by the development of 1D and 3D analytical models. The 1D analytical model resulted from the anisotropic thermal conductivity of the cylindrical battery cell ( $k_r \ll k_z$ ), coupled with the convection in the radial direction where the gradient of temperature and surface are important. A test case was used to study and compare the models. The comparison to the 3D CFD simulation on the open source softwares SALOME.7.4/SYRTHES.4 in the case of forced convection cooling, led to a very good match with the 3D simulation, when the surface in the axial direction was supposed adiabatic and to a discrepancy less than 2% in the case of natural convection. This analysis was followed by the PCM/CENG cooling case. The PCM/CENG was modelled by one equation with effective physical properties due to the fast thermal equilibrium between the PCM and the CENG graphite, resulting from the high surface contact between both entities. Contrary to the battery, The PCM/CENG had a radial effective conductivity much higher than the one in the axial direction. The anisotropic thermal conductivity in the battery and PCM/CENG composite combined with the cooling in the radial direction, led to the development of a 1D analytical model of the battery cooled by a PCM/CENG. This analytical model used physical properties based on experimental correlations and the effective specific heat for the PCM/CENG. A 1D computational model based on the thermal network method, was developed in order to include the phase change of the PCM as a function of temperature. A test case was built with the same configuration for the battery and convective coefficient depicted in the forced convection case, and also the n-heptadecane paraffin as phase change material. The analytical solution and 1D computational model were compared to a 3D CFD simulation on SALOME.7.4/SYRTHES.4, with only the specific heat taken into account. A very good match was observed between all the models with adiabatic condition on the surfaces in the axial direction and less than 2% discrepancy with natural convection on the same surfaces. In practice, this discrepancy is expected to be lower, due to the surface in the axial direction, usually occupied by the electric wires connecting the batteries with each other. In consequence, a one-dimensional modelling of the battery cooled by a PCM/CENG was sufficient to describe the temperature distribution in the battery cell.

In addition, the 1D computational model with the consideration of the latent heat was able to predict the temperature rise in the battery and PCM/CENG with only 23 nodes, when the 3D CFD used 75009 nodes. The model showed, with the chosen PCM, that the maximum temperature was kept under 40°C for 2.9 hours. The cooling by PCM/CENG was able to reduce the maximum temperature and skin temperature from respectively 75°C to 45.9°C and 61°C to 31.1°C compared to the forced convection cooling case with the same convective coefficient of  $20 \text{ W}\cdot\text{m}^{-2}\cdot\text{K}^{-1}$ . Moreover, 3.8 times the previous convection coefficient was needed for the forced convection cooling in order to reach the same temperature obtained with the PCM/CENG cooling. This implies that the PCM/CENG can be effectively used in the battery cooling system.

The 1D computational model can be used to design the PCM/CENG from the bulk density, and dimensions, to the choice of PCM. The influence of the bulk density was studied because of its impact on the porosity and thermal conductivity of the PCM/CENG. Identical dimensions, convective coefficient and PCM, to the PCM/CENG cooling case were used with variation of the bulk density from 50 to  $500 \text{ kg}\cdot\text{m}^{-3}$ . The increase of density reduces the porosity and PCM quantity at the same time, and increases also the effective conductivity. The increase of the bulk density becomes ineffective at certain value of density. This ineffectiveness was depicted by a low impact on the final maximum temperature reduction and a more significant effect on the reduction of the length of the phase change plateau. The estimation of the equivalent thermal resistance of the PCM/CENG showed that this resistance was approaching quite fast the convection thermal resistance. For the test case presented,  $200 \text{ kg}\cdot\text{m}^{-3}$  was sufficient to be close to this limit. Therefore, for a fixed thickness of the PCM/CENG composite, the only way to improve the performances is the reduction of the convection thermal resistance. This resistance is reduced by increasing the convection surface by adding fins and/or increasing the convective heat coefficient. Moreover, this result is independent of the PCM chosen, since the PCM does not affect the effective thermal conductivity of the PCM/CENG graphite.

Nevertheless, an important gradient higher than 10°C was observed in the battery for the cooling by PCM/CENG. This gradient was predicted by the 3D CFD model, 1D analytical-PCM/CENG and the 1D computational model. This result is perhaps due to a single set of representative data for an example battery, used to build the test case. The choice of various representative data was made to demonstrate the capacity of the models to work in various configurations. Real battery data would be useful to confirm the origin of this gradient of temperature. An experimental study would be useful to verify certain hypotheses made and to test the 1D computational model for designing a PCM/CENG composite. Furthermore, the 1D computational and the analytical models developed previously were only dedicated to the study of a single battery, with possible extension to a module scale analysis in limited configurations. In this optic, a new model is necessary to extend the one-dimensional model to a multidimensional one. The next chapter will present the numerical method used to develop this new approach.

## Chapter 4: Development of the cell-centred Lagrangian diffusion code

### 4.1. Introduction

The study of passive cooling systems was presented in the previous chapter, with models developed in order to predict the thermal behaviour of the battery cooled by these systems. However these models were only dedicated to the study of a single cell and cannot be used for battery module or pack simulations. To extend the methods to multi-dimensional applications, numerical simulations in 2D or 3D are essential as analytical solutions become unavailable. In this context, a finite volume code was developed in order to analyse the passive cooling of a battery module or pack, i.e. the extension of the one-dimensional model to a multidimensional model.

This chapter is dedicated to the development of the Cell-Centred Lagrangian Diffusion (CCLAD) mathematical code, where the numerical method closely followed that by Maire and Breil [67, 68] with further developments in the boundary conditions. The method is a finite volume numerical resolution of equations for unstructured meshes. The method is well described by the authors [67, 68] and only few generalities will be presented first in this chapter, followed by the modification applied to the boundary conditions. The code was created for analysing the PCM/graphite cooling presented in Chapter 3, of a cylindrical battery module with constant and electrochemistry based heat generation. Finally, validation tests against different models are performed, using constant and electrochemistry based heat generation. The electrochemistry model and the temperature distribution of the cylindrical battery module are fully described in Chapter 5, but are used to show the capabilities of this finite volume method.

Besides, simulations on SYTHES4.0 described in the next chapter, have shown that only a two-dimensional simulation was sufficient to predict the temperature distribution of the cylindrical module cooled by PCM/CENG. In consequence, the two-dimensional version of the CCLAD finite volume method [67, 68] is presented. The code based on this CCLAD method, is written in PYTHON and the mesh is generated by the open-source software SALOME7.4. For avoiding any misunderstanding, the word “cell” used in this chapter designates one element of the computational domain.

### 4.2. CCLAD generality

The CCLAD method developed by Maire and Breil [68] is used to describe the thermal behaviour of battery cells cooled by a PCM/CENG at a multidimensional level, while the 1D computational is only limited to the study of a single cell. The global thermal equation is presented as follows:

$$mc_v \frac{dT}{dt} = \nabla \cdot (K \nabla T) w_g + \phi_{gen} \quad (4.1)$$

Where  $\varphi_{gen}$  represents the heat generation of the single battery, taken either constant or depending on the temperature by the addition of the electrochemistry model, and  $w_g$  represents the global volume of the battery. Moreover, the specific heat  $c_v$  is taken constant for the battery domain and described by an equivalent thermal capacity model for the PCM/CENG composite. The equivalent thermal capacity model [66] allows the addition of the phase change phenomena in the transient simulation.

The main difficulty of the finite volume method for unstructured grid is the calculation of the fluxes exchanged between each cells composing the computational domain.

#### 4.2.1. Flux calculation

The computational domain is divided in polygonal cell  $\omega_c$ , which also are divided into subcell  $\omega_{pc}$ . A subcell  $\omega_{pc}$  is defined by connecting the centre or centroid of the cell  $\omega_c$  to the midpoint of the edges impinging to node  $p$  of the cell  $\omega_c$ , as presented in Fig. 84. Besides, each edge has two half-edge normal fluxes and two half-edge temperatures. The heat fluxes for a cell  $\omega_c$  are obtained by the calculation of the half-edge normal fluxes exchanged for all the subcells  $\omega_{pc}$ .

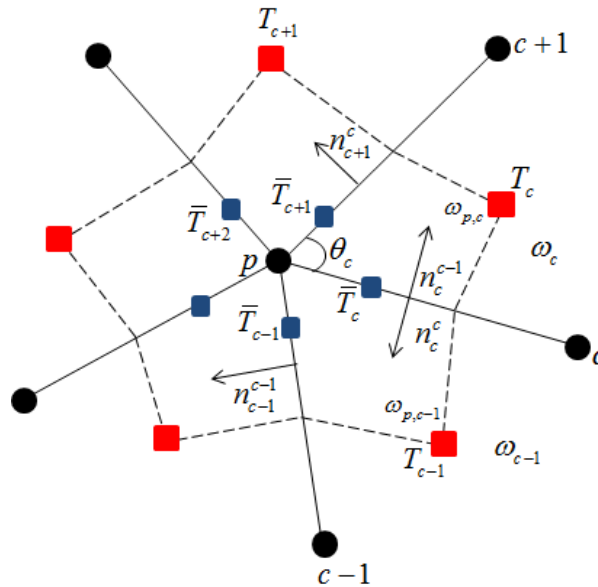


**Fig. 84.** Notation for sub-cells surrounding the node  $p$  located in the computational domain.

The first step is to find a relation between the half-edge fluxes of the subcell connected to the same node  $p$ . The discretisation of the half-edge fluxes is derived from the local variational formulation of the Fourier's law for each sub-cell and presented in a general form as follows:

$$q_{Fourier} = -K\nabla T \quad (4.2)$$

Different notations are used in order to build the mathematical relation between the half-edge fluxes of the subcells connected to the same node. In this respect,  $C(p)$  represents the set of cells surrounding a node  $p$ , as shown in Fig. 84, and the cell numbering follows the edge

numbering, i.e. cell  $\omega_c$  is located between edge  $c$  and edge  $c+1$ . In addition, the two half-edge normal fluxes with the application of the temperature continuity between adjacent cells are expressed by:

$$\begin{pmatrix} q_c^c \\ q_{c+1}^c \end{pmatrix} = -\frac{1}{w_{pc}} K_{pc} \begin{bmatrix} l_c (\bar{T}_c - T_c) \\ l_{c+1} (\bar{T}_{c+1} - T_c) \end{bmatrix} \quad (4.3)$$

where  $\bar{T}_c$ ,  $\bar{T}_{c+1}$  designate the two half-edge temperatures and  $T_c$  represents the cell-centred temperature. The half-edge fluxes  $q_c^c$  and  $q_{c+1}^c$  represent the normal flux at edge  $c$  and edge  $c+1$  respectively, viewed from cell  $\omega_c$ . Besides,  $l_c$  designates the half of the length of edge  $c$  and  $K_{pc}$  is the conductivity tensor calculated on the sub-cell  $\omega_{pc}$  of cell  $\omega_c$ , connected to the node  $p$ .

$$K_{pc} = \begin{pmatrix} K_c n_c^c \cdot n_c^c & K_c n_{c+1}^c \cdot n_c^c \\ K_c n_c^c \cdot n_{c+1}^c & K_c n_{c+1}^c \cdot n_{c+1}^c \end{pmatrix} \quad (4.4)$$

This tensor is described by Eq. (4.2), with  $n_c^c$  and  $n_{c+1}^c$  representing the unit outward normal to cell  $\omega_c$ , at edge  $c$  and edge  $c+1$  respectively. Because the thermal conductivity is isotropic in the domain of study for both the battery and the PCM/CENG composite, Eq. (4.4) can be simplified as follows:

$$K_{pc} = k_c \begin{pmatrix} 1 & -\cos \theta_c \\ -\cos \theta_c & 1 \end{pmatrix} \quad (4.5)$$

The thermal conductivity  $k_c$  is different from the battery to PCM/CENG, and  $\theta_c$  is the angle between edge  $c$  and  $c+1$  of the cell  $\omega_c$  and is connected to the node  $p$ , as shown in Fig. 84. The final expression for the half-edge fluxes for a two-dimensional problem with isotropic thermal conductivity is:

$$\begin{pmatrix} q_c^c \\ q_{c+1}^c \end{pmatrix} = -\frac{1}{w_{pc}} k_c \begin{pmatrix} 1 & -\cos \theta_c \\ -\cos \theta_c & 1 \end{pmatrix} \begin{bmatrix} l_c (\bar{T}_c - T_c) \\ l_{c+1} (\bar{T}_{c+1} - T_c) \end{bmatrix} \quad (4.6)$$

The conservation of the flux at the half-edge  $c$ , i.e. between cells  $\omega_c$  and  $\omega_{c-1}$  is given by Eq. (4.7). The writing of Eq. (4.7) for all the half-edge  $c$  of the set  $C(p)$  leads to a matrix system described by Eq. (4.8).

$$l_c q_c^c + l_c q_c^{c-1} = 0; \quad \forall c \in C(p) \quad (4.7)$$

$$[M][\bar{T}] = [S][T] \quad (4.8)$$

This equation gives the relation between the vectors of half-edge temperatures  $[\bar{T}]$  and the cell-centered temperature  $[T]$  for the cells connected to the same node  $p$ . It is important to notice that the matrices  $[M]$  and  $[S]$  of Eq. (4.8) are written for a node  $p$  and there will be as many as the nodes in the computational domain.

Therefore, the half edge temperature can be eliminated by the inversion of the tridiagonal cyclic matrix  $[M]$ , as presented in Eq. (4.9).

$$[\bar{T}] = [M]^{-1}[S][T] \quad (4.9)$$

The implementation of the boundary condition is similar to the previous calculation with the conservation of fluxes between the half-edges not located at the boundaries of the domains

(Eq. (4.10.b)). The difference is in the addition of the boundary conditions at the first (Eq. (4.10.a)) and last half-edge, (Eq. (4.10.c)) as described in Fig. 85. Therefore, the set  $C(p)$  at a node  $p$  is open, i.e. there are  $N_p$  cells connected to a node  $p$  located at the boundary and  $N_p + 1$  edges.

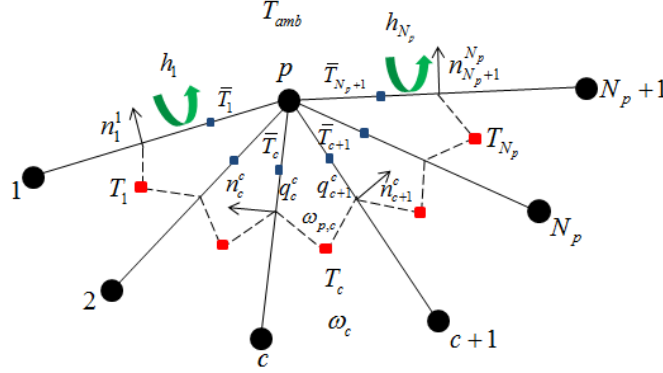


**Fig. 85.** Notation for sub-cells surrounding the node  $p$  located at the boundary with Robin boundary condition applied at the external half-edge.

From the notation of Fig. 85 the new system of equations is defined as follows:

$$l_1 q_1^1 = l_1 h_1 (\bar{T}_1 - T_{amb}) \quad (4.10.a)$$

$$l_c q_c^c + l_c q_c^{c-1} = 0; \text{ for } c = 2, \dots, N_p \quad (4.10.b)$$

$$l_{N_p+1} q_{N_p+1}^{N_p} = l_{N_p+1} h_{N_p+1} (\bar{T}_{N_p+1} - T_{amb}) \quad (4.10.c)$$

The final matrix system obtained for a node  $p$  located at the boundary is written by Eq. (4.11).

$$[M][\bar{T}] = [S][T] + [B] \quad (4.11)$$

Where the matrix  $[B]$  takes into account the terms due to Robin boundary condition applied on the half-edge 1 and  $N_p + 1$ , as presented in Fig. 85. Furthermore, the half-edge temperatures are eliminated similarly to the previous case, by the inversion of the matrix  $[M]$ , as presented in Eq. (4.12).

$$[\bar{T}] = [M]^{-1}[S][T] + [M]^{-1}[B] \quad (4.12)$$

The final expression of the half-edge temperatures, when the node  $p$  is located or not at the boundary of the computational domain is used to build the final matrix resolution of the problem.

#### 4.2.2. Global cell-centered system

The building of the global matrix is presented in this section, by considering the cells  $\omega_c$  and  $\omega_c^*$  located respectively in the domain and close to the boundary, as presented in Fig. 86 with a mesh generated by the open-source software SALOME7.4. The thermal equation for a cell  $\omega_c$  is written as follows:

$$m_c c_{vc} \frac{dT_c}{dt} + \sum_{p \in P(c)} Q_{pc} = \varphi_{gen,c}; \quad Q_{pc} = l_c q_c^c + l_{c+1} q_{c+1}^c \quad (4.13)$$

For the sake of homogeneity, it is important to notice that the mass  $m_c$  and the flux  $Q_{pc}$  are expressed respectively by  $m_c = w_c \rho_c H$  and  $Q_{pc} = (l_c q_c^c + l_{c+1} q_{c+1}^c) H$ . However, the two-dimensionality of the problem allows putting the height to  $H = 1$ , leading to the Eq. (4.13).

Different meshes from unstructured to structured, can be used, but only triangular ones were considered in this study. In consequence, Eq. (4.13) can be simplified by Eq. (4.13a), with  $P(c) = \{p_1, p_2, p_3\}$  presented in Fig. 86.

$$m_c c_{vc} \frac{dT_c}{dt} + \sum_{p_i=1}^3 Q_{pc} = \varphi_{gen,c} \quad (4.13a)$$

The total half-hedge flux  $Q_{pc}$  exchanged by the subcell  $\omega_{pc}$  with the other subcells impinging at a node  $p$  of the cell  $\omega_c$  is transformed into Eq. (4.14) by using Eq. (4.6).

$$Q_{pc} = -[\tilde{S}]_{c,c} (\bar{T}_c - T_c) - [\tilde{S}]_{c+1,c} (\bar{T}_{c+1} - T_c) \quad (4.14)$$

In the case of symmetric thermal conductivity tensor [68], the matrix  $[S]$  is identical to  $[\tilde{S}]$ . Moreover, due to the sparse structure of the  $[\tilde{S}]$ , Eq. (4.14) can be rewritten into Eq. (4.14a) with the subscript  $d$  designating a cell belonging to  $C(p)$ .

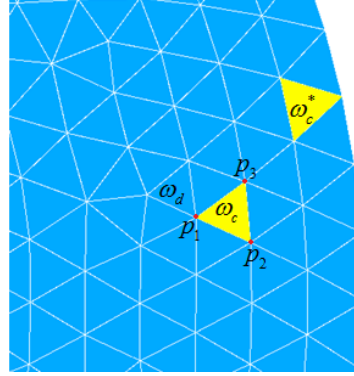


**Fig. 86.** Triangular meshes on SALOME with an inner cell  $\omega_c$  and a cell  $\omega_c^*$  close to the boundary.

$$Q_{pc} = - \sum_{d \in C(p)} [\tilde{S}]_{c,d}^t (\bar{T}_d - T_c) = - \left( \sum_{d \in C(p)} [\tilde{S}]_{c,d}^t \bar{T}_d - \left( \sum_{d \in C(p)} [\tilde{S}]_{c,d}^t \right) \delta_{c,d} T_c \right) \quad (4.14a)$$

Finally Eq. (4.12) is used in Eq. (4.14a), with  $[B]$  set to zero for a cell  $\omega_c$  located in the computational domain as shown in Fig. 86. Finally, Eq. (4.15a) is obtained with  $G_{c,d}^p$  seen as the thermal conductance between cells  $\omega_c$  and  $\omega_d$  belonging to  $C(p)$  through a node  $p$ .

$$Q_{pc} = - \sum_{d \in C(p)} G_{c,d}^p \bar{T}_d - (S_B)_c \quad (4.15a)$$

$$(S_B)_c = ([\tilde{S}]^t [M]^{-1} [B])_c \quad (4.15b)$$

$$G^p = [\tilde{S}]^t [M] [S] - \Lambda \quad (4.15c)$$

$$\Lambda = \left( \sum_{d \in C(p)} [\tilde{S}]_{c,d}^t \right) \delta_{c,d}; \text{ with } \delta_{c,d} = \begin{cases} 1 & ; \text{if } c = d \\ 0 & ; \text{if } c \neq d \end{cases} \quad (4.15d)$$

The thermal equation of a cell  $\omega_c$  can be transformed from Eq. (4.13a) to Eq. (4.13b).

Besides,  $(S_B)_c^p$  is seen as a source term accounting for the boundary conditions applied on the half-edges of the cell located at the boundary ( $\omega_c^*$ ) of the domain. This term is equal to zero for the cell  $\omega_c$  not connected to the boundary.

$$m_c c_{vc} \frac{dT_c}{dt} - \sum_{p_i=1}^3 \sum_{d \in C(p)} G_{c,d}^p \bar{T}_d = \varphi_{gen,c} + \sum_{p_i=1}^3 (S_B)_c^p \quad (4.13b)$$

Finally Eq. (4.13b) is written for all the cells composing the computational domain and put in a global matrix system equation as follows:

$$[C_v] \frac{d[T]}{dt} + [A][T] = [Q] \quad (4.16)$$

$[C_v]$ ,  $[A]$  and  $[Q]$  designate the global thermal capacity matrix of the cell-centered nodes, the global thermal conductance matrix between the cell-centered nodes of the entire domain and the global source term of the problem respectively. Eq. (4.16) has an identical form to the global equation of the 1D computational model [66] of a battery cell, but described the 2D simulation of a battery module scale. Furthermore, the transient solution is obtained by an Euler implicit discretization of Eq. (4.16).

It is important to be sure that the maximum principle is respected during a simulation, i.e. the increase of the half-hedge temperatures coordinates with the increase of the cell-centered temperatures.

$$\forall c \in C(p) \left\{ \begin{array}{l} \theta_c \in \left[ -\frac{\pi}{2}, \frac{\pi}{2} \right] \\ \cos \theta_c \leq \min \left( \frac{l_{c+1}}{l_c}, \frac{l_c}{l_{c+1}} \right) \end{array} \right. \quad (4.17)$$

Sufficient geometric conditions on the meshes were highlighted by Maire and Breil [68], in order to respect this principle. For an isotropic thermal conductivity tensor, the geometric conditions are simplified into Eq. (4.17). This condition is very restrictive and can be difficult to achieve in the case of complex geometries. Nonetheless the CCLAD code is studied first for a test case and compared to other CFD code and methods in order to validate its capabilities.

### 4.3. Test case and validation

A cylindrical battery cell of 7 mm radius and 65 mm height is considered for the test, in order to compare the results to the analytical and computational model developed before [66]. This battery is surrounded by a PCM/CENG composite of 7 mm thickness, identical to the one used by Greco et al. [66], i.e. a graphite density of  $\rho_{CENG} = 200 \text{ kg.m}^{-3}$  and the paraffin heptadecane as PCM. Besides, a convective coefficient of  $20 \text{ W.m}^{-2}.K^{-1}$  is applied on the

external surfaces of the battery cell with an ambient temperature fixed at 20°C. The meshes of the two-dimensional problem presented in Fig. 87, are generated with the open-source software SALOME7.4, where the battery cell is coloured in orange and the PCM/CENG composite in green. The meshes generated by SALOME7.4 are exported to the CCLAD code as a “.dat” file. This file contains the coordinates of the nodes and the reference number of the different nodes composing each cell, in order to calculate the parameters (volume, length, etc.) used to build the global matrix of the problem.

The CCLAD code is compared to the 1D computational model, SYRTHES and analytical solution, when it is possible. The temperature is compared first, followed by the addition of the phase change in the code and finally the implementation of the electrochemistry model fully presented in Chapter 5. Moreover, the temperature and phase change validations are performed with a constant heat generation power per volume of  $240 \text{ kW.m}^{-3}$ .

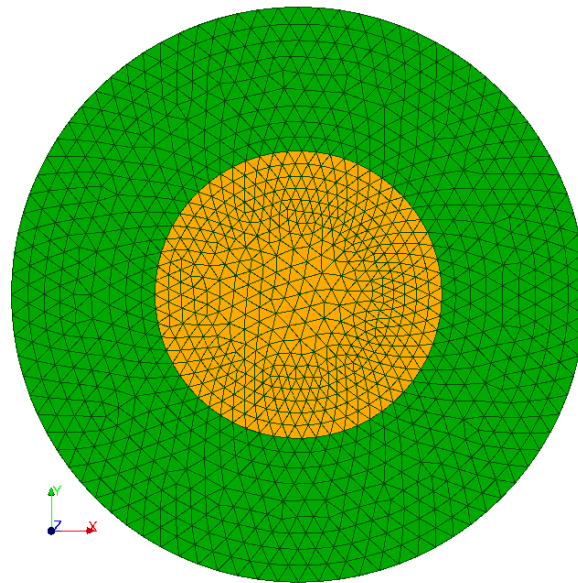
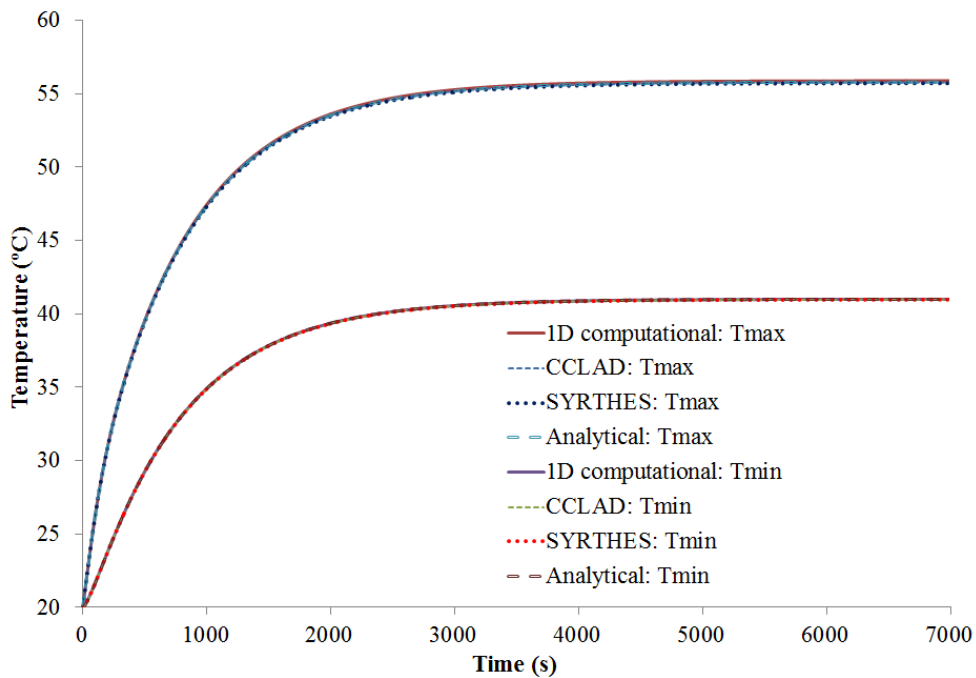


**Fig. 87.** Meshes of the test case of the cylindrical battery cell cooled by a PCM/CENG matrix.

#### 4.3.1. Temperature and phase change validation

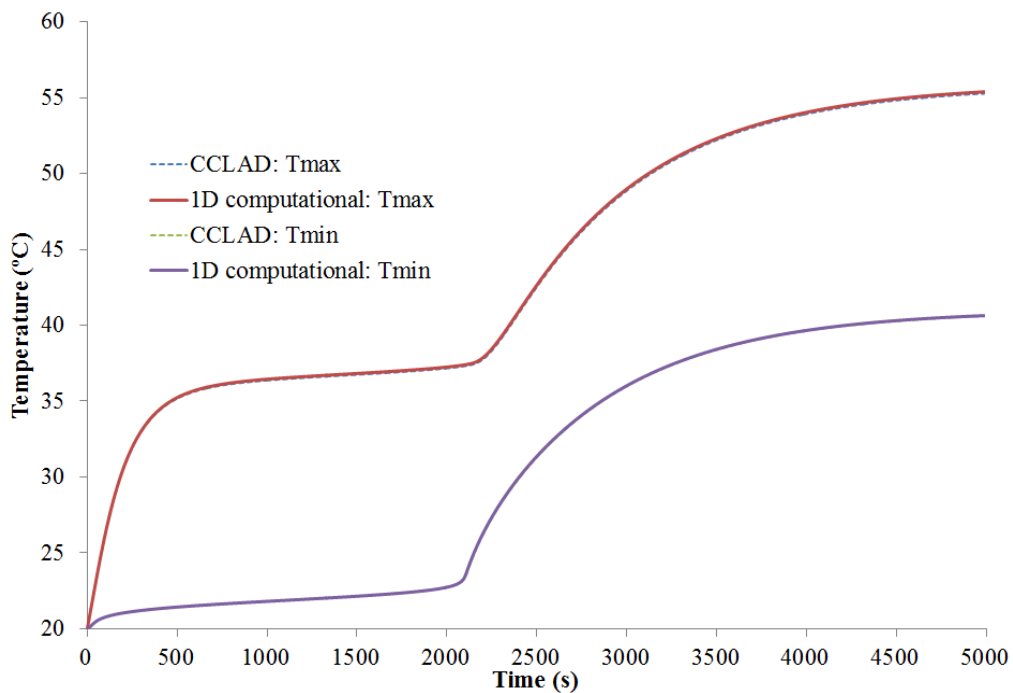
The temperature prediction is tested with a constant power and by taking only into account the specific heat of the PCM/CENG i.e. the latent heat of the PCM fixed at zero ( $l_f = 0$ ).

Fig. 88 presents the results between the CCLAD code, the analytical solution obtained in [66], the 1D computational code and the open-source software SYRTHES4.0. The 1D computational code used 23 nodes and the meshes presented in Fig. 87 were used for both SYRTHES and the CCLAD code. A close match is obtained between the different models, showing the capacity of the CCLAD code to predict accurately the temperature.



**Fig. 88.** Comparison of the maximum and minimum temperatures of the battery cell cooled by PCM/CENG matrix between the CCLAD code, 1D computational model, analytical solution and SYRTHES.

Next, the phase change is added in the CCLAD code and compared to the 1D computational model. The phase change model is added with the latent heat  $l_f \neq 0$  and a constant heat power generation. The CCLAD code is compared to the 1D computational code with the phase change model included.



**Fig. 89.** Comparison between the 1D computational model and the CCLAD code with the addition of the phase change model.

Fig. 89 shows an agreement between the CCLAD code and the 1D computational model for the maximum and minimum temperatures. These results have shown the capability of the CCLAD code to describe the phase change behaviour in the PCM/CENG matrix and its impact on the temperature rise.

The final test is dedicated to the addition of the electrochemistry model in order to describe the heat generation of the battery during different constant discharge rates.

#### 4.3.2. Effects of the electrochemistry

The electrochemistry model described in Chapter 5 is added to both the CCLAD code and 1D computational model. The solid and solution diffusion coefficients are taken constant as well as the ionic conductivity. This hypothesis was made due to the lack of proper correlation [25] and also because the different data used to run the simulations were randomly taken in order to show the capabilities of the CCLAD code and 1D computational model to describe the thermal behaviour of a cylindrical battery cell cooled by a PCM/CENG composite. This simplification will lead to slightly higher temperatures which can ensure a conservative PCM/CENG composite design.

The simulations are performed for 2C, 4C and 8C constant discharge rates with a cut-off condition activated, when the Li-ion concentration on the spherical particle surface of the anode or cathode reaching a certain value fixed by the manufacturer for safety considerations. The comparison of maximum and minimum temperatures between the CCLAD code and the 1D computational code for the 2C, 4C and 8C discharge rates are presented in Figs. 90, 91 and 92 respectively.

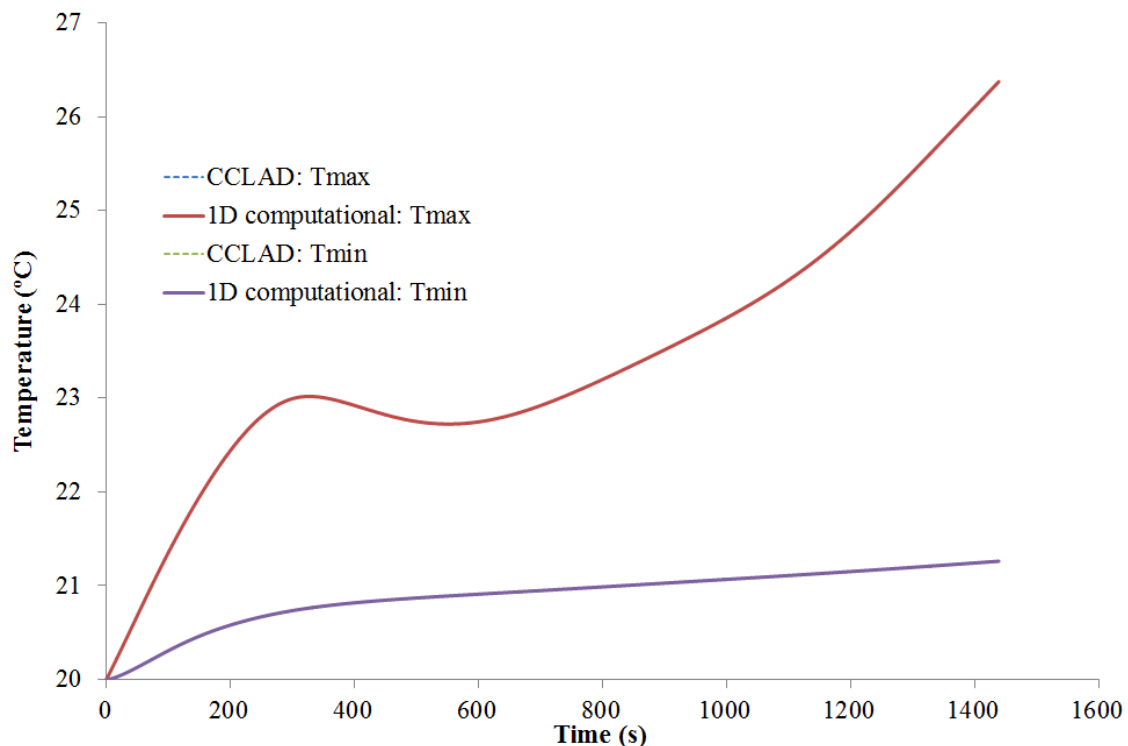


**Fig. 90.** Comparison between the 1D computational model and the CCLAD code with the addition of the electrochemistry model (AM) for the 2C discharge rate.

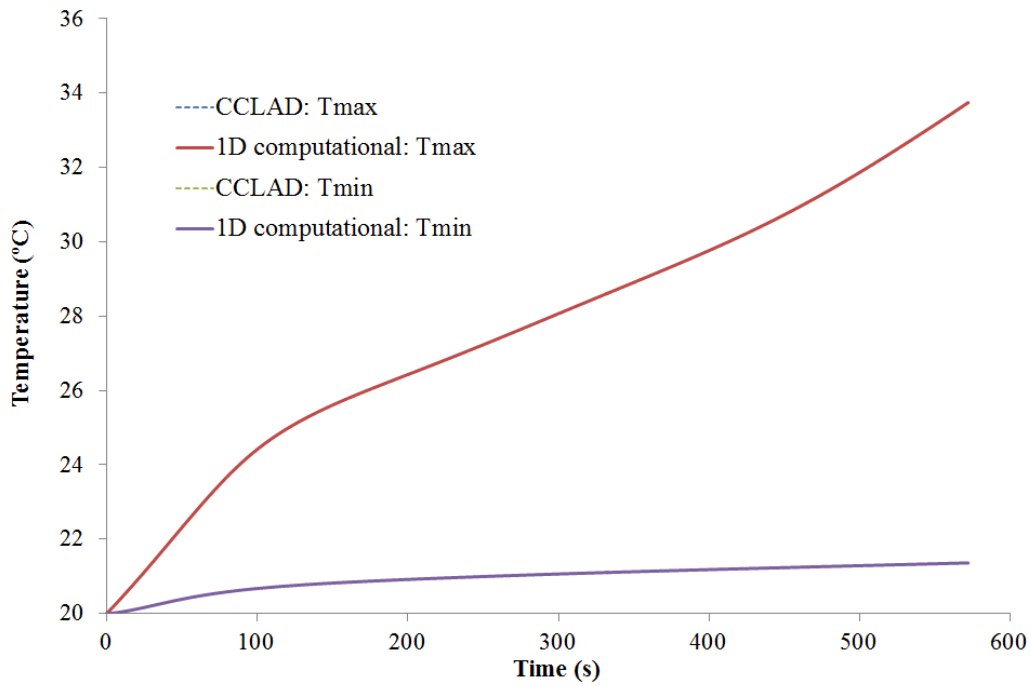


**Fig. 91.** Comparison between the 1D computational model and the CCLAD code with the addition of the electrochemistry model (AM) for the 4C discharge rate.

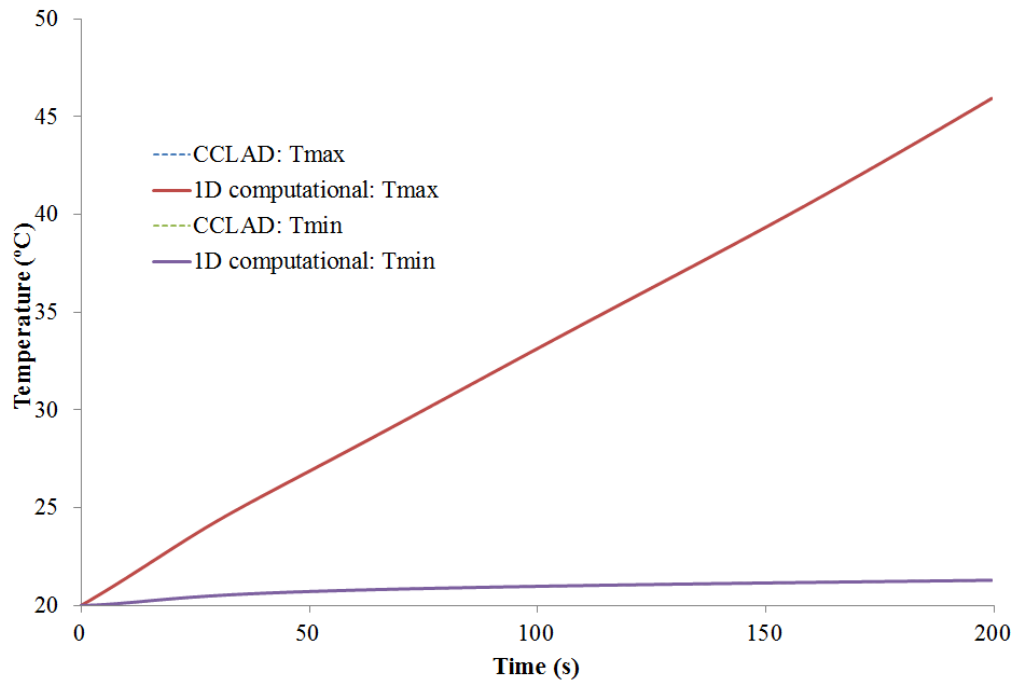


**Fig. 92.** Comparison between the 1D computational model and the CCLAD code with the addition of the electrochemistry model (AM) for the 8C discharge rate.

The number of nodes of the 1D computational is fixed at 103 and the meshes for the CCLAD code are identical to the ones presented in Fig. 87. A close agreement is observed between the 1D computational and the CCLAD code despite the very different approaches used in these codes.

The 1D computational model is based on the configuration symmetries and the anisotropic thermal conductivity of the cell [66]. Therefore, the 1D computational model involves discretisation in the radial direction only, with different nodes connected to each other by thermal conductance calculated from the geometrical and material properties parameters. In

the meantime, the CCLAD code is a 2D cell-centred finite volume code for unstructured meshes. The close agreement obtained between both models despite their different approach, has confirmed the capacity of the CCLAD code to simulate the cooling of battery cell cooled by PCM/graphite composite with a heat generation based on the electrochemistry.

Finally, the impact of the phase change on the temperature rise of the single battery cell is additionally studied. The 1D computational model is only used for this study, since both CCLAD code and 1D computational model had shown identical results for this test case (Figs.90, 91 and 92). For the different discharge rates presented previously, the latent heat is fixed at zero ( $l_f = 0$ ) and the heat generation is still described by the electrochemistry model.

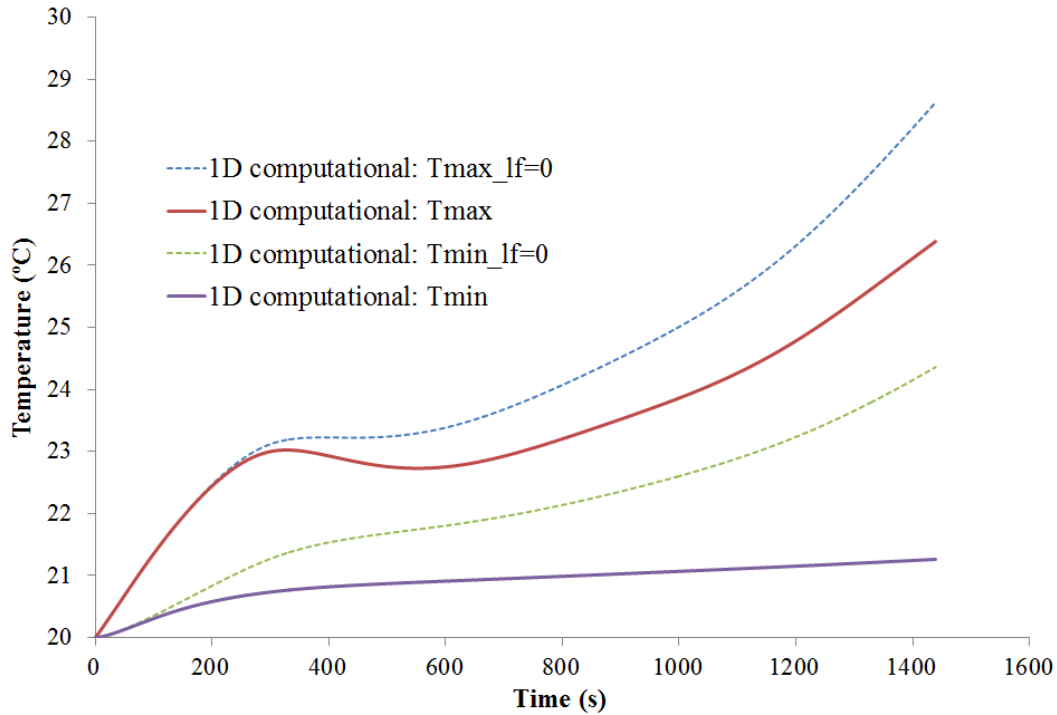


**Fig. 93.** Impact of the enthalpy on the temperature rise for the 2C discharge rate of cylindrical battery cell cooled by a PCM/CENG composite.

Figs. 93, 94 and 95 present the comparison of the temperature rise, where the phase change is taken or not into account, for the 2C, 4C and 8C discharge rate respectively. This comparison highlights the effect of the phase change on the temperature rise. Furthermore, the phase change leads to a variation of the temperature field resulting to a slightly higher gradient of temperature. This variation of the temperature field in the battery cell is caused by the low thermal conductivity and the high cooling effect of the PCM/CENG composite.

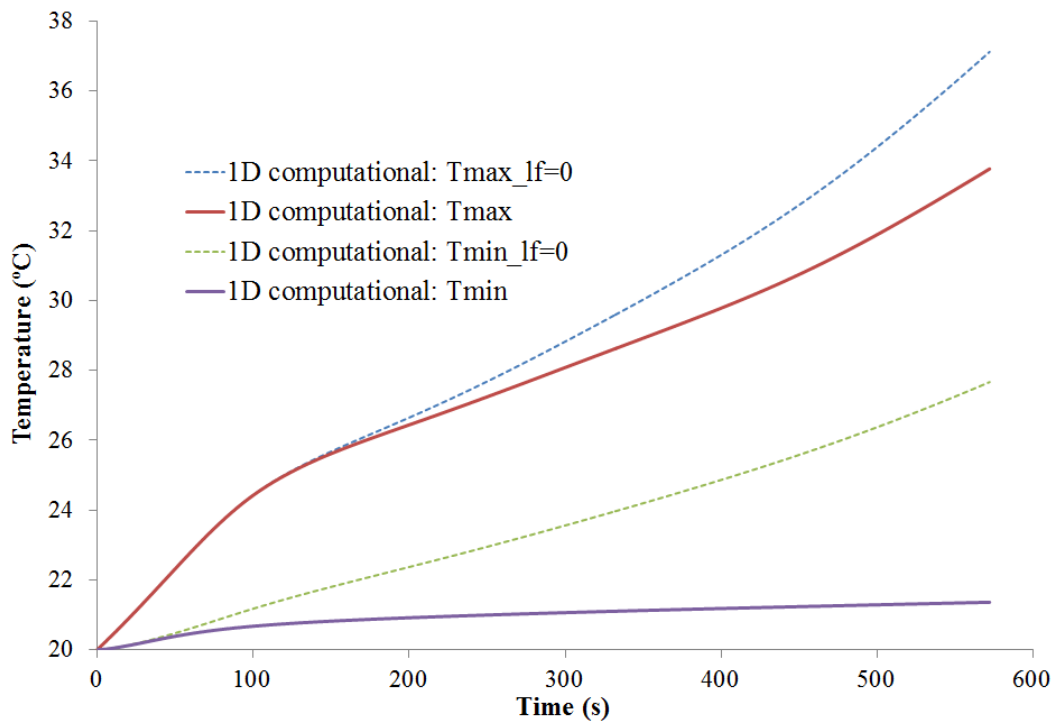


**Fig. 94.** Impact of the enthalpy on the temperature rise for the 4C discharge rate of cylindrical battery cell cooled by a PCM/CENG composite.

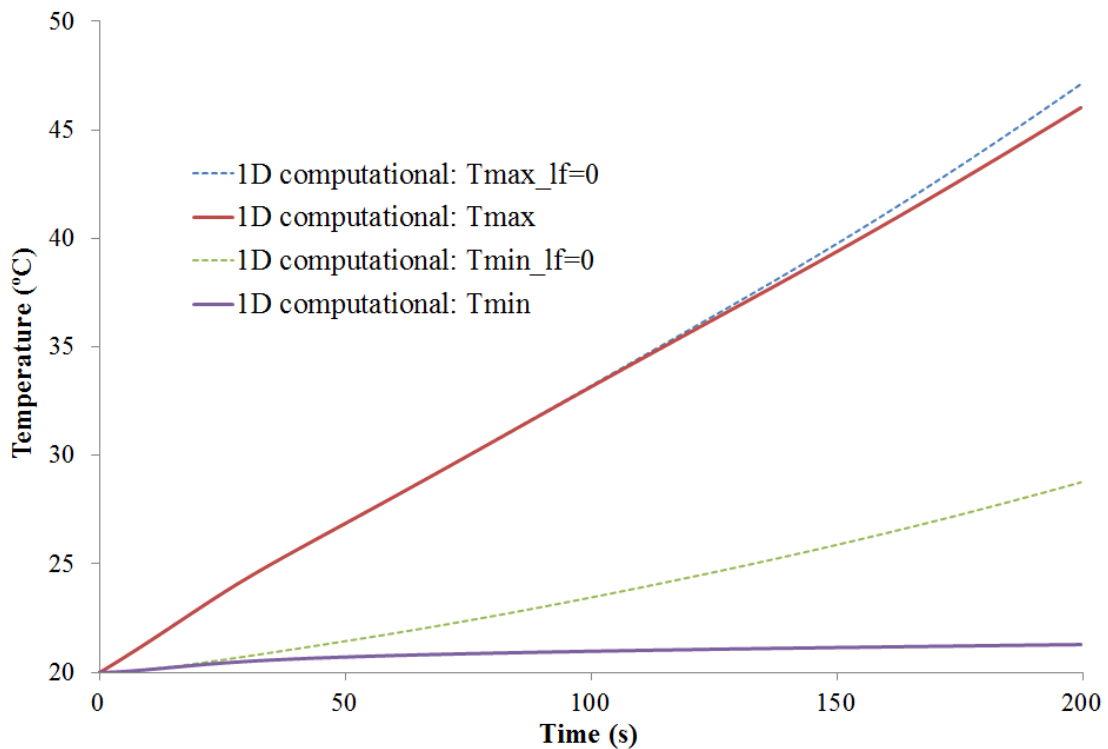


**Fig. 95.** Impact of the enthalpy on the temperature rise for the 8C discharge rate of cylindrical battery cell cooled by a PCM/CENG composite.

At higher discharge rate like the 8C rate, the temperature rise is fast and more noticeable. The low conductivity of the battery does not allow the cooling effect of the PCM/CENG to reach the centre of the battery cell, as fast as the temperature rise. In the meantime, the border of

the cell is directly subject to the cooling effect of the composite, as shown in Fig. 95. It is important to keep in mind that these results can change for different graphite density  $\rho_{CENG}$ , dimensions and PCM type, but the main behaviour will remain the same.

#### **4.4.Conclusion**

The Cell-Centered LAgrian Diffusion mathematical method developed by Maire and Breil [67, 68] was briefly presented in this chapter as well as the modification applied to the boundary conditions. The CCLAD method provides also a high order finite volume cell-centered scheme for unstructured grid. This method was used to develop a code written in PYTHON for the LINUX environment, with the mesh and geometry generated by the open-source software SALOME7.4.

A test case made of a single battery cell cooled by PCM/CENG [66] was proposed in order to compare the CCLAD code to the 1D computational model, analytical and CFD software. The CCLAD code has proven its effectiveness in predicting the temperature behaviour of the cylindrical cell cooled by PCM/CENG composite with, addition of the phase change and an electrochemistry model.

Furthermore, the impact of the phase change was highlighted when an electrochemistry model was used to model the heat generation of the battery. This impact on the temperature prediction will be fully studied in the next chapter with the description of the electrochemistry modelling. After the validation of the CCLAD code on simple test cases, the next chapter will extend the study to a cylindrical battery module cooled by PCM/CENG with the addition of an electrochemistry model.

## **Chapter 5: A coupled thermal and electrochemical study of lithium-ion battery cooled by paraffin/porous-graphite-matrix composite**

### **5.1.Introduction**

Electrical and hybrid electrical vehicles are alternatives in the global effort of reducing the carbon dioxide emissions from the transport sector. Batteries are normally used as the power source for these vehicles, and the high power requirement has made the Li-ion battery the best candidate. However, the performance of Li-ion battery is limited by temperature during the discharge/charge processes, despite its high capacity and energy density. Temperature affects the reliability, safety, and efficiency of the battery. Besides, the temperature uniformity is important in order to avoid thermal runaway and hotspots, leading to short circuit in the battery module [1, 2].

The developments of efficient and reliable cooling solutions were investigated and can be classified into two main categories. In active cooling methods, heat is removed by the movement of a coolant in the battery module. A dedicated pump which uses the energy from the battery in order to move the fluid and the cooling flow is adapted in function of the battery heat generation status, during the driving operation. The systems are usually bulky and require a parallel configuration in order to maintain uniformity between each battery in the module [6, 17]. In addition, studies were performed in order to optimise the flow management system [32, 33] by reducing the pump power, moving the fluid while keeping the cooling efficient.

The other category is dedicated to the passive cooling management of the battery using the phase change phenomenon. Heat pipes based on the liquid/vapour phase change were studied experimentally [35, 36] and theoretically/numerically [55] in battery thermal management. The design of a heat pipe set in the case of prismatic battery cell showed a high level of efficiency [55]. The solid/liquid phase change phenomenon was used in order to reduce the temperature rise of the battery during discharge. Passive cooling material (PCM) showed a good capacity in maintaining the temperature uniformity, despite extreme environmental temperature conditions [43]. However, their low conductivity limits their application [41, 42]. In this context, composite materials made of high conductive material and PCM were investigated in order to study their effectiveness in the thermal management of the discharge process.

Kizilel et al. [47] showed that a composite made of a graphite matrix and PCM was able to bring back the battery module to thermal uniformity after a thermal runaway. However, the equations presented did not consider the effect of the latent heat. The experimental properties of the compressed expanded natural graphite (CENG)/PCM composite [44], were used by Greco et al. [66] with the consideration of the phase change of the PCM, in order to develop a model predicting the thermal behaviour of a cylindrical battery cell cooled by this composite. This model can be used for designing the composite and to predict the temperature at any points in the battery cell. In addition, design parameters were highlighted which can be optimised for achieving maximum cooling effectiveness.

The studies carried out previously considered a constant heat generation source in the battery. This simplification is cost effective in term of thermal cooling design, where the main objective of the cooling process is to maintain the temperature under a certain limit. Sato [69] studied experimentally the thermodynamics of a Li-ion battery and decomposed the heat generated into a reaction heat, polarisation heat and Joule heat. The Joule and polarisation heating was represented by resistances depending only on the state of charge (SOC). The reaction heat due to the chemical reaction during charge or discharge was taken only depending on the SOC. Despite the absence of temperature dependency in the heat generation model, the results were close to the experiment but discrepancies appeared after a SOC of 50%. Nieto et al. [19] simulated the cooling of pouch battery module by cold plates, during charge and discharge from 1C to 3C. The heat generation was represented by the entropy heat and Joule heat, depending both on the SOC and temperature.

Their model agreed well with the experiment at the lower charge/discharge rate (1C) but unsatisfactorily at the higher rate (3C), with a discrepancy of 7%. This solution seems satisfactory for representing the heat generation of the battery at low discharge rates. Nonetheless, this model does not give access to electrical parameters of the battery and their behaviour with the rise of temperature. Therefore, an electrochemistry model of the battery cell has to be introduced in order to describe the electrical parameters and to represent a more realistic behaviour of the battery heat generation during charge/discharge.

Based on the porous electrode and concentrated solution theories, the pseudo two-dimensional (P2D) model was developed by the group of Newman [20, 21]. The model was well validated in galvanostatic discharge (constant discharge rate conditions) and has been widely used. The phase concentration and potential were assumed to vary only in one dimension. The solution domain is taken as continuous and the solid phase is assumed to be composed of identical spherical particles of a predetermined size in the radial direction. The P2D model can give satisfactory results with appropriate calibrations, but it is time consuming for cycling simulation or when used for on-board battery management system applications. This is why Smith and Wang [22] coupled the P2D model with a lumped thermal model in order to explore pulse power limitations and thermal behaviour of a battery pack.

Simplifications were applied to the P2D model and led to the porous electrode model with polynomial approximation (PP) and single particle (SP) models, in order to reduce the computing time. The PP model approximates the solid diffusion with a polynomial function and still takes into account the solution phase diffusion and migration in the electrolyte. The SP model neglects the diffusion in the electrolyte and represents each electrode by a single particle with an area equivalent to the active area of the solid phase described in the P2D model. In addition, the solid diffusion in the SP model is approximated by a parabolic profile. Santhanagopalan et al. [70] compared the three different models at different discharge rates. They observed a close match between the three models at low discharge rates, but larger discrepancy appeared between the P2D (or PP) and SP models at high discharge rates. This difference is mainly due to the absence of solution phase diffusion in the SP model, which has a major impact at high rates.

Moreover, Guo et al. [71] extended the SP model presented by Santhanagopalan et al. [70] with the additions of an energy balance and a solid phase diffusion coefficient depending on the temperature. Their model was validated against the PP model for different galvanostatic

operations at low charge/discharge rates. However, the model does not take into account the diffusion in the electrolyte and may lead to discrepancies at high rates.

Similar to the SP model by considering one particle for each electrode, Prada et al. [25] proposed the average model (AM). However, the AM leads to differential equations with the current density approximation, while the SP model gives algebraic-differential equations. Furthermore, the solid and solution phase diffusion was taken into account in the AM, in order to use the model at high discharge rates. The authors coupled the AM with a lumped thermal model made of one node, in order to observe the impact of the temperature on the electrochemistry and also to predict the temperature behaviour of the battery cell during charge/discharge. They linked the internal node of their lumped model to the skin temperature of the battery cell by considering internal and external thermal resistances for modelling the diffusion in the battery cell and the convection cooling with the environment. The comparison with the experiment for low and high discharge/charge rates showed agreements for the cell voltage. The trend of the transient behaviour of the skin temperatures was in good accordance with experiments, but with small discrepancies for the high rates of charge/discharge (4C and 8C). The higher temperature prediction observed for the high charge/discharge operations may be due to the neglecting of the radiation heat removal and also to the consideration of a lumped thermal model with only one node.

Zhang [72] investigated the thermal analysis of a cylindrical lithium-ion battery by coupling a SP based model for the electrochemistry with a lumped thermal model taking into account convection and radiation heat removal. The solid diffusion of the lithium-ion in the electrode was modelled by a parabolic approximation, and the diffusion of lithium-ion in the electrolyte was included in the model. The diffusion in the electrolyte was solved by a finite volume method, where the concentration of lithium was supposed to follow a second order polynomial function of the coordinate along the thickness direction of the cell components. The comparison between the experiment and the lumped model was in close agreement with 40 °C and 39.43 °C respectively for the skin temperature at a discharge rate of 1.7C (5A). Moreover, the author showed that the lithium-ion gradient concentration in the electrolyte played an important role in the precise determination of the heat generated during charge/discharge operations.

The lumped thermal model is frequently used to model the energy balance when the electrochemistry model is studied with more details. In fact, the coupling of the electrochemistry model with a thermal model remains complex despite the simplifications presented before. The simplification by a lumped model did not take into account the gradient of temperature in the battery cell. This gradient can be important due to the low conductivity of the battery cell in the thickness and radial directions for the prismatic and the cylindrical battery cells respectively. Furthermore, the description of this gradient is important for the design of an efficient battery thermal management system, especially when the design of the cooling system is included in the model.

The one-dimensional (1D) computational model developed by Greco et al. [66] described the temperature behaviour of both battery cell and PCM/CENG with a constant power. However, the constant power assumption poses a severe limitation on its scope of applications. The combined effect of the cylindrical battery cell cooled by a PCM/CENG composite with the additions of the melting process and heat generation described by an electrochemistry model has not been investigated. The present study is motivated by the lack of investigation on the

thermal behaviour of the battery cell when electrochemistry is considered. This analysis will allow studying the performances of both battery cell and PCM/CENG composite in more realistic conditions. The AM [25] was selected as the electrochemistry model due to its simplicity and satisfactory results against experiment at high and low charge/discharge rates. In addition, the solution and solid diffusion of lithium-ion of the AM was replaced by two 1D computational models, validated against analytical solutions.

The aforementioned 1D model was developed for the study of one cylindrical battery cell only and could not be used for simulations of more complex configurations. In consequence, an extension from the one-dimensional model to a multi-dimensional model is performed in order to extend the study of the battery cell cooled by PCM/CENG composite to the battery module scale. The extension was made possible by developing a new code based on the cell-centred Lagrangian diffusion (CCLAD) mathematical method developed by Maire and Breil [67, 68]. This method allows the solution of the thermal equations by a finite volume scheme with anisotropic diffusion on unstructured grids. The phase change model [66] and the modified AM model for the electrochemistry are included in this new code, called CCLAD code for the sake of simplicity. The code is used to compare two different module designs with constant power and power based on the electrochemistry model (AM).

In this chapter, the problem and geometry of a cylindrical battery cell cooled by the PCM/CENG are briefly presented first, followed by the presentation of the electrochemistry model with the description of the modifications applied to it. Next, the analysis of the battery module scale is performed. Comparison is made between the usual and new module designs, with results and discussions subsequently presented. Finally, a summary of the research is presented.

## **5.2. Cylindrical battery cell cooled by a PCM/CENG composite**

A cylindrical battery cell is cooled by PCM/CENG composite, with the battery cell completely surrounded by the cylindrical shape composite. The cylindrical battery cell is represented by a one-dimensional model due to the anisotropic thermal conductivity [13] and the PCM/CENG composite is modelled by one equation due to the thermal equilibrium between the PCM and graphite (CENG). The thermal equilibrium between the PCM and graphite is assured by the large surface contact during the melting process. In addition, experimental correlations were used to calculate the density and conductivity of the composite with the modelling of the phase change by an equivalent thermal capacity [66].

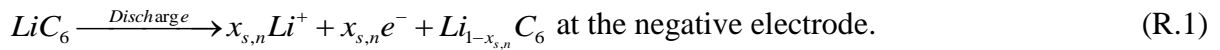
In our previous studies, an analytical solution based on the separation variable technique and a 1D computational model based on the thermal network method were developed [55]. The analytical solution took into account the specific heat of the PCM/CENG composite only, while the 1D computational method included the phase change process [66]. The different hypotheses made in place of the development of the analytical solution and 1D computational model were validated against a 3D model simulated by the open-source software SYRTHES4.0 (software dedicated to transient thermal simulations in complex solid geometries by EDF <http://researchers.edf.com/software/syrthes-44340.html>).

Our previous work considered constant power only, which is not the case for real discharge conditions. In this study, the thermal behaviour of the battery cell cooled by a PCM/CENG coupled with an electrochemistry is investigated in order to predict more realistic behaviours

of the battery during discharge process and the impact on the cooling effectiveness of the PCM/CENG composite. The extension of the model will allow analysing the performances of the PCM/CENG composite at different discharge rates. The next Section is dedicated to the description of the AM and to the modifications applied to it.

### 5.3. Electrochemistry model

A lithium-ion battery with a lithium iron phosphate cathode and graphite anode is considered in this study, as shown in Fig. 96. The chemical reaction for the discharge of the battery is described by the following reactions.



The governing equations and descriptions of the mechanisms during discharge process are presented via the P2D model.

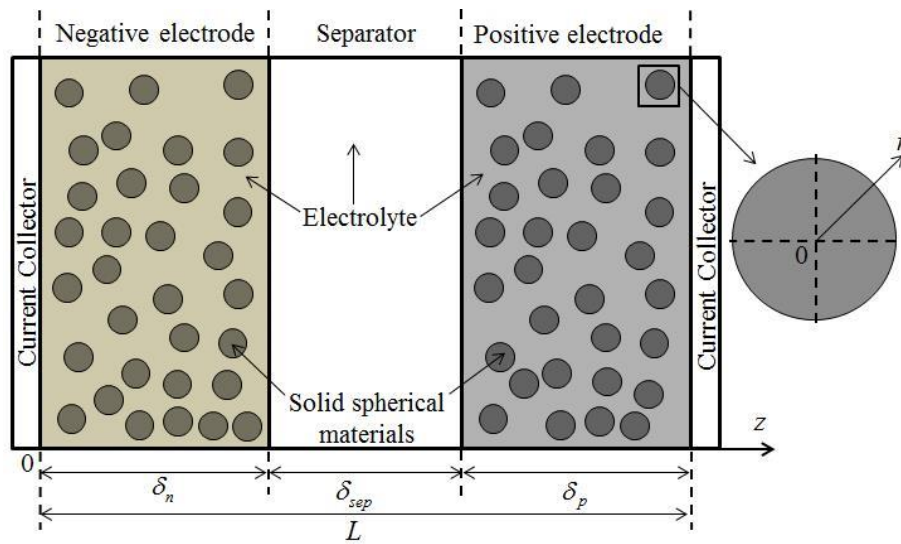


**Fig. 96.** P2D model of the Li-ion battery.

#### 5.3.1. Pseudo two-dimensional model (P2D)

The equations of the P2D model describe the charge conservation and diffusion of species in the solid and electrolyte phases. The conservation of lithium species is represented by:

$$\frac{\partial c_s}{\partial t} = \frac{1}{r^2} \frac{\partial}{\partial r} \left( r^2 D_s \frac{\partial c_s}{\partial r} \right), \quad (5.1)$$

$$\frac{\partial \varepsilon_e c_e}{\partial t} = \frac{\partial}{\partial z} \left( D_e^{eff} \frac{\partial c_e}{\partial z} \right) + (1 - t_+) \frac{j_f}{F}. \quad (5.2)$$

The conservation of charge is represented by the following equations:

$$\frac{\partial}{\partial z} \left( \sigma^{eff} \frac{\partial \phi_s}{\partial z} \right) = j_f, \quad (5.3)$$

$$\frac{\partial}{\partial z} \left( \kappa^{eff} \frac{\partial \phi_e}{\partial z} \right) + \frac{\partial}{\partial z} \left( \kappa_D^{eff} \frac{\partial \ln c_e}{\partial z} \right) + j_f = 0. \quad (5.4)$$

The electrode overpotential and electrochemical kinetics are respectively calculated as follows:

$$\eta = \phi_s - \phi_e - U, \quad (5.5)$$

$$j_f = a_s i_0 \left[ \exp \left( \frac{\alpha_{ox} F}{RT} \eta \right) - \exp \left( -\frac{\alpha_{red} F}{RT} \eta \right) \right], \quad (5.6)$$

with the following boundary conditions:

$$D_s \frac{\partial c_s}{\partial r} (r=0) = 0 \quad ; \quad -D_s \frac{\partial c_s}{\partial r} (r=R_s) = \frac{j_f}{a_s F}, \quad (5.1a)$$

$$\frac{\partial c_e}{\partial z} (r=0) = \frac{\partial c_e}{\partial z} (z=L) = 0, \quad (5.2a)$$

$$-\sigma^{eff} \frac{\partial \phi_s}{\partial z} (r=0) = -\sigma^{eff} \frac{\partial \phi_s}{\partial z} (z=L) = \frac{I}{A}, \quad (5.3a)$$

$$\frac{\partial \phi_s}{\partial z} (r=\delta_n) = \frac{\partial \phi_s}{\partial z} (z=L-\delta_p) = 0, \quad (5.3b)$$

$$\frac{\partial \phi_e}{\partial z} (r=0) = \frac{\partial \phi_e}{\partial z} (z=L) = 0. \quad (5.4a)$$

During the discharge process, the Li-ion is removed from the spherical sites by diffusion at the negative electrode. This diffusion of Li-ions from the centre to the external face, as described by Eq. (5.1), is caused by the current generated during the discharge, as described in Eq. (5.6). The Li-ions removed from the spherical sites at the negative electrode are transferred through the electrolyte by migration and diffusion in order to reach the positive electrode, as described in Eq. (5.2). The separator avoids exchanges between the anode and cathode but lets the Li-ions travel through, in order to reach the spherical site of the positive electrode. A diffusion process occurs at the surface of the sphere from the surface to the centre. This insertion of Li-ion in the spherical site at the cathode is also described by Eq. (5.1), with a change of sign for the boundary condition shown in Eq. (5.1a).

The extraction and insertion of Li-ions at the negative and positive electrode generate electrons in the solid phase, collected by the metallic collectors at  $z=0$  and  $z=L$ . An electric potential in the electrolyte exists due to the transfer of charge in the electrolyte, as shown in Eq. (5.4). It is interesting to notice the conservation of the electric charge by adding Eq. (5.3) and Eq. (5.4). The coupling of this model with a detailed thermal model is time consuming when cycle simulation and/or pack/module level designed are addressed.

### 5.3.2. Average model

In this study, the average model proposed by Prada et al. [25] which was based on simplifications of the P2D model is chosen in order to reduce the computing time. The model has shown agreements with experiments for low and high charge/discharge rates. The AM is

similar to the SP model by neglecting the solid concentration distribution along the electrode and considering the material diffusion inside a representative solid particle. Nevertheless, the AM leads to partial differential equation with the current density approximation while the SP model gives algebraic-differential equations:

$$\int_0^{\delta_n} j_{f,n}(z) dz = \frac{I}{A} = \bar{j}_{f,n} \delta_n, \quad (5.7)$$

$$\int_0^{\delta_p} j_{f,p}(z) dz = -\frac{I}{A} = \bar{j}_{f,p} \delta_p. \quad (5.8)$$

This approximation transforms the equations of the P2D model into simple partial differential equations which are solved subject to the boundary conditions. In consequence, Eq. (5.3) and Eq. (5.4) are integrated for the negative electrode, separator and positive electrode regions with the boundary conditions given in Eq. (5.3a), Eq. (5.3b), and Eq. (5.4a). The solution of these equations led to the following expression of the cell voltage [25]:

$$V_{cell}(x_{s,p}^{surf}, x_{s,n}^{surf}, c_e(0), c_e(L), T) = U_p(x_{s,p}^{surf}) - U_n(x_{s,n}^{surf}) + \frac{2RT}{F} \ln \left( \frac{\xi_p + \sqrt{\xi_p^2 + 1}}{\xi_n + \sqrt{\xi_n^2 + 1}} \right), \quad (5.9)$$

$$+ (1-t^+) \frac{2RT}{F} \ln \left( \frac{c_e(L)}{c_e(0)} \right) - \frac{I}{2A} \left( \frac{\delta_n}{\kappa_n^{eff}} + 2 \frac{\delta_{sep}}{\kappa_{sep}^{eff}} + \frac{\delta_p}{\kappa_p^{eff}} \right)$$

with

$$\kappa_n^{eff} = \kappa (1 - \varepsilon_{f,n} - \varepsilon_{s,n})^{Brugg,n}; \quad \kappa_{sep}^{eff} = \kappa (1 - \varepsilon_{s,sep})^{Brugg,sep}; \quad \kappa_p^{eff} = \kappa (1 - \varepsilon_{f,p} - \varepsilon_{s,p})^{Brugg,p};$$

$$\xi_n = \frac{R_{s,n}}{6\varepsilon_{s,n} i_{0,n} A \delta_n} I; \quad \xi_p = -\frac{R_{s,p}}{6\varepsilon_{s,p} i_{0,p} A \delta_p} I.$$

The parameters  $x_{s,p}^{surf} = c_{s,p}^{surf} / c_{s,p,max}$  and  $x_{s,n}^{surf} = c_{s,n}^{surf} / c_{s,n,max}$  represent the normalised Li-ion concentrations at the surface of the cathode and the anode respectively. Furthermore,  $U_p$  and  $U_n$  designate the equilibrium potential of the LiFePO4 electrode (cathode) [73] and the graphite (anode) respectively [22], which are experiment based correlations depending on the normalized lithium-ion concentrations at the surface of spherical sites. The cell voltage calculation depends on the solid and solution phase diffusion processes with the necessity of providing the concentration of the lithium at the surface of both electrode particles and also the concentration of lithium-ion in the electrolyte at  $z=0$  and  $z=L$ .

As presented before, the addition of the solution diffusion in the electrolyte is really important in order to describe properly the heat generation at high discharge rate [25, 70].

The heat generation is defined as follows:

$$\varphi_{gen} = -I \left( \left( V_{cell} - (U_p(x_{s,p}^s) - U_n(x_{s,n}^s)) \right) + \left( \frac{dU_p}{dT}(x_{s,p}^s) - \frac{dU_n}{dT}(x_{s,n}^s) \right) T \right). \quad (5.10)$$

The intensity  $I$ , is positive for the discharge and negative for the charge. The term  $dU/dT$  is linked to the entropy by  $dU/dT = \Delta S / F$  when only one electron is exchanged. For the sake of simplicity,  $dU/dT$  is called entropy term, with  $dU_p/dT$  and  $dU_n/dT$  [74] designating the

experimental based correlation of the entropy of the cathode and anode respectively, in function of the normalized lithium-ion concentrations at the surface of spherical sites. The coefficients of the polynomial interpolation based on the experimental data of the entropic terms are presented in Appendix D.

Consequently, the calculation of the cell voltage and heat generation implies knowing the concentration of lithium-ion at the surface of the electrode particles, and in the electrolyte. The transformation into simple partial differential equations based on the current density approximation, is used to calculate the Li-ion concentrations in the solid and liquid phases. The determinations of these parameters are performed by resolving the solid and solution diffusion with the nodal network method [55]. The data used to perform the electrochemistry simulation are taken from [25], unless they are stated from other sources.

### 5.3.3. Solid phase diffusion

The nodal network method used to develop the 1D computational thermal model [66] is applied in this case with the lithium concentration representing the nodes, as shown in Fig. 97(a). The conductance of the electrolyte between two nodes is determined by considering the following particle flux between the nodes:

$$\gamma_{i,i+1} = -4\pi D_s r^2 \frac{dc_s}{dr}. \quad (5.11)$$

The integration of Eq. (5.11) with the hypothesis of a constant flux between the nodes  $i$  and  $i+1$  gives the final expression of the electrolyte conductance:

$$c_{s,i} - c_{s,i+1} = \frac{1}{4\pi D_s} \frac{r_{i+1} - r_i}{r_{i+1} r_i} \gamma ; \frac{1}{G_{s,i,i+1}} = \frac{1}{4\pi D_s} \frac{r_{i+1} - r_i}{r_{i+1} r_i}. \quad (5.11a)$$

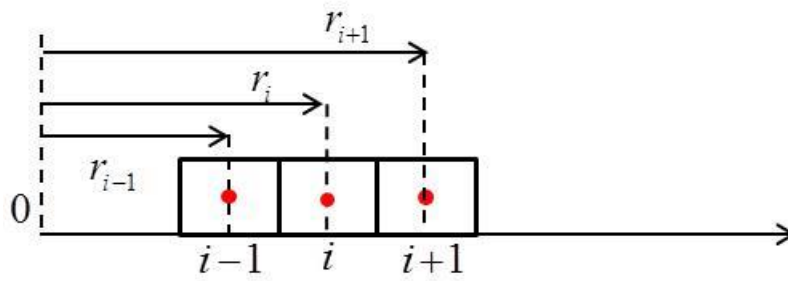
Therefore, each node obeys the following equation from the node  $1$  to  $N-1$ :

$$V_{s,i} \frac{dc_{s,i}}{dt} = G_{s,i,i+1} (c_{s,i+1} - c_{s,i}) + G_{s,i-1,i} (c_{s,i-1} - c_{s,i}). \quad (5.12)$$

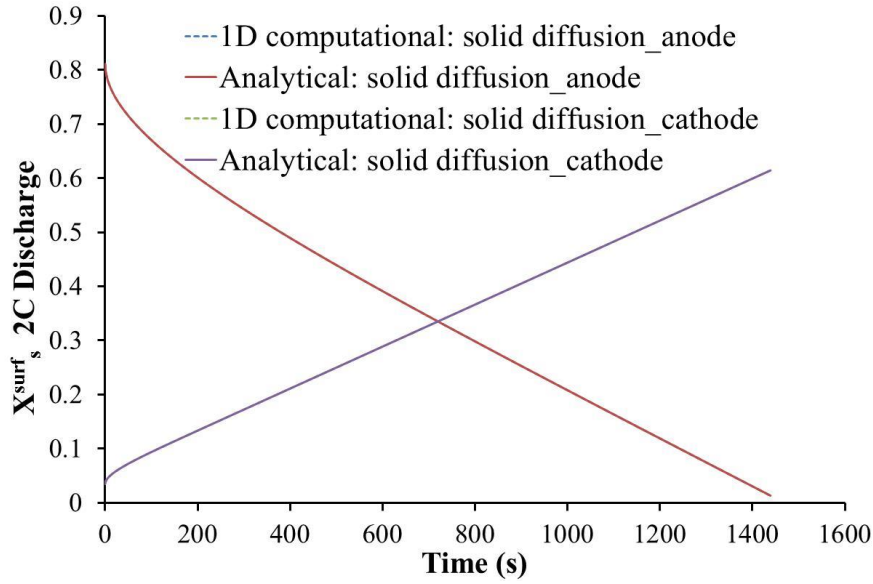
If  $N$  designates the last node, i.e. the node linked to the surface of the spherical particle, the equation becomes:

$$V_{s,N} \frac{dc_{s,N}}{dt} = G_{s,N,N-1} (c_{s,N-1} - c_{s,N}) - 4\pi R_s^2 \frac{\bar{j}_f}{a_s F}. \quad (5.12a)$$

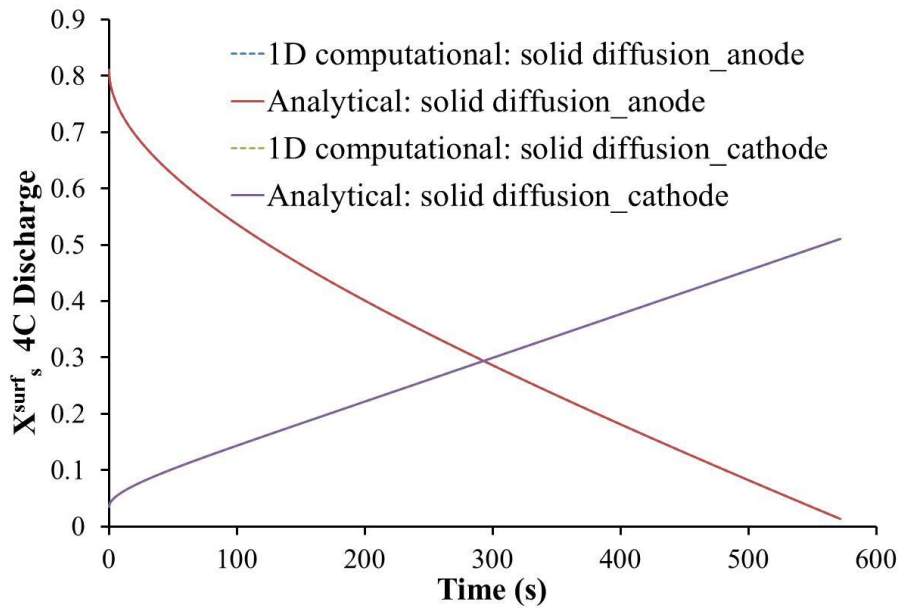
A global matrix system is finally obtained and solved similar to the 1D computational thermal model [66] with an implicit Euler decomposition to perform the transient simulation.



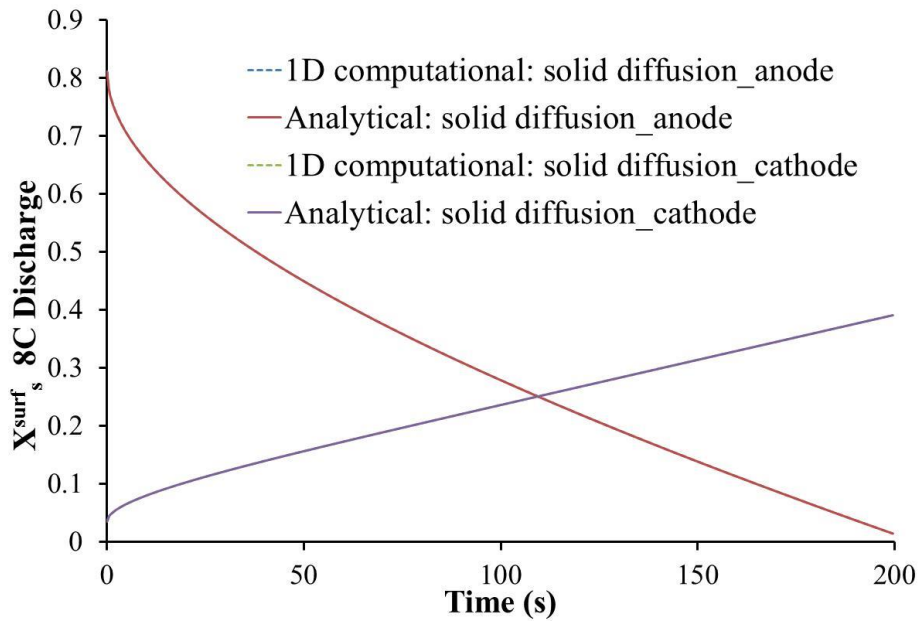
(a)



(b)



(c)



(d)

**Fig. 97.** (a) Spatial discretization of the spherical particle in the solid phase, and the normalised Li-ion concentration at the surface of the electrode particles for the discharge rate of: (b) 2C; (c) 4C; and (d) 8C.

The consideration of constant volumetric heat generation for the battery cell [55, 66] implies that a steady state is reached as function of the cooling solution and battery geometry at the end of the simulation. Nonetheless, the addition of an electrochemical model changes this behaviour by stopping the simulation when the battery voltage reaches a certain cut-off value or a certain concentration at the surface of the electrode. These values are defined by the manufacturer in order to assure better safety and lifespan of the battery. In consequence, the solid phase diffusion plays an important role in the determination of the heat generation (equilibrium voltage, entropy) and the simulation time.

The insertion/extraction process of Li-ions is very complex due to the partial solution regions and difference in capacity restitutions during charge/discharge processes [25]. A shrinking-core model was developed in order to account for the mechanisms with the use of a particle size distribution. However, such an approach is very time consuming and the use of only one equivalent particle per electrode for the AM do not allow its application. Therefore, the radius of the sphere in the solid phase was taken as dependent on the C-rate by Prada et al. [25], in order to account for differences in capacity restitution after extraction/insertion of the Li-ions. This adjustment of the particle sizes was in good accordance with experimental results. Table 11 presents the particle size radius dependencies on the discharge rate with C=2.3Ah.

**Table 11.** Particle size radius in function of the discharge rate [25].

Discharge rate	Positive particle radius [nm]	Negative particle radius [ $\mu\text{m}$ ]
2C	6.9	4.12
4C	6.0	4.0
8C	5.11	3.87

The 1D computational model of the solid diffusion is compared to the analytical solution developed by Subramanian et al. [75], which was obtained for a constant solid diffusion coefficient  $D_s$ . The study is only focused on the discharge operations, and the simulation stopped (the cut-off condition was met) when the normalised Li-ion concentration reaches  $x_{s,n}^{surf} \Big|_{0\%}$  at the surface of the negative particle or  $x_{s,p}^{surf} \Big|_{0\%}$  at the surface of the positive electrode [25].

The comparison between the analytical solution and the particle diffusion model is performed for 2C, 4C and 8C discharge rates. The results presented in Figs. 97(b), 97(c) and 97(d) showed a close match between the models at different discharge rates, supporting the validity of the solid diffusion computational model. In addition, compared to the analytical one, this model is simple to apply and can be implemented with zones based on different solid diffusion coefficient values and/or solid diffusion coefficients depending on the temperature.

The diffusion of the Li-ions in the solution phase is also described and solved with the same method used in the case of the solid diffusion.

#### 5.3.4. Solution phase diffusion

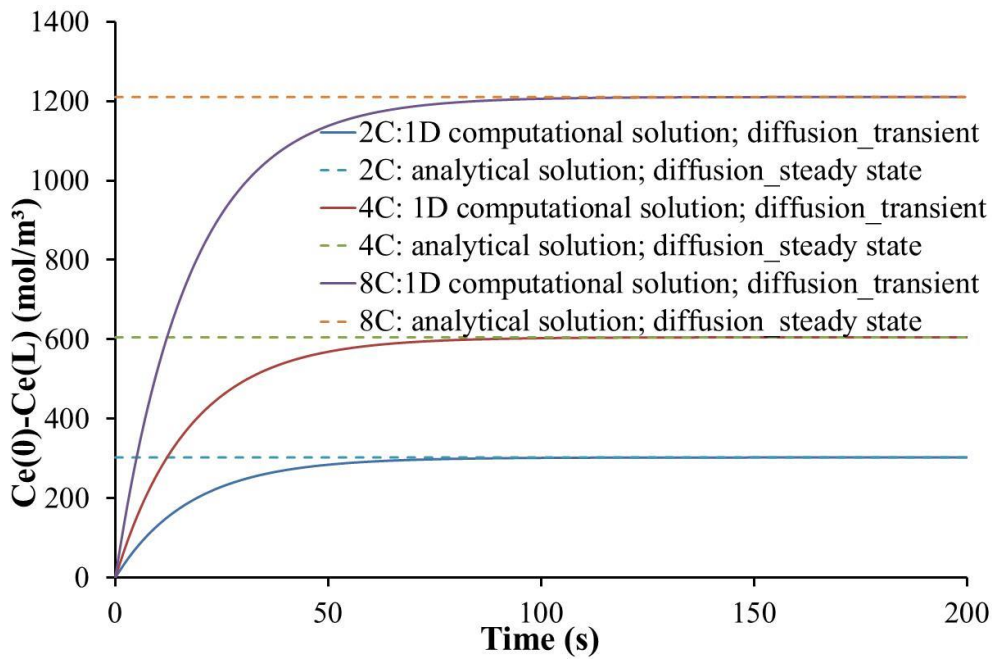
The diffusion of lithium-ions in the electrolyte affects directly the cell voltage and heat generation and has an important impact at high discharge rates. The general equation for each node is presented as follows:

$$\begin{aligned} \varepsilon_{e,k} V_i \frac{dc_{e,i}}{dt} &= G_{e,i,i+1} (c_{e,i+1} - c_{e,i}) + G_{e,i-1,i} (c_{e,i-1} - c_{e,i}) + q_k V_i \\ G_{e,i,i+1} &= \frac{D_{e,k}^{eff} A}{z_{i+1} - z_i} ; q_k = (1 - t_+) \frac{j_{f,k}}{F} ; D_{e,k}^{eff} = D_e \varepsilon_{e,k}^{brugg} \end{aligned} \quad (5.13)$$

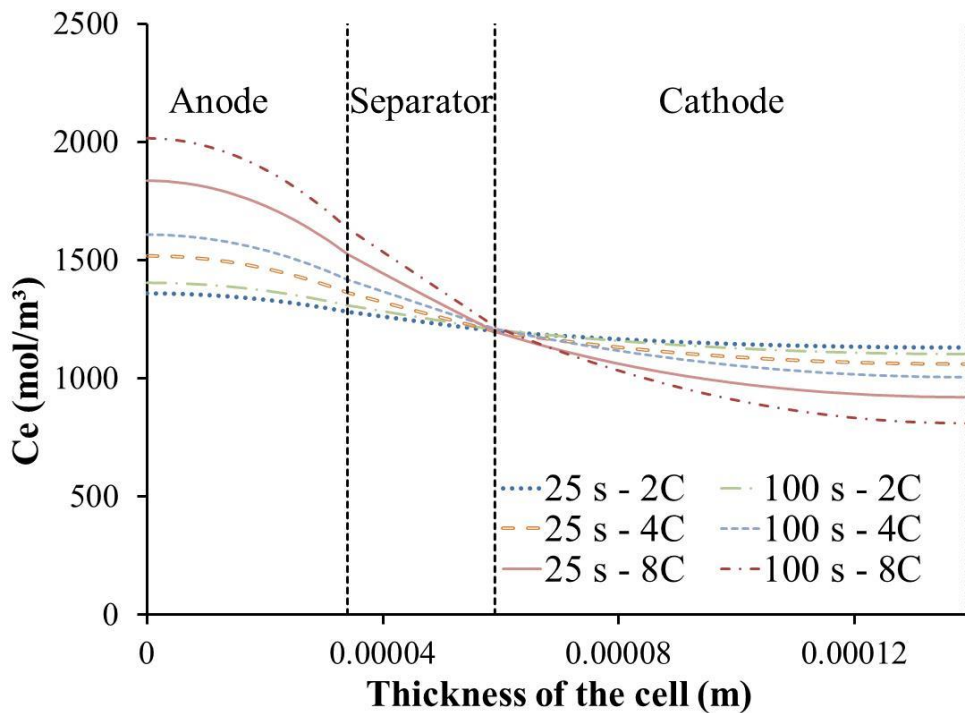
with the subscript  $k$  designating the anode, cathode and separator. A total of 30 nodes were needed to compute the solution phase diffusion, i.e. 10 nodes per zone (separator, negative and positive electrodes). Considering a constant electrolyte diffusion coefficient and an average current density, an analytical solution for the steady state of the solution phase diffusion is obtained as:

$$c_e(0) - c_e(L) = -q_n \delta_n^2 \left( \frac{1}{D_{e,sep}^{eff}} - \frac{1}{2D_{e,n}^{eff}} \right) + q_p \delta_p^2 \left( \frac{1}{D_{e,sep}^{eff}} - \frac{1}{2D_{e,p}^{eff}} \right) - \frac{q_p \delta_p}{D_{e,sep}^{eff}} L. \quad (5.13a)$$

The demonstration of this solution is fully explained in Appendix E. The transient 1D computational electrolyte diffusion model is compared to the analytical solution obtained for the steady state, as shown in Fig. 98(a).



(a)



(b)

**Fig. 98.** (a) Comparison between the transient 1D computational solution diffusion model and the steady state analytical solution for different discharge rates. (b) Solution phase concentration at different discharge rates at t=25s and t=100s.

The agreement between the two models indicates that the solution phase diffusion model and the number of nodes chosen are adequate. The solution concentrations presented in Fig. 98(a) for different discharge rates, are plotted in function of the thickness of the cell at t=25s and t=100s, in Fig. 98(b). The 1D computational solution of the diffusion has shown its capabilities for describing the transient variation of the lithium-ion concentrations in the electrolyte domain.

Furthermore, the solution diffusion model can be implemented with an electrolyte diffusion coefficient depending on the concentration of lithium in the electrolyte and/or the temperature, while the analytical solution describes only the steady state with a constant electrolyte diffusion coefficient for each zone (anode, separator and cathode).

The AM proposed by Prada et al. [25] is modified by the addition of the 1D computational model for the diffusion in the solid and electrolyte phases. Prada et al. [25] used an average constant ionic conductivity based on experimental results due to a lack of experimental correlation for the LiFePO<sub>4</sub> and obtained close results to their experiments. This value is used in this study for all the simulations performed.

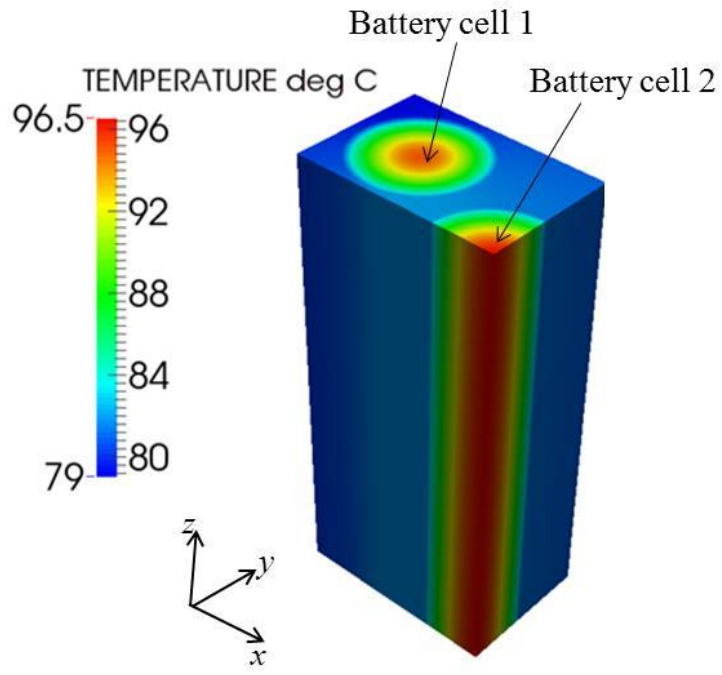
#### 5.4. Analysis of the battery module scale

This section is dedicated to the analysis of the battery module with cylindrical batteries presented. Five identical LiFePO<sub>4</sub> cylindrical batteries of 7 mm radius and 100 mm height are inserted in the PCM/CENG block. The parameters of the PCM/CENG are the same as those used in [66], i.e. a graphite density of  $\rho_{CENG}=200 \text{ kg.m}^{-3}$  and the paraffin heptadecane as the PCM. A convective coefficient of  $20 \text{ W.m}^{-2}.\text{K}^{-1}$  is applied on the external surfaces of the battery module with an ambient temperature fixed at 20°C. Moreover, the surfaces in the height direction (z-direction) are supposed adiabatic due to the low surface of exchange and convective coefficient [66], while the power generation for each battery is taken as constant and fixed at  $240 \text{ kW.m}^{-3}$ . The boundary conditions in the z-direction made it possible to study the half-height of the battery module and the ones applied in the x and y- directions made it possible to consider only a quarter of the block.

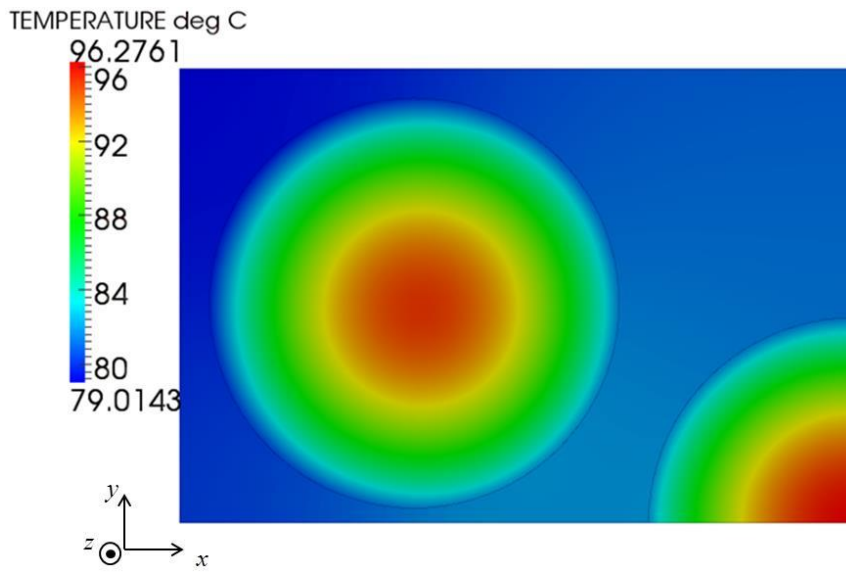
The simulation is performed using SYRTHES4.0 and post-processed using PARAVIEW via SALOME7.4 (software dedicated to build geometry/mesh and post processing of CFD results by EDF <http://researchers.edf.com/software/salome-44339.html>) for the three-dimension (3D) and two-dimensional (2D) simulations. Fig. 99(a) and Fig. 99(b) present the 3D and 2D simulations respectively, of the battery module with the positions of the battery cells.

The maximum temperatures of the battery cells in both 2D and 3D simulation are presented in Fig. 99(c), where  $T_{1,\max 1}$  and  $T_{1,\max 2}$  represent the maximum temperature of the battery cell 1, as shown in Fig. 99(a), located at the bottom ( $z = L_b / 2$ ) and top ( $z = L_b$ ) of the battery cell respectively. An identical notation is applied for battery cell 2 in the 3D simulation and only  $T_{1,\max}$  and  $T_{2,\max}$  are chosen for designating the maximum temperatures of battery cell 1 and cell 2 in the 2D simulation.

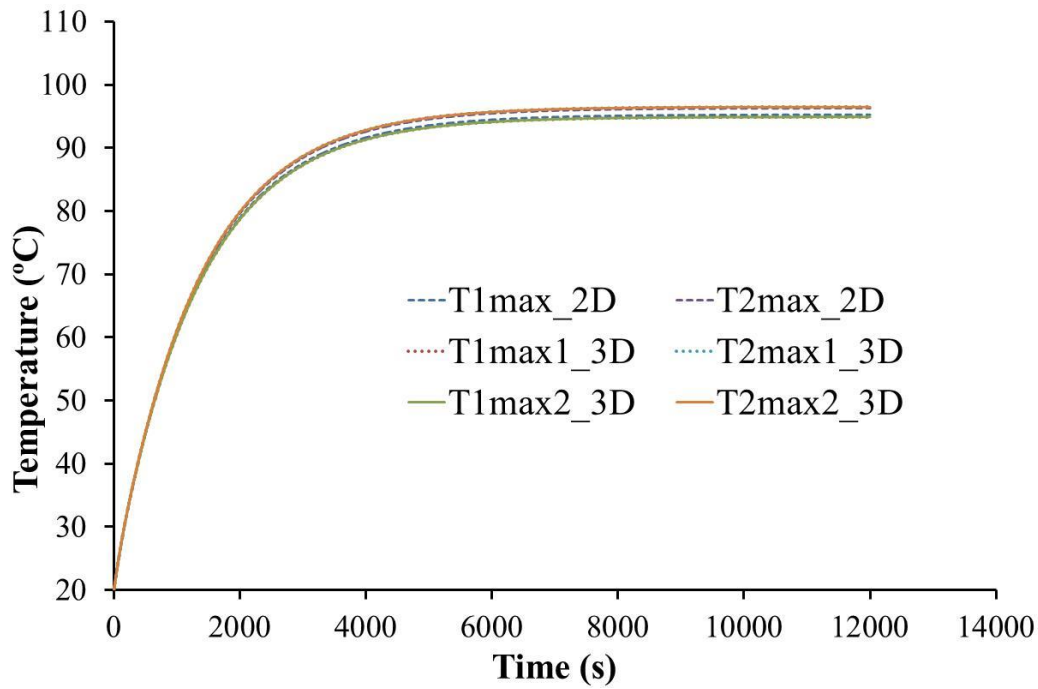
A close match is observed between the 3D simulation at different heights (z-direction) and the 2D simulation. Moreover, the results show that the PCM/CENG matrix is able to maintain the battery cells of the module at a quasi-identical temperature distribution with a maximum temperature difference less than 2 °C and a minimum skin temperature difference less than 3 °C, between the two battery cells. This analysis has shown that a 2D simulation is sufficient to study the behaviour of the battery module embedded in a PCM/CENG block.



(a)



(b)



(c)

**Fig. 99.** Cylindrical battery cells embedded in a PCM/CENG block: (a) 3D simulation; (b) 2D simulation. (c) Comparison between the 2D and 3D results for battery cells 1 and 2.

In this study, a new design is investigated in order to reduce the volume of the PCM/CENG used and also to enhance the cooling by increasing its surface. The design presented in Fig. 100 has a thickness of 2 mm and twelve identical fins integrated into its structure. Each fin has a length of 3 mm and a width of 1 mm, with the final shape of the PCM/CENG matrix supposed to be moulded as described in detail in [44]. It is worth noting that the prescribed minimum and maximum densities of the CENG matrix for such shape have not been analysed/optimised in order to ensure favourable mechanical properties during operations. Despite this technical uncertainty, the new shape is considered and extended to a battery module made of only 4 battery cells. Each battery is surrounded by the PCM/CENG composite with fins and separated from others by thermal insulators in order to ensure the safety of the battery module. In fact, this separation is made for avoiding the propagation of a thermal runaway from a battery to another and also to achieve efficient cooling of each cell in the z-direction as shown in Fig. 100. This parallel cooling distribution [6] is aimed to maintain an even temperature distribution in the battery module.

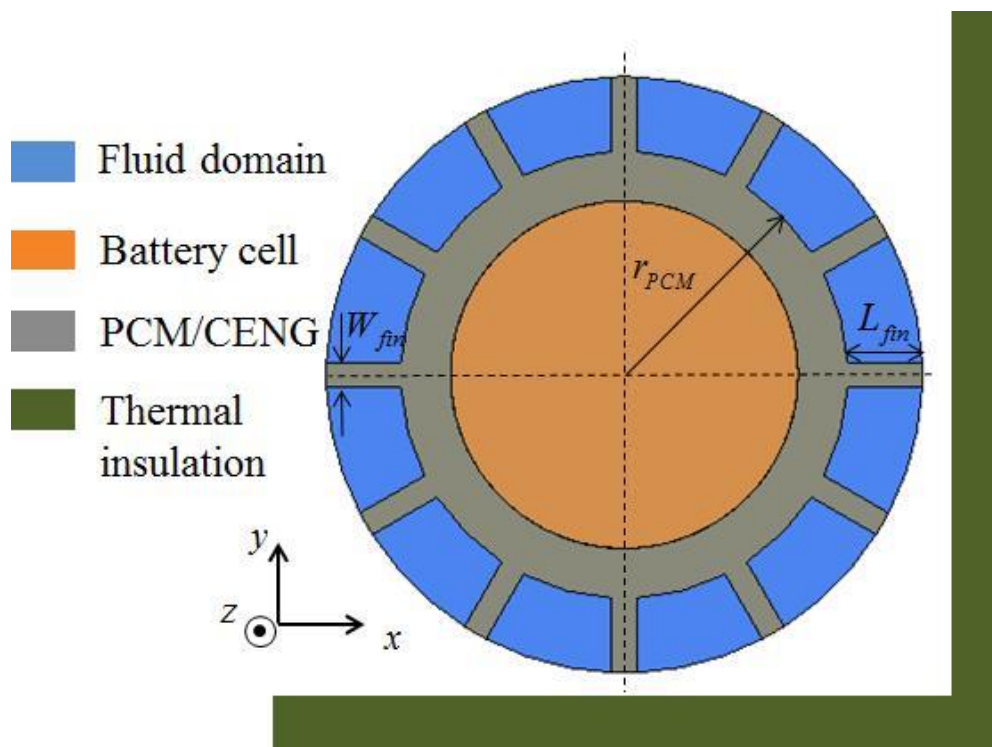


**Fig. 100.** A new design of the battery module: a quarter of the battery module cooled by the PCM/CENG with fins ( $L_{fin}=3\text{ mm}$ ;  $r_{PCM}=9\text{ mm}$ ;  $W_{fin}=1\text{ mm}$ ).

In consequence, only one battery cell cooled by the PCM/CENG with fins needs to be studied since all of them are subject to the same conditions. Moreover, the symmetries allow using the 1D computational code of the battery cell cooled by a PCM/CENG [66] in order to study the thermal behaviour of this new configuration. The fins in the 1D computational model [66] are only modelled in term of cooling surface due to the high conductivity of the composite and the small volume occupied by the fins with regard to the rest of the PCM/CENG structure.

The 1D computational model of the battery cell cooled by a PCM/CENG becomes inadequate for complex geometries and cannot be applied for module or pack studies. The extension of the study to more complex geometries (module/pack designs) with the additions of the phase change and the electrochemistry model (AM) has led to develop a new code based on the CCLAD mathematical method. This method originally developed by Maire and Breil [67, 68] is a finite volume cell-centred scheme for anisotropic diffusion on unstructured grids.

Considering that a 2D simulation is sufficient to study the module design, the code is developed for 2D geometries and unstructured grids. This code will be designated as CCLAD code in the rest of the article and is used to verify the hypothesis concerning the representation of the fins only in term of equivalent convection cooling and also, to investigate and compare two different designs of battery module cooling. These two designs are designated by the usual and new designs, where the cylindrical battery cells in the usual design are inserted in a PCM/CENG composite as presented in Fig. 99(b), and the new design is presented in Fig. 100, i.e. the configuration of PCM/CENG with fins.

### 5.5. Comparison between the new and usual battery module design configurations

The CCLAD code is used to study and compare both the new and usual design configurations presented previously in Section 4. The module in the new and usual configurations is made of four batteries of 7 mm radius and 65 mm height. The volume of the PCM/CENG composite is taken as the same in order to compare the two configurations, where the cooling surface in the new design is 3.7 times of the one in the usual design configuration (Table 12). Due to the symmetries in the x and y-directions, only a quarter of the module is considered for both the new and usual design configurations.

**Table 12.** Surface and volume cooling of the two module designs.

	Usual module design	New module design with fins
surface of cooling [cm <sup>2</sup> ]	83.55	22.55
Volume [cm <sup>3</sup> ]	8.87	8.87

The PCM/CENG composite is identical to the one used before and a convective coefficient of  $20 \text{ W.m}^{-2}.\text{K}^{-1}$  is applied on the cooling surfaces of the module with the ambient temperature fixed at 20°C. The meshes of the usual and new design are presented in Fig. 101(a), Fig. 101(b) and Fig. 101(c) respectively, with the PCM/CENG composite coloured in green and the cylindrical battery cell in orange. Both design configurations are studied with a constant volumetric heat generation of  $240 \text{ kW.m}^{-3}$  and the electrochemistry model (AM).

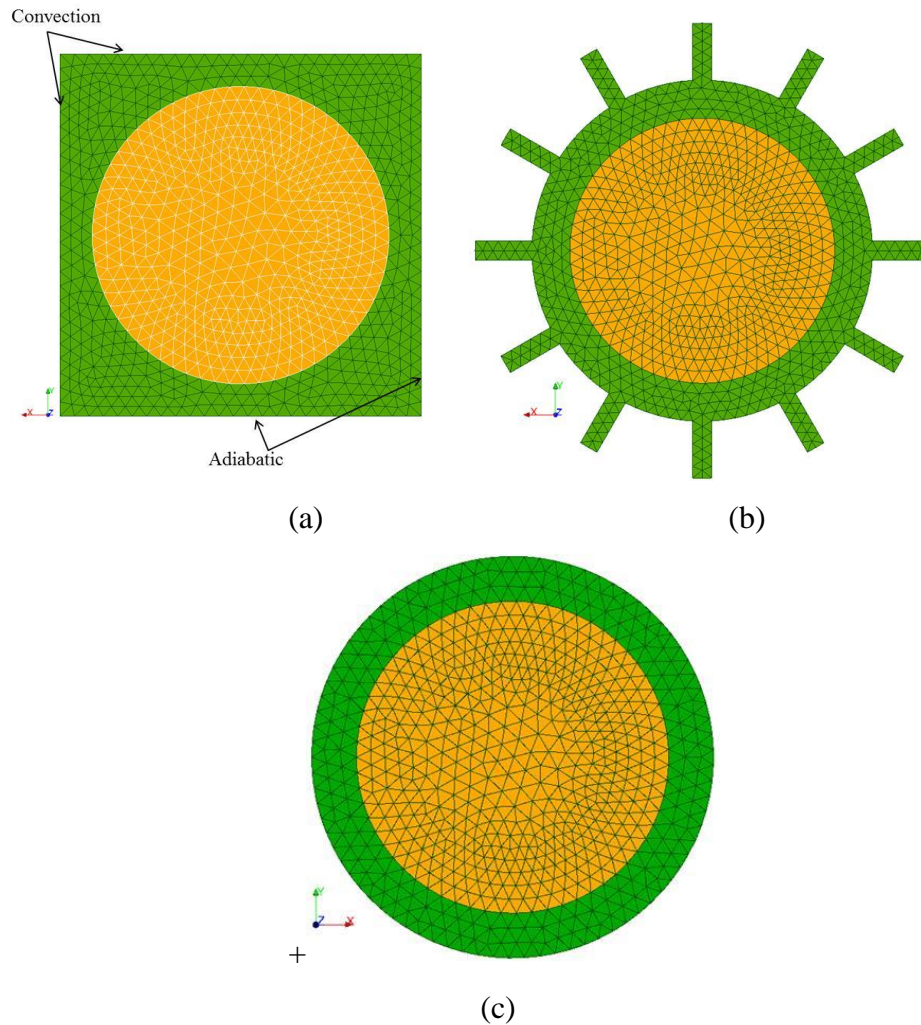


**Fig. 101.** Battery module configurations (a quarter of the domain is shown): (a) the usual design; (b) the new design; and (c) the new design without the fins.

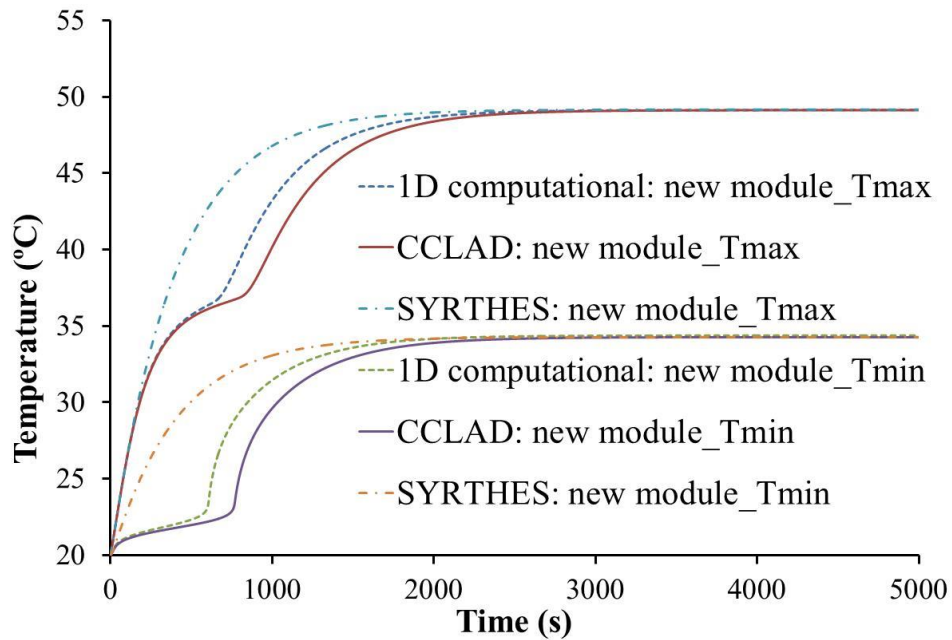
### 5.5.1. Analysis of both configurations with constant heat generation

The configuration (geometry and cooling process) of the new design allows using the 1D computational model, since all the battery cells of the module are subject to the same conditions. It was considered that the fins of the PCM/CENG composite could be modelled only in term of convective effect due to the small volume and high conductivity of the composite. The CCLAD code is used in this case to verify this hypothesis. Besides, a comparison with SYRTHES is performed for both the new and usual designs in order to firstly show the effect of the phase change and finally to verify the temperature at the steady state. In fact, only the specific heat of the PCM/CENG composite is implemented into the open-source code SYRTHES, i.e.  $l_f = 0$ . Both the CCLAD code and 1D computational model are expected to reach the same temperature as that obtained by SYRTHES.

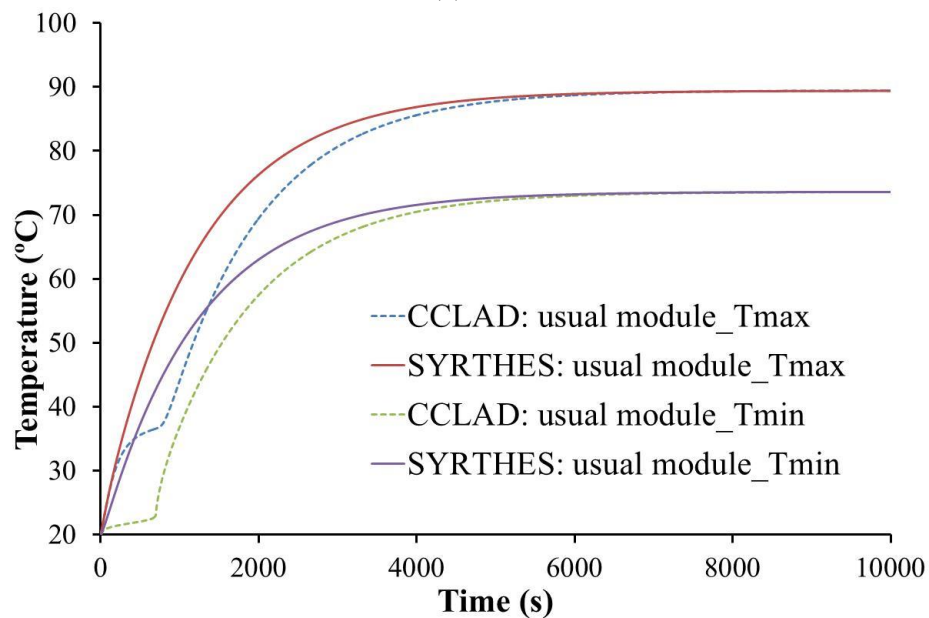
Fig. 102(a) shows the comparison of the results. The 1D computational model is not valid to represent the complete transient thermal behaviour due to the simplification made for the description of the fins. Neglecting the volume of the fins leads to a faster temperature rise

compared to the case when it is modelled by the CCLAD code. Nonetheless, the steady state is identical for all the models/codes, and is confirmed by the comparison with SYRTHES. The usual design configuration is compared to SYRTHES in Fig. 102(b) with a close agreement for the steady state.

The temperature rises for both the new and usual designs are presented in Fig. 102(c) for a constant heat generation. The new design of the PCM/CENG leads to maximum and minimum temperatures of 49.11°C and 34.26 °C, while the usual design points to 89.11 °C and 73.57 °C respectively.



(a)



(b)

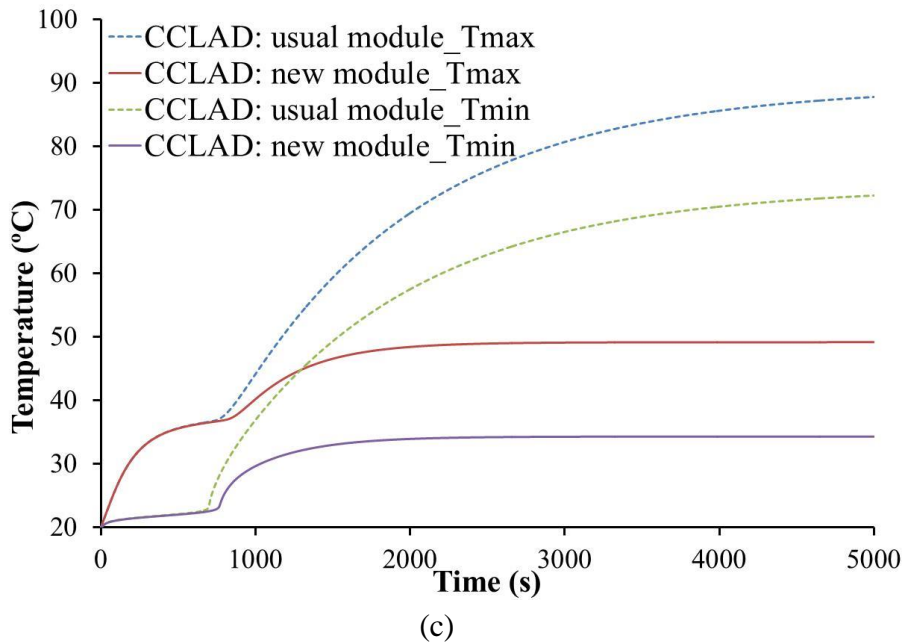


**Fig. 102.** (a) Comparison between SYRTHES, CCLAD code and the 1D computational model for the new design with constant heat generation. (b) Comparison between SYRTHES and CCLAD code for the usual design with constant heat generation. (c) Comparison of the maximum and minimum temperatures with constant heat generation between the new and usual designs.

The comparison between the new and usual design configurations, with a constant heat generation, has shown the superiority of the new design despite an identical volume of PCM/CENG in both configurations. The higher cooling surface obtained by the separation of the cells in the new configuration and the addition of the fins, provide a lower temperature in the module.

The thermal behaviour of both designs is analysed with the addition of the electrochemistry model (AM) subsequently. Moreover, the 1D computational model will only be used to highlight the impact of the fins in the new design configuration.

### 5.5.2. Analysis of both configurations with the electrochemistry model (AM)

The CCLAD code is used to compare the new and usual designs, with the same electrochemistry model and simulation conditions in both cases, i.e. same PCM/CENG configuration and convective coefficient. The 4C and 8C discharge rates are investigated and the positions of the cell monitored for this study are presented in Fig. 103(a).

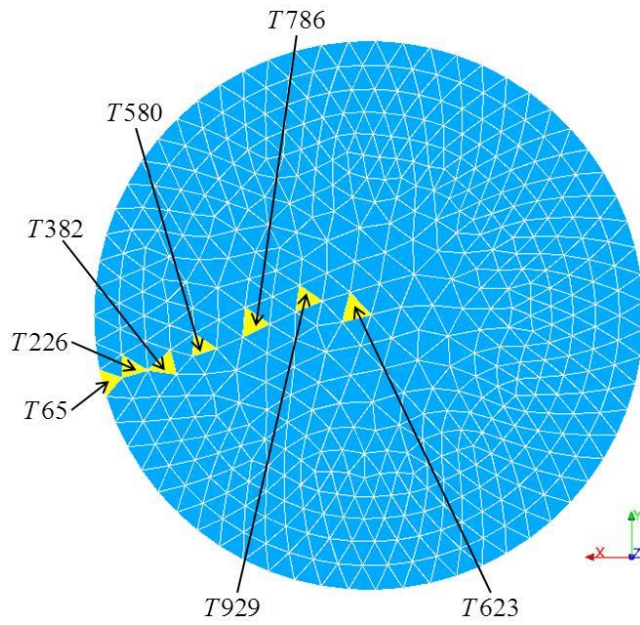
The comparison between the two configurations at different points, presents no major differences in term of temperature as shown in Fig. 103(b). This behaviour is due to the short simulation time, caused by the cut-off conditions and initial capacity of the cell, in which the cooling effects of the fins do not have time to be differentiated from the usual cooling configuration. Besides, it can be seen that a similar behaviour is observed in Fig. 102(c), for

the simulation with constant power, where the two design configurations present no difference until 600 s.

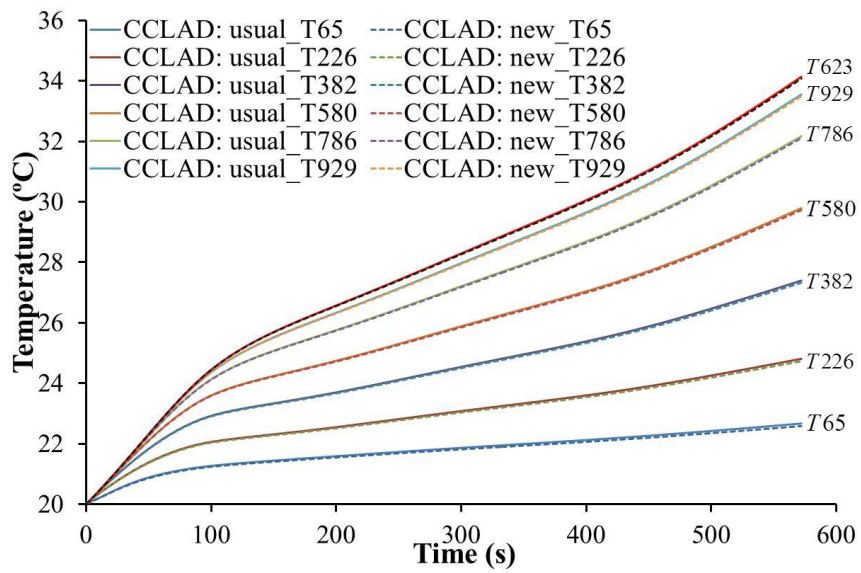
In general, a difference will be clearly seen on a battery with a higher heat generation and longer discharge period. Nevertheless, the 8C discharge rate has a shorter simulation time than the 4C presented before. Therefore, the initial concentration of Li-ion is artificially increased ( $c_{s,n,max} = 60.10^3 \text{ mol.m}^{-3}$  and  $c_{s,p,max} = 40.10^3 \text{ mol.m}^{-3}$ ), compared to the ones used [25] in the previous simulations, in order to have a longer simulation time so that the differences between the two design configurations can be observed. This modification implies an increase of the battery capacity, but the discharge is performed at 8C with C still designating the precious capacity of 2.3Ah [25]. However, the increase of the capacity will imply the increase of the battery size too. Since both the new and usual designs are analyzed under the same electrochemistry and operating conditions, the new design has been proven to be more effective.

Fig. 103(c) presents the results obtained from the increase of the initial Li-ion concentration in the solid phase. As expected, no difference would have been seen if the original Li-ion concentration values were kept [25], with a cut-off condition at around 200 s as shown in Fig. 103(c) by the black vertical broken line. Furthermore, the simulation is long enough in order to observe the difference between the two design configurations, with slower temperature rise and lower temperature in the new design compared to the usual one. The results call for efforts on simulating and testing experimentally more powerful cell with longer discharge time.

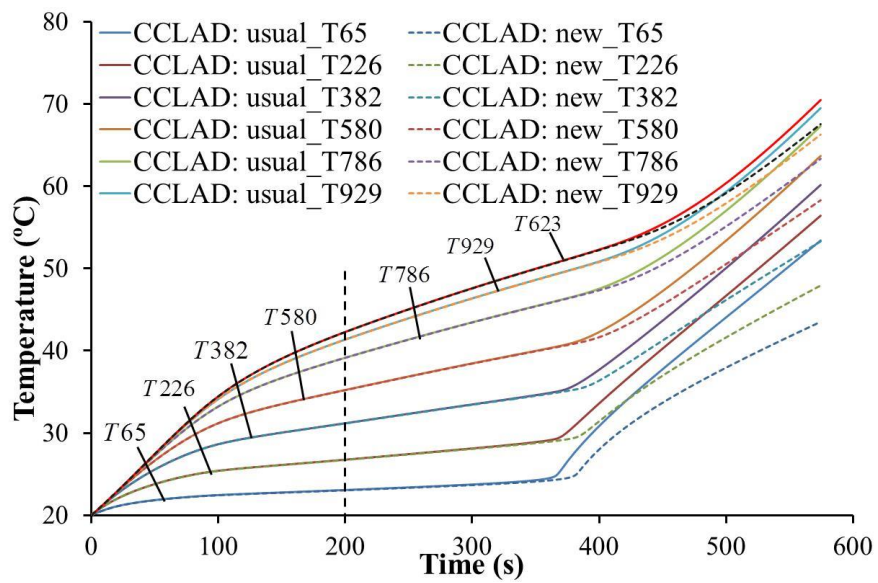
The last simulation is dedicated to the impact of the fins on the temperature rise, with the simulation setup identical to the previous one for the 8C discharge rate. In this pursuance, the fins added on the new design are removed, as presented in Fig. 101(c), with the thickness of the PCM/CENG composite kept at 2 mm.



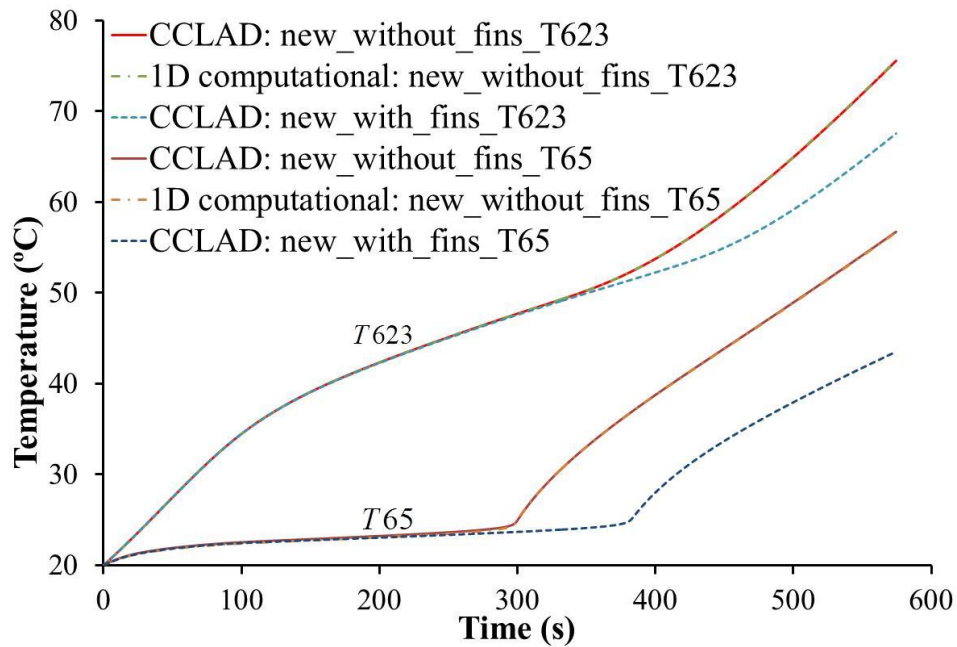
(a)



(b)



(c)



(d)

**Fig. 103.** (a) Positions and names of the monitored cells. Comparisons between the new and usual designs at T65, T226, T382, T580, T786, T929, T623 for the discharge rate of: (b) the 4C; (c) the 8C, with modified  $c_{s,n,max}$  and  $c_{s,p,max}$ . (d) Comparison of the maximum and minimum temperatures for the new design configuration with and without the fins.

Fig. 103(d) shows that the design incorporating the fins leads to maximum and minimum temperatures of 67.55 °C and 43.52 °C, while the one without them leads to 75.57 °C and 56.73 °C respectively. According to this comparison, the impact of the fins is non-negligible on the decrease of the temperature. In addition, the 1D computational model and the CCLAD code are predicting identical results when the geometry does not have the fins, since their impact was modelled in term of cooling effect in the 1D computational model.

The analysis of the cooling impact of both the new and usual designs on the temperature rise for constant heat generation and an electrochemistry model were performed in this Section. The analysis with a constant heat generation, showed the superiority of the new module design configuration compared to the usual one. However, the results are different, when the electrochemistry is included in the simulation. The short simulation time at high discharge rates (4C, 8C) leads to no important differences between the two configurations. In consequence, the initial concentrations of Li-ion were increased for the 8C discharge rate in order to perform a longer simulation, where the differences were clearly seen, with advantageous cooling performances for the new design with the fins. In consequence, the usual design is sufficient to cool the batteries, if the battery module is discharged at a high rate during a very short period of time, i.e. when there is no time for the temperature to be differentiated from the new design module configuration. Besides, the addition of the fins implies extra cost due to the additional manufacture procedure and structural constraints.

## 5.6. Summary

The extension of the cylindrical battery cell cooled by a PCM/CENG composite to a battery module scale was investigated in this study, based on a 1D computational model of a cylindrical battery cell cooled by a PCM/CENG composite [66] in order to predict the temperature behaviour. The thermal and electric prediction of the battery during discharge is very important in order to design an efficient battery thermal management system. The heat generated can be approximated with a reversible and irreversible heat source, based on experimental internal electric resistance and experimental entropy data, depending or not, on the temperature and the SOC [19, 69]. This modelling approach is simple and not time consuming, but limited at high discharge without giving detailed electrical information on the battery. An electrochemistry model has been included in the 1D computational model, where the P2D model is used for describing the electrochemistry of the battery cell.

The complexity of the P2D model does not allow its effective use for battery systems equipped with cooling systems, or on board battery management system. In consequence, the SP and PP models were proposed based on simplification of the P2D model and compared between each other [70], with satisfactory results at low discharge rate and discrepancies at high rate for the SP model. The average model (AM) proposed by Prada et al. [25] includes the diffusion in the electrolyte and showed satisfactory results compared with experiments at very high discharge rates. In this study, the average model was modified by the addition of the nodal network method [55] to describe the solid and solution diffusion of the lithium ions during discharge/charge operations. The model is simply referred to as the 1D computational solid diffusion and solution diffusion model. In the case of constant solid diffusion coefficient, it was in good accordance with the analytical solution developed by Subramanian et al. [75]. Close agreement was obtained between the 1D computational solution diffusion model and the steady state analytical solution.

The AM was included in the 1D computational thermal model [66], but was limited to one cell only. The extension of the model to the module scale was analysed by the comparison between the 3D and 2D simulations of a battery module made of five cells embedded in a PCM/CENG block. These simulations were performed using the open-source software SYRTHES4.0 and showed that a 2D model was sufficient to predict accurately the temperature.

A finite volume code for unstructured meshes, based on the cell-centred Lagrangian diffusion method [67, 68], was developed. Since the module scale was shown to be sufficiently described by a 2D problem, the code was only developed for 2D applications using unstructured meshes, with the additions of the phase change model and the electrochemistry model (AM).

The CCLAD code was used to investigate a battery module made of four batteries, studied in two different configurations and using the same PCM/CENG volume. The first usual design configuration was composed of the cells embedded in a PCM/CENG block, while the second new design configuration was made of a PCM/CENG including twelve fins in its structure. The comparison between the two configurations with a constant power showed the superiority of the new design. However, the addition of the AM revealed a complete different behaviour. No major discrepancies were observed between the two configurations due to the short simulation time. The simulation time is correlated to the solid diffusion in the

electrochemistry model, leading to shorter discharge time at high discharge rate. Accordingly the initial concentration of lithium was increased in order to have a longer simulation. In this case, clear differences were observed between the two configurations and the new design was still superior to the usual one, in term of cooling performances. Nonetheless, this comparison between the new and usual design has shown that, no major differences may be observed at high discharge rates for a short period. In such case, the usual design would be preferred due to its simple manufacturing process compared to the new design. In all the simulations performed, the electrochemical model used entropy and equilibrium potential of the electrodes, based on experimental correlation that can be easily modified in order to match a specific battery.

The last chapter will present an overall conclusion of the PhD work as well as future developments and recommendations concerning the battery thermal management.

## Chapter 6: Conclusions and future recommendations

### 6.1.Introduction

Temperature affects the lifespan, performances, reliability and safety of the batteries during driving operations. In this optic, battery thermal management systems have become essentials and widely studied by engineers and researchers in order to maintain the temperature between 20°C and 40°C. Active cooling management system using flow management systems have been used for years. However, they are bulky and inefficient to maintain temperature uniformity between the battery cells composing the pack at high discharge rate. In fact, these systems use energy from the battery and the cooling requirements increase with the increase of the discharge rate. This PhD work has investigated the numerical and analytical modelling of battery thermal management using passive cooling management. Several experimental study [35, 36, 43] where focused on the passive cooling systems, but not on their modelling and coupling with a battery cell or pack during transient discharge/charge operation. In addition, this work was aimed to provide fast and accurate simulations approaches for battery thermal management in electric vehicles.

The heat pipe cooling of a single prismatic battery cell was investigated first. The battery cell was modelled by a homogeneous body and considered equivalent physical properties. This simplification was validated experimentally and numerically [9, 10, 11, 12]. The Battery cooled by heat pipes was shown to be modelled only by a one dimensional thermal equation due to the anisotropic thermal conductivity of the cell. This anisotropy observed in the thickness direction of the cell [53], is a direct consequence of the internal composition of the battery cell.

An analytical model of this one dimensional problem was presented in order to predict the temperature and behaviour of the battery cell cooled by heat pipes and forced convection. This model was limited in the case of the heat pipe cooling due to the necessity to have a transient description of the internal behaviour of the heat pipe. A second model based on the nodal network method was proposed. This nodal network method [55] is analogical to an electrical circuit problem, where the temperatures are equivalent to electrical potentials and the transfer between each node of temperature is modelled by a thermal resistance.

The nodal model approach for the heat pipe was already tested in literature [38, 39] and was coupled to a nodal network model of the battery. This coupling led to the 1D computational model of the prismatic cell cooled by heat pipes. Besides, the heat generation was taken constant, with the maximum value obtained from experimental tests [53]. This approach was chosen, due to the focus on the cooling system analysis. Despite this conservative configuration and design, the heat pipe was shown to be superior to a forced convection cooling.

The second part was dedicated to the study of a single cylindrical cell cooled by a composite matrix of phase change material (PCM) and compress expanded natural graphite (CENG). This composite was called PCM/CENG for the sake of simplicity and was used in pursuance of a future cylindrical module design. In fact, it is more compact and easier to have one block

of PCM/CENG, where cylindrical cells are inserted. The properties of a cylindrical cell measured experimentally and predicted analytically by Drake et al. [13], has shown a thermal conductivity in the radial direction ten to twenty times lower than the one in the axial direction. This property of the battery coupled to the presence of the highest surface of exchange and cooling in the radial direction has led to consider only a one-dimensional thermal problem located in the radial direction of the cell. This approach was validated experimentally and numerically by Onda et al. [49], Al Hallaj et al. [52] and Zhang [72]. The phase change material alone was not efficient for cooling the battery due to its low thermal conductivity and a conductive material was added with the PCM in order to increase the thermal conductivity. Graphite (CENG) was used in this case to build a matrix where the PCM was injected. This PCM/CENG was shown experimentally by Py et al. [44], to have an anisotropic thermal conductivity independent of the PCM used. Moreover, it was shown experimentally that the convection into the graphite matrix was negligible during the melting of the PCM. The high surface contact between the PCM and the graphite matrix [59] has led to consider only one temperature variable for describing the temperature of the PCM/CENG composite, with equivalent physical properties based on experimental correlations. Finally, the phase change was modelled by a Gaussian distribution. These observations have led to consider a one dimensional problem, where a 1D computational model could be applied to describe the transient variation of temperature.

An analytical solution developed from the mathematical method used in the case of the heat pipe cooling was also applied in this case for a cylindrical geometry. This solution used only the specific heat of the PCM/CENG composite and a constant generation. The 1D computational model was able to take into account the phase change and was incorporated in a FORTRAN code for the simulation and a PYTHON code for the post processing. The code was used to identify the graphite density of the matrix as an important parameter for the thermal efficiency. The PCM/CENG was shown to be promising in the cooling of cylindrical Li-ions battery cell compared to forced cooling convection.

An electrical vehicle is equipped of more than a single cell and the heat generation is not constant during discharge, but driven by an electrochemistry reaction. The numerical and analytical models presented before were only dedicated to a single cell analysis, with limited possibility of extension to a battery module analysis. In this optic a new numerical model was developed using a finite volume method for unstructured based on the cell-centered lagrangian diffusion (CCLAD) mathematical model developed by Breil and Maire. This numerical model was aimed to extend the study of a single battery cell to a module or pack with the possibility of using any geometry. In fact, the geometry and mesh were generated automatically with the open-source software SALOME7.4 and the mesh file was exported to the new model as a “.dat” file.

A CFD analysis of the battery module has shown that a two-dimensional resolution was sufficient to describe the cooling of cylindrical battery inserted in a PCM/CENG matrix. This observation has led to develop a two-dimensional finite volume code for unstructured mesh, called simply CCLAD code. The phase change model developed before was implemented as well as an electrochemistry model in order to have a better accuracy in the temperature and for optimizing the PCM/CENG design. The average model (AM) developed by Prada et al. [25] was preferred to the Pseudo Two-Dimensional developed by the team of Newman [20,

21]. The AM model was time-effective and validated against experimental test at very high discharge rate. The model was modified by the addition of two 1D computational models describing the solution and solid diffusion of the Li-ions during discharge. These 1D computational models were validated against analytical solutions based on constant diffusion coefficient. In addition, experimental diffusion coefficient or temperature based coefficient could be easily implemented in these 1D computational models.

The CCLAD code was used to investigate a different design of cylindrical battery module. This different design was designated by new design, while the usual design designated the PCM/CENG composite block with cylindrical battery cell embedded into it. The new design was made for reducing the quantity of PCM/CENG used and for increasing the surface of cooling. Besides, the parallel configuration used in this new design ensured an identical temperature distribution for the battery cell composing the module, while the usual design may not achieved this goal with a larger number of battery cells. The new design investigated in this study was superior to the usual design, when using constant power and power generation based on the electrochemistry model. Nevertheless, the difference between both designs may not be important when the simulation time is very small at high discharge rate. In fact it was demonstrated that both design did not have time to be differentiated from one to another due to the short simulation time and thermal inertia caused by an identical volume in both designs.

The CCLAD code was only developed for two-dimensional problem and its extension to a three-dimensional parallel code with different electrochemistry models [15, 20, 21, 25] will be investigated. A better mathematical modelling of the heat pipes will be studied as well as their integration to a larger battery module, with the insertion of variable discharge rate conditions. This mathematical model is aimed to have better information about the pressure and velocity in the heat pipes. Finally, the developments of optimization tool for simulating the cooling of large battery pack are proposed.

## **6.2.Heat Pipe Modelling**

The thermal network model of the heat pipe may be further studied experimentally in order to verify the impact of the approximations and hypotheses made in following-on researches. Experimental data of the battery cell will allow the addition of a heat generation term depending on time in the cooling system model (numerical and analytical). Therefore, a future study will target the thermal behaviour of the battery during practical driving scenarios. Such scenarios are already available in literature and were monitored from real test driving [51].

However, the working fluid (ammonia) used in the heat pipe design presented in chapter 2 may not be suitable for automotive industry. In fact a high pressure would be expected in the heat pipe at high temperature and could strongly disturb its proper functioning. The modelling of the pressure in the heat pipe will need to be addressed in the next iteration with water as the working fluid.

The final goal will be to extend the heat pipe cooling to a prismatic battery module and pack. However the preliminary design presented in Fig. 104 is not viable for automotive industry

due to its mass. In addition, the large number of battery cells composing a battery pack would have made the global cost of the vehicle too important. A new design will be investigated using flat heat pipe in order to cover the surface of the battery but also for reducing the number of heat pipe used.

Therefore, a new analytical development may be explored in order to improve the previous analytical model developed by Greco et al. [55] and study carefully the battery module scale.

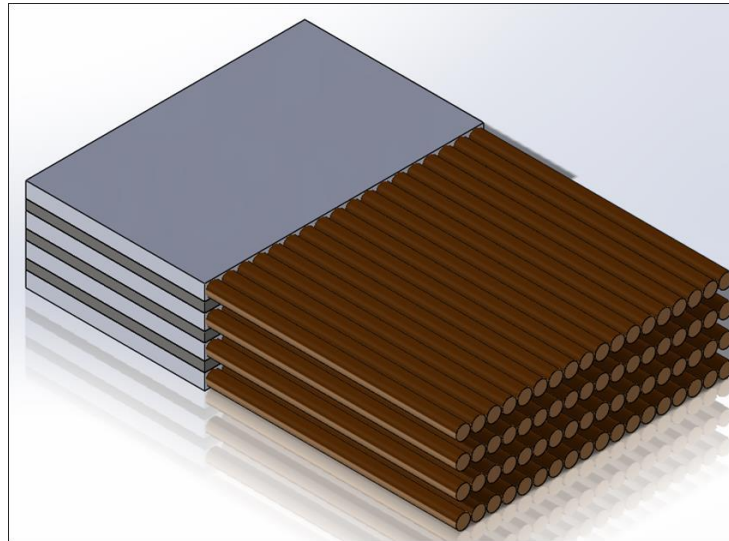


**Fig. 104.** Prismatic battery module cooled by heat pipe sets.

In this optic, Lips and Lefevre [76] developed a 3D analytical model for the temperature couple to a 2D pressure and velocity fields. The solution developed can be employed for cylindrical shape heat pipe or flat heat pipe. Their model can be used to determine a thermal resistance and the different limit of the heat pipe. Besides, the prediction of heat pipes performance in function of the capillarity structure is possible.

The 3D analytical model of the wall temperature of the heat pipe was based on the Fourier expansion. This expansion, to be applied, needs certain symmetries (created by the boundary condition). Two configurations of flat heat pipe were considered with different surface of capillary structure and a last configuration for a cylindrical shape heat pipe.

Firstly, the geometry of each heat pipe in the different consideration was geometrically transformed depending of the position and surface of the capillary structure (Fig. 105(b)). This first transformation had defined an upper plate and lower plate linked in certain way also depending on the capillary structure position. Finally, the wall geometries obtained previously were transformed to have a non-dimensional domain for applying the Fourier expansion. The fluid and pressure fields are obtained using the Darcy's law, necessitating the determination of the permeability coefficient. This coefficient was also calculated by Greco et al. [55] using the same method in order to determine the capillarity limit. Contrary to the model used by Greco et al. [55], Lips and Lefevre [76] considered the conduction in the entire heat pipe wall.

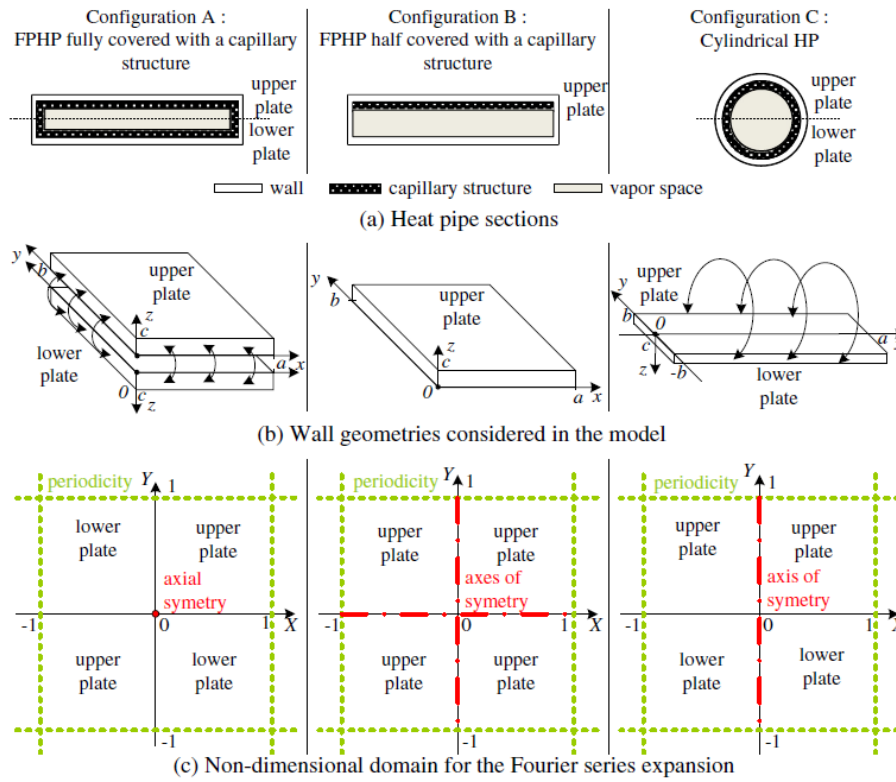


**Fig. 105.** Geometries and corresponding domains for three heat pipe configurations [76].

However, the solutions were obtained for heat source and heat sink applied directly to the surface of the heat pipe, with the necessity of homogenous boundary conditions and thermal equation. In fact, in the case of a battery cell modelling, the thermal equation is non-homogeneous due to the volumetric heat generation rate. Nonetheless, their approach can be used to have a better modelling at the contact between the battery cell and the heat pipe, especially in the case of flat heat pipe. In addition, the domain transformation used by the author [76] allows a remarkable simplification of the geometry in order to apply the Fourier expansion.

Besides, the development of a model using flat heat pipes coupled with prismatic battery cell may be investigated based on the previous work presented [55,76]. A mixing of heat pipe and PCM/graphite composite may be considered in order to improve the cooling efficiency of a battery module.

The next paragraph will present the ongoing development of the PCM/graphite cooling.

### 6.3.CCLAD code

The CCLAD code was presented in the previous chapter and had shown capabilities for simulating the cooling of a cylindrical battery cell module. To further develop and validate the model presented in Chapter 5, experimental studies will be valuable. A more powerful battery with longer discharge time could be useful in order to have more information on the new design with the fins.

Additionally, the CCLAD code as a first prototype is much slower than the 1D computational model for battery cell simulations. A parallelization of the CCLAD code and its extension to

3D unstructured meshes may be considered. Hybridisation of the CCLAD method and the 1D computational model may also be investigated in order to build a powerful design tool for the PCM/CENG design.

The geometry of the battery cells studied in this thesis was idealised, by considering homogeneous shape. The description of the battery cell with a cylinder or a prismatic shape was validated against numerical and experimental study. However at very high discharge rate, a resistance at the connection between the wire and the battery cell is observed and may have an impact on the temperature distribution [77]. This resistance is sometime estimated or modelled based on experimental results.

The influence of this contact resistance may be investigated on a single cylindrical battery with the current version of the CCLAD code in a forced convection cooling and PCM/CENG cooling. In fact, the symmetry of the simulation allows modelling only a slice of the cell in the height-direction, similarly to the test case treated in Fig. 69.

In parallel to this study, the CCLAD code may be upgraded to a three-dimensional version with the addition of a the P2D model for the electrochemistry. The P2D model may be similarly modelled like the solid/solution diffusion in the AM model, with the nodal network, which was proven to be fast and simple to implement. Besides, this approach was well validated against analytical solution. Furthermore, analytical modelling of heat pipes will be only possible in the light of certain simplifications and compromises, due to the multiplicity of phenomena. In consequence, the additions of a solver for the fluid and biphasic fluid transport are considered, in order to model properly the heat pipe cooling of a battery cell.

It is also important to notice that the CENG density used in the Chapter 5 was fixed at the optimum value obtained in [66] for the study. This parameter was shown to be very important in the development of an efficient PCM/CENG composite. A development of an automatic method to determine the optimised CENG density value of a larger battery module/pack, in function of the convective heat, the electrochemistry model and the geometry will also be explored.

## **6.4. Optimization of BTMS**

This part will present some perspective in the optimization of active cooling and method for analysing large system configuration.

### *6.4.1. Active cooling*

The optimization of an active cooling system require to find a compromise between cooling efficiency (maximum temperature and temperature uniformity ) and the pump specifications, since the latter one drawn power from the battery. The studies performed by Jarret and Kim [32, 33] had shown the difficulty of finding a global optimum when off-design conditions were applied. In fact, the optimized serpentine geometry was found to be less effective at off-

design conditions. Moreover, the computation resources needed, can be an obstacle for the development of this method.

A study using the open-source software CODE SATURNE3.0.3 and SYRTHES4.1, both developed by EDF, was performed in order to have an optimum design close to the global one and therefore reducing at the same time the computation time of the CFD tool. Fig. 106 presents the schematic of the coupling between the different open-source software cited before.

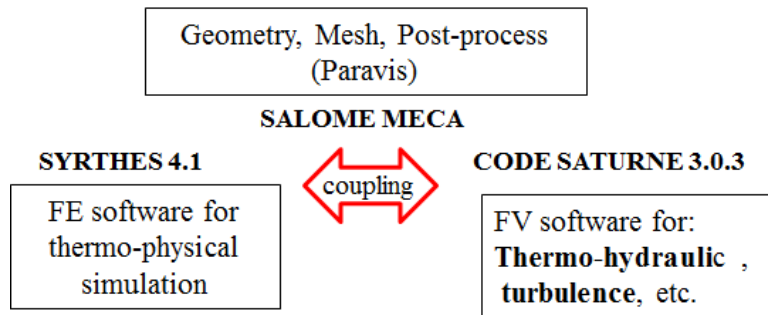


**Fig. 106.** Schematic of the coupling between the thermal and fluid dynamic software.

The test was performed on a random serpentine channel design close to the one used by Jarret and Kim [32, 33] and presented in Fig. 107. The geometry and mesh were written in a PYTHON script, which could be read by SALOME7.4. The coupling between these codes was used to test the analytical model developed to determine the maximum temperature at the surface of the battery cell.

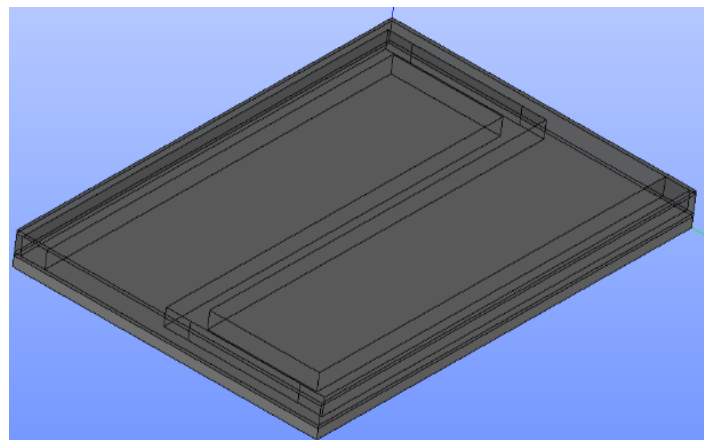


**Fig. 107.** Geometry generated in SALOME7.4 with a python script.

The simulation was performed using a constant heat generation for the battery cell (Fig. 108) and compared to the analytical model which only considered an average surface. The discrepancy between the CFD result and the analytical model was important as shown in Fig. 109, for the maximum temperature.

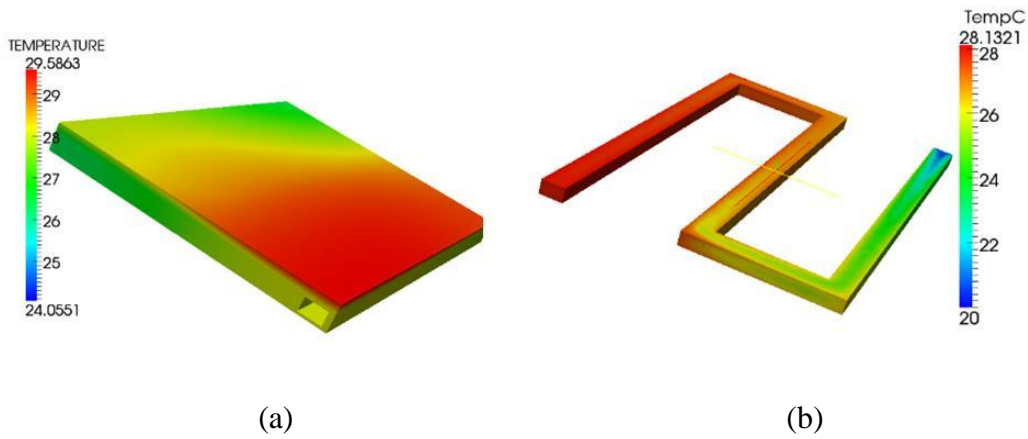


**Fig. 108.** Temperature results of the cooling of a prismatic battery cell by a cold plate: (a) solid domain of the cold plate, (b) liquid domain at the end of the simulation.

This discrepancy is mainly due to the use of a constant average convection heat coefficient between the cold plate and the cooling fluid. In consequence, the study may be completely reformulated and simplified.

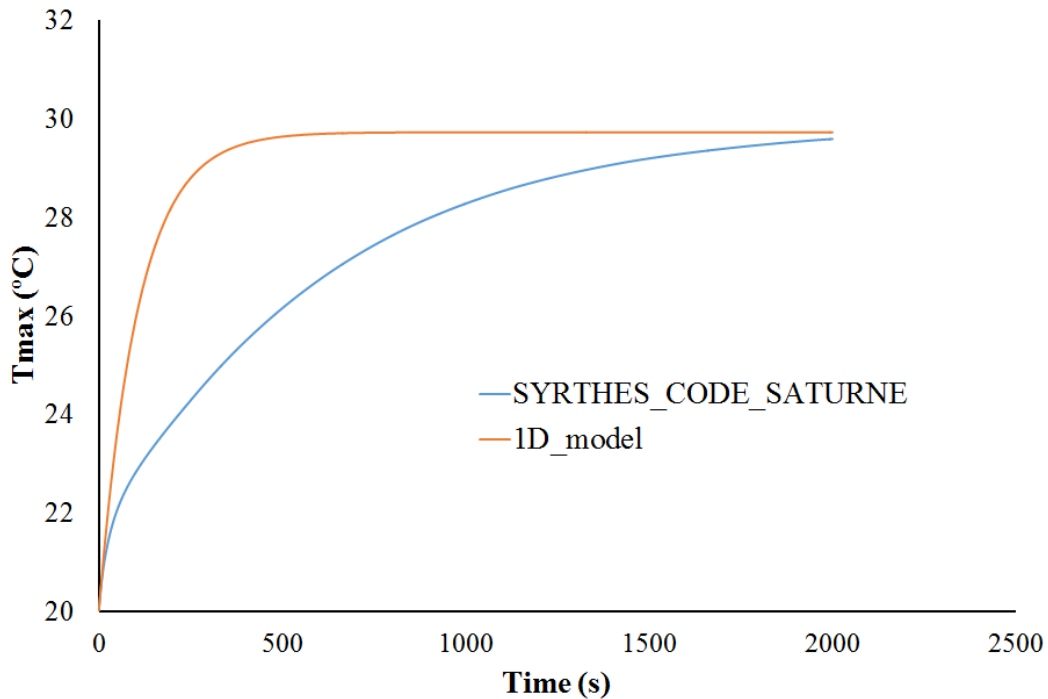


**Fig. 109.** Comparison between analytical model and CFD model for the optimization modelling procedure.

Straight lines will be considered first with heat generation based on the Bernardi et al [15] model. Besides, a better correlation will be investigated in order to describe the heat exchange between the fluid and the solid domain of the cold plate. For example, Nieto et al. [19] determined an average convective heat coefficient based on several simulations of a battery pack cooled by cold plates [19]. Close agreement was obtained with experiments and allow simplifying the CFD model.

The last part will present the thermal behavioural modelling of a component in order to create a more adaptive model and faster to use for simulation. This model is aimed to have a relatively low discrepancy even at off-design boundary conditions. This method is presented using the example of electronic components, which were its initial target.

#### 6.4.2. Dynamic compact thermal model using genetic algorithm

A Compact Thermal Model is a behavioural model developed in the electronic cooling analysis in order to perform complex thermal analysis and accelerate the simulation by replacing a component in a CFD simulation. It exists two types of compact model, the CTM (Compact Thermal Model) describing the steady state behaviour and the DCTM (Dynamic Compact Thermal Model) describing the transient behaviour. A CTM generation technique should be adaptable to standard conduction codes for performing a package-level thermal analysis and capable of insertion into standard numerical codes for system-level analysis.

The methodology was initially developed for electronic component, and one example is used to present the different steps. This methodology was developed by the DELPHI Research Consortium [78], which completed a 3-year research project from 1993 to 1996. The project was partially funded by the European Community under ESPRIT III Contract # 9197. The results of the Consortium's investigation into compact package models is non-proprietary and in the public domain. The consortium proposed a methodology for the generation of compact models with a high degree of boundary condition independence.

##### 6.4.2.1. DELPHI Methodology

This following picture presents the different steps to generate a thermal compact model:

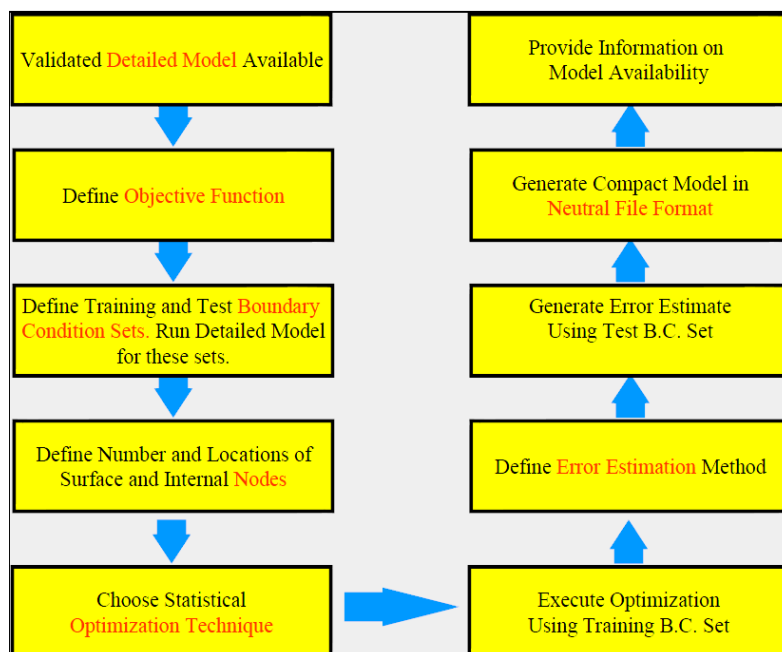


**Fig. 110.** DELPHI methodology

The different steps of the DELPHI methodology will be illustrated with the example of an electronic component called the QFN32, presented as follows:

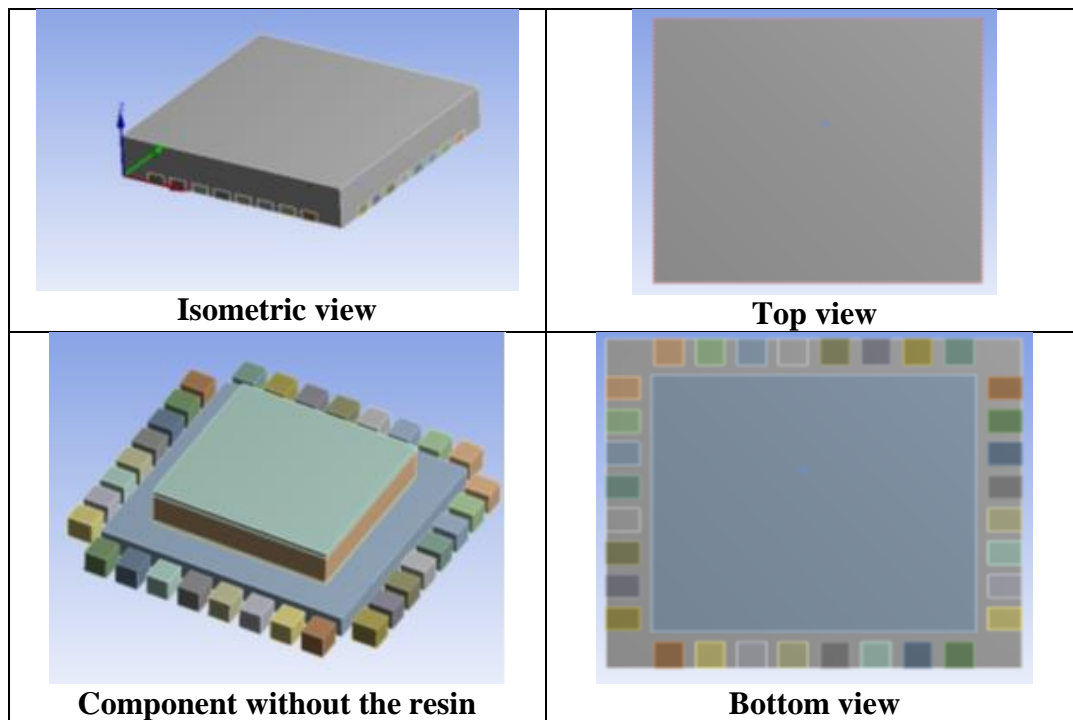


**Fig. 111.** 3D detailed model of the electronic component QFN32.

The picture above represents the detailed model of the component validated with experiment. Next, an objective function or score is defined, in order to determine if the compact model obtained by the optimization technique, is the best respecting the specification, in regard of the cases tested. The cases or scenarios are really important for obtaining low discrepancies at off-design boundary conditions.

#### *6.4.2.2. Boundary conditions set or scenarios*

The Boundary conditions set or scenarios were defined by the DELPHI Research Consortium and represent usual environmental conditions encountered by the component during its duty cycle and life. Each boundary condition is run with the component and the results on the particular surfaces or nodes are registered. The temperature for each node is then used as reference for the calculation of the objective function in order to find the compact model of the component.

The development of a battery cell compact model will imply the determination of suitable scenarios representing real driving operations. This following table presents an example of boundary conditions set used to generate the compact model of the QFN32.

**Table 13.** Example of boundary condition set.

trial	htop	hbottom	hside
1	5	5	1
2	5	10	5
3	5	25	5
4	5	50	5
5	20	800	10
6	5	100	5
7	15	1	15
8	15	10	15
9	15	25	15
10	15	50	15
11	1000	10	1
12	15	100	15

The suffix in front of each convective coefficient locates the application of the boundary condition on the top, bottom or side of the component. After the scenarios or boundary set defined, the nodes or surfaces must be chosen and depend on which part of the component is crucial to study.

*6.4.2.3. Choice of the nodes*

A node is a surface temperature cut from the external surface of the component based on the observation of the temperature distribution. Besides, internal nodes are chosen for representing the sensitive part of the electronic package. For example, Fig. 112 represents the nodes of the QFN32, where the different boundary conditions described in the scenarios are applied.

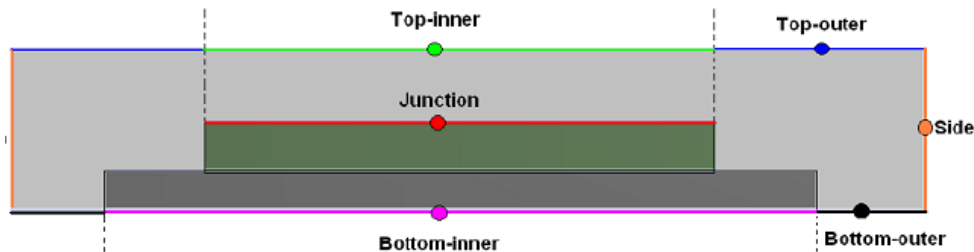


**Fig. 112.** Choice of the internal and external node of the QFN32.

All the nodes are linked with lines (Fig. 113), representing the thermal resistance, which are determined by the optimization technique, in function of the environment, i.e. the boundary conditions used.

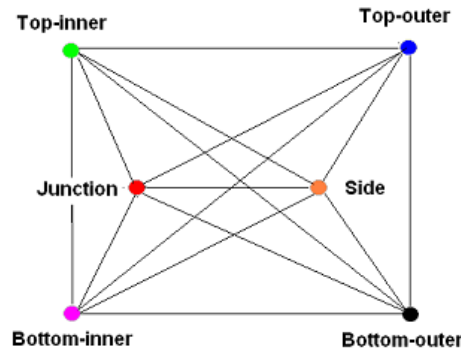


**Fig. 113.** Initial compact model before optimization process.

#### 6.4.2.4. Genetic algorithm

A genetic Algorithm was used for the Optimization and is based on the natural evolution theory. At the beginning, an initial population is chosen and the environment is simulated by the boundary condition set presented before. The purpose is to find the best individual which is more adapted to the environment or boundary conditions. The final aim is to obtain a compact model with the lowest discrepancy ([-5%; 5%]) between the temperature of the node given by the compact model and the results of the CFD for each boundary condition of Table 13.

The different steps of the algorithm are presents as follows:

- *Evaluation and Selection:*

The Initial Population  $Y$  is evaluated (Evaluation step) by a Score function, usually more the score is close to 1, and more the individual is adaptable (or can survive to the environment). Then, the  $\mu$  best candidates are selected for the reproduction and produce  $\lambda$  children. During the reproduction a rate of Crossover and Mutation fixed before is applied.

- *Crossover:*

The crossover increases the diversity in the population. More diversified individuals are better the chance to be more adaptable.

- *Mutation:*

The Mutation avoids local optimum, but a huge rate of mutation can destroy the evolution trend created. This is why the initial population is fixed ( $Y = \mu + \lambda$ ). Besides, the children obtained by mutation are evaluated through the score function and they are eliminated if they are inferior to the parents, which are kept instead. The contrary is programmed if the children are better than the parents.

This condition will avoid any degradation of the evolution process.

The entire procedure can be summarized in Fig. 114. Moreover, the final individual will be more adaptable if the number of scenario is important as well as their variability from one to another.

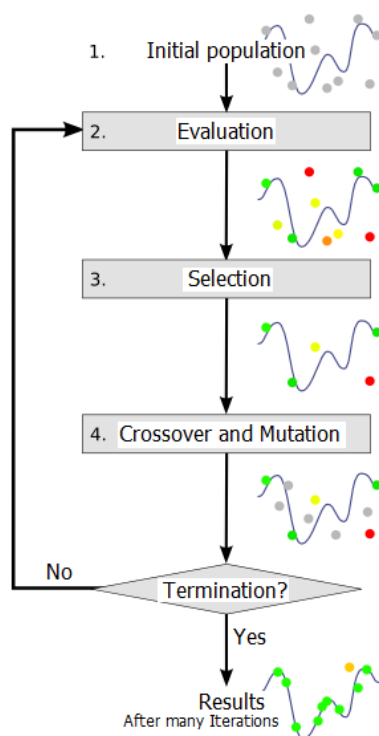


**Fig. 114.** Genetic Algorithm process [79].

#### 6.4.2.5. Error estimation

The error estimation is used for validating the Compact model and is usually estimated during the runtime of the genetic algorithm. The discrepancy tolerated, depends on the domain of application. The DELPHI Research Consortium for example fixed a maximum discrepancy of  $\pm 10\%$  on the internal and external node, because the model was just dedicated for pre-design study.

Moreover, an experiment was performed on an electronic component QFN32 connected to an electronic card 2S2P called PCB or Board, with an orthotropic conductivity ( $\lambda_x = 20$ ;  $\lambda_y = 20$ ;  $\lambda_z = 0.35$ ). There is natural convection on the top of the card and also heat radiation transfer during the experiment. The power generated by the component was 1.023W and the ambient temperature was 21.02°C.

A first case was performed with the 3D detailed component, the calculation took 50 minutes and the discrepancy with the experiment was +2.5% [79]. A second case was performed by replacing the real component by its compact model. The calculation took less than 2 min and the discrepancy on the junction temperature, compared to the experiment was +4.0% [79].

The compact model finally obtained, is stored and can be used again in CFD software, or coupled to an analytical model.

The compact modelling was never applied on a battery cooling analysis, but the general methodology can be adapted to it. The only disadvantage is the number of scenarios, which can be very important in order to have a compact model with low discrepancies for off-design cases. Furthermore, the detailed design must be fixed and not changed; otherwise everything would have to be recalculated. If the design of the battery is not fixed, the method would become less attractive since the compact model need the CFD results for the different scenarios used.

## References

- [1] L. Lu, X. Han, J. Li, J. Hua, M. Ouyang, A review on the key issues for lithium-ion battery management in electric vehicles, *J. Power Sources* 226 (2013) 272-288.
- [2] Z. Rao, S. Wang, A review of power battery thermal energy management, *Renew. Sustain. Energy Rev.* 15 (2011) 4554-4571.
- [3] T. Zhang, C. Gao, Q. Gao, G. Wang, M. Liu, Y. Guo, C. Xiao, Y.Y. Yan, Status and development of electric vehicle integrated thermal management from BTM to HVAC, *Appl. Therm. Eng.* 88 (2015) 328-409.
- [4] A. A. Pesaran, A. Vlahinos, T. Stuart, Cooling and Preheating of Batteries in Hybrid Electric Vehicles, *Japanese Soc. Mech. Eng. : The 6th ASME-JSME Therm. Eng. Jt. Conf.* (2003) 1-7.
- [5] T. Yuksel, J. Michalek, Development of Simulation Model to Analyse the Effect of Thermal Management on Battery Life. *SAE International* (2012).
- [6] A. A. Pesaran, Battery thermal models for hybrid vehicle simulations, *J. Power Sources* 110 (2002) 377-382.
- [7] L. Gao, S. Liu, A. Dougal, Dynamic Lithium-Ion Battery Model for System Simulation, *IEEE Trans. Compon. Packag. Technol.* 25 (2002) 495-505.
- [8] S. X. Chen, K. J. Tseng, S. S. Choi, Modeling of Lithium-Ion Battery for Energy Storage System Simulation, *IEEE Power. Energy Soc.* (2009) 1-4.
- [9] S.C. Chen, Zhu, C.C. Wan, Y.Y. Wang, Thermal analysis of lithium-ion batteries, *J. Power Sources* 140 (2005) 111-124.
- [10] C. Lin, K. Chen, F. Sun, P. Tang, H. Zhao, Research on thermo-physical properties identification and thermal analysis of EV Li-ion battery, *Vehicle Power and Propulsion Conference, VPPC'09, IEEE* (2009) 1643-1648.
- [11] M. C. Niculuta, C. Veje, Analysis of the thermal behavior of a LiFePO<sub>4</sub> battery cell, *J. Phys. : Conf Ser.* 395 (2012) 012013.
- [12] Y. Inui, Y. Kobayashi, Y. Watanabe, Y. Watase, Y. Kitamura, Simulation of temperature distribution in cylindrical and prismatic lithium ion secondary batteries, *Energy Convers. Manag.* 48 (2007) 2103-2109.
- [13] S.J. Drake, D.A. Wetz, J.K. Ostanek, S.P. Miller, J.M. Heinzl, A. Jain, Measurement of anisotropic thermophysical properties of cylindrical Li-ion cells, *J. Power Sources* 252 (2014) 298-304.

- [14] X. Hu, S. Lin, S. Stanton, W. Lian, 2011. A Foster Network Thermal Model for HEV/EV Battery Modeling. *IEEE Transaction on Industry Applications*, 47 (2011), pp.1692-1699.
- [15] D. Bernardi, E. Pawlikowski, J. Newman, A General Energy Balance for Battery Systems, *J. Electrochem. Soc.*, 132 (1985) 5-12.
- [16] H. Horie, T. Abe, T. Kinoshita, Y. Shimoida, A Study on an Advanced Lithium-ion Battery System for EVs, *The World Electr. Veh. J.* 2 (2008) 25-31.
- [17] G. Karimi, X. Li, Thermal management of lithium-ion batteries for electric vehicles, *Int. J. Energy Res.* 37 (2013)13-24.
- [18] R. Liu, J. Chen, J. Xun, K. Jiao, Q. Du, Numerical investigation of thermal behaviors in lithium-ion battery stack discharge, *Appl. Energy* 132 (2014) 288-297.
- [19] N. Nieto, L. Diaz, J. Gastelurrutia, F. Blanco, J. C. Ramos, Novel thermal management system design methodology for power lithium-ion battery, *J. Power Sources* 272 (2014) 291-302.
- [20] J. Newman, K.E. Thomas-Alyea, *Electrochemical Systems*, third ed., John Wiley & Sons Inc., New Jersey, 2004.
- [21] M. Doyle, T. Fuller, J. Newman, Modeling of galvanostatic charge and discharge of the lithium/polymer/insertion cell, *J. Electrochem. Soc.* 140 (1993) 1526-1533.
- [22] K. Smith, C. Wang, Power and thermal characterization of a lithium-ion battery pack for hybrid-electric vehicles, *J. Power Sources* 160 (2006) 662-673.
- [23] C. Zhu, X. Li, L. Song, L. Xiang, Development of a theoretically based thermal model for lithium ion battery pack, *J. Power Sources* 223 (2013) 155-164.
- [24] Y. Ye, Y. Shi, N. Cai, J. Lee, X. He, Electro-thermal modeling and experimental validation for lithium ion battery, *J. Power Sources* 199 (2012) 227-238.
- [25] E. Prada, D. Di Domenico, Y. Creff, J. Newman, J. Bernard, V. Sauvant-Moynot, F. Huet, Simplified Electrochemical and Thermal Model of LiFePO<sub>4</sub>-Graphite Li-Ion Batteries for Fast Charge Applications, *J. Electrochem. Soc.* 159 (2012) 1508-1519.
- [26] S. Santhanagopalan, Q. Guo, P. Ramadass, R. E. White, Review of models for predicting the cycling performance of lithium ion batteries, *J. Power Sources* 156 (2006) 620-628.
- [27] S. Chacko, Numerical analysis of unsteady heat transfer for thermal management. Ph. D. United Kingdom: Warwick University, 2012.
- [28] R. Liu, J. Chen, J. Xun, K. Jiao, Q. Du, Numerical investigation of thermal behaviors in lithium-ion battery stack discharge, *Appl. Energy* 132 (2014) 288-297.

- [29] J. Xun , R. Liu, K. Jiao, Numerical and analytical modeling of lithium ion battery thermal behaviors with different cooling designs, *J. Power Sources* 233 (2013) 47-61.
- [30] R. Mahamud, C. Park, Reciprocating air flow for Li-ion battery thermal management to improve temperature uniformity, *J. Power Sources* 196 (2011) 5685-5696.
- [31] M. Moussavi, S. Hoque, S. Rahnamayan, I. Dincer, G. F. Naterer, Optimal Design of an Air-Cooling System for a Li-Ion Battery Pack in Electric Vehicles with a Genetic Algorithm, *IEEE Congress on Evolutionary Computation (CEC)* (2011) 1848-1854.
- [32] A. Jarrett, I.Y. Kim, Design optimization of electric vehicle battery cooling plates for thermal performance, *J. Power Sources* 196 (23) (2011) 10359-10368.
- [33] A. Jarrett, I.Y. Kim, Influence of operating conditions on the optimum design of electric vehicle battery cooling plates, *J. Power Sources* 245 (2014) 644-655.
- [34] L.W. Jin, P.S. Lee, X.X. Kong, Y. Fan, S.K. Chou, Ultra-thin minichannel LCP for EV battery thermal management, *Appl. Energy* 113 (2014) 1786-1794.
- [35] M. S. Wu, K. H. Liu, Y. Y. Wang, C. C. Wan, Heat dissipation design for lithium-ion batteries, *J. Power Sources* 109 (2002) 160-166.
- [36] Z. Rao, S. Wang, M. Wu, Z. Lin, F. Lin, Experimental investigation on thermal management of electric vehicle battery with heat pipe, *Energy Convers. Manag.* 65 (2013) 92-97.
- [37] Z. J. Zuo, A. Faghri, A network thermodynamic analysis of the heat Pipe, *Int. J. Heat Mass Transf.* 41, 11 (1998) 1473-1484.
- [38] C. Romestant, Etudes théoriques et expérimentales de caloducs et de thermosiphons soumis à de fortes accélérations, Ph. D. France: ENSMA (Ecole Nationale Supérieure de Mécanique et d'Aérotechnique), 1992.
- [39] R. Bertossi, Modélisation des transferts de chaleur et de masse dans les caloducs : Contribution à l'analyse des phénomènes d'interfaces intervenant dans écoulements diphasiques. Ph. D. France: ENSMA (Ecole Nationale Supérieure de Mécanique et d'Aérotechnique), 2009.
- [40] Y. Avenas, Etude et réalisation de caloducs plats miniatures pour l'intégration en électronique de puissance. Ph. D. France: INPG (Institut National Polytechnique de Grenoble), 2009.
- [41] Z. H. Rao, S. F. Wang, Y. L. Zhang, Simulation of heat dissipation with phase change material for cylindrical power battery, *J. Energy Inst.* 85, 1 (2012) 38-43.
- [42] M. Y. Ramandi, I. Dincer, G. F. Naterer, Heat transfer and thermal management of electric vehicle batteries with phase change materials, *Heat Mass Transf.* 47 (2011) 777-788.

- [43] X. Duan, G. F. Naterer, Heat transfer in phase change materials for thermal management of electric vehicle battery modules, *Heat Mass Transf.* 53 (2010) 5176-5182.
- [44] X. Py, R. Olives, S. Mauran, Paraffin/Porous-graphite-matrix composite as a high and constant power thermal storage material, *Heat Mass Transf.* 44 (2011) 2727-2737.
- [45] S. Lingamneni, M. Asheghi, K.E. Goodson, A Parametric Study of Microporous Metal Matrix-Phase Change Material Composite Heat Spreaders for Transient Thermal Applications, *IEEE Intersociety Conference on Thermal and Thermomechanical Phenomena in Electronic Systems (ITHERM)*, Orlando, FL, USA (2014).
- [46] Z. Ling, J. Chen, X. Fang, Z. Zhang, T. Xu, X. Gao, S. Wang, Experimental and numerical investigation of the application of phase change materials in a simulative power batteries thermal management system, *Appl. Energy* 121 (2014) 104-113.
- [47] R. Kizilel, R. Sabbah, J.R. Selman, S. Al-Hallaj, An alternative cooling system to enhance the safety of Li-ion battery packs, *J. Power Sources* 194 (2009) 1105-1112.
- [48] G.H. Kim, J. Gonder, J. Lustbader, A. Pesaran, Thermal Management of Batteries in Advanced Vehicles Using Phase-Change Materials, *The World Electr. Veh. J.* 2 (2008) 46-52.
- [49] K. Onda, T. Ohshima, M. Nakayama, K. Fukuda, T. Araki, Thermal behavior of small lithium-ion battery during rapid charge and discharge cycles *J. Power Sources* 158 (2006) 535-542.
- [50] G. Guo, B. Long, B. Cheng, S. Zhou, P. Xu, B. Cao, Three-dimensional thermal finite element modeling of lithium-ion battery in thermal abuse application, *J. Power Sources* 195 (2010) 2393-2398.
- [51] P. Amiribavandpour, W. Shen, D. Mu, A. Kapoor, An improved theoretical electrochemical-thermal modelling of lithium-ion battery packs in electric vehicles, *J. Power Sources* 284 (2015) 328-338.
- [52] S. Al Hallaj, H. Maleki, J.S. Hong, J.R. Selman, Thermal modeling and design considerations of lithium-ion batteries, *J. Power Sources* 83 (1999) 1-8.
- [53] P. Taheri, M. Bahrami, Temperature Rise in Prismatic Polymer Lithium-Ion Batteries: An Analytic Approach, *SAE Int. J. Passeng. Cars - Electron. Electr. Syst.* 5,1 (2012) 164-176.
- [54] S. Saedodin, M. Torabi, Algebraically Explicit Analytical Solution of Three-Dimensional Hyperbolic Heat Conduction Equation, *Adv. Theor. Appl. Mech.* 3 (2010) 369-383.

- [55] A. Greco, D. Cao, X. Jiang, H. Yang, A theoretical and computational study of lithium-ion battery thermal management for electric vehicles using heat pipes, *J. Power Sources* 257 (2014) 344-355.
- [56] P. Lamberg, K.Siren, Approximate analytical model for solidification in a finite PCM storage with internal fins, *J. Appl. Math. Model.* 27 (2003) 491-513.
- [57] P. Lamberg, K.Siren, Analytical model for melting in a semi-infinite PCM storage with an internal fin, *Heat Mass Transf.* 39 (2003) 167-176.
- [58] K. Nithyanandam, R. Pitchunani, A. Mathur, Analysis of a latent thermocline storage system with encapsulated phase change materials for concentrating solar power, *Appl. Energy* 113 (2014) 1446-1460.
- [59] B. Wu, Y.M. Xing, Numerical study of graphite foams saturated with phase change materials in power system thermal management, *IEEE Power and Energy Engineering Conference (APPEEC)* (2010) 978-982.
- [60] S. Singh, P.K. Jain, Rizwan-Uddin, Analytical solution of time-dependent multilayer heat conduction problems for nuclear applications, *Int. J. Therm. Sci.* 47 (2008) 261-273.
- [61] F. de Monte, An analytic approach to the unsteady heat conduction processes in one-dimensional composite media, *Int. J. Heat Mass Transf.* 45 (2002) 1333-1343.
- [62] M.H. Belghazi, Modelisation analytique du transfert instationnaire de la chaleur dans un materiau bicouche en contact imparfait et soumis a une source de chaleur en mouvement, Ph. D. Thesis, Université de Limoges, France (2008).
- [63] F. de Monte, Transverse eigenproblem of steady-state heat conduction for multi-dimensional two-layered slabs with automatic computation of eigenvalues, *Int. J. Heat Mass Transf.* 47 (2004) 191-201.
- [64] S. Himran, A. Suwono, G. A. Mansoori, Characterization of alkanes and paraffin waxes for application as phase-change energy-storage medium, *Energy Sources.* 16 (1994) 117-128.
- [65] G. Sciuto, Innovative latent heat thermal storage elements design based on nanotechnologies, Ph.D. thesis, University of Trieste, Italy (2012).
- [66] A. Greco, X. Jiang, D. Cao, An investigation of lithium-ion battery thermal management using paraffin/porous-graphite-matrix composite, *J. Power Sources* 278 (2015) 50-68.
- [67] J. Breil, P.-H. Maire, A cell-centered diffusion scheme on two-dimensional unstructured meshes, *J. Comput. Phys.* 224 (2007) 785-823.

- [68] P.-H. Maire, J. Breil, A nominally second-order accurate finite volume cell-centered scheme for anisotropic diffusion on two-dimensional unstructured grids, *J. Comput. Phys.* 231 (2012) 2259-2299.
- [69] N. Sato, Thermal behaviour analysis of lithium-ions batteries for electric and hybrid vehicles, *J. Power Sources* 99 (2001) 70-77.
- [70] S. Santhanagopalan, Q. Guo, P. Ramadass, R. E. White, Single-Particle Model for a Lithium-Ion Cell: Thermal Behavior, *J. Power Sources* 156 (2006) 620-628.
- [71] M. Guo, G. Sikha, R. E. White, Thermal analysis of a cylindrical lithium-ion battery, *J. Electrochem. Soc.* 158 (2011) 122-132.
- [72] X. Zhang, Thermal analysis of a cylindrical lithium-ion battery, *Electrochem. Acta* 56 (2011) 1246-1255.
- [73] U. S. Kasavajjula, C. Wang, P. E. Arcea, Discharge Model for LiFePO<sub>4</sub> Accounting for the Solid Solution Range, *J. Electrochem. Soc.* 155 (2008) 866-874.
- [74] V. V. Viswanathan, D. Choi, D. Wang, W. Xu, S. Towne, R. E. Williford, J. Zhang, J. Liu, Z. Yang, Effect of entropy change of lithium intercalation in cathodes and anodes on Li-ion battery thermal management, *J. Power Sources* 195 (2010) 3720-2729.
- [75] V. R. Subramanian, R. E. White, New separation of variables method for composite electrodes with galvanostatic boundary conditions, *J. Power Sources* 96 (2001) 385-395.
- [76] S. Lips, Frederic Lefevre, A general analytical model for the design of conventional heat pipes, *Heat Mass Transf.* 72 (2014) 288-298.
- [77] M. Xu, Z. Zhang, X. Wang, Li. Jia, L. Yang, Two-dimensional electrochemical-thermal coupled modeling of cylindrical LiFePO<sub>4</sub> batteries, *J. Power Sources* 256 (2014) 233-243.
- [78] JEDEC Solid State Technology Association (2008). *JEDEC Standard: DELPHI Compact Thermal Model.Guideline (JEDEC15-4)*, Arlington (USA).
- [79] A. Greco, C.T. Dia, Optimization of behavioural models: Thermal model of electronic components in transient mode using a Genetic Algorithms. THALES GLOBAL SERVICES (2011). pp14-108.

## Appendix A

The demonstration of the orthogonality condition (3.11) is considered for  $\mu_n \neq \mu_m$ :

$$\langle \tilde{X}_n | \tilde{X}_m \rangle_r = \int_0^R r J_0(\mu_n r) J_0(\mu_m r) dz = 0 \quad (\text{A.1})$$

The functions  $J_0(\mu_n r)$  and  $J_0(\mu_m r)$  verify Eq. (3.5a), as presented in Eq. (A.2a) and (A.2b).

$$\frac{d}{dr} \left( r \frac{dJ_0(\mu_n r)}{dr} \right) + \mu_n^2 r J_0(\mu_n r) = 0 \quad (\text{A.2a})$$

$$\frac{d}{dr} \left( r \frac{dJ_0(\mu_m r)}{dr} \right) + \mu_m^2 r J_0(\mu_m r) = 0 \quad (\text{A.2b})$$

Eq. (A.2a) and (A.2b) are multiplied respectively by  $J_0(\mu_m r)$  and  $J_0(\mu_n r)$ , and subtracted as follows:

$$(\mu_n^2 - \mu_m^2) r J_0(\mu_m r) J_0(\mu_n r) + J_0(\mu_m r) \frac{d}{dr} \left( r \frac{dJ_0(\mu_n r)}{dr} \right) - J_0(\mu_n r) \frac{d}{dr} \left( r \frac{dJ_0(\mu_m r)}{dr} \right) = 0 \quad (\text{A.3})$$

However,

$$\begin{aligned} \frac{d}{dr} \left( J_0(\mu_m r) \left( r \frac{dJ_0(\mu_n r)}{dr} \right) - J_0(\mu_n r) \left( r \frac{dJ_0(\mu_m r)}{dr} \right) \right) = \\ J_0(\mu_m r) \frac{d}{dr} \left( r \frac{dJ_0(\mu_n r)}{dr} \right) - J_0(\mu_n r) \frac{d}{dr} \left( r \frac{dJ_0(\mu_m r)}{dr} \right) \end{aligned} \quad (\text{A.4})$$

Eq. (A.4) is then replaced in Eq. (A.3) and integrated between 0 and R.

$$(\mu_n^2 - \mu_m^2) \int_0^R r J_0(\mu_m r) J_0(\mu_n r) + [-J_0(\mu_m r) r \mu_n J_1(\mu_n r) + J_0(\mu_n r) r \mu_m J_1(\mu_m r)]_0^R = 0 \quad (\text{A.5})$$

The simplification of Eq. (A.5) leads to

$$(\mu_n^2 - \mu_m^2) \int_0^R r J_0(\mu_m r) J_0(\mu_n r) + -J_0(\mu_m R) R \mu_n J_1(\mu_n R) + J_0(\mu_n R) R \mu_m J_1(\mu_m R) = 0 \quad (\text{A.6})$$

The transcendental equation (3.7) is used, which leads to:

$$\begin{aligned} (\mu_n^2 - \mu_m^2) \int_0^R r J_0(\mu_m r) J_0(\mu_n r) + -Bi_r J_0(\mu_m R) J_0(\mu_n R) + Bi_r J_0(\mu_n R) J_0(\mu_m R) = 0 \\ (\mu_n^2 - \mu_m^2) \int_0^R r J_0(\mu_m r) J_0(\mu_n r) = 0 \end{aligned} \quad (\text{A.7})$$

Because  $\mu_n \neq \mu_m$ , the relation (A.7) gives finally  $\int_0^R r J_0(\mu_m r) J_0(\mu_n r) = 0$

The calculation of  $E_n = \int_0^R r \tilde{X}_n dr$  is obtained using Eq. (3.5a) and the transcendental equation

(3.7) leading to the following equation

$$\frac{d}{dr}(\mu_n r J_1(\mu_n r)) = \mu_n^2 r J_0(\mu_n r) \quad (\text{A.8})$$

Consequently the following equation results from the integration of Eq. (A.8) between 0 and R:

$$\int_0^R \frac{d}{dr}(\mu_n r J_1(\mu_n r)) dr = \mu_n^2 \int_0^R r J_0(\mu_n r) dr \quad (\text{A.9})$$

The calculation of the left-hand side of Eq. (A.9) gives finally to the solution:

$$\int_0^R r J_0(\mu_n r) dr = E_n = \frac{R J_1(\mu_n R)}{\mu_n} \quad (\text{A.10})$$

The right-hand side of Eq. (A.9) is dedicated to the calculation of

$$\langle \tilde{X}_n | \tilde{X}_n \rangle_r = \Omega_n = \int_0^R r J_0(\mu_n r)^2 dr. \text{ The eigenfunction } \tilde{X}_n \text{ is replaced in Eq. (3.5a) and}$$

multiplied by  $2 \frac{d}{dr}(J_0(\mu_n r))$ , leading to

$$2r \frac{d}{dr}(J_0(\mu_n r)) \frac{d}{dr} \left( r \frac{dJ_0(\mu_n r)}{dr} \right) + 2\mu_n^2 r^2 \frac{d}{dr}(J_0(\mu_n r)) J_0(\mu_n r) = 0 \quad (\text{A.11})$$

Eq. (A.11) can be rewritten as follows:

$$\frac{d}{dr} \left[ \left( r \frac{dJ_0(\mu_n r)}{dr} \right)^2 \right] + \mu_n^2 r^2 \frac{d}{dr} \left[ (J_0(\mu_n r))^2 \right] = 0 \quad (\text{A.12})$$

Integration of Eq. (A.12) between 0 and R leads to

$$\int_0^R \frac{d}{dr} \left[ \left( r \frac{dJ_0(\mu_n r)}{dr} \right)^2 \right] dr + \mu_n^2 \int_0^R r^2 \frac{d}{dr} \left[ (J_0(\mu_n r))^2 \right] dr = 0 \quad (\text{A.13})$$

The first integral of Eq. (A.13) is integrated directly and simplified with the transcendental equation (3.7). The second one is modified with integration by parts.

$$R^2 \left( \frac{h}{k_r} J_0(\mu_n R) \right)^2 + \mu_n^2 \left( (J_0(\mu_n R))^2 R^2 - 2 \int_0^R r (J_0(\mu_n r))^2 dr \right) = 0 \quad (\text{A.14})$$

Finally some arrangement in Eq. (A.14) gives the solution Eq. (A.15).

$$\int_0^R r (J_0(\mu_n r))^2 dr = \frac{(\mu_n^2 + (h_r/k_r)^2) R^2}{2\mu_n^2} (J_0(\mu_n R))^2 \quad (\text{A15})$$

## Appendix B

The orthogonality condition (3.33a) is demonstrated in this Appendix for  $n \neq m$ . The subscripts  $i = 1, 2$ , designate the battery and the PCM/CENG respectively.

The functions  $\tilde{R}_{i,n}$  and  $\tilde{R}_{i,m}$  verify the following equations:

$$\frac{d}{dr} \left( r \frac{d\tilde{R}_{i,n}}{dr} \right) + \frac{\lambda_{1,n}^2 \alpha_1}{\alpha_i} r \tilde{R}_{i,n} = 0, \text{ with } \lambda_{1,n}^2 \alpha_i = \lambda_{1,n}^2 \alpha_1 \quad (\text{B.1a})$$

$$\frac{d}{dr} \left( r \frac{d\tilde{R}_{i,m}}{dr} \right) + \frac{\lambda_{1,m}^2 \alpha_1}{\alpha_i} r \tilde{R}_{i,m} = 0, \text{ with } \lambda_{1,m}^2 \alpha_i = \lambda_{1,m}^2 \alpha_1 \quad (\text{B.1b})$$

Eqs. (B.1a) and (B.1b) are multiplied respectively by  $k_i \tilde{R}_{i,m}$  and  $k_i \tilde{R}_{i,n}$ , and subtracted. This operation is followed by the integration between  $r_{i-1}$  and  $r_i$ , leading to

$$\int_{r_{i-1}}^{r_i} k_i \left( \tilde{R}_{i,m} \frac{d}{dr} \left( r \frac{d\tilde{R}_{i,n}}{dr} \right) - \tilde{R}_{i,n} \frac{d}{dr} \left( r \frac{d\tilde{R}_{i,m}}{dr} \right) \right) dr + \int_{r_{i-1}}^{r_i} k_i (\lambda_{1,n}^2 - \lambda_{1,m}^2) \frac{\alpha_1}{\alpha_i} r \tilde{R}_{i,n} \tilde{R}_{i,m} dr = 0 \quad (\text{B.2})$$

$$\tilde{R}_{i,m} \frac{d}{dr} \left( r \frac{d\tilde{R}_{i,n}}{dr} \right) - \tilde{R}_{i,n} \frac{d}{dr} \left( r \frac{d\tilde{R}_{i,m}}{dr} \right) = \frac{d}{dr} \left( \tilde{R}_{i,m} \left( r \frac{d\tilde{R}_{i,n}}{dr} \right) - \tilde{R}_{i,n} \left( r \frac{d\tilde{R}_{i,m}}{dr} \right) \right), \text{ therefore, Eq. (B.2)}$$

can be rewritten as Eq. (B.3).

$$k_i \left[ \tilde{R}_{i,m} \left( r \frac{d\tilde{R}_{i,n}}{dr} \right) - \tilde{R}_{i,n} \left( r \frac{d\tilde{R}_{i,m}}{dr} \right) \right]_{r_{i-1}}^{r_i} + \int_{r_{i-1}}^{r_i} k_i (\lambda_{1,n}^2 - \lambda_{1,m}^2) \frac{\alpha_1}{\alpha_i} r \tilde{R}_{i,n} \tilde{R}_{i,m} dr = 0 \quad (\text{B.3})$$

Eq. (B.3) is then summed from 1 to 2 with  $r_0$  representing the origin of the battery.

$$\sum_{i=1}^2 k_i \left[ \tilde{R}_{i,m} \left( r \frac{d\tilde{R}_{i,n}}{dr} \right) - \tilde{R}_{i,n} \left( r \frac{d\tilde{R}_{i,m}}{dr} \right) \right]_{r_{i-1}}^{r_i} + \sum_{i=1}^2 \int_{r_{i-1}}^{r_i} k_i (\lambda_{1,n}^2 - \lambda_{1,m}^2) \frac{\alpha_1}{\alpha_i} r \tilde{R}_{i,n} \tilde{R}_{i,m} dr = 0 \quad (\text{B.4})$$

The calculation of the first term of Eq. (B.4) is developed and calculated for each value.

$$\begin{aligned} \sum_{i=1}^2 k_i \left[ \tilde{R}_{i,m} \left( r \frac{d\tilde{R}_{i,n}}{dr} \right) - \tilde{R}_{i,n} \left( r \frac{d\tilde{R}_{i,m}}{dr} \right) \right]_{r_{i-1}}^{r_i} &= k_1 \left[ \tilde{R}_{1,m} \left( r \frac{d\tilde{R}_{1,n}}{dr} \right) - \tilde{R}_{1,n} \left( r \frac{d\tilde{R}_{1,m}}{dr} \right) \right]_0^{r_1} \\ &+ k_2 \left[ \tilde{R}_{2,m} \left( r \frac{d\tilde{R}_{2,n}}{dr} \right) - \tilde{R}_{2,n} \left( r \frac{d\tilde{R}_{2,m}}{dr} \right) \right]_{r_1}^{r_2} \end{aligned} \quad (\text{B.4a})$$

The term of the sum (Eq. (B.4a)) at  $r = r_0 = 0$  is equal to zero due to the boundary condition (3.29c). Moreover, the value of the sum at  $r = r_1$  is also equal to zero due to continuity of the flux at the interface (Eq. (3.29f)). Finally the value of the sum at  $r = r_2$ , leads to zero with the use of the boundary condition (3.29d). Therefore, Eq. (B.4a) is equal to zero leading to Eq. (B5).

$$\sum_{i=1}^2 \int_{r_{i-1}}^{r_i} k_i (\lambda_{1,n}^2 - \lambda_{1,m}^2) \frac{\alpha_1}{\alpha_i} r \tilde{R}_{i,n} \tilde{R}_{i,m} dr = 0 \quad (\text{B.5})$$

Because  $\lambda_{1,n} \neq \lambda_{1,m}$ , it can be conclude that  $\sum_{i=1}^2 \int_{r_{i-1}}^{r_i} \frac{k_i}{\alpha_i} r \tilde{R}_{i,n} \tilde{R}_{i,m} dr = 0$

The calculation of  $H_n = \sum_{i=1}^2 \int_{r_{i-1}}^{r_i} \frac{k_i}{\alpha_i} r \tilde{R}_{i,n} \tilde{R}_{i,n} dr$  is explained in detail in the next part. Integration

by part is performed to determine an expression of  $\int_{r_{i-1}}^{r_i} r \tilde{R}_{i,n} \tilde{R}_{i,n} dr$ .

$$\int_{r_{i-1}}^{r_i} r \tilde{R}_{i,n} \tilde{R}_{i,n} dr = \left[ \frac{r^2}{2} \tilde{R}_{i,n}^2 \right]_{r_{i-1}}^{r_i} - \int_{r_{i-1}}^{r_i} r^2 \tilde{R}_{i,n} \frac{d\tilde{R}_{i,n}}{dr} dr \quad (\text{B.6})$$

Integration by part is performed again on the second term Eq. (B.6) as follows:

$$\int_{r_{i-1}}^{r_i} (r \tilde{R}_{i,n}) \left( r \frac{d\tilde{R}_{i,n}}{dr} \right) dr = \left[ \left( \int_0^r r \tilde{R}_{i,n} dr \right) \left( r \frac{d\tilde{R}_{i,n}}{dr} \right) \right]_{r_{i-1}}^{r_i} - \int_{r_{i-1}}^{r_i} \left( \int_0^r r \tilde{R}_{i,n} dr \right) \frac{d}{dr} \left( r \frac{d\tilde{R}_{i,n}}{dr} \right) dr \quad (\text{B.7})$$

One primitive of  $r \tilde{R}_{i,n}$  is evaluated using Eq. (B.1a). The value of this primitive is then calculated.

$$\int_0^r r \tilde{R}_{i,n} dr = -\frac{1}{b_{i,n}} \int_0^r \frac{d}{dr} \left( r \frac{d\tilde{R}_{i,n}}{dr} \right) dr = -\frac{1}{b_{i,n}} r \frac{d\tilde{R}_{i,n}}{dr}; \text{ with } b_{i,n} = \frac{\lambda_{1,n}^2 \alpha_1}{\alpha_i} \quad (\text{B.7a})$$

The application of Eq. (B.7a) leads finally to Eq. (B.7b).

$$\int_{r_{i-1}}^{r_i} (r \tilde{R}_{i,n}) \left( r \frac{d\tilde{R}_{i,n}}{dr} \right) dr = \left[ -\frac{1}{2b_{i,n}} \left( r \frac{d\tilde{R}_{i,n}}{dr} \right)^2 \right]_{r_{i-1}}^{r_i} \quad (\text{B.7c})$$

The final evaluation of  $H_n$ , i.e. for  $n = m$  is:

$$H_n = \sum_{i=1}^2 \frac{k_i}{\alpha_i} \left( \left[ \frac{r^2}{2} \tilde{R}_{i,n}^2 \right]_{r_{i-1}}^{r_i} + \left[ \frac{1}{2b_{i,n}} \left( r \frac{d\tilde{R}_{i,n}}{dr} \right)^2 \right]_{r_{i-1}}^{r_i} \right) \quad (\text{B.8})$$

The calculation of  $F_n = \int_0^{r_1} r \tilde{R}_{1,n} dr$  is obtained directly by the integration of Eq. (B.1a).

$$F_n = \int_0^{r_1} r \tilde{R}_{1,n} dr = -\frac{1}{b_{1,n}} \int_0^{r_1} \frac{d}{dr} \left( r \frac{d\tilde{R}_{1,n}}{dr} \right) dr = -\frac{1}{\lambda_{1,n}^2} r_1 \frac{d\tilde{R}_{1,n}}{dr} (r = r_1) \quad (\text{B.9})$$

## Appendix C

First 74 roots of the analytical solution of the cylindrical battery cell cooled by PCM/CENG, for the test case described in sub-section 3.4.1. Besides, the first 75 roots of the analytical solution with the n-Octadecane as PCM are presented.

**Table C.1:** Roots of the transcendental equation (3.32b).

PCM-Heptadecane		PCM-Octadecane	PCM-Heptadecane		PCM-Octadecane
n	$\lambda_{1,n}r_1$	$\lambda_{1,n}r_1$	n	$\lambda_{1,n}r_1$	$\lambda_{1,n}r_1$
0	0.90406	0.84005	44	121.32970	118.67150
1	2.55506	2.52747	45	123.33140	121.73940
2	5.55632	5.54482	46	125.28740	124.81370
3	8.64337	8.63506	47	128.15930	127.84420
4	11.74172	11.73205	48	131.20480	130.54840
5	14.83152	14.81054	49	134.28030	132.11840
6	17.87622	17.77773	50	137.34850	134.52510
7	20.62239	19.79482	51	140.35270	137.51900
8	22.19799	21.52734	52	142.94210	140.58770
9	24.55516	24.42774	53	144.58500	143.66140
10	27.54876	27.49174	54	147.10430	146.68830
11	30.62166	30.57424	55	150.09800	149.36350
12	33.70391	33.63308	56	153.16420	150.91850
13	36.76118	36.52108	57	156.24010	153.36730
14	39.67398	38.32945	58	159.28970	156.36640
15	41.70658	40.34037	59	162.18880	159.43590
16	43.59414	43.27992	60	164.23490	162.50900
17	46.46122	46.34362	61	166.15180	165.53230
18	49.50976	49.42210	62	169.00780	168.17850
19	52.58787	52.47131	63	172.05050	169.72300
20	55.65839	55.30796	64	175.12540	172.20990
21	58.66390	57.02047	65	178.19450	175.21390
22	61.23787	59.16958	66	181.20360	178.28400
23	62.85983	62.12859	67	183.82960	181.35650
24	65.40282	65.19342	68	185.48180	184.37630
25	68.40341	68.27016	69	187.95790	186.99310
26	71.47217	71.31323	70	190.94460	188.53100
27	74.54900	74.11082	71	194.00940	191.05310
28	77.59739	75.76692	72	197.08530	194.06130
29	80.48086	78.00508	73	200.13720	197.13210
30	82.46088	80.97644	74		200.20400
31	84.43086	84.04241			
32	87.31091	87.11810			
33	90.35845	90.15645			
34	93.43465	92.92067			
35	96.50281	94.53867			
36	99.50404	96.84358			
37	102.06770	99.82402			
38	103.70410	102.89100			
39	106.25240	105.96590			
40	109.25120	109.00020			

41	112.31870	111.73380
42	115.39470	113.32420
43	118.44270	115.68380

---

## Appendix D

The polynomial coefficients of the experimental entropy data, for the cathode (LFP-NEI) and anode (G-A) [74] are presented in Table D.1. The polynomial function of one electrode is written as follows:

$$\Delta S = \frac{dU}{dT} F = \sum_{i=0} a_i \left( x_s^{surf} \right)^i \quad (\text{D.1})$$

where  $x_s^{surf}$  is the variables of the functions, representing the normalized Li-ion concentration at the anode and cathode. Only one polynomial function was used in the case of the cathode, when two functions were needed in order to fit properly the experimental data of the anode. The second polynomial function of the anode is used when  $x_{s,n}^{surf} \geq 0.54955$ .

**Table D.1:** Coefficients of the polynomial function of the entropy for the cathode and anode.

$a_i$	Cathode	Anode
0	-11.14138245	-35.79940532
1	167.6848766	255.302722
2	-1747.202821	-2903.98837
3	9468.722633	43159.48593
4	-28924.67064	-300008.0962
5	51710.03116	1075121.128
6	-53542.27784	-2085195.488
7	29656.09707	2092539.924
8	-6765.32763	-858896.4461
		If $x_{s,n}^{surf} \geq 0.54955$ then:
0		-97.19653542
1		14628.2168
2		-90082.83437
3		223120.8766
4		-274283.8687
5		166924.9281
6		-40189.67948

## Appendix E

This Appendix presents the demonstration of the Li-ion concentration gradient in the electrolyte  $c_e(0) - c_e(L)$  at the steady state.

The electrolyte diffusion coefficient  $D_{e,k}^{eff} = D_e \varepsilon_{e,k}^{brugg}$  is supposed constant, and the source

term is represented by  $q_k = (1 - t_+) \frac{j_{f,k}}{F}$ , with  $k$  designating the anode, separator and cathode.

In the steady state, and with the assumption of constant electrolyte diffusion, Eq. (5.2) becomes:

$$D_{e,k}^{eff} \frac{\partial^2 c_{e,k}}{\partial z^2} = -q_k \quad (\text{E.1})$$

Besides, the concentration in the electrolyte is considering only depending on  $z$

$$D_{e,k}^{eff} \frac{d^2 c_{e,k}}{dz^2} = -q_k \quad (\text{E.1a})$$

The integration of Eq. (E.1a) at the anode leads to Eq. (E.2). The constant  $a_n$  is obtained with the boundary conditions Eq. (5.2a) at  $z = 0$  and gives Eq. (E.2a).

$$c_{e,n}(z) = -\frac{q_n}{D_{e,n}^{eff}} \frac{z^2}{2} + a_n z + b_n \quad (\text{E.2})$$

$$c_{e,n}(z) = -\frac{q_n}{D_{e,n}^{eff}} \frac{z^2}{2} + b_n \quad (\text{E.2a})$$

The integration of Eq. (E.1a) is performed at the separator with  $q_{sep} = 0$  which leads to Eq. (E.3).

$$c_{e,sep}(z) = a_{sep} z + b_{sep} \quad (\text{E.3})$$

The continuity of the flux at  $z = \delta_n$  described by Eq. (E.3a) is used to obtain the constant  $a_{sep}$ .

$$D_{e,n}^{eff} \frac{dc_{e,n}}{dz}(z = \delta_n) = D_{e,sep}^{eff} \frac{dc_{e,sep}}{dz}(z = \delta_n) \quad (\text{E.3a})$$

$$c_{e,n}(z = \delta_n) = c_{e,sep}(z = \delta_n) \quad (\text{E.3b})$$

Therefore, Eq. (E.3) becomes Eq. (E.3c), while the continuity of the concentration at  $z = \delta_n$  described by Eq. (E.3b) leads to Eq. (E.3d) between  $b_n$  and  $b_{sep}$ .

$$c_{e,sep}(z) = \frac{-q_n \delta_n}{D_{e,sep}^{eff}} z + b_{sep} \quad (\text{E.3c})$$

$$b_n - b_{sep} = -q_n \delta_n^2 \left( \frac{1}{D_{e,sep}^{eff}} - \frac{1}{2D_{e,n}^{eff}} \right) \quad (\text{E.3d})$$

Then, the identical method is applied at the cathode and leads from the integration of Eq. (E.1a) and the use of the Boundary equation Eq. (5.2a) at  $z = L$ , to Eq. (E.4).

$$c_{e,p}(z) = -\frac{q_p}{D_{e,p}^{eff}} \frac{z^2}{2} + \frac{q_p L}{D_{e,p}^{eff}} z + b_p \quad (\text{E.4})$$

$$D_{e,sep}^{eff} \frac{dc_{e,sep}}{dz}(z = L - \delta_p) = D_{e,p}^{eff} \frac{dc_{e,p}}{dz}(z = L - \delta_p) \quad (\text{E.4a})$$

$$c_{e,sep}(z = L - \delta_p) = c_{e,p}(z = L - \delta_p) \quad (\text{E.4b})$$

Moreover, the continuity of the flux and concentration at  $z = L - \delta_p$ , described by Eq. (E.4a) and Eq. (E.4b), leads to Eq. (E.4c) and Eq. (E.4d) respectively.

$$-q_n \delta_n = q_p \delta_p \quad (\text{E.4c})$$

$$b_{sep} - b_p = q_p (L - \delta_p) \left( \frac{L}{2D_{e,p}^{eff}} + \frac{\delta_p}{2D_{e,p}^{eff}} - \frac{\delta_p}{D_{e,sep}^{eff}} \right) \quad (\text{E.4d})$$

In addition, Eq. (E2.a) and Eq. (E.4) leads to the following equations at  $z = 0$  and  $z = L$  respectively.

$$b_n = c_{e,n}(z = 0) = c_e(0) \quad (\text{E.5})$$

$$b_p = c_{e,p}(z = L) - \frac{q_p L^2}{2D_{e,p}^{eff}} = c_e(L) - \frac{q_p L^2}{2D_{e,p}^{eff}} \quad (\text{E.6})$$

Next, Eq. (E.4d) and Eq. (E.3d) are added and gives Eq. (E7).

$$b_n - b_p = -q_n \delta_n^2 \left( \frac{1}{D_{e,sep}^{eff}} - \frac{1}{2D_{e,n}^{eff}} \right) + q_p (L - \delta_p) \left( \frac{L}{2D_{e,p}^{eff}} + \frac{\delta_p}{2D_{e,p}^{eff}} - \frac{\delta_p}{D_{e,sep}^{eff}} \right) \quad (\text{E.7})$$

Finally, Eq. (E.5) and Eq. (E.6) are replaced into Eq. (E.7) and gives Eq. (E7.a).

$$c_e(0) - c_e(L) + \frac{q_p L^2}{2D_{e,p}^{eff}} = -q_n \delta_n^2 \left( \frac{1}{D_{e,sep}^{eff}} - \frac{1}{2D_{e,n}^{eff}} \right) + q_p (L - \delta_p) \left( \frac{L}{2D_{e,p}^{eff}} + \frac{\delta_p}{2D_{e,p}^{eff}} - \frac{\delta_p}{D_{e,sep}^{eff}} \right) \quad (\text{E.7a})$$

The solution presented at Eq. (5.13a) is finally obtained from rearrangements of Eq. (E7.a).